2019

High Loading Oxide Anodes For Lithium Ion Batteries Via A Superelastic Graphene Composite Approach

Zhichao Zhang
University of Pennsylvania

High Loading Oxide Anodes For Lithium Ion Batteries Via A Superelastic Graphene Composite Approach

Abstract

ABSTRACT

HIGH LOADING OXIDE ANODES FOR LITHIUM ION BATTERIES VIA A SUPERELASTIC GRAPHENE COMPOSITE APPROACH

Zhichao Zhang

Dr. I-Wei Chen

Although nanotechnology has ushered in many new materials storing a high density of electrochemical energy, the performance has only been demonstrated at low material densities, typically ~0.15 g cm-3 and ~ 1 mg cm-2. Such densities fall far short of the loading requirement of commercial electrodes, which is 1.6 g cm-3 and 10 mg cm-2. Yet progress in overcoming this problem has been slow because of fundamental thermodynamic and kinetic difficulties. This thesis solves the problem for anodes of lithium-ion batteries.

We start by developing a new graphene network monolith that is superelastic, meso-porous, three-dimensional and metallic conducting. The network already features excellent electrochemical performance, but it can also support relatively insulating active materials while endowing them much improved conductivity to aid electrochemical reactivity. With active-material nanoparticles robustly deposited and adhered to the network, the three-dimensional composite monolith, starting as an composite aerogel, can be non-destructively and conformally deformed to high compression ratios to reach the requisite volumetric and areal loadings and to obtain an anode that fits into a coin cell. Although the resulting high-density electrode already has most of its void space removed, it still has undisturbed nanoparticles, with their local structure connected to a continuous conduit of liquid and ion transport. This allows active electrochemical processes to proceed in the assembled cell at high charging/ discharging rates.

The active materials studied are SnO_2, GeO_2, ZnO, Fe_2O_3 and TiO_2. Except for TiO_2, they feature theoretical capacities ranging from 2152 mAh g-1 to 988 mAh g-1, but also suffer from volumetric expansions varying from 376% to 93% when Li is incorporated by insertion, conversion and alloying reactions. Such large expansion is usually destructive rendering the materials useless, but when such materials in the form of nanoparticles are incorporated into our composites, they have delivered superior areal and volumetric capacities much higher than those of high-performance experimental materials in the literature and even commercial graphite anode.

This thesis has thus demonstrated a promising approach that can help transition nanomaterials to practical use in lithium-ion batteries. Specifically, it provides several new anodes that can realistically replace commercial graphite anode with significantly improved performance.

Degree Type

Dissertation

Degree Name

Doctor of Philosophy (PhD)

HIGH LOADING OXIDE ANODES FOR LITHIUM ION BATTERIES VIA A SUPERELASTIC GRAPHENE COMPOSITE APPROACH

Zhichao Zhang

A DISSERTATION

in

Materials Science and Engineering

Presented to the Faculties of the University of Pennsylvania

in

Partial Fulfillment of the Requirements for the

Degree of Doctor of Philosophy

2019

Supervisor of Dissertation

_____

I-Wei Chen

Skirkanich Professor of Materials Innovation of Materials Science & Engineering

Graduate Group Chairperson

_____

I-Wei Chen, Skirkanich Professor of Materials Innovation of Materials Science & Engineering

Dissertation Committee

Sue Ann Bidstrup Allen, Professor of Chemical and Biomolecular Engineering

Peter K. Davies, Class of 1942 Term Professor of Materials Science and Engineering

Eric Detsi, Stephenson Term Chair Assistant Professor of Materials Science & Engineering

ACKNOWLEDGMENTS

I would like to thank my advisor, Dr. I-Wei Chen, for the education, training and patience to me throughout my PhD study. He has introduced me to the fantastic world of scientific research and used his high-standard for research to teach me how to conduct research creatively and rigorously. I have learnt from him how a world-class scientist devotes to his research, with great passion and endless energy. Moreover, he provided me with outstanding environment to conduct research. He is truly my role model and life coach from whom I will learn throughout my study and career. I would like to thank my committee members, Dr. Davies, Dr. Detsi, and Dr. Allen for their valuable suggestions and time, and my qualifying exam committee members, Dr. Davies, Dr. Murray and Dr. Pope for their questions and challenges. I would like to thank Dr. Fuqiang Huang for the guidance and help on my research. Specifically, I am very grateful for his constant advice on materials processing and generosity in providing experimental facilities.

I would like to thank my labmates Dr. Yang Lu, Dr. Yanhao Dong, Ana Alvarez, Shuang Wu and Dr. Hoon Choi for their help, support and friendship. I appreciate the helps from Zhurun Ji, Hongru Du, Han Ye, Dr. Yu Xia on my research and study.

I feel lucky to be a part of UPenn MSE and LRSM community, which has a great environment for study and research. I would like to express my sincere thanks to Steve Szewczyk, Vicky Lee, Irene Clements, Pat Overend for their professional services.

Lastly and most importantly, I would like to thank my wife, Ying Jing, for her love, understanding and encouragement. I also would like to thank my parents, for their love and support.

ABSTRACT

HIGH LOADING OXIDE ANODES FOR LITHIUM ION BATTERIES VIA A SUPERELASTIC GRAPHENE COMPOSITE APPROACH

Zhichao Zhang

Dr. I-Wei Chen

Although nanotechnology has ushered in many new materials storing a high density of electrochemical energy, the performance has only been demonstrated at low material densities, typically ~0.15 g cm^{-3} and ~ 1 mg cm^{-2}. Such densities fall far short of the loading requirement of commercial electrodes, which is 1.6 g cm^{-3} and 10 mg cm^{-2}. Yet progress in overcoming this problem has been slow because of fundamental thermodynamic and kinetic difficulties. This thesis solves the problem for anodes of lithium-ion batteries.

We start by developing a new graphene network monolith that is superelastic, meso-porous, three-dimensional and metallic conducting. The network already features excellent electrochemical performance, but it can also support relatively insulating active materials while endowing them much improved conductivity to aid electrochemical reactivity. With active-material nanoparticles robustly deposited and adhered to the network, the three-dimensional composite monolith, starting as an composite aerogel, can be non-destructively and conformally deformed to high compression ratios to reach the requisite volumetric and areal loadings and to obtain an anode that fits into a coin cell. Although the resulting high-density electrode already has most of its void space removed, it still has undisturbed nanoparticles, with

their local structure connected to a continuous conduit of liquid and ion transport. This allows active electrochemical processes to proceed in the assembled cell at high charging/discharging rates.

The active materials studied are SnO_2, GeO_2, ZnO, Fe_2O_3 and TiO_2. Except for TiO_2, they feature theoretical capacities ranging from 2152 mAh g^{-1} to 988 mAh g^{-1}, but also suffer from volumetric expansions varying from 376% to 93% when Li is incorporated by insertion, conversion and alloying reactions. Such large expansion is usually destructive rendering the materials useless, but when such materials in the form of nanoparticles are incorporated into our composites, they have delivered superior areal and volumetric capacities much higher than those of high-performance experimental materials in the literature and even commercial graphite anode.

This thesis has thus demonstrated a promising approach that can help transition nanomaterials to practical use in lithium-ion batteries. Specifically, it provides several new anodes that can realistically replace commercial graphite anode with significantly improved performance.

TABLE OF CONTENTS

LIST OF TABLES

LIST OF ILLUSTRATIONS

Figure 1.22 (A) Cross-sectional SEM image of HGF/Nb_2O_5 composite. (B) TEM image of graphene sheets etched by H_2O_2 for 1 h. (Reprinted from Ref. 30 with permission.)

Figure 1.23 SEM/TEM images of yolk-shell/core-shell nanostructures for (A) Si-C composite, (B) Sn-C composite and (C) FeO-C composite. (Reprinted from Ref. 31, 32 and 33 with permission.)

Figure 1.24 (A) Components of lithium ion batteries packs and a mass content breakdown. (B) Ragone plots of electrical energy storage devices on a gravimetric basis. (Reprinted from Ref. 34 and 35 with permission.)

Figure 1.25 (A) Side view cross-sectional SEM of sintered $LiCoO_2$ cathodes with continuous linear pores (scale bar, 200 μm). (B) SEM of freeze-cast carbon. (C) SEM of vertical nanosheets on horizontally aligned MXene current collector. The red dashed line illustrates ion transport path after bending of MXene layers in the vertical direction. The inset is illustration of Maxene direction from side view. (Reprinted from Ref. 36, 37 and 38 with permission.)

Figure 1.26 High angle annular dark-field electron microscopy of (A) graphene tube and (B) SnO_2-based 3D composite. (C) Elemental mapping of (B) showing C and Sn distribution. (Scale bar = 50 nm.)

Figure 1.27 Specific capacity vs. areal loading for all 3D network composites, 3D graphene and commercial graphite. The capacities are recorded after 12.5% decay under the current density of 0.2 A g^{-1}, except for Fe_2O_3 at 0.5 A g^{-1}. Upper panel: gravimetric capacities for all oxide composites are relatively insensitive to areal loadings. Lower panels: despite a 10× increase in the packing density, (left) physical

resistance and (right) geometrical specific surface area are constant in SnO_2-based network composite. At relative density 1, R_0=353.1 Ω and S_0= 311.8 m^2 g^{-1}.

Figure 2.1 Fabrication schematic from 3D silica template to mesoporous 3D graphene scaffold by CVD. Doping in 3D graphene can be achieved through the use of dopant-containing carbon source.

Figure 2.2 Material characterization of 3D graphene. **(A-B)** 3D graphene in scanning electron microscopy (SEM) images showing tetragonal coordination in the inset in (**A**) with a scale bar of 500 nm, **(C)** TEM of 3D graphene tube with selected area electron diffraction pattern of graphene in the inset, **(D)** low angle x-ray diffraction patterns for silica template and 3D graphene. Both are consistent with hexagonal packing of rods, 3D graphene having less order and shorter packing spacing. **(E)** High-resolution TEM, **(F)** high angle annular dark-field TEM, **(G)** Raman spectra of 3D graphene, **(H)** electron energy loss spectra of 3D graphene, and **(I)** nitrogen adsorption/desorption pore size distribution with adsorption/desorption isotherm in the inset.

Figure 2.3 Material characterization of N-doped 3D graphene. **(A-B)** N-doped 3D graphene in scanning electron microscopy (SEM) images showing tetragonal coordination in the inset in (**A**) with a scale bar of 1μm, **(C)** TEM of N-doped 3D graphene tube with selected area electron diffraction pattern of graphene in the inset, **(D)** high-resolution TEM , **(E)** high angle annular dark-field TEM, **(F)** nitrogen adsorption/desorption pore size distribution with adsorption/desorption isotherm in the inset, **(G)** Raman spectra of N-doped 3D graphene, 3D graphene and rGO, **(H)** X-ray photoelectron spectra of N-doped 3D graphene, and **(I-J)** high resolution X-ray

photoelectron spectra of C 1*s* and N 1*s*.

Figure 2.4 Material characterization of N-B codoped 3D graphene. **(A-B)** N-B codoped 3D graphene in scanning electron microscopy (SEM) images showing tetragonal coordination in the inset in (**A**) with a scale bar of 0.5 μm, **(C)** TEM of N-B codoped 3D graphene tube with selected area electron diffraction pattern of graphene in the inset, **(D)** high-resolution TEM, **(E)** high angle annular dark-field TEM, **(F)** nitrogen adsorption/desorption pore size distribution with adsorption/desorption isotherm in the inset, **(G)** Raman spectra of N-B codoped 3D graphene, 3D graphene and rGO, **(H)** X-ray photoelectron spectra survey of N-B codoped 3D graphene, and **(I-J)** high resolution X-ray phonon spectra of C 1*s*,N 1*s*, and B 1*s*.

Figure 2.5 Mechanical and electrical properties of undoped 3D graphene. **(A)** Stress-strain curve of 3D graphene up to 90% strain with intermediate unloading. Inset: enlarged view of loading and unloading slopes. (**B**) Normalized conductivity of 3D graphene as a function of temperature from 2K to 300K.

Figure 2.6 Electrochemical performance of undoped, N doped and N-B codoped 3D graphene. **(A)** Cyclic voltammetry (first 3 cycles) of undoped 3D graphene at 1.7 mg cm^{-2}. **(B)** Specific capacity and coulombic efficiency vs. cycle number of undoped 3D graphene at 1.7 mg cm^{-2} under 0.2 A g^{-1}. **(C)** Rate performance of undoped 3D graphene at 1.7 mg cm^{-2} under 0.2, 0.5, 1 and 2 A g^{-1}. **(D)** Areal and volumetric capacity vs. cycle number of undoped 3D graphene at 1.7 mg cm^{-2} and 2.8 mg cm^{-2}, at 0.2 A g^{-1} **(E)** charge-discharge curve at 10^{th} cycle of 3D graphene, N-doped 3D graphene and N-B codoped 3D graphene at 2.8 mg cm^{-2} under 0.2 A g^{-1}. **(F)** Specific

capacity vs. cycle number of B-N codoped 3D graphene at 3 mg cm^{-2} under 1 A g^{-1} after 800 cycles.

Figure 2.7 Comparison of properties with those of literature at 100^{th} cycle (except for our 6.2 mg cm^{-2} 3D graphene electrode, which is at 80^{th} cycle.) Thickness of 25 μm assumed if the thickness of the electrode was not given in the literature.

Figure 3.1 Functionally invariant affine transformation approach: a superelastic, highly conducting network backbone, such as one provided by a 3D tubular graphene, can be used as a scaffold for depositing nanoparticles of another material, acquiring a core-shell structure (upper left). The resulting electrochemically active network can be next compressed uniformly to form a high-loading electrode (upper right). Although there is a 10× increase in the packing density, physical, chemical and geometrical properties are invariant, exemplified by a nearly constant resistance *R* (lower left), gravimetric capacity *Q* (lower middle) and surface area *S* (lower right). At relative density 1, R_0=353.1 Ω, Q_0=1330.6 mAh g^{-1}, S_0= 311.8 m^2 g^{-1}.

Figure 3.2. Materials characterization. (A) Fabrication schematic from silica template to graphene scaffold to SnO_2 coating to final affine transformation, generating high volumetric and areal electrode in a coin cell. (B) Contact angle of water on 3D graphene before acidification (top); after acidification with (bottom), water disappeared into 3D graphene indicative of good wetting. Characterization of SnO_2-based network composite by (C) TEM image showing (D) elemental mapping with scale bar = 100 nm, (E) X-ray diffraction pattern with rutile SnO_2 (PDF#77-0450) peaks shown as markers below, (F) Raman spectra showing SnO_2 with the

characteristic 600 cm^{-1} excitation, (G) X-ray photoelectron spectra showing characteristic spectra of Sn^{4+}, (H) high-resolution TEM image with selected area electron diffraction pattern of SnO_2 in the inset, and (I) thermal gravimetric analysis from 25°C to 900°C in air.

Figure 3.3 Deformation and morphology of superelastic SnO_2-based network composite. (A) Stress-strain curve up to 80% strain with intermediate unloading. Inset: Enlarged view of loading and unloading slopes. (B) Stress at 90% strain versus cycle number. Inset: Stress-strain curves of 1st and 10th cycle. (C to F) SEM at strains of 0%, 40%, 95% and back to 0%. (G) High magnification SEM at 0% strain, and after 95% compression then back to 0% strain for (H).

Figure 3.4 Electrochemical impedance spectra of SnO_{2-x}-based network composite, (grey curve) and slurry-cast SnO_2/rGO composite (light blue curve) anodes, both at total mass loading of 10 mg cm^{-2}. Inset: Enlarged view near origin.

Figure 3.5 Electrochemical performance of SnO_2-based network composite anode of various loadings unless otherwise noted. (A) Cyclic voltammetry (first 4 cycles) of with 5 mg cm^{-2}. Specific reactions (i-iv) as indicated. (See text for details.) (B) Successive charge-discharge curves with 10 mg cm^{-2} at 0.2A g^{-1}. Inset: The 70th cycle charge-discharge curves of three electrodes with loadings as shown. (C) Coulombic efficiency at three loadings: 1.76 g cm^{-3}/5 mg cm^{-2}, 2.47 g cm^{-3}/7 mg cm^{-2}, and 3.53 g cm^{-3}/10 mg cm^{-2}. (D) Areal and volumetric capacity vs. cycle numbers at three loadings. Also shown in bands are anode data of commercial graphite, Si[4,7,11,19], SnO_2 [2,3,10,18,20-22], and theoretical capacity of lithium metal and Si-Li alloy. (E) Areal capacity and volumetric capacity of slurry-cast SnO_{2-x}/rGO composite electrode, at

1.76 g cm^{-3}/5 mg cm^{-2}, as a function of cycles. (F) Rate performance at two loadings.

Figure 3.6 (A-E) Postmortem analysis of SnO_{2-x}-based network composite electrode (10 mg cm^{-2}) after 50 cycles at the 3 V charged state. (A) Transmission electron microscopy image (bar=50 nm). Inset: Selected area diffraction pattern showing polycrystalline SnO_2 without metallic Sn. (B) High angle annular dark-field electron microscopy with bright regions corresponding to SnO_{2-x} rich compositions (bar=50 nm). Many SnO_{2-x} nanoparticles visible along two edges because, in viewing a tube in the transverse direction, transmitting electrons see more mass at two edges. (C) Corresponding elemental mapping (bar=50 nm). (D) XPS of Sn after cycling showing only Sn^{4+}. (E) Characteristic SnO_2 Raman spectrum. Inset: Crystallites detectable by TEM (Fig. 3.2 H) were too small to detect by X-ray diffraction because of 56× longer wavelength. (F) Voltage-range-specific capacity of network composite electrode with a mass loading of 3.53 g cm^{-3}/10 mg cm^{-2} as a function of cycles. 1^{st} and 2^{nd} differential discharge capacity of (G) SnO_{2-x}-based network composite electrode, to be compared with (H) slurry cast SnO_{2-x}/rGO composite electrode, both at 5 mg cm^{-2}.

Figure 3.7 Comparison of properties of our network composite, various SnO_2-based anode materials in the literature, and commercial graphite, all after 100 cycles. Thickness of 25 μm assumed if the thickness of the electrode was not specified in the literature.

Figure 4.1 Materials characterization of GeO_2-based network composite. (A) X-ray diffraction pattern of GeO_2-based composite with broad diffusion peak between 20~ 30°, (B) Transmission electron microcopy (TEM) image, (C~F) Mapping of C,

assumed if the thickness of the electrode was not specified in the literature.

Figure 6.1 Materials characterization of ZnO-based network composite. **(A)** X-ray diffraction pattern with ZnO (PDF#36-1451) peaks, **(B)** transmission electron microcopy (TEM) image, **(C~F)** mapping of C, Fe, Zn and Zn, **(G)** TEM image with selected area electron diffraction pattern of ZnO in the inset, **(H)** high-resolution TEM image, and **(I)** thermogravimetric analysis spectrum.

Figure 6.2 Electrochemical performance of ZnO-based network composite with 7 mg cm^{-2} unless otherwise noted. **(A)** Cyclic voltammetry (first 4 cycles), **(B)** successive charge-discharge curves at 0.2 A g^{-1}, **(C)** areal and volumetric capacity vs. cycle numbers of ZnO-based network composites with 7 and 11 mg cm^{-2} at 0.2 A g^{-1}, and **(D)** rate performance of ZnO-based network composite with 7 mg cm^{-2} at 0.2 and 0.5 A g^{-1}.

Figure 6.3 Comparison of properties of our composite with those of commercial graphite and ZnO-based materials in the literature after 100 cycles. Thickness of 25 μm assumed if the thickness of the electrode was not specified in the literature.

Figure 7.1 Materials characterization of TiO_2-based network composite unless otherwise noted. (A) X-ray diffraction pattern with TiO_2 (PDF#21-1272) peaks. (B) UV-Vis spectra of pristine TiO_2 powder and N-doped reduced TiO_2 powder (after NH_3-treatment). (C-D) Transmission electron microcopy (TEM) image, (E) high-resolution TEM image and (F) thermogravimetric analysis spectrum.

Figure 7.2 Electrochemical performance of TiO_2-based 3D composite with 7 mg cm^{-2} unless otherwise noted. (A) Cyclic voltammetry (first 4 cycles). (B) Successive charge-discharge curves at 0.168 A g^{-1} (1 C). (C) Areal and volumetric capacity vs.

cycle numbers with 7 and 9 mg cm^{-2} at 0.168A g^{-1}(1 C). (D) Rate performance with 5, 7 and 9 mg cm^{-2} at 0.2C, 0.5C, 1C, 2C and 5C.

Figure 7.3 Comparison of properties of our network composite with those of literature materials after 100 cycle. Thickness of 25 μm assumed if the thickness of the electrode was not specified in the literature.

Figure 8.1 (A) Specific capacity vs. areal loading for oxide-based composites, capacities recorded after 12.5% decay under current density of 0.2 A g^{-1}, except for Fe_2O_3 under 0.5 A g^{-1}. **(B)** Normalized capacity of **(A)**. **(C)** Specific capacity vs. cycle number for oxide-based composites: SnO_2-based composite at 10 mg cm^{-2}, GeO_2-based composite at 13 mg cm^{-2}, ZnO-based composite at 11 mg cm^{-2} and Fe_2O_3-based composite at 9 mg cm^{-2}; capacities recorded under current density of 0.2 A g^{-1}, except for Fe_2O_3 under 0.5 A g^{-1}. **(D)** Normalized capacity of **(C)**, with dotted line indicating capacity retention of 87.5%. **(E)** Specific capacity vs. gravimetric rate for 3D composites at same loading of 7 mg cm^{-2}. **(F)** Normalized capacity of **(E)**.

Figure 8.2 Comparison of properties of oxide-based network composites, 3D graphenes and commercial graphite, at 100^{th} cycle.

Figure 8.3 Comparison of properties of selected oxide-based network composites, 3D graphene and commercial graphite at 700^{th} cycle.

Chapter 1 Introduction

1.1 Introduction to lithium-ion battery

1.1.1 History and development of lithium ion battery

The limited supply of fossil fuels and the environmental pollution caused by burning them have urged the society to pursue alternative renewable energies such as solar energy and wind energy. Thanks to a very significant drop in the cost, for example, the cost of solar energy has dropped by 60% in 10 years to become $2.8/watt in 2017,[1] renewable energy is now highly viable. The fast development of energy harvesting technologies has in turn motivated R&D of energy storage technologies, among them rechargeable lithium-ion batteries for use in electric vehicles and grid-scale electricity have attracted most interest. Beginning in 1970s, the interest in rechargeable batteries started with sodium-ion batteries utilizing liquid sodium anode and beta-alumina solid electrolyte, which has a very high sodium ion conductivity.[2] As the research on inserting alkaline metals into solid compounds progressed, the interest was also extended to similar behavior in solid electrodes, e.g., layered compound Ti_2S which may be used as a cathode to store lithium ions by intercalation. The lithium ion batteries initially used (solid) lithium metal as anodes, but they suffer from formation of dendrites that short-circuit the batteries and cause fire. To alleviate this problem, carbon-based anodes were developed in 1990s to store lithium ions by lithium intercalation, forming LiC_6. Meanwhile, $LiCoO_2$ cathode was invented as an intercalation cathode. This configuration of carbon-$LiCoO_2$ electrodes with organic liquid electrolyte has been essentially adopted in commercial lithium ion batteries

since then.[2,3]

1.1.2 Fundamentals

1.1.2.1 Basic reactions

Rechargeable batteries reversibly convert chemical energy into electrical energy. During this process, microstructure and physiochemical properties often change drastically. The pertinent basic reactions and properties are as follows.

1.1.2.1.1 Alloying reactions

This reaction can be expressed as

$$zLi + A = Li_zA \quad (1\text{-}1)$$

where A is a pure element. So the reaction may be considered as forming an alloy Li_zA in which atoms of Li and A are mixed in a solid solution. During the reaction, lithium ions must cross the A (i.e. electrode) interface but the original crystalline and microstructure features of A is largely preserved except for a major volume increase. Such is the case of Li alloying into Sn, Si, and Ge, which are all anode materials.

1.1.2.1.2 Conversion reaction

This reaction is a displacement reaction expressed as

$$zLi + AX = A + Li_zX \quad (1\text{-}2)$$

where lithium displaces A forming a compound Li_zX, which generally has a different lattice structure from AX, leaving an elemental phase A.

1.1.2.1.3 Insertion reaction

The insertion reaction, also called intercalation reaction, forms an intercalation compound by inserting the guest species Li into the unoccupied space of the host

material. It is described by

$$zLi + AB = Li_zAB \quad (1\text{-}3)$$

The unoccupied space may be interstitial sites or between atomic layers as in a layered compound. Typically, despite the very different composition of the intercalated material, its crystal structure is not significantly different from that of the host. The insertion-induced stresses and energy changes, however, may result in a kinetics hysteresis, even structural instability, in some materials.

1.1.2.2 Thermodynamics

Reactions proceed because there is an attendant decrease in the Gibbs free energy, ΔG_r, which may be calculated from the Gibbs free energies of the product and the reactants. Individually, the chemical potential of the *i*-th specie in a constituent phase α is

$$\mu_i = \partial G_\alpha / \partial n_i \quad (1\text{-}4)$$

where G_α is the molar Gibbs free energy of the α phase, and n_i is the number of mole of the *i*-th species in α. We can then derive the integral form as:

$$\Delta\mu_i = \Delta G_\alpha \quad (1\text{-}5)$$

In an electrochemical cell under the open-circuit condition, the two electrodes are separated by an electrolyte in which there is no net flux. Therefore, any chemical potential difference of the *i*-th species must be balanced by a difference in the electrostatic potential between the two electrodes ΔV, which is the open-circuit voltage

$$\Delta\mu_i = -z_i F \Delta V \quad (1\text{-}6)$$

Here z_i is the number of elementary charge on the *i*-th species, and *F* is the Faraday

constant. As an example, we consider a concentration cell in which the two electrodes are identical solutions that differ only in composition. The chemical potential of the *i*-th species is a function of its concentration, often expressed as activity a_i (in an ideal solution a_i is the molar fraction of the *i*-th species)

$$\mu_i = \mu_i^o + RTlna_i \qquad (1\text{-}7)$$

where *R* is the gas constant (8.315 J/mol degree), *T* is the absolute temperature, and μ_i^o is the chemical potential of the *i*-th species in the standard state. So there is a concentration-related difference in the chemical potentials of the two electrodes, $\mu_i(+)$ and $\mu_i(-)$, for the positive and the negative electrodes, respectively,

$$\mu_i(+) - \mu_i(-) = RT[lna_i(+) - lna_i(-)] = RTln[a_i(+)/a_i(-)] \qquad (1\text{-}8)$$

Therefore,

$$\Delta V = -\left(\frac{RT}{z_i F}\right)\ln[a_i(+)/a_i(-)] \qquad (19)$$

which is known as the Nernst Equation.

Phase diagram as a two-dimensional plot in composition and temperature may be used to delineate the stability ranges of phases under equilibrium conditions.

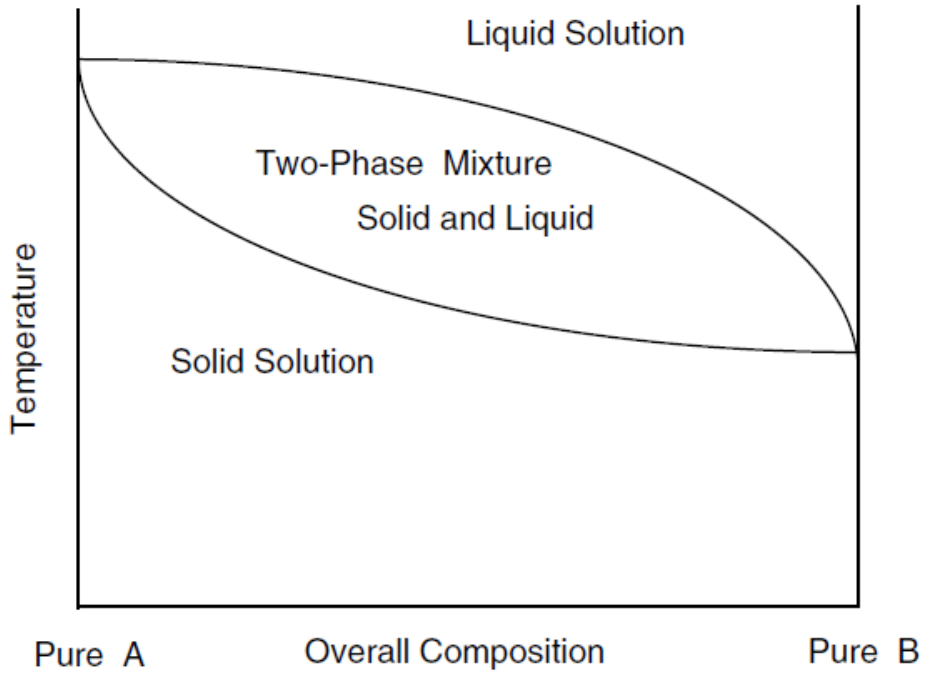

Figure 1.1 Schematic phase diagram of binary system. (Reprinted from Ref.4 with permission.)

One example is shown in **Fig. 1.1**[4] for a binary *A*-*B* system with fully miscible solid and liquid phases. The different melting points of *A* and *B* is reflected in an extended two-phase solid-liquid region, bordered above by the liquidus where the formation of liquid solution begins, and below by the solidus where the formation of solid solution is initiated.

Across the phase diagram, the activity and the chemical potential vary monotonically within a single-phase region reflecting the compositional dependence of activity/chemical potential, and they remain constant within a two-phase region reflecting the two-phase equilibrium

$$\mu_{A\alpha} = \mu_{A\beta} \qquad (1\text{-}10)$$

This is also manifested in the voltage vs composition plot, essentially a titration curve, as shown in **Fig. 1.2A**[4]. It has a constant-voltage segment across the two-phase region (**Fig. 1.2B**[4]), sandwiched between two monotonically-varying voltage segments on both sides which are single-phase regions.

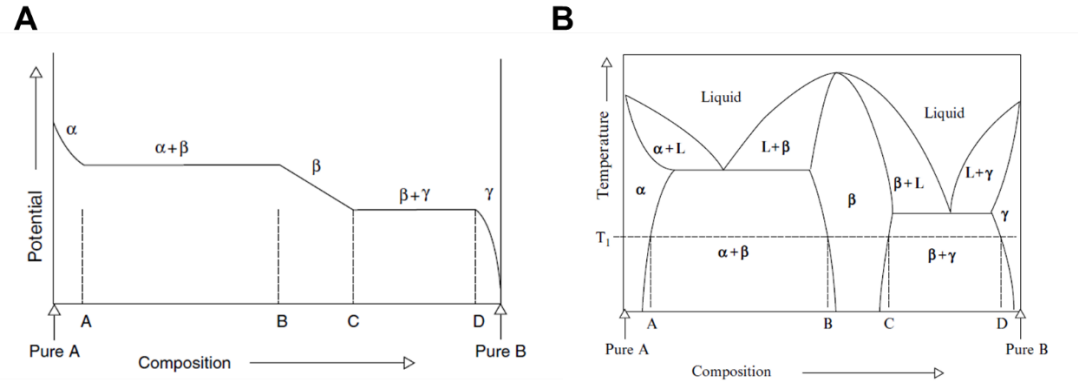

Figure 1.2 (A) Schematic variation of electrical potential as a funtion of composition across the binary phase diagram in (B) and (B) schemtic binary phase diagram with an intermidate phase β between two terminal phases α and γ . (Reprinted from Ref.4 with permission.)

Note that some phases may be line compounds. In such a case, the composition range is infinitely narrow, so the corresponding voltage drop in this single-phase region is infinitely sharp appearing as an abrupt change, i.e., a vertical segment.

We now discuss the phase diagram of antimony and lithium, **Fig 1.3A**[4], which has an alloying reaction between them. In an electrochemical cell with a lithium anode and an antimony electrode, at 360 ^{o}C, there are the following reactions

$$2Li + Sb = Li_2Sb \qquad (1\text{-}11)$$

$$Li + Li_2Sb = Li_3Sb \qquad (1\text{-}12)$$

The corresponding voltage vs composition plot is shown in **Fig. 1.3B**[4], which can be

derived from the standard Gibbs free energies of formation of Li_2Sb (-176.0 kJ/mol) and Li_3Sb (-260.1kJ/mol), with zero potential set at pure Li. Starting from the Li end, we set it as zero voltage. In binary thermodynamics, $Li_3Sb=4(Li_{0.75}Sb_{0.25})$, so the free energy of $Li_{0.75}Sb_{0.25}$ is -65 kJ relative to pure Li. Likewise, $Li_2Sb=3(Li_{0.667}7Sb_{0.333})$, so the free energy of $Li_{0.667}Sb_{0.333}$ is -59 kJ. Constructing the free energy diagram using lines, we connect the two energies of $Li_{0.75}Sb_{0.25}$ and $Li_{0.667}Sb_{0.333}$ to extrapolate to 100% Li to obtain the chemical potential of Li of $Li_{0.75}Sb_{0.25}$ to be -83kJ, which is 0.86 V. This is the Li chemical potential of the Li_3Sb phase. For the Li_2Sb phase, we connect the zero energy of Sb (i.e., 0% Li)—it is also a standard state in thermodynamics and has zero formation energy—and the free energy of $Li_{0.66}Sb_{0.33}$ and extrapolate it to 100% Li to obtain the chemical potential of -88 kJ. So the chemical potential of $Li_{0.66}Sb_{0.33}$ is 0.912 V.

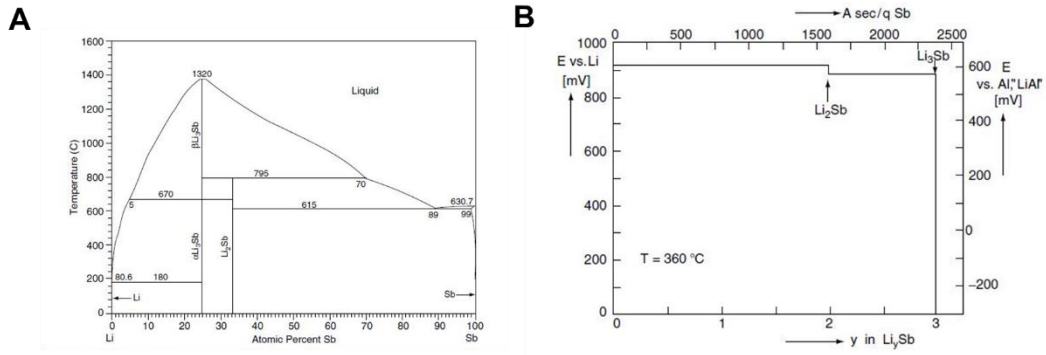

Figure 1.3 (A) Phase diagram of Li-antimony; (B) coulometric titration of Li-antimony system at 360 °C. (Reprinted from Ref. 4 with permission.)

Before proceeding, we should mention that in this thesis, we refer to cathode as positive electrode, which has a relatively higher operating voltage. This is the case of

$LiCoO_2$ and $LiFePO_4$. We also refer to anode as negative electrode, which has a relatively lower operating voltage. This is the case of graphite, Sn, Si and Ge.

1.1.2.3 Phases and thermodynamics of materials of interest

In this thesis, we aim to explore 6 materials system as the active anode materials for lithium-ion batteries. In this section, we review the phases and thermodynamics of each material system to establish an elementary understanding and to provide a reference for the electrochemical characterization described later.

1.1.2.3.1 Graphite

Graphite anode can store lithium by the insertion reaction up to

$$Li + 6C = LiC_6 \quad (1\text{-}13)$$

At less Li, the operating voltage (U) of the corresponding reaction varies with x in Li_xC_6: U= 0.21 V for 1/20 <x < 1/6, U = ~ 0.1 V for 1/5 < x <1/2, and U = ~ 0.08 V for 1/2 < x < 0.95. These ranges cover multiple phases in the phase diagram in **Fig. 1.4**[5], and the voltage corresponds to the transformation free energy between them.

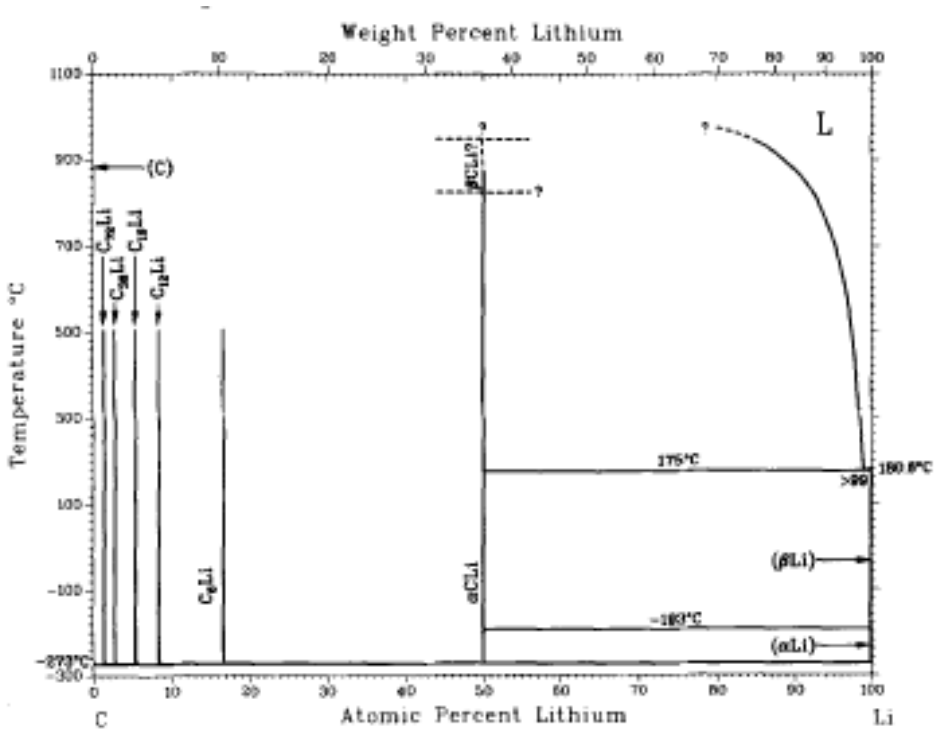

Figure 1.4 Li-C phase diagram. (Reprinted from Ref. 5 with permission.)

1.1.2.3.2 SnO_2

SnO_2 has the following conversion and alloying reactions:

$$2\ Li + SnO_2 = Li_2O + SnO \qquad (1\text{-}14)$$

$$2\ Li + SnO = Li_2O + Sn \qquad (1\text{-}15)$$

$$Sn + x\ Li = Sn_xLi \qquad (1\text{-}16)$$

In the above, x is up to 4.4. The reaction free energy is the difference of the Gibbs free energy of formation of various phases on the two sides of the reaction. This has been computed: 1.88 V for (1-14), 1.58 V for (1-15) and 0.66 to 0.38V for (1-16) when x increases from 0 to 4.4.

The ternary phase diagram is shown in **Fig. 1.5.**[4] Starting from SnO_2, lithiation proceeds toward the Li corner following the dotted line between the two. As the

reaction proceeds, the composition enters various compatibility triangles, starting from Li_2O-SnO-SnO_2 and forming Li_2O and SnO at the expense of SnO_2 and Li (reaction (1-14)). After crossing the Li_2O-SnO line, the composition then enters the Li_2O-SnO-Sn triangle, forming Li_2O and Sn at the expense of SnO and Li (reaction (1-15)). After that, subsequent reactions all involve the progressive formation of increasingly Li-richer Sn-Li alloys from Sn and Li (reaction (1-16)).

Since the chemical potentials remain constant in each triangle of three insoluble phases, there is no variation of the electrical potential during the reaction throughout the compositional range in such triangle. This is reflected in the voltage plateau in the Coulombic titration curve. That is, each triangle corresponds to a specific voltage, e.g., 1.88 V in the Li_2O- SnO_2- SnO triangle. The next plateau at 1.58 V is in the Li_2O-SnO- Sn triangle. After that, there are several more plateaus in the range of 0.66 V to 0.38V, each with a very narrow compositional range corresponding to various pairs of compatible Li_xSn phases.

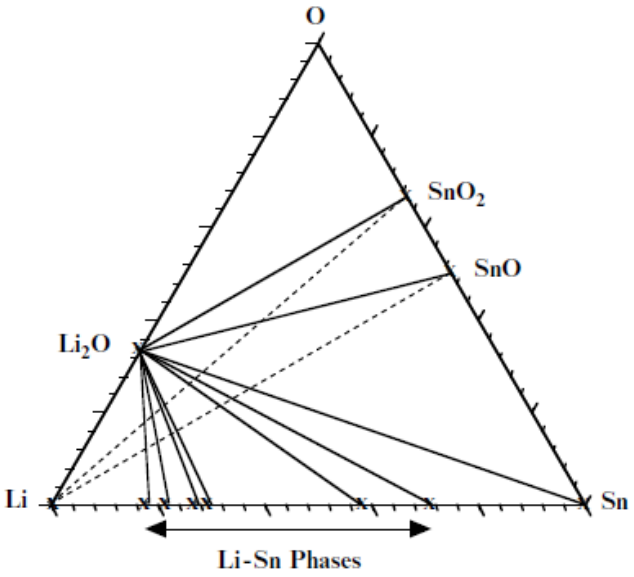

Figure 1.5 Isothermal ternary phase diagram for the Li-Sn-O system. (Reprinted from Ref.4 with permission.)

1.1.2.3.3 GeO_2

During the lithiation procedure, GeO_2 undergoes the following conversion and alloying reactions:

$$2\ Li + GeO_2 = Li_2O + GeO \qquad (1\text{-}17)$$

$$2\ Li + GeO = Li_2O + Ge \qquad (1\text{-}18)$$

$$Ge + 4.4\ Li = Ge_{4.4}Li \qquad (1\text{-}19)$$

From the Gibbs free energy of formation (-562 kJ mol^{-1} for Li_2O, -502.5 kJ mol^{-1} for GeO_2, and -371.4 kJ mol^{-1} for GeO), we can calculate the operating voltages for the above reactions: 2.23 V for equation (1-17) and 0.99 V for equation (1-18). For the alloy reaction of (1-19), the voltage is smaller than 0.6 V when $x = 0 \sim 4.4$ in Ge_xLi.

The phase diagram of Li-Ge-O is presented using Li_2O- GeO_2 binary because

GeO_2 is the only Ge oxide. This is shown in **Fig. 1.6.**[6] In addition, the Li-Ge alloy has 5 phases, LiGe, Li_9Ge_4, $Li_{16}Ge_5$, $Li_{15}Ge_4$ and $Li_{22}Ge_5$ according to the (400°C) coulometric titration curve in **Fig 1.7**[7]**.**

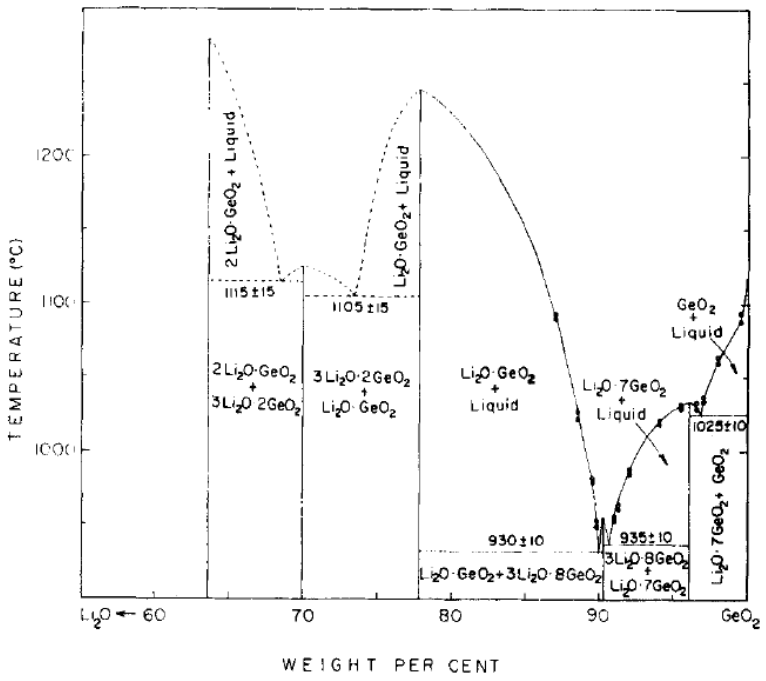

Figure 1.6 GeO_2-Li_2O phase diagram. (Reprinted from Ref. 6 with permission.)

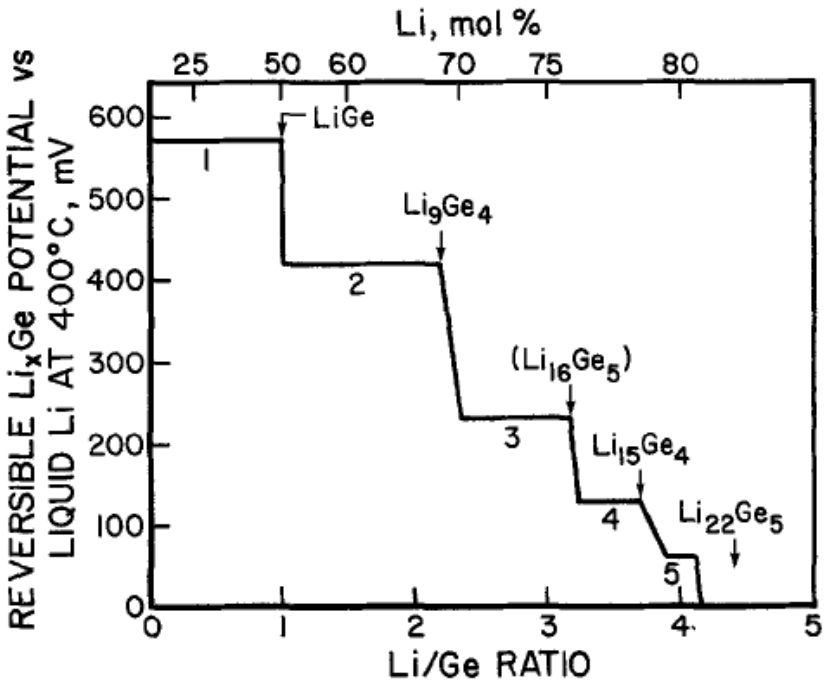

Figure 1.7 Coulometric titration of Li-Ge alloy system. (Reprinted from Ref.7 with permission.)

1.1.2.3.4 Fe_2O_3

Fe_2O_3 anode has the following reaction with Li

$$6\ Li + Fe_2O_3 = 3Li_2O + 2Fe \qquad (1\text{-}20)$$

From the Gibbs free energy of formation (-562 kJ mol^{-1} for Li_2O; -740 KJ $mol^{-1}$for Fe_2O_3), we can obtain the reaction voltage of 1.63 V. The ternary phase diagram constructed from the (420°C) Coulometric titration measurements is shown in **Fig. 1.8**[4] Upon lithiation, Fe_2O_3 undergoes transformations to progressively form Fe_3O_4, $LiFe_5O_8$, $LiFeO_2$, Li_5FeO_4, and Li_2O, along with Fe.

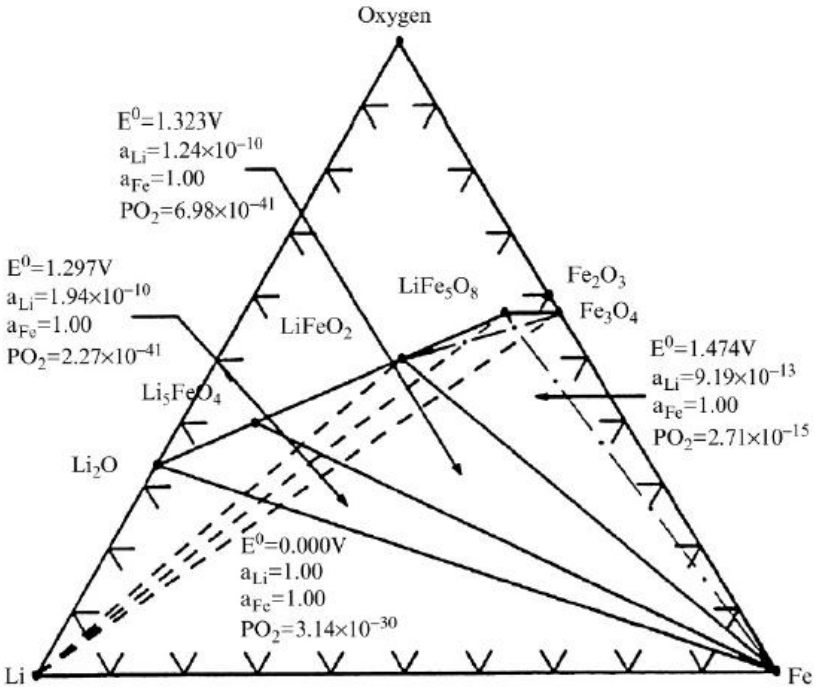

Figure 1.8 Ternary phase diagram for Li-Fe-O system at 420°C. (Reprinted from Ref.4 with permission.)

1.1.2.3.5 ZnO

During the lithiation process, ZnO undergoes the following conversion and alloying reactions

$$2\ Li + ZnO = Li_2O + Zn \qquad (1\text{-}21)$$

$$1.5\ Zn + Li = Zn_{1.5}\,Li \qquad (1\text{-}22)$$

From the Gibbs free energy of formation (-562 kJ mol^{-1} for Li_2O, and -320.4 kJ mol^{-1} for ZnO), we can calculate the operating voltage for reaction (1-21) to be 1.25 V. The phase diagram of Li-Zn alloy contains four phases, $Li_{0.4}Zn$, $Li_{0.5}Zn$, $Li_{0.67}Zn$, and LiZn, according to the room-temperature coulometric titration curve in **Fig 1.9**[8]. The voltage

range for the alloy reaction, (1-22), lies below 0.256 V when $x = 0.4 \sim 1$.

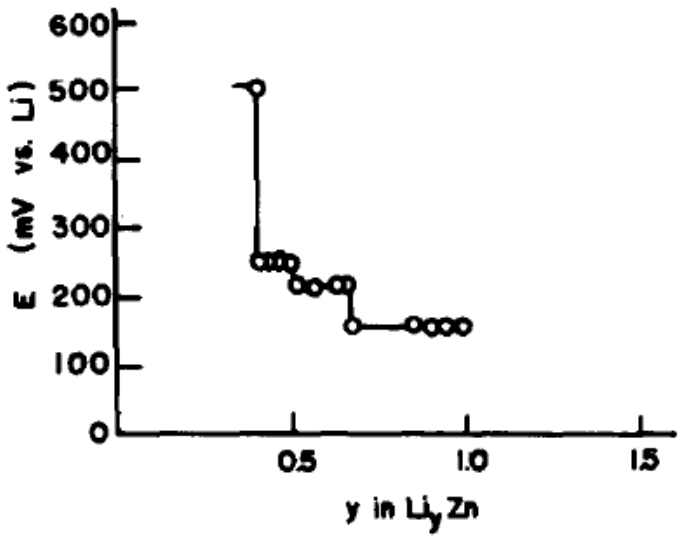

Figure 1.9 Coulometric titration of Li-Zn alloy system. (Reprinted from Ref.8 with permission.)

1.1.2.3.6 Anatase-TiO_2

The anatase phase TiO_2 uptakes 0.5 mole Li by the insertion reaction

$$Li+ TiO_2 = Li_{0.5}TiO_2 \qquad (1\text{-}23)$$

This reaction takes place at the voltage of 1.7 V. In the ternary phase diagram (**Fig. 1.10**[9]), the above reaction falls within the triangle of $LiTi_2O_4$, and $Li_4Ti_5O_{12}$ and TiO_2.

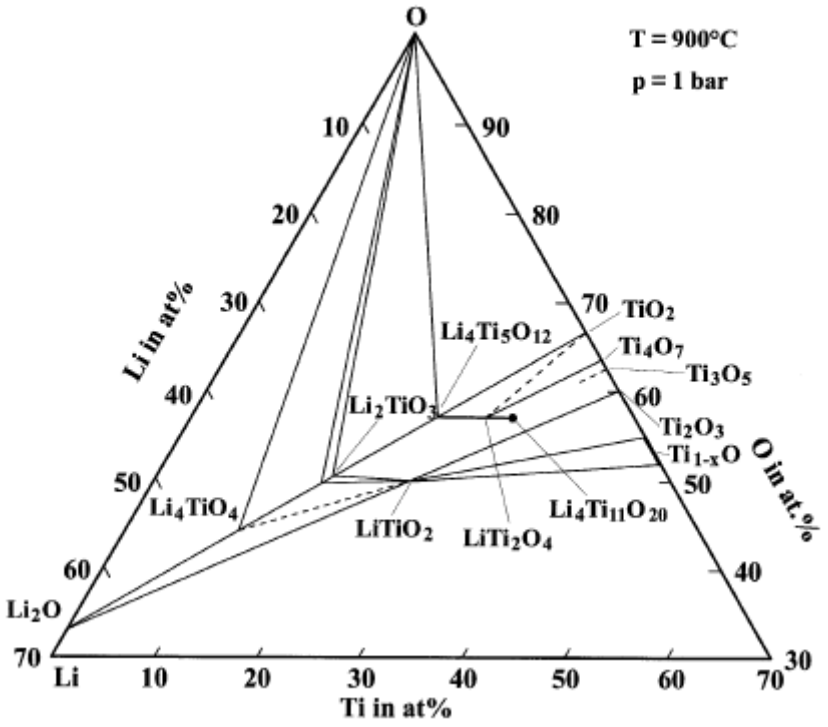

Figure 1.10 Isothermal ternary phase diagram of Li-Ti-O system at 900ºC and 1 bar total pressure. (Reprinted from Ref. 9 with permission.)

1.1.3 The state of the art

In this section, we will discuss electrode materials in the state-of-the-art commercial lithium ion batteries. In cathodes, they are mainly two types, layered materials and poly-anion materials.

Layered materials: Lithium cobalt oxide, $LiCoO_2$ (LCO), is the most important layered cathode material with intercalation reactions. It is made of alternating layers of Co octahedra and Li^+ in hexagonal stacking as shown in **Fig 1.11A**[10]. LCO delivers a high theoretical capacity of 274 mAh g^{-1} and 1263 mAh cm^{-3}, and has low self-discharge as well as a high operating voltage. However, LCO suffers from high cost of

Li and Co, low thermal stability and fast capacity decay when operated under high current and deep cycling. Related to LCO are two materials: $LiNi_{0.8}Co_{0.15}Al_{0.05}O_2$ (NCA) with a similar layered structure but cheaper and more stable, having Co mostly replaced by Ni and benefiting from Al doping which improves the thermal stability, and $LiNi_{1-x-y}Co_xMn_yO_2$ (NCM) with Ni and Mn replacing Co thus achieving similar cost advantage and enhanced performance.

Poly-anion materials: Lithium iron phosphate, $LiFePO_4$ (LFP), is the most prominent poly-anion cathode material with intercalation reactions. It has an (orthorhombic) olivine structure of **Fig 1.11B**[10] with an alternating stacking of Li and Fe octahedra arranged in a manner to allow their oxygens to form PO_4 tetrahedra. Alternatively, it may be described as having hexagonal-close-packed oxygens with one half of the octahedral interstitial sites filled by Li and Fe and one quarter of the tetragonal interstitial sites filled by P. While this structure is highly stable, LFP has a low average potential and poor ionic and electrical conductivity. Therefore, extensive effort has been made on modifying its microstructure, e.g., forming nanoparticles or carbon coating, to improve the performance.

In commercial Li-ion batteries, carbon materials are widely used as anodes. They store lithium ions by intercalation between graphene planes, reaching 1 Li atom per 6 carbon atoms in the limit as shown in **Fig 1.11C**[10]. Carbon materials have several advantages: cheap, low lithiation voltage, long cycle life, high lithium diffusivity, high electrical conductivity, and small volume change despite extensive intercalation. However, their volumetric capacities of 330~430 mAh cm^{-3} are much lower than those of commercial cathode materials.

Carbon materials come with various degrees of graphitization, ranging from graphene and graphite with perfect (sp^2) graphitization to hard carbons with low graphitization.

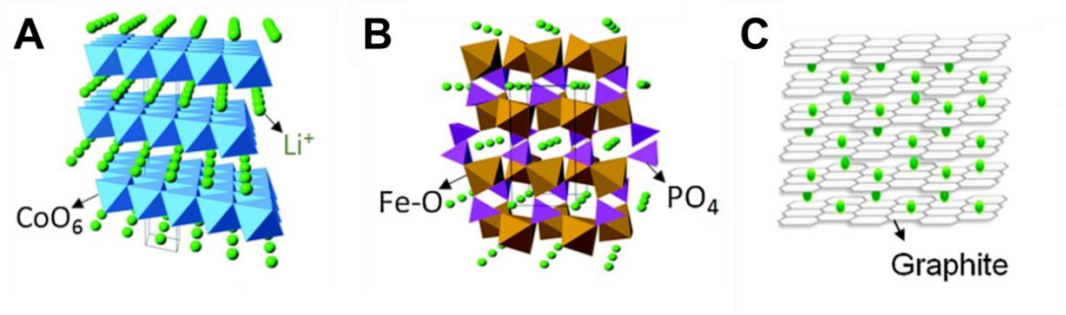

Figure 1.11 (A) Crystal structure of $LiCoO_2$, (B) $LiFePO_4$ and (C) graphite. (Reprinted from Ref. 10 with permission.)

With a high degree of graphitization, the material can achieve higher capacity but propylene carbonate (PC)-based electrolyte can also enter between the graphene layers to cause exfoliation and capacity decay. It too tends to form a solid-electrolyte-interphase (SEI) preferentially along the in-plane (basal plane) directions, and such SEI can be easily damaged by just 10% strain induced by lithium intercalation resulting in a fast decay of capacity.

Hard carbon materials have fewer graphitic grains and many amorphous regions, which endow the materials with better resistance to electrolyte-induced exfoliation. Their capacity is also higher than the theoretical capacity (372 mAh g^{-1}) of graphite because nanovoids within their defects or amorphous regions can store lithium. However, these defects provide a very large surface area, which allows excessive formation of SEI hence a low initial columbic efficiency. In addition, the void space can significantly reduce the packing density, which lowers the volumetric

capacity of lithium ion batteries containing hard-carbon anodes.

1.1.4 Advanced anode materials

Since anode materials is the focus of this thesis, below we briefly review the current research on advanced anode materials that seeks to exploit alloying and conversion reactions to provide higher capacities than available to the commercial carbon anode materials as shown in **Table 1**. These gravimetric and volumetric capacities several times of those of carbon anodes can better match the capacity of cathodes, hence boosting the capacity of the battery.

Table 1.1 Comparison of volume change, theoretical gravimetric and volumetric capacities of anode materials: graphite, and seven advanced materials with alloying and conversion reactions.

Materials	Volume change (%)	Theoretical gravimetric capacity (mAh g^{-1})	Theoretical volumetric capacity (mAh cm^{-3})
Graphite	10	372	843
Si	270	4200	9744
Ge	240	1624	8645
Sn	255	994	7266
SnO_2	376	1494	10383
GeO_2	306	2152	9098
ZnO	153	988	5533

Fe_2O_3	93	1007	5279

While the capacity of advanced materials is much higher, **Table 1.1** also makes clear that there is a huge amount of volume change during the conversion and alloying reactions. This causes material pulverization as well as electrode swelling, eventually resulting in the loss of electrical contact and severe capacity fading. It can also damage the SEI, exposing fresh surfaces on the active material to form new SEI repeatedly, which consumes lithium and degrades the Coulombic efficiency. Therefore, despite their impressive initial gravimetric capacity, these advanced materials have not been made into practical anodes worthy of replacing the commercial graphite anodes.

1.2 Nanostructured functional porous graphene materials and composites as anodes for lithium ion batteries

1.2.1 Advanced functional porous graphene as anodes for lithium ion batteries

Graphite and carbon materials have been widely used as anode materials in commercial lithium-ion batteries. To improve gravimetric and volumetric capacities, researchers have extensively investigated their nanostructured porous derivatives, especially those based on graphene. Note that in the strictest definition, graphene is the single-layer graphite, but few-layer sp^2 carbon materials have also often been termed graphene in the work of nanostructured porous derivatives, a practice that we will follow in this thesis. Below is a brief summary of the recent advances in this area.

1.2.1.1 Lithium storage mechanisms of nanostructured porous graphene

1.2.1.1.1 Additional covalent lithium storage

As mentioned before, lithium storage in graphite takes the form of intercalation forming LiC_6 with a theoretical capacity of 372 mAh g^{-1} for graphite. However, in 1994[11], Li_2C_6 was found in some materials that have an especially large spacing between graphene layers, e.g., a material synthesized by carbonization of poly (*p*-phenylene). Indeed, NMR confirmed the existence of Li_2 molecules in bulk carbon material. This covalent form of lithium, shown in **Fig. 1.12**[11], can have a huge impact on the electronic structure of the lithiated graphite. Specifically, electrons can charge covalent lithium instead of entering the graphene layer.

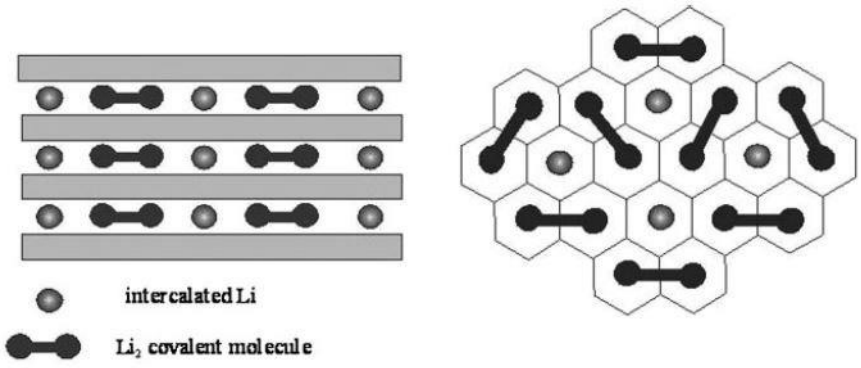

Figure 1.12 Schematic illustration of covalent and intercalated Li-sites in carbon. (Reprinted from Ref. 11 with permission.)

1.2.1.1.2 Lithium storage in nanostructured pores and cavities

Graphite is typically synthesized at temperatures above 2000°C to achieve a high degree of graphitization. Such fabrication method is known to reduce the defects present in the original graphite of a lower quality. However, some nanostructured porous graphene materials are synthesized at <1000 °C. Not surprisingly, they contain

abundant cavities and pores, which turn out to have a three-dimensional architecture. Such cavities and pores provide free space for storing lithium as shown in **Fig 1.13**[12] In the case of open-structured pores, lithium storage can be understood by the "job-sharing" model of Maier et al.[13,14] In this model, an open pore with access to liquid electrolyte forms a heterogeneous structure composed of a conductive carbon skeleton and some electrolyte. This allows electron storage in carbon, while lithium ions are stored in the nearby electrolyte region in the space-charge layer, which satisfies the requirement of charge neutrality overall. In the case of closed-structured pores, lithium storage is not aided by liquid electrolyte, to which close pores have little access. To reach these pores, lithium diffusion in the graphitic carbon is obviously needed.

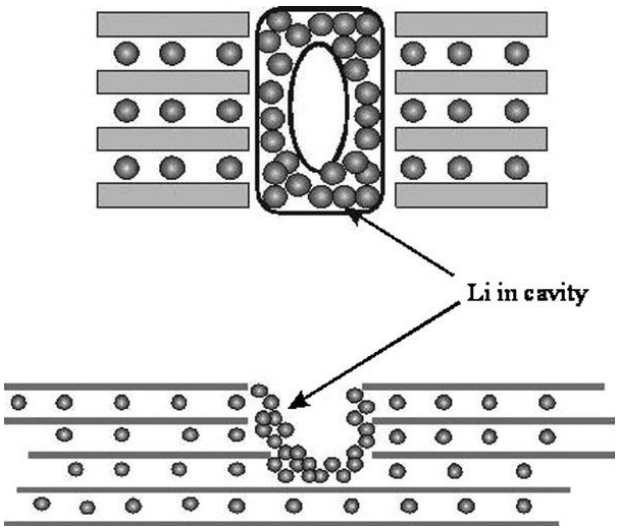

Figure 1.13 Schematic of lithium storage in cavities and nanopores. (Reprinted from Ref 12 with permission.)

1.2.1.1.3 Mechanisms of surface and interfacial storage

Surface and interfacial storage of lithium can take place either on the surfaces of

variously oriented graphene sheets or at their corners and edges. Surface storage is attributed to lithium absorption on the two surfaces of a single layer graphene sheet, which are randomly stacked like in a "house of cards." This mechanism applies to disordered carbon materials as shown in **Fig. 1.14**[15], which can deliver 740 mAh g^{-1}, which suggests the formation of LiC_3 that has twice the Li:C ratio as in graphite. This is because in random carbon an individual graphene sheet has two surfaces for adsorption but in graphite each graphene sheet has only one interlayer space for intercalation. Multi-layer absorption can also happen, in effect forming lithium metal in the subsequent layers as if in lithium plating.

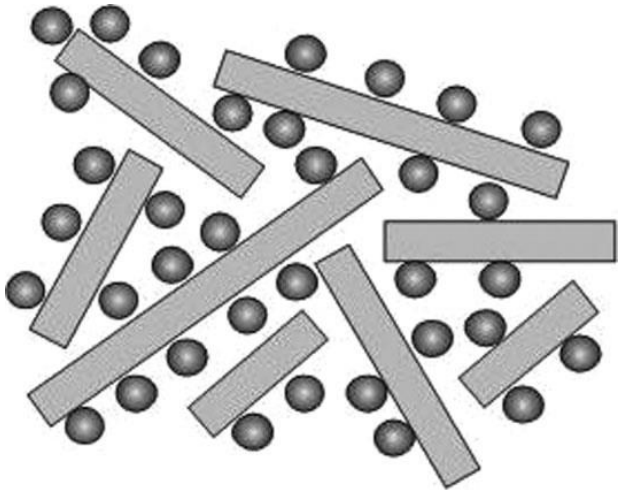

Figure 1.14 Schematic of lithium adsorption on two sides of graphene sheets. (Reprinted from Ref 15 with permission.)

1.2.1.1.4 Lithium storage mediated by defects in doped graphene materials

Hetero-atom doped graphene materials have been widely studied for photovoltaic cells, semiconductors, etc., and they have also been explored for energy storage. For

example, supercapacitors made of nitrogen-doped few-layered graphene materials have shown outstanding capacitance because of faradaic type pseudo-capacitance.[16] Doped/modified graphene materials have also shown enhanced capability for lithium storage, for example in $Li_{1.16}(B_{0.17}C_{0.83})_6$, as shown in **Fig. 1.15**[17], which suggests the beneficial role of acceptor dopants.

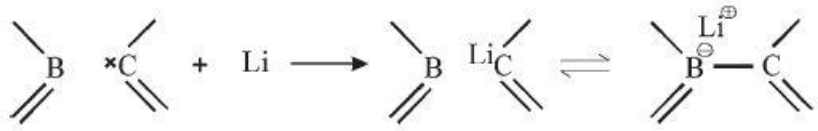

Figure 1.15 Schematic of lithium storage in boron-doped carbon. (Reprinted from Ref 17 with permission.)

On the other hand, nitrogen doping can also result in increased lithium storage as shown in **Fig. 1.16**[18], in which the graphitic N (N1-GN) site offers more favorable lithium adsorption than on top of a carbon sheet. Another possible site is at the center of defects created by pyrrolic and pydridinic N doping (N2-GN and N3-GN).

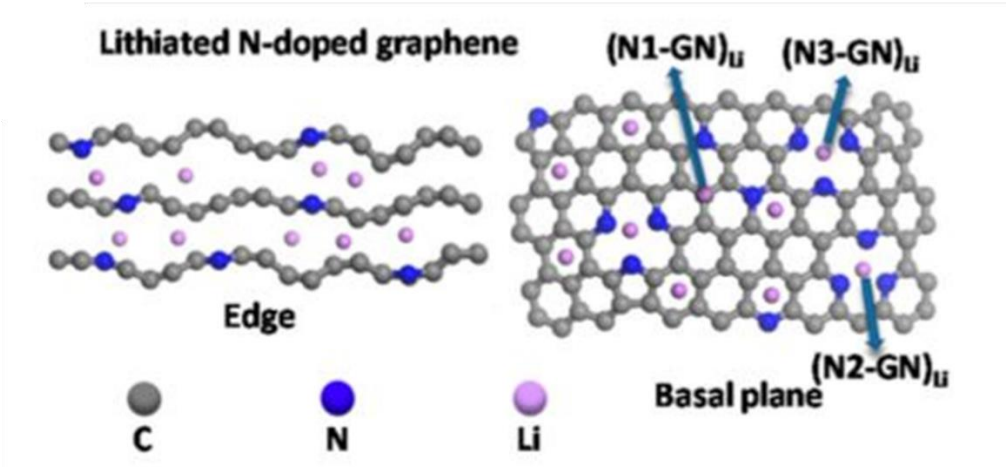

Figure 1.16 Schematic of lithium storage in N-doped graphene. (Reprinted from Ref 18 with permission.)

Indeed, even mono-valence doping of hydrogen in which H enters the interstitial sites can enhance lithium adsorption, presumably by association with H at the same or nearby interstitial sites.

1.2.1.2 Nanostructured porous graphene materials

In this section, we will introduce two representative nanostructured porous graphene materials as anodes in lithium-ion batteries.

1.2.1.2.1 Ordered mesoporous carbon

Ordered mesoporous carbon can be synthesized starting from a template of ordered porous silica, which is known as man-made molecule sieves. Zhou et al.[19] utilized such anode material, called CMK-3 and shown in **Fig 1.17**[19], to obtain a reversible capacity of 1000 mAh g^{-1}. This value is about three times higher than that of conventional graphite. Although carbon nanotubes have pores of a similar diameter, only CMK-3 has an ordered pore structure. Therefore, it was thought that the ordered structure may facilitate electrolyte transport and access, which benefits capacity.

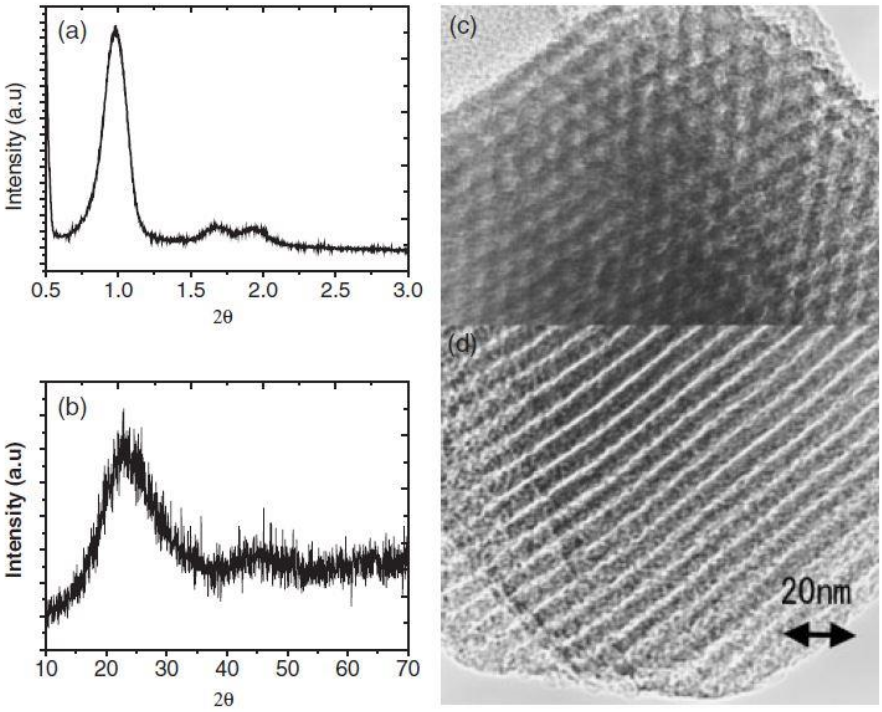

Figure 1.17 (A) Small angle and (B) wide angle X-ray diffraction patterns of CMK-3, TEM images of CMK-3 carbons along (C) and perpendicular (D) to the direction of hexagonal pores. (Reprinted from Ref 19 with permission.)

1.2.1.2.2 Hierarchical porous graphene materials

Macropores and mesopores may also coexist in the so-called hierarchical porous graphene materials as shown in the **Fig.1.18**[20] As in the case of mesoporous ordered graphene materials, these materials are prepared using a template of silica monolith that possesses a parent hierarchical meso-macro porous structure. Such hierarchical carbon delivers better capacity than commercial graphite as shown in **Fig1.19**[20], and this advantage is maintained even at 60C (1C= 372 mA g^{-1}.)

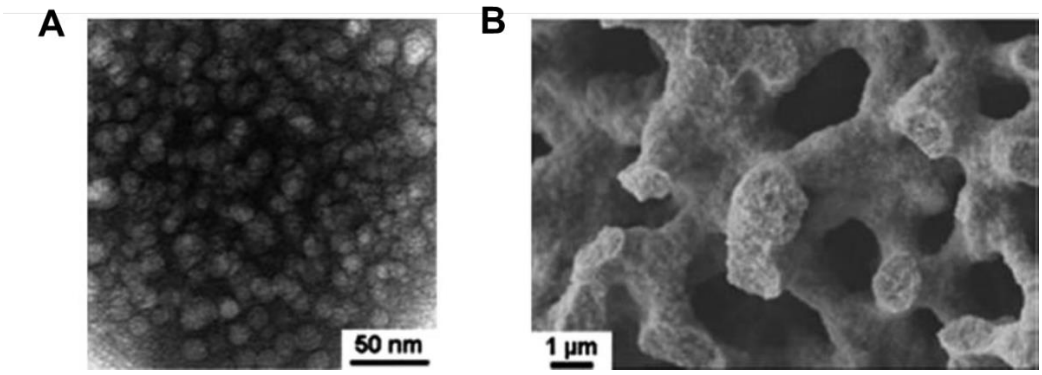

Figure 1.18 (A) TEM images of hierarchical carbon, (B) SEM of hierarchical carbon at high resolution. (Reprinted from Ref. 20 with permission.)

These results suggest that nanostructured porous graphene materials may be advantageously used as anodes. Indeed, their storage capacity suggests the formation of Li_3C_6 compared to the standard intercalation compound LiC_6 of graphite, and they have the additional advantage of delivering rate capability. Apparently, nanostructured pores can provide a more favorable setting for Li intercalation/storage, as well as transport pathways and/or reaction sites for Li ions, electrons and liquid electrolyte.

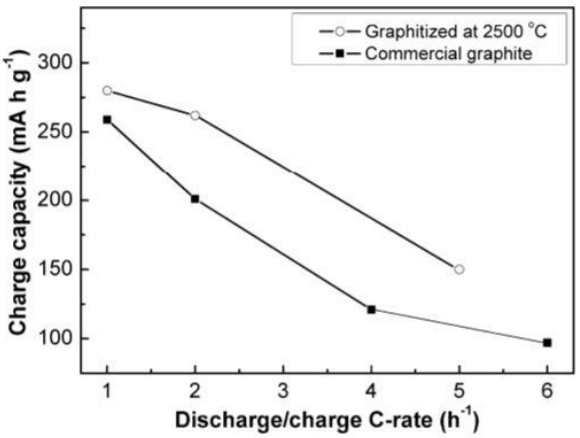

Figure 1.19 Charge capacity vs rate of hierarchical carbons and commercial graphite. (Reprinted from Ref. 20 with permission.)

However, three major drawbacks are known for these advanced graphene materials. First, it is obvious that they have low packing densities because of high porosity, delivering inadequate volumetric capacities for practical carbon electrodes. Second, there is a large initial irreversible capacities due to the formation of SEI and the H-C bonds, which sequester dormant Li unavailable for repeated use. Because of the very large specific surface area, the amount sequestered and the detriment to the Coulombic efficiency are very large. Third, although Zheng et al.[21] found that the irreversibility decreases as the H/C ratio decreases, there is a large voltage hysteresis (1-3V) coming from the over-potentials in forming the SEI and/or storing Li at the C-H sites. This leads to a further lowering of the energy efficiency.

1.2.2 Composite anode materials made of active materials and graphene

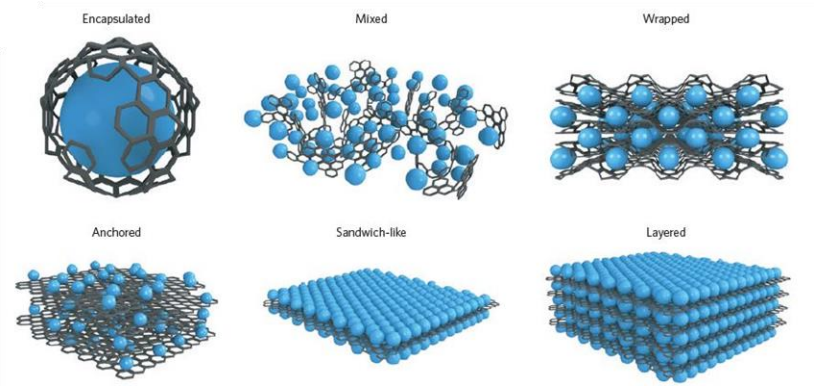

Figure 1.20 Structural models of graphene composites. (Reprinted from Ref. **22** with permission.)

Not contributing to the capacity, graphene is mostly an inactive part when it is combined with an electrochemically active material to form a composite. Composites of active materials and porous graphene may be constructed in the ways shown in **Fig.**

1.20[22], encapsulated, mixed, wrapped, anchored, sandwiched, and layered. Depending on the type, the composite structures may offer distinct advantages. For example, having graphene encapsulation can endow the active materials within with a more stable SEI and better cycling stability. Below we will discuss their functionalities by way of examples.

Table 1.2 Comparison of conductivity of graphene and various advanced anode materials

Materials	Conductivity (S/m)	References
graphene	~10^{5}	Ref. 22
Si	~10^{-3}	Ref. 23
Ge	~2	Ref. 23
Sn	~10^{7}	Ref. 23
SnO_2	~10^{-3}	Ref. 24
GeO_2	~10^{-9}	Ref. 25
ZnO	~10^{-3}	Ref. 26
Fe_2O_3	~10^{-5}	Ref. 27

The first and most important function of graphene is its servicea as an internal connector between nanoscale active anode materials and bulk metal electrodes. This is achieved by providing electron transport, since semi-conductive active anode materials generally has rather poor electrical conductivity as shown in **Table 1.2**.

Therefore, despite the rather short distance of electrical transport in nanomaterials, their electrical conduction is still totally inadequate for the fast rate processes expected of practical electrode materials. Depending on the architecture, composite materials may have greatly improved one-to-three dimensional (1D to 3D) electronic transport. For example, in the upper panel of **Fig. 1.21A and B**[28], the composite monolith of carbon nanotubes and active materials offers both 1D and 3D conducting pathways for coated silicon anodes. Likewise, in the lower panel of **Fig. 1.21C and D**[29], graphene sheets provide 2D conduction for SnO_2 nanoparticles. As a result, these composites have an improved rate performance.

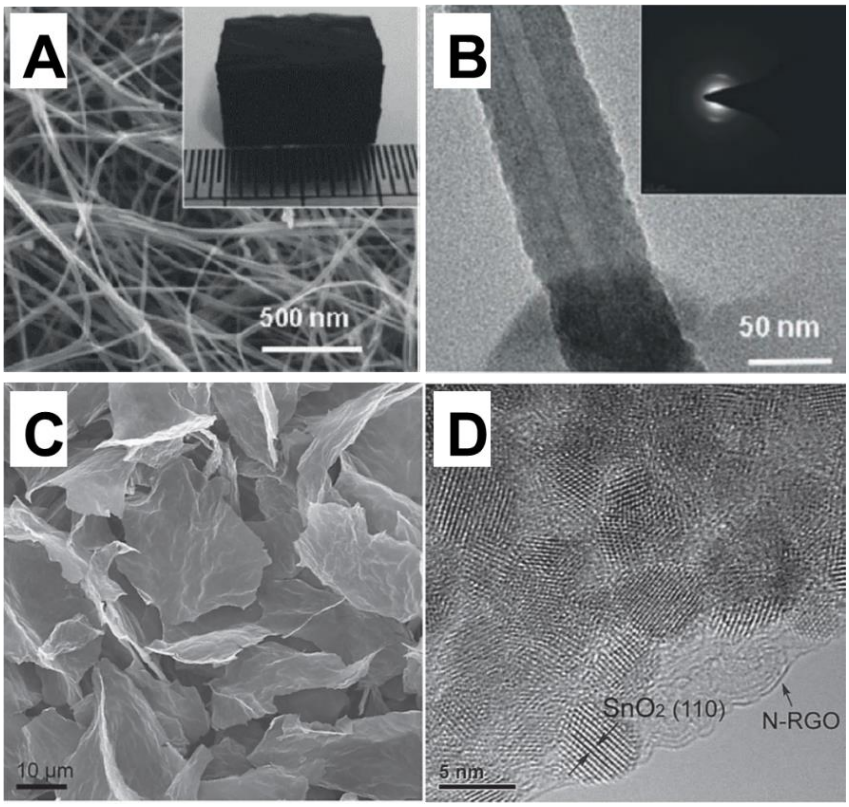

Figure 1.21 (A) SEM image of silicon-carbon sponge with digital photo of the sponge in the inset. (B) TEM image of silicon-carbon coaxial morphology with selected area electron

diffraction pattern in the inset. (C) SEM image and (D) high resolution TEM image of SnO_2@N-RGO. (Reprinted from Ref. 28 and Ref. 29 with permission.)

Providing easy transport and ready access to liquid electrolyte is the second important function of the porous graphene materials, which have much porosity and a high specific surface area. Because of this, ion transport is made more efficient and supportive to high rate operation. This is especially important in electrodes that have a high areal loading, as is the case in all practical electrodes. The porous graphene framework can still provide efficient ion-transport pathways despite the much reduced void space and the interference between the active materials in these highly loaded electrodes. This is demonstrated, for example, in the holey graphene material **Fig. 1.22** [30] that is packed with nano Nb_2O_5 to high loading; it still obtains high capacity at high rates.

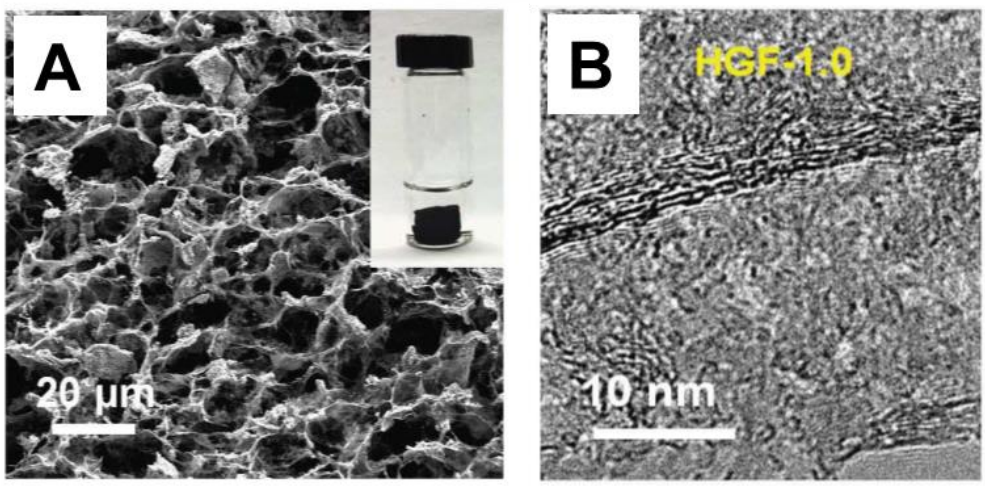

Figure 1.22 (A) Cross-sectional SEM image of HGF/Nb_2O_5 composite. (B) TEM image of graphene sheets etched by H_2O_2 for 1 h. (Reprinted from Ref. 30 with permission.)

Another beneficial function of porous graphene material is to help accommodate

the large volume change during the conversion and alloying reactions of active materials. For example, active materials can be housed within the graphene materials in a yolk-shell/core-shell construct as shown in **Fig. 1.23 A**[31]**, B**[32] and **C**[33] for Si-C, Sn-C and FeO-carbon composites, respectively. This helps mitigate the loss of electrical contact of active materials which often happens during conversion and alloying reactions. This in turn helps maintain the integrity of SEI, which often breaks as a result of the large volume change. For example, the same composites in **Fig. 1.23 A**[31]**, B**[32] and **C**[33] all have more stable SEI, which greatly enhances the cycle life of electrodes.

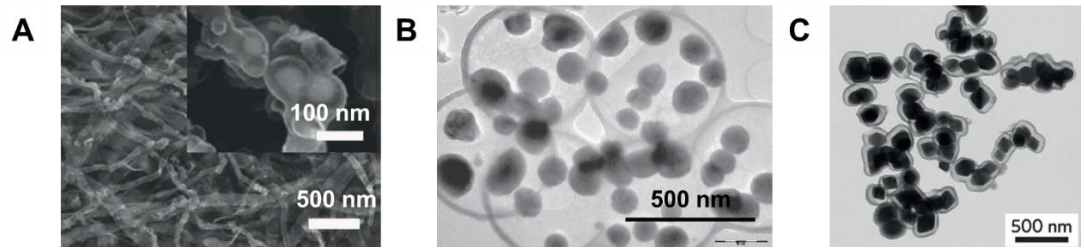

Figure 1.23 SEM/TEM images of yolk-shell/core-shell nanostructures for (A) Si-C composite, (B) Sn-C composite and (C) FeO-C composite. (Reprinted from Ref. 31, 32 and 33 with permission.)

1.3 High loading electrodes in lithium-ion batteries

1.3.1 Practical needs for high loadings

A packaged battery contains some components that bear no capacity. In **Fig. 1.24A**[34], the active electrode materials that are responsible for all the capacity only account for 1/3 of the device mass. This is the case if the electrode materials are

loaded to ~10 mg cm^{-2} in the device. To estimate the gravimetric capacity of the device, one thus need to divide the gravimetric capacity of the electrode materials by 3, and if a lower mass loading is used, then the denominator is even bigger. For example, in a device that has both electrodes loaded with 1 mg cm^{-2} of active materials, then the denominator is 12 (see **Fig. 1.24 B**[35]). Since almost all the advanced electrode materials reported in the literature were demonstrated at a loading lower (sometimes much lower) than 1 mg cm^{-2}, the high gravimetric capacities of the active materials have little practical implication unless they can first be repeated at a much higher loading. To set the goal, one may aim at the loading levels in commercial electrodes, which are 10 mg cm^{-2} on the areal basis and 1.6 g cm^{-3} on the volumetric base.

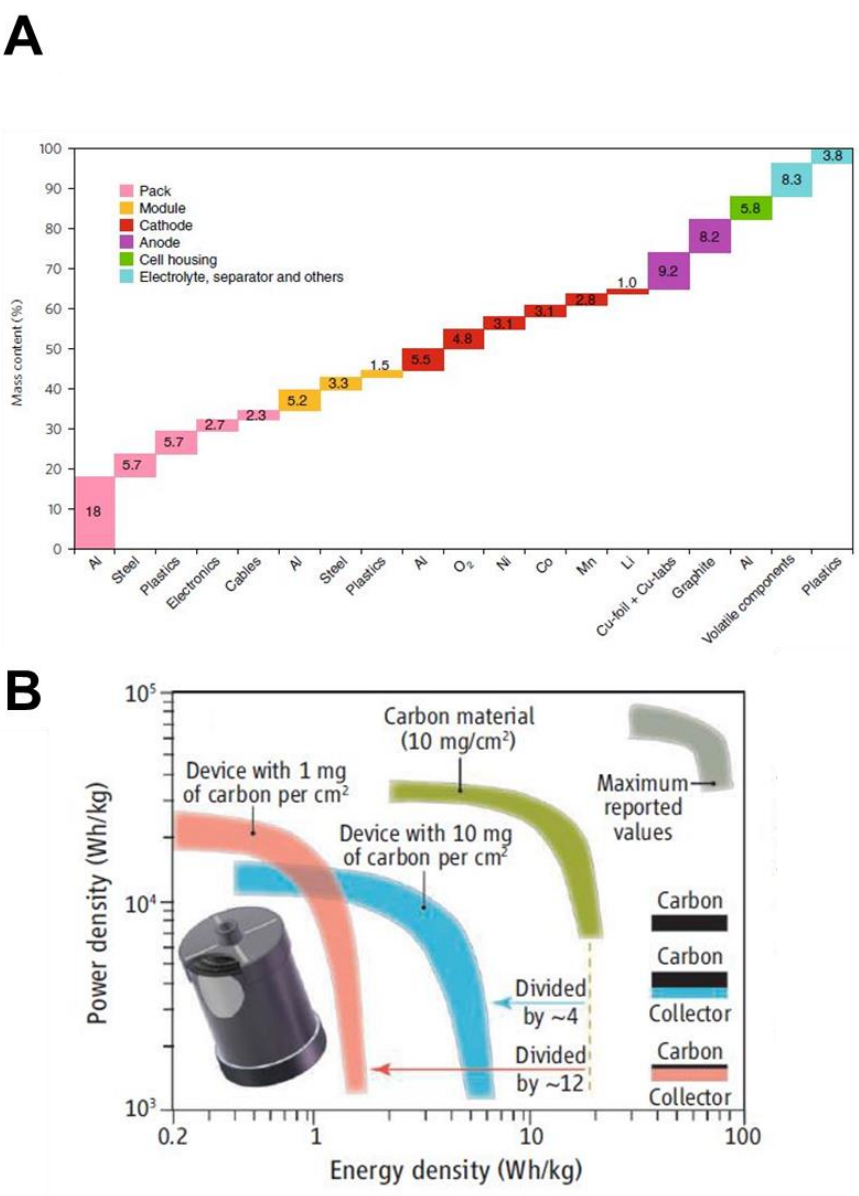

Figure 1.24 (A) Components of lithium ion batteries packs and a mass content breakdown. (B) Ragone plots of electrical energy storage devices on a gravimetric basis. (Reprinted from Ref. 34 and 35 with permission.)

1.3.2 Challenges of achieving high loadings for advanced nanostructured materials

To achieve the above goal proves to be rather challenging for nanomaterials. First, scaling up nanomaterial synthesis to larger thickness and higher density may be fundamentally difficult because the process kinetics and thermodynamics are usually strongly non-linear. Therefore, by merely lengthening the processing time or increasing the reactant concentrations, one may obtain a thicker, denser product that does not resemble the original nanomaterial and not possess the same physical and electrochemical characteristics. Second, the manufacturing process to achieve high areal loading typically calls for a thick electrode, but its microstructure may not be conducive to ion and electrolyte transport. For example, it may have a very long transport distance instead of the more desirable conduits that provide rapid transport perpendicular to the electrode; failing that, poor electrode kinetics will result especially in high rate operations. This is the case in calendaring compression, which is commonly used to manufacture commercial graphite anodes that have a high volumetric loading with about 20% porosity. Their porosity takes the form of anisotropic pores and channels that lie along the horizontal direction, which is not favorable for ion transport. Regarding nanomaterials, it is especially difficult to achieve high loading because of its highly porous nature, so even if they are subject to the same compression ratio by calendaring, the loading level is still lower than that of the commercial graphite electrode. What is worse is that the compression process may remove the structural advantages of nanomaterials, because in highly compressed nanomaterials the high specific surface area that endows high reactivity to

nanomaterials may become blocked by severe inter-particle interference and agglomeration. As a result, the liquid electrolyte that must have access to the active surface of nanomaterials has difficulty in infiltrating and transport.

1.3.3 Current approaches to high loading electrodes

Several approaches have been developed to address the above challenge. First, architectures with vertically aligned channels have been designed to provide better electrolyte transport in thick electrodes. For example, Chiang et al. used magnetic templating and freeze-casting, etc., to create such channels for both (see **Fig. 1.25A**)[36] cathodes and (see **Fig 1.25B**)[37] anodes in lithium ion batteries to obtain a several-fold improvement in areal capacity. Yang et al. utilized a liquid crystal template to vertically align 2D "Maxene" platelets to again create such channels in thick electrodes (see **Fig 1.25C**[38]). However, while a high areal loading is achieved in these approaches by increasing the thickness, they suffer from low volumetric loading because of the large quantity of macro-scale channels.

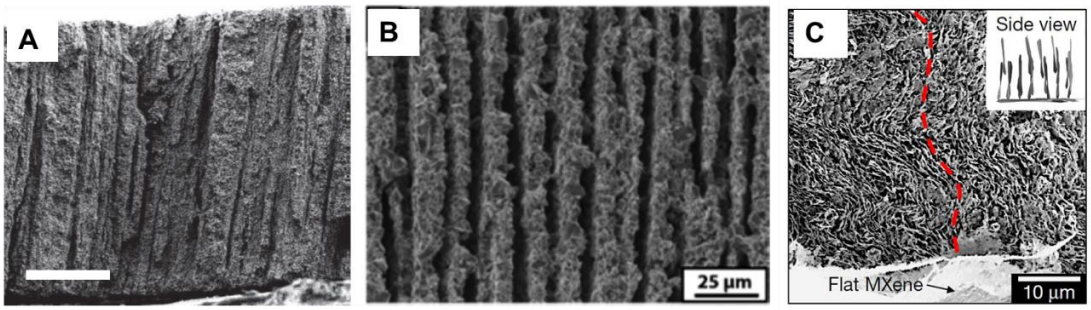

Figure 1.25 (A) Side view cross-sectional SEM of sintered $LiCoO_2$ cathodes with continuous linear pores (scale bar, 200 µm). (B) SEM of freeze-cast carbon. (C) SEM of vertical nanosheets on horizontally aligned MXene current collector. The red dashed line

illustrates ion transport path after bending of MXene layers in the vertical direction. The inset is illustration of Maxene direction from side view. (Reprinted from Ref. 36, 37 and 38 with permission.)

Regardless of electrochemical performance, existing composites of nanomaterials and 3D graphene composite electrodes all have relatively low areal loadings as shown in **Table 1.3** and **Table 1.4**. This is because either they cannot be compressed or they crumble into fine dust after compression due to the lack of elasticity. [39-43] [39-48] Such outcome is not unexpected, for inorganic active electrode materials are typically brittle ceramics, so despite the support of 3D graphene they can easily break or fall off during mechanical deformation. In addition, most 3D graphenes reported in the literature are not very elastic themselves, some actually quite brittle. Crumbled dusts and even intact composites usually have poor electrochemical performance for the same reason as mentioned in the previous section: their pores and pore channels are flattened and aligned along the electrode plane rather than normal to the plane, thus depriving the nanomaterials of effective ion/liquid/electron transport.

Table 1.3 Comparison of properties of various crumbled 3D composites

3D composite	Electrode processing	Areal loading (mg cm^{-2})	Elasticity	References

Fe_2O_3/rGO 3D assembly	Slurry-casting	1.0	No	Ref. 41
Dense density N-doped holey graphene monolith	Slurry-casting	0.62~2.75	No	Ref. 39
Dense integration of sulfur/3D graphene compact cathode	Slurry-casting	0.8~1	No	Ref. 40
SnO_2/rGO 3D assembly	Slurry-casting	1.87	No	Ref. 42
Co3O4@ 3D carbon foam derived from melamine foam	Slurry-casting	1.0	No	Ref. 43
Superelastic graphene monolithic composite	Free-standing monolith	>10	Yes	This work

Note:

3D composites of the literature in this table easily crumble after compression. Electrodes for electrochemical tests are prepared using dust of crumbled composite by slurry-cast process.

Table 1.4 Comparison of properties of various 3D composite monoliths.

3D composite	electrode processing	Areal loading (mg cm^{-2})	Elasticity	References
Li_2S/ doped 3D graphene aerogel	Free standing monolith	1.8~2.3	No	Ref. 44
Ge@3D graphene grown on nickel foam	Free-standing monolith	1.8	No	Ref. 45
Si@3D graphene grown on nickel foam	Free-standing monolith	0.4~1.5	No	Ref. 46
$CoMoO_4$ @ 3D graphene grown on nickel foam	Free-standing monolith	0.51	No	Ref. 47
Fe_2O_3@ CNT/3D graphene grown on nickel foam	Free-standing monolith	1.85	No	Ref. 48
Superelastic graphene monolithic	Free-standing monolith	>10	Yes	This work

composite

Note:

In this table, 3D composite monoliths are not elastic enough to be compressed.

In this table, monolithic electrodes in the literature were all tested at low loading.

1.4 Plan of the thesis

The goal of this thesis is to develop a new generic approach to manufacture electrodes with high loading levels of nanomaterial/3D graphene composites. We will utilize a new generation of superelastic 3D porous graphene scaffold, and deposit onto it nanoparticles of active materials capable of conversion and alloying reactions to form robust composites that (a) remain superelastic despite severe compression and (b) maintain intact adhesion between nanoparticles and scaffold. We will demonstrate that such composites can achieve simultaneously high areal and volumetric loadings for advanced anode electrodes in lithium ion batteries. As such, the research may provide a possible pathway to transform “loose” nanostructured advanced materials into dense bulk engineering materials ready for practical use. A specific plan for each chapter follows.

In **Chapter 2**, we will investigate 3D porous graphene monoliths prepared at various temperatures and evaluate their superelastic performance. Nitrogen and boron codoping will be introduced to enhance their electrochemical performance. In

Chapter 3-7, we will respectively investigate the following representative anode materials: SnO_2, GeO_2, ZnO, Fe_2O_3 and TiO_2, which have decreasing amounts of volume change upon lithiation. Specifically, we will synthesize and deposit their nanoparticles, in situ, onto a scaffold of 3D graphene, forming composites. A systematic comparison of their electrochemical performance in terms of capacity, cycle life, columbic efficiencies, microstructural transformation, etc., will also be provided in these chapters. In the above, SnO_2 has 376% volume change, and TiO_2 has no volume change, so successes in their composites with 3D graphene as described in **Chapter 7** will serve as strong evidence that our approach is equally applicable to other active electrode nanomaterials that have huge or no volume change during electrochemical reactions. Additional information will be provided in **Appendix.**

1.5 A precap of the thesis

Oxides studied here have a specific gravity ranging from 4-7 (6.95 g cm^3 for SnO_2, 4.23 g cm^3 for GeO_2, 5.6 g cm^3 for ZnO and 5.24 g cm^3 for Fe_2O_3). They constitute 66 +/- 3 wt.% in the as-formed composite monolith, which is more appropriately termed composite aerogel in view of its very low density, about 0.07 g cm^{-3}. With the theoretical density of 2.2 for graphite/graphene/carbon and an initial density of 0.07 g cm^{-3} for the aerogel, we estimate the aerogel has 1.0 +/- 0.3 vol.% oxide, 1.2 +/- 0.2 vol.% carbon, and void for the rest. Carbon (graphene) above takes a tubular form of 200 nm diameter with a wall thickness of 20 nm. Therefore, oxide, if ~50% dense and fully covering the graphene tube, should have a thickness of 25 nm to be consistent with the oxide/graphene ratio of their respective weight and volume

percentages. In **Fig. 1.26,** we illustrate the representative microstructure of 3D graphene and its aerogel composites with oxides using SnO_2 as an example. For each oxide, identical composites were prepared using the same method: with the same starting material (3D graphene) and the same precipitation method to deposit oxide nanoparticles onto the graphene network via a hydrothermal or sol-gel reaction.

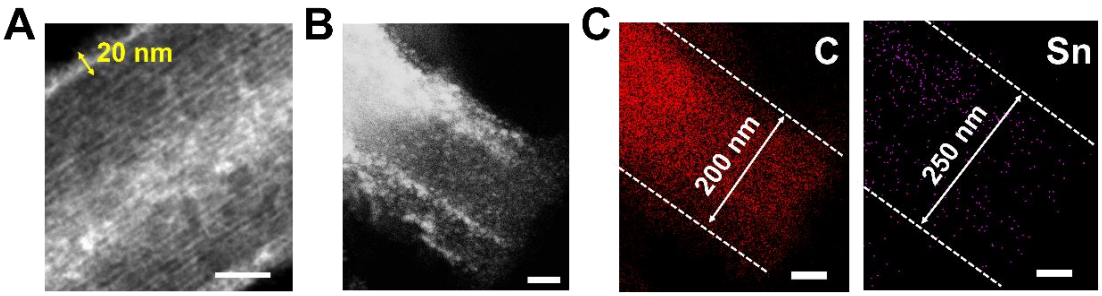

Figure 1.26 High angle annular dark-field electron microscopy of (A) graphene tube and (B) SnO_2-based 3D composite. (C) Elemental mapping of (B) showing C and Sn distribution. (Scale bar = 50 nm.)

Starting with the as-formed aerogel, areal loading of various values can be achieved by using different initial weight of the aerogel, which is determined by the initial thickness of the aerogel. The final loading in the compressed composite is corrected by the area change during compression, which is relatively small because the aerogel composite has a very small Poisson ratio. For example, if an aerogel of an initial diameter of 0.4 cm and an initial thickness of 0.15 cm is compressed to the final thickness 0.0028 cm, the diameter increases to 0.478 cm, for a thickness compression ratio of 56, a volume compression ratio of 41, and an area ratio of only 1.39. Because

the percentage areal increase observed is almost independent of the compression ratio, we believe most of the increase occurs during initial compression, after that the relatively dense composite shrinks in the thickness direction only without further lateral expansion. With an initial mass of 1.43 mg, the above composite after compression and areal expansion has an areal loading of 8 mg cm^{-2} and volumetric loading of 2.83 g cm^{-3}, of which 28 vol.% is oxide, 39 vol.% is carbon, and 33 vol.% is void. Likewise, in a composite of an areal loading of 6.7 mg cm^{-2} and volumetric loading of 2.3 g cm^{-3}, 23 vol.% is oxide, 33 vol.% is carbon, and 44 vol.% is void. Therefore, the vol.% of void gradually decreases when the loading increases. The above volume ratios are for the composites containing SnO_2, but they have also been calculated for all the composites as summarized in **Appendix Table 5.1**, giving roughly comparable numbers**.** For example, in a composite of GeO_2 with an areal loading of 5.6 mg cm^{-2} and volumetric loading of 2 g cm^{-3}, 30 vol.% is oxide, 31 vol.% is carbon, and 39 vol.% is void. In a composite of ZnO with an areal loading of 8.1 mg cm^{-2} and volumetric loading of 2.9 g cm^{-3}, 32 vol.% is oxide, 47 vol.% is carbon, and 21 vol.% is void. In a composite of Fe_2O_3 with an areal loading of 7.9 mg cm^{-2} and volumetric loading of 2.8 g cm^{-3}, 34 vol.% is oxide, 45 vol.% is carbon, and 21 vol.% is void. Even higher loading is possible. In our experience, we have obtained areal loading as high as 13 mg cm^{-2}.

The void space in the compressed composite is enough for accommodating some volume expansion during lithiation of the oxide. For example, in a composite of SnO_2 at 6.7 mg cm^{-2} and 2.3 g cm^{-3}, up to 192% (376%*51%) volume expansion of oxide can be accommodated, whereas 117% (376%*31%) can be accommodated if the SnO_2

composite is loaded to 8 mg cm^{-2} and 2.8 g cm^{-3}. Given the available void in the composite and the capacity from graphene (1412 mAh g^{-1} at 2.8 mg cm^{-2} and 1850 mAh g^{-1} at 1.7 mg cm^{-2}), we can calculate the expected capacity of the composites: 760.9 mAh g^{-1} for SnO_2-based composite at 8 mg cm^{-2} and 2.8 g cm^{-3}, and 1098.5 mAh g^{-1} for the same oxide-based composite at 6.7 mg cm^{-2} and 2.3 g cm^{-3}. Comparing these calculated capacities with the actual capacities, we find that there is still a capacity of 18.2 % unaccounted for in the 8 mg cm^{-2} and 2.8 g cm^{-3} composite, and 4.5% in the 8 mg cm^{-2} and 2.8 g cm^{-3} composite. These remaining capacities are obtained because our coin cells are not full (the diameter of the coil cell is 1.6 cm, vs. 0.5 cm for the electrodes.) So there is definitely free space in the coin cell to accommodate all the expansion called for by oxide lithiation. It is also obvious that the lower the loading, the less the need for electrode expansion since the electrode already has proportionally more void to accommodate oxide expansion. These calculations have been performed for all composites as summarized in **Appendix Table 5.1**

Advantages of high loading go beyond the energy of the battery pack. Since many advanced materials have a very high gravimetric capacity, high loading also allows high charging rate to be attained on the areal or volumetric basis without using a very high charging rate on the gravimetric basis. This lessens the damage to the cell. For example, using GeO_2 with 1518 mA h g^{-1} at 13 mg cm^{-2}, we have obtained an areal capacity of 19.7 mA h cm^{-2} at a rate of 2.6 mA cm^{-2}, which corresponds to a volumetric capacity of 6961 mA h cm^{-3} at a rate of 917 mA cm^{-3}, even though the electrode is nominally charged/discharged at only 0.2 A g^{-1}. Likewise, using Fe_2O_3 with 714 mA h g^{-1} at 9 mg cm^{-2}, we have obtained an areal capacity of 6.5 mA h cm^{-2}

at a rate of 4.7 mA cm^{-2} and a volumetric capacity of 2341 mA h cm^{-3} at a rate of 1640 mA cm^{-3} even though the electrode is nominally charged/discharged at only 0.5 A g^{-1}. Another advantage of high loading is that it allows high areal and volumetric capacities to be attained even with inferior gravimetric capacities. For example, GeO_2-based 3D composite at 12 mg cm^{-2} suffers a 85% loss in the gravimetric capacity after 700 cycles, leaving only 369 mAh g^{-1} that is relatively modest. Yet thanks to high loading this composite after 700 cycles still affords an areal capacity of 4.4 mAh cm^{-2} and a volumetric capacity of 1563 mAh cm^{-3}, which is 2.3 and 8 times those of commercial graphite, respectively. Therefore, being able to achieve high loading of advanced electrochemical oxides is decidedly an advantage.

The approach is scalable because the intrinsic material performance is almost independent of loading, even up to very high loading. This is best seen by plotting the gravimetric capacity against areal loading, which is relatively constant for all the composites as shown in the upper panel of **Fig. 1.27**. Except for TiO_2-based composite, all the gravimetric capacities well exceed that of commercial graphite at 12.5 mg cm^{-2}. This is a good proof of functional invariance in that the property is independent of the areal and volumetric density or thickness.

There are at least three reasons why functional invariance is achieved in our materials. First, they all use the same starting material (namely the aerogel composite) processed in exactly the same way following the same thermodynamics and kinetics, hence having the same phase assemblage, nanostructure and interfacial adhesion. Second, because of good oxide adhesion to the 3D graphene backbone, the composite shares the same superelasticity of the graphene backbone. Therefore, there is no

change in the local structure, in terms of the local construct of “tubular graphene of 200 nm diameter and 20 nm wall thickness, coated by 25 nm oxide”, despite extreme compression. That is, the same local structure is obtained regardless how much excess void space is squeezed out, which increases the solid loading from roughly 2 vol.% to 65 vol.%. Third, after compression, apparently there is still enough contiguous void space open to the outside thus allowing liquid electrolyte and ion to transport into the composite, which is evident by the same specific area before and after compression as shown in the lower right panel of **Fig. 1.27**. This is because, during compression, the network microstructure behaves like a compressed “wire basket”, which remains transparent to liquid even after extreme compression. Meanwhile, the same electrical conductance is maintained by the contiguous graphene backbone as shown in the lower left panel of **Fig. 1.27**. Therefore, the same electrochemical performance including capacity and resistance is obtained regardless of the compression ratio (see the top panel of **Fig. 1.27**).

With these results, we have demonstrated a scalable approach to incorporate new active nano-oxides into high loading anodes to deliver high areal and volumetric capacities at high areal and volumetric charging/discharging rates. The approach is especially advantageous for those active oxides that experience extraordinarily large volume changes during lithiation/delithiation, which invariably causes pulverization, destruction, or otherwise rapid capacity decay when the oxides are incorporated into other forms of anodes.

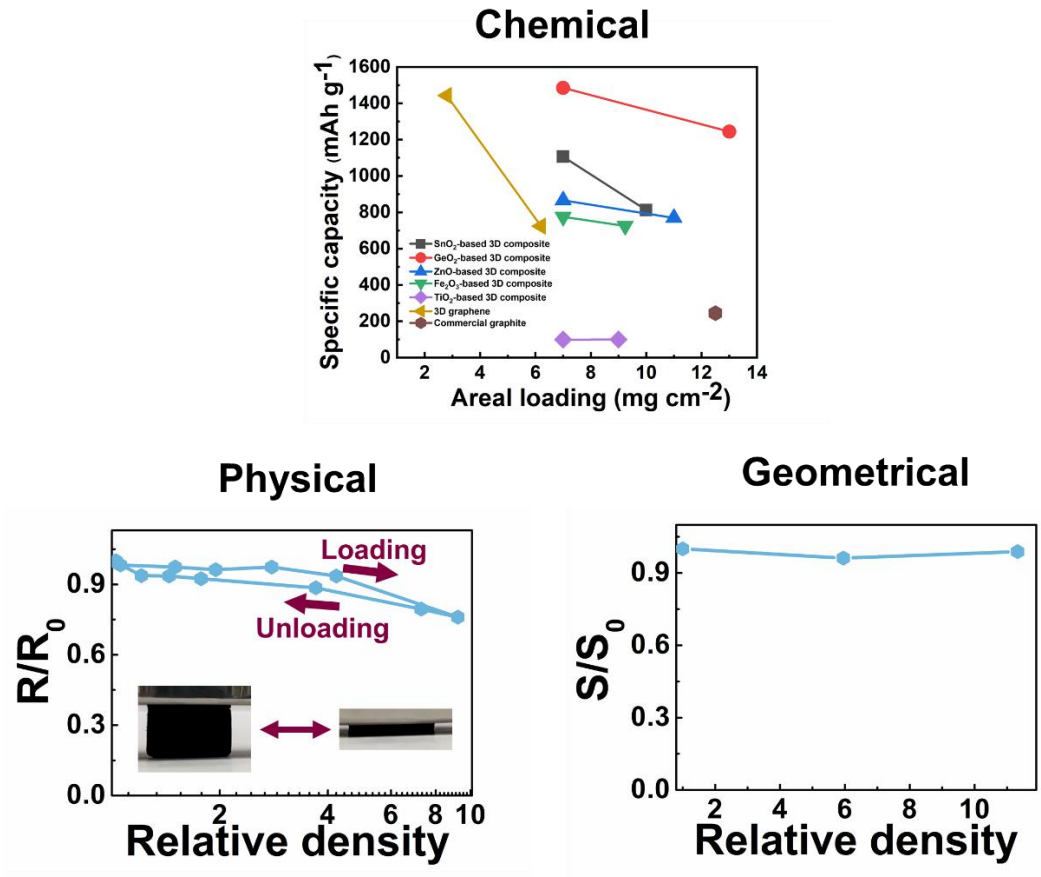

Figure 1.27 Specific capacity vs. areal loading for all 3D network composites, 3D graphene and commercial graphite. The capacities are recorded after 12.5% decay under the current density of 0.2 A g^{-1}, except for Fe_2O_3 at 0.5 A g^{-1}. Upper panel: gravimetric capacities for all oxide composites are relatively insensitive to areal loadings. Lower panels: despite a 10× increase in the packing density, (left) physical resistance and (right) geometrical specific surface area are constant in SnO_2-based network composite. At relative density 1, R_0=353.1 Ω and S_0= 311.8 m^2 g^{-1}.

References

1 The cost of solar energy. *https://blog.pickmysolar.com/the-price-of-a-solar-panel-system-over-the-years*.

2 Whittingham, M. S. J. P. o. t. I. History, evolution, and future status of energy storage. **100**, 1518-1534 (2012).

3 Etacheri, V. *et al.* Challenges in the development of advanced Li-ion batteries: a review. **4**, 3243-3262 (2011).

4 Huggins, R. *Advanced batteries: materials science aspects*. (Springer Science & Business Media, 2008).

5 Okamoto, H. J. J. o. P. E. The C-Li (carbon-lithium) system. **10**, 69-72 (1989).

6 Murthy, M. K. & Ip, J. J. J. o. t. A. C. S. Studies in Germanium Oxide Systems: I, Phase Equilibria in the System Li2O—GeO2. **47**, 328-331 (1964).

7 John, M. S., Furgala, A. & Sammells, A. J. J. o. T. E. S. Thermodynamic Studies of Li-Ge Alloys: Application to Negative Electrodes for Molten Salt Batteries. **129**, 246-250 (1982).

8 Wang, J., King, P. & Huggins, R. J. S. S. I. Investigations of binary lithium-zinc, lithium-cadmium and lithium-lead alloys as negative electrodes in organic solvent-based electrolyte. **20**, 185-189 (1986).

9 Kleykamp, H. J. F. e. & design. Phase equilibria in the Li–Ti–O system and physical properties of Li2TiO3. **61**, 361-366 (2002).

10 Nitta, N., Wu, F., Lee, J. T. & Yushin, G. J. M. t. Li-ion battery materials: present and future. **18**, 252-264 (2015).

11 Sato, K., Noguchi, M., Demachi, A., Oki, N. & Endo, M. J. S. A mechanism of lithium storage in disordered carbons. **264**, 556-558 (1994).

12 Winter, M., Besenhard, J. O., Spahr, M. E. & Novak, P. J. A. m. Insertion electrode materials for rechargeable lithium batteries. **10**, 725-763 (1998).

13 Zhukovskii, Y. F., Balaya, P., Kotomin, E. A. & Maier, J. J. P. r. l. Evidence for interfacial-storage anomaly in nanocomposites for lithium batteries from first-principles simulations. **96**, 058302 (2006).

14 Zhukovskii, Y. F., Kotomin, E., Balaya, P. & Maier, J. J. S. S. S. Enhanced interfacial lithium storage in nanocomposites of transition metals with LiF and Li2O: Comparison of DFT calculations and experimental studies. **10**, 491-495 (2008).

15 Zheng, T., Xing, W. & Dahn, J. J. C. Carbons prepared from coals for anodes of lithium-ion cells. **34**, 1501-1507 (1996).

16 Lin, T. *et al.* Nitrogen-doped mesoporous carbon of extraordinary capacitance for electrochemical energy storage. **350**, 1508-1513 (2015).

17 Way, B. & Dahn, J. J. J. o. T. E. S. The Effect of Boron Substitution in Carbon on the Intercalation of Lithium in Li x (B z C 1− z) 6. **141**, 907-912 (1994).

18 Wang, X. *et al.* Atomistic origins of high rate capability and capacity of N-doped graphene for lithium storage. **14**, 1164-1171 (2014).

19 Zhou, H., Zhu, S., Hibino, M., Honma, I. & Ichihara, M. J. A. M. Lithium storage in ordered mesoporous carbon (CMK-3) with high reversible specific energy capacity and good cycling performance. **15**, 2107-2111 (2003).

20 Hu, Y. S. *et al.* Synthesis of hierarchically porous carbon monoliths with highly

ordered microstructure and their application in rechargeable lithium batteries with high-rate capability. **17**, 1873-1878 (2007).

21 Zheng, T., Xue, J. & Dahn, J. J. C. o. m. Lithium insertion in hydrogen-containing carbonaceous materials. **8**, 389-393 (1996).

22 Raccichini, R., Varzi, A., Passerini, S. & Scrosati, B. J. N. m. The role of graphene for electrochemical energy storage. **14**, 271 (2015).

23 Metal conductivty *https://www.thoughtco.com/table-of-electrical-resistivity-conductivity-608499*.

24 The electricla properties of SnO_2. *https://pdfs.semanticscholar.org/c5ea/a918adde33db22a6cd33b388568ac2a3f5a4.pdf*.

25 Böhm, H. J. J. o. A. P. Electrical Conductivity of Vitreous GeO2. **43**, 1103-1107 (1972).

26 Dasari, M., Godavarti, U. & Mote, V. J. P. A. C. Structural, morphological, magnetic and electrical properties of Ni-doped ZnO nanoparticles synthesized by co-precipitation method. **12**, 100-110 (2018).

27 Ito, S., Yui, Y. & Mizuguchi, J. J. M. t. Electrical properties of semiconductive α-Fe2O3 and its use as the catalyst for decomposition of volatile organic compounds. **51**, 1163-1167 (2010).

28 Hu, L. *et al.* Silicon–Carbon Nanotube Coaxial Sponge as Li-Ion Anodes with High Areal Capacity. **1**, 523-527 (2011).

29 Zhou, X., Wan, L. J. & Guo, Y. G. J. A. m. Binding SnO2 nanocrystals in nitrogen-doped graphene sheets as anode materials for lithium-ion batteries. **25**, 2152-

2157 (2013).

30 Sun, H. *et al.* Three-dimensional holey-graphene/niobia composite architectures for ultrahigh-rate energy storage. **356**, 599-604 (2017).

31 Wu, H. *et al.* Engineering empty space between Si nanoparticles for lithium-ion battery anodes. **12**, 904-909 (2012).

32 Zhang, W. M. *et al.* Tin-nanoparticles encapsulated in elastic hollow carbon spheres for high-performance anode material in lithium-Ion batteries. **20**, 1160-1165 (2008).

33 Zhang, H. *et al.* Tailoring the void size of iron oxide@ carbon yolk–shell structure for optimized lithium storage. **24**, 4337-4342 (2014).

34 Kwade, A. *et al.* Current status and challenges for automotive battery production technologies. **3**, 290 (2018).

35 Gogotsi, Y. & Simon, P. J. S. True performance metrics in electrochemical energy storage. **334**, 917-918 (2011).

36 Sander, J., Erb, R. M., Li, L., Gurijala, A. & Chiang, Y.-M. J. N. E. High-performance battery electrodes via magnetic templating. **1**, 16099 (2016).

37 Amin, R., Delattre, B., Tomsia, A. P. & Chiang, Y.-M. J. A. A. E. M. Electrochemical Characterization of High Energy Density Graphite Electrodes Made by Freeze-Casting. **1**, 4976-4981 (2018).

38 Xia, Y. *et al.* Thickness-independent capacitance of vertically aligned liquid-crystalline MXenes. **557**, 409 (2018).

39 Wang, X. *et al.* High-Density Monolith of N-Doped Holey Graphene for

Ultrahigh Volumetric Capacity of Li-Ion Batteries. *Advanced Energy Materials* **6**, 1502100 (2016).

40 Li, H. *et al.* Dense integration of graphene and sulfur through the soft approach for compact lithium/sulfur battery cathode. *Nano Energy* **12**, 468-475 (2015).

41 Wang, H. *et al.* One-step preparation of single-crystalline Fe2O3 particles/graphene composite hydrogels as high performance anode materials for supercapacitors. *Nano Energy* **7**, 86-96 (2014).

42 Han, J. *et al.* Caging tin oxide in three-dimensional graphene networks for superior volumetric lithium storage. *Nature communications* **9**, 402 (2018).

43 Wang, L. *et al.* Ultralight flower ball-like Co3O4/melamine-derived carbon foam as anode materials for lithium-ion batteries. *Journal of Alloys and Compounds* **724**, 1117-1123 (2017).

44 Zhou, G., Paek, E., Hwang, G. S. & Manthiram, A. High-Performance Lithium-Sulfur Batteries with a Self-Supported, 3d Li2s-Doped Graphene Aerogel Cathodes. *Advanced Energy Materials* **6**, 1501355 (2016).

45 Mo, R., Rooney, D., Sun, K. & Yang, H. Y. 3D nitrogen-doped graphene foam with encapsulated germanium/nitrogen-doped graphene yolk-shell nanoarchitecture for high-performance flexible Li-ion battery. *Nature communications* **8**, 13949 (2017).

46 Ji, J. *et al.* Graphene-Encapsulated Si on Ultrathin-Graphite Foam as Anode for High Capacity Lithium-Ion Batteries. *Advanced Materials* **25**, 4673-4677 (2013).

47 Yu, X., Lu, B. & Xu, Z. Super long-life supercapacitors based on the construction of nanohoneycomb-like strongly coupled CoMoO4–3D graphene hybrid electrodes.

Advanced materials **26**, 1044-1051 (2014).

48 Chen, M. *et al.* Porous α-Fe2O3 nanorods supported on carbon nanotubes-graphene foam as superior anode for lithium ion batteries. *Nano Energy* **9**, 364-372 (2014).

Chapter 2 Mesoporous 3D graphene and doped 3D graphene as high areal and volumetric capacity anodes of lithium-ion batteries

2.1 Introduction

Carbon is a common material in electrochemical devices. In commercial lithium ion batteries (LIB), graphite is the anode material that stores lithium ion by intercalation, while in cathodes carbon black and the like are included to improve electrical conduction. Carbonaceous materials have also been broadly explored in research, either as a high-performance anode itself or combined with other active electrode materials to form a composite electrode, such as $LiFePO_4$/C cathode. To fully take advantage of the uniqueness of carbon, an ideal carbon material for electrode applications should have the following attributes.

First, it should be highly porous. Commercial graphite has served the battery community well because it has good electrical conductivity, stability and a relatively high packing density, but is limited in lithium storage by its theoretical capacity of 372 mAh g^{-1}, which requires six C to accommodate one intercalated Li. As mentioned in Chapter 1, highly porous carbon materials can augment intercalation storage with pore and cavity storage, thus have a higher storage capacity. Even non-active carbon materials should be porous since porosity can provide sites to accommodate active materials. In addition, ordered mesoporous structures with strategically aligned pathways may facilitate ion/liquid transport with less interference, which help deliver high-rate capability during electrochemical energy storage and release.

Second, it should be electrically conducting. Electrical conductivity of carbon increases with the degree of graphitization. Commercial graphite is highly

conducting because it has undergone high-temperature graphitization leaving few defects. Graphene having a completely graphitic two-dimensional net can also deliver high conductivity. On the other hand, few-layer graphene and other carbon materials have varying degrees of conductivity depending on the extent of graphitization and the fraction of amorphous domains. This is especially common in low-temperature pyrolyzed polymers which are generally unsuitable for electrode applications.

Third, it should be functionalized. Carbon materials without functionalization are generally hydrophobic and electrically neutral. In this way, it cannot provide good nucleation sites to oxides, nitrides, sulfides, etc., during electrode preparation. More importantly, the adhesion between carbon materials and active materials should be strong enough to withstand the application, or else they will lose electrical contact and capacity fading will result. A case in point is the carbon-sulfur composite. It is widely reported that carbon functionalization rendering its surface polar is beneficial for trapping sulfur.[1,2] In addition, dopant sites in doped carbon have been reported to contribute to additional capacity for Li storage.

Fourth, it should withstand severe compression. This is because the high porosity despite its benefits necessarily results in a low areal loading and volume packing density, which is not practical for commercial applications. While in principle a higher loading density may be achieved by compression that squeezes away unnecessary porosities, most carbon materials are pulverized by this operation, and the pulverized materials experience particle agglomeration and poor electrolyte transport. Thus, carbon materials capable of sponge-like severe compression without dislodging active materials deposited on them would be ideal:

they can maintain the pore channels required for electrolyte transport while forgoing useless void space. This should help achieve high areal and volumetric loading.

Guided by the above discussion and the literature review in the following section, the goal of this research is to develop such an “ideal” carbon material for composite electrode applications in lithium ion batteries. Several forms of high-quality superelastic mesoporous 3D graphene were prepared according to the schematic in **Fig. 2.1**. This graphene material platform being porous, electrically conducting, functionalized and superelastically monolithic fulfills all the above requirements. It contains a motif of covalently tetrahedral junctions made of few-layer graphene tubes that are bending-and-buckling tolerant thus capable of severe compression without crumbling. This form of 3D graphene can be made from an ordered-mesoporous 3D silica monolith template, followed by chemical vapor deposition (CVD) of carbon. In this process, too, hydrogen gas is used to etch away some nano-meso regions of the silica template, which leaves a large quantity of mesopores on the later-templated graphene tubes. The process was also optimized by using small molecules (which allow dopants such as N and B to aid later functionalization) to ensure conformal coating of the template and facilitate the growth of high-quality graphene, which leads to good electrical conductivity. This 3D graphene provides superior electrochemical performance itself, and it can also be used as the backbone of a composite bearing carbon-active deposits, which will be explored in the remainder of this thesis.

2.1.1 Literature review: functionally active graphene materials

The ideal graphene form is useful as either an active component contributing to capacity or a non-active component making no capacity contribution. In this part,

we focus on graphene materials as an active component of anodes in lithium-ion batteries. Pristine and hetero-atom doped graphene materials have been explored for this purpose, showing a higher capacity than that of commercial graphite anode. In contrast to bulk graphite, few-layer graphene can have extra-capacity due to lithium absorption on both sides of graphene sheets. For example, Lian[3] et al. utilized the Hummer method to exfoliate graphite into graphene sheets, which were used to form LIB anodes. The material delivered 848 mAh g^{-1} after 40 cycles at the current density of 100 mA g^{-1}, significantly higher than 375 mAh g^{-1} of graphite anode. A similar approach was also reported by Wang et al.[4], in which graphene sheets offered 460 mAh g^{-1} after 100 cycles under 372 mA g^{-1}. In addition to pristine graphene sheets, hetero-atom doping of graphene has been explored. For example, Cui et al.[5] annealed graphene oxide (GO) sheets in an ammonia atmosphere to prepare N-doped graphene sheets, and a capacity of 900 mAh g^{-1} at 42 mA g^{-1}, which was higher than that (600 mAh g^{-1} at 42 mA g^{-1}) of pristine graphene sheets, was claimed. Sun et al.[6] also demonstrated an enhanced capacity of 684 mAh g^{-1} of a N-doped graphene after 500 cycles, and they attributed the superior capacity and cycle stability to the structural defects induced by doping. Carbon materials with B and N co-doping have too been investigated. For example, Zhang et al.[7] used ammonia borane as a boron and nitrogen source to dope a carbon material and obtained 900 mAh g^{-1} after 100 cycles at 200 mA g^{-1}.

Another form of carbon explored is hierarchically structured porous graphene and carbon materials that promise to provide a better rate capability. For example, Xie et al. synthesized porous N-doped carbon on graphene sheets with a hierarchical sandwich structure by pyrolyzing a zeolitic imidazolate framework. The anode made of this material had a capacity of 530 mAh g^{-1} at 5 A g^{-1} after 400

cycles.[8] The superior rate performance was attributed to the facile ion transport in the hierarchical structure. Hou et al.[9] derived hierarchically porous N-doped carbon sheets by the graphitization of natural silk, and the anodes made thereof delivered 790 mAh g^{-1} after 300 cycles under 3720 mA g^{-1}.

Despite the considerable success of the above high-performance carbon anodes, none of them was made into a high loading form. Yet high loading is mandatory for any practical electrode. Therefore, in this chapter, we aim to explore the use of superelastic 3D graphene in both the pristine form and the doped form as a material for high-loading, high-performance practical anodes.

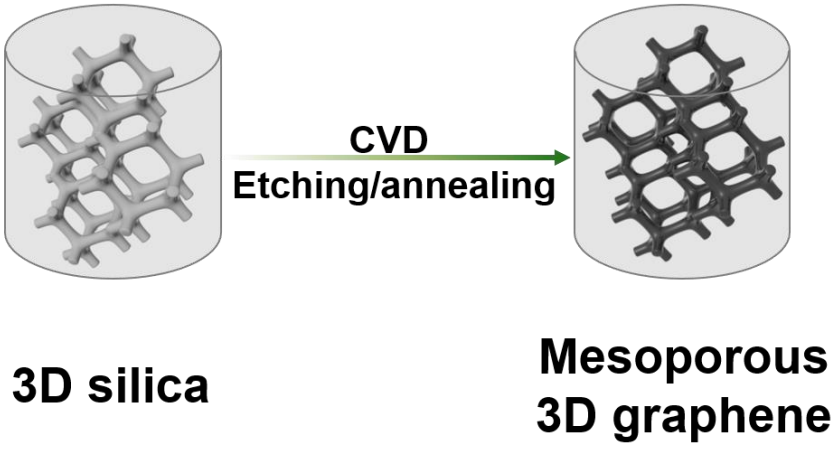

Figure 2.1 Fabrication schematic from 3D silica template to mesoporous 3D graphene scaffold by CVD. Doping in 3D graphene can be achieved through the use of dopant-containing carbon source.

2.2 Experimental procedures

2.2.1 Material synthesis

2.2.1.1 Mesoporous silica

Mesoporous silica preform was synthesized with the aid of a surfactant, pluronic block copolymer (P123, sigma Aldrich, Mw = 5800.) The surfactant of 1.286 g was first dissolved in 50 ml distilled water, then 7.14 ml HCl solution (12

mol/L) was added before adding the Si source, tetraethylsilicate (TEOS, ARCOS), at room temperature. After vigorous stirring for 30 min, the resultant sol was transferred into a PTFE-lined autoclave. Hydrothermal reaction was immediately initiated by heating the autoclave to 130^{o}C, then held there for 36 h. The recovered sample in the form of a wet monolith was dried in air, then ramped up at 1^{o}C/min to 550^{o}C for calcination for 6 h to obtain a monolith, to be called 3D silica, with a mesoporous ordered structure. This procedure was used to produce 3D silica monoliths of up to 1 L quantity apiece.

2.2.1.2 Mesoporous 3D graphene

3D graphene was grown onto the above 3D silica, which serves as a template with its mesoporous ordered structure. During preparation, Ar and H_2 at a flow rate of 300 sccm and 50 sccm, respectively, were first used to flush a tube furnace with 3D silica inside. This continued for 20 min, after that the furnace was ramped to 800^{o}C in 50 min. Next, CH_4 at a flow rate of 20 sccm was used as the carbon source to grow CVD graphene. This proceeded at 800^{o}C for 30 min, and was followed by an additional 60 min at 1100^{o}C. After CVD growth, the silica template in the harvested product was leached away by hydrofluoric acid, and the remaining graphene monolith, to be called 3D graphene, was dried and further graphitized at 2,250^{o}C for 1 h.

2.2.1.3 N-doped mesoporous 3D graphene

N-doped mesoporous graphene was similarly prepared by CVD growth, but additional source chemicals were provided during CVD for incorporating dopants. In this procedure, Ar at a flow rate of 100 sccm was used to carry N-containing liquid carbon sources, a mixture of Acetone nitrile (Alfa Aesar) and N,N-dimethylformamide (DMF, Alfa Aesar) at 8:2 (volume) ratio, and with additional

saturated dicyandiamide (DCDA, Alfa Aesar). The tube furnace with 3D silica inside was first flushed for 20 min at room temperature using the above gas mixture, after that the furnace was ramped to 1100^{o}C in 80 min and held there for 20 min, with the above argon/carbon source flow continuing at 100 sccm throughout the process, to grow graphene. After growth and cooling, the silica template in the harvested product was leached away by hydrofluoric acid, and the remaining N-doped 3D graphene monolith product was dried.

2.2.1.4 N-B codoped mesoporous 3D graphene

N,B- codoped mesoporous 3D graphene was similarly prepared by CVD growth with the same process parameters except for a different liquid carbon source that contains C, N and B. This was a pyridine-borane mixture with a borane concentration of 8 mol/L, which was designed to provide B and N dopants simultaneously.

2.2.1.5 Pre-lithiation treatment of 3D graphene

The 3D graphene electrode was pre-lithiated by directly contacting the electrode with a lithium foil while the electrolyte was added to facilitate Li transfer. Specifically, a 3D graphene electrode was placed over a lithium foil, and $LiPF_6$ electrolyte in a 50:50 w/w mixture of dimethyl carbonate (DMC) and ethylene carbonate (EC) was dropped into 3D graphene. After this, the contact between lithium foil and 3D graphene electrode was reinforced by slight compression using another piece of lithium foil placed on the top. Over the next 24 h, Li entered the composite to pre-lithiate it. After this treatment, the pre-lithiated composite electrode was ready for use without further treatment.

2.2.2 Characterization

2.2.2.1 Material characterization

Scanning electron microscopy (SEM) images were obtained in a field emission Magellan 400 microscope (FEI Company). Transmission electron microscopy (TEM), high angle annular dark field (HAADF) imaging, electron energy loss spectroscopy (EELS, Gatan), and elemental mapping were conducted in a JEOL 2100F microscope operated at 200 kV. Nitrogen adsorption-desorption isotherms at 77 K were measured in a Micromeritics Tristar 3000 system using vacuum-degassed samples (200 °C for 12 h). These isotherms were used to calculate (*a*) the specific surface area by the Brunauer-Emmett-Teller (BET) method and (*b*) the pore volume and pore size by the Barrett−Joyner−Halenda (BJH) method. Small and wide angle X-ray diffraction was performed in a Brucker D8 powder X-ray diffractometer using Cu *K*α radiation. X-ray photoelectron spectra (XPS) were collected in a Thermo Escalab 250Xi with Al *K*α radiation (hν =1,486.6 eV). Binding energies were calibrated using the 284.8 eV peak of delocalized sp^2-hybridized adventitious carbon. Raman spectra were collected in a Thermal Dispersive Spectrometer using a 10 mW laser with an excitation wavelength of 532 nm. Contact angle of water was measured with a Data-Physics OCA 20 goniometer. Electrical characterization was performed using an electrochemistry workstation (CHI 660) or in a cryostation equipped with a magnetic field (PPMS, Quantum Design). Compression tests were conducted using rectangular monolith samples with a height-to-width ratio of 0.8. Such tests used a single-column mechanical testing system (Instron-5566) operated at a constant loading speed of 2 mm min^{-1}.

2.2.2.2 Electrochemical measurement

The 3D graphene monolith was sliced into disks, which could be directly used as free-standing, binder-free, additive-free and current-collector-free electrodes. Stacking two or more sheets together (i.e., using twice or more thickness) gave a composite of twice or more areal loading. Regardless of initial thickness and final volumetric/areal loading, the final electrodes fit into the coin cells all had the same thickness, and used the same dimensions for the electrolyte, separator and counter electrodes (Li for half-cell). This was the working electrode (anode), used against lithium foils (China Energy Lithium Co., Ltd) as the counter electrode in the half-cell configuration, in conjunction with a polymer membrane (Celgard) separator and $LiPF_6$ electrolyte in a 50:50 w/w mixture of dimethyl carbonate (DMC) and ethylene carbonate (EC). This configuration was assembled in a 2016 coin cell in argon in a glovebox with less than 1 ppm oxygen and moisture. Galvanostatic charge and discharge measurements were conducted using a LAND-CT 2001C testing system within a voltage window of 0.01 V to 3.0 V. The rate capability was investigated by changing the current density from 0.2 A g^{-1} to 5 A g^{-1}. Cyclic voltammetry (CV) was conducted by an automated electrochemical workstation (CHI660E) at a scan rate of 0.2 mV/s in the voltage window of 0.01 V to 3 V.

2.3 Results

2.3.1 Materials Characterization

2.3.1.1 Mesoporous 3D graphene

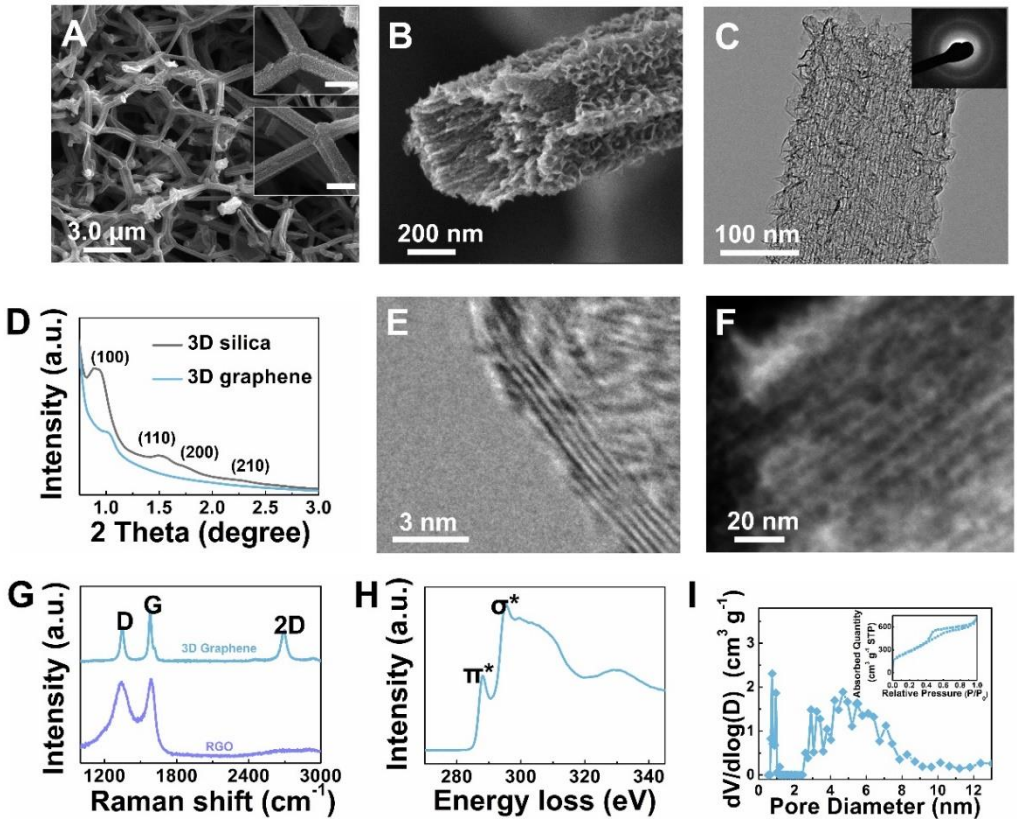

Figure 2.2 Material characterization of 3D graphene. **(A-B)** 3D graphene in scanning electron microscopy (SEM) images showing tetragonal coordination in the inset in (**A**) with a scale bar of 500 nm, **(C)** TEM of 3D graphene tube with selected area electron diffraction pattern of graphene in the inset, **(D)** low angle x-ray diffraction patterns for silica template and 3D graphene. Both are consistent with hexagonal packing of rods, 3D graphene having less order and shorter packing spacing. **(E)** High-resolution TEM, **(F)** high angle annular dark-field TEM, **(G)** Raman spectra of 3D graphene, **(H)** electron energy loss spectra of 3D graphene, and **(I)** nitrogen adsorption/desorption pore size distribution with adsorption/desorption isotherm in the inset.

The as-synthesized product, 3D graphene, has a density of 0.021 g cm^{-3},

which is 99.07% porous relative to graphite. The 3D graphene has a hierarchical structure including a tetrahedrally coordinated network (**Fig. 2.2A**) that partitions the space into continuous pores of 3~5 μm in diameter making it transparent to gas/fluid. In each tetrahedrally coordinated 100-400 nm diameter rod there is another level of mesostructure that consists of a bundle of nanotubes hexagonally organized at 5.8 nm apart (see **Fig. 2.2B and C** and small angle diffraction pattern in **Fig. 2.2D**). The nanotubes with a diameter of 3-6 nm have the characteristic layer-like structure of graphene at high resolution (**Fig. 2.2E**). But the hollow tubes are actually porous as revealed by transmission electron microscopy (TEM, see **Fig. 2.2F**): the pores are the dark spots (1~2 nm in size) that lie along the bright strips, which correspond to the tubular walls.

The nature of few-layer graphene (≤5 layers) is similar to the one reported in the literature[10] according to high-resolution TEM (**Fig. 2.2E**) and Raman spectra (**Fig. 2.2G**). It is polycrystalline (see the selected area diffraction pattern in **Fig. 2.2C**), and its electron loss energy spectra (**Fig. 2.2H**) taken from both the tetrahedral junctions and rod surfaces show identical peaks centered at 287 eV and 295 eV, respectively due to the C1*s* to π* and σ* transitions that are consistent with the expected sp^2 bonding in the graphene-like structure. Lastly, adsorption and desorption (**Fig. 2.2I**) revealed pores of 1 nm and 3-6 nm in size, which give rise to a surface area of 1,035 $m^2\ g^{-1}$ and a pore volume of 0.973 $cm^3\ g^{-1}$ with an average pore width of 3.76 nm.

After high temperature annealing, mesoporous 3D graphene is hydrophobic according to **Fig. 3.2B** (top). However, after a further hydrothermal (100^{o}C for 12 h) treatment by nitric acid, the 3D graphene becomes hydrophilic (**Fig. 3.2B** bottom).

2.3.1.2 N-doped mesoporous 3D graphene

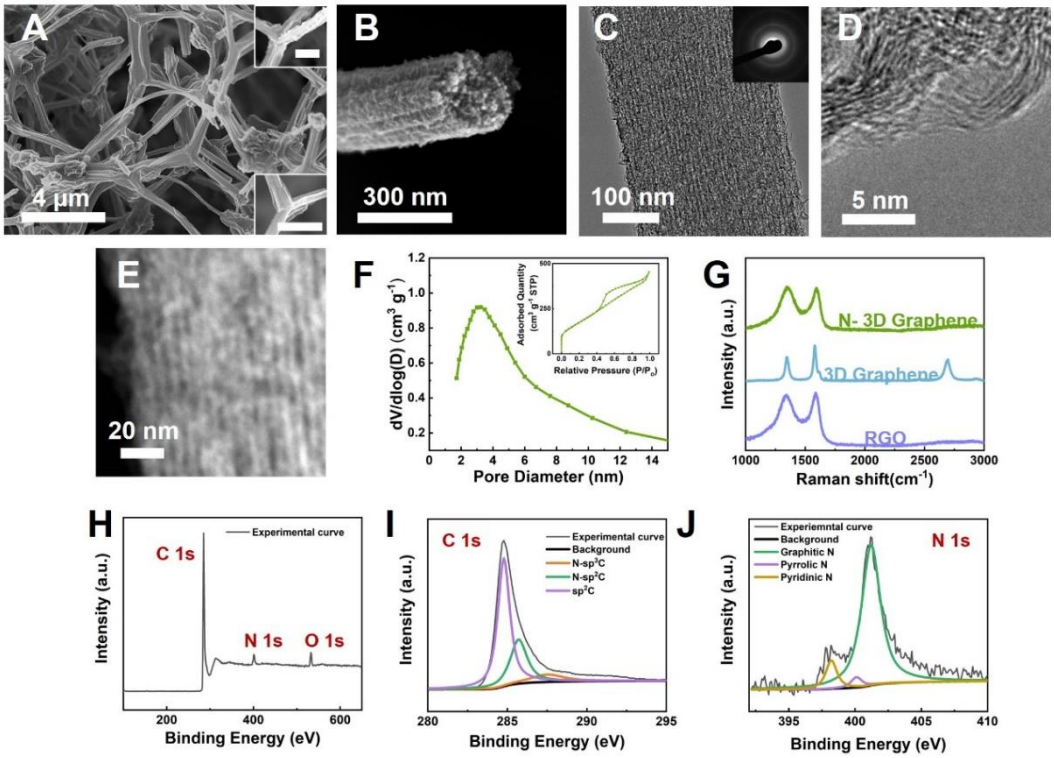

Figure 2.3 Material characterization of N-doped 3D graphene. **(A-B)** N-doped 3D graphene in scanning electron microscopy (SEM) images showing tetragonal coordination in the inset in (**A**) with a scale bar of 1μm, **(C)** TEM of N-doped 3D graphene tube with selected area electron diffraction pattern of graphene in the inset, **(D)** high-resolution TEM , **(E)** high angle annular dark-field TEM, **(F)** nitrogen adsorption/desorption pore size distribution with adsorption/desorption isotherm in the inset, **(G)** Raman spectra of N-doped 3D graphene, 3D graphene and rGO, **(H)** X-ray photoelectron spectra of N-doped 3D graphene, and **(I-J)** high resolution X-ray photoelectron spectra of C 1*s* and N 1*s*.

The synthesis method of N-doped 3D graphene described in the last section is similar to that of mesoporous 3D graphene but the carbon source now includes a

N dopant. Here acetone nitrile, DMF and DCDA were used because they have high N/C ratios (acetone nitrile= 0.5, DMF=0.33, DCDA=2), which could provide a higher amount of N dopant in the as-prepared graphene. DCDA seems most attractive as it has the highest ratio and been reported to form graphene materials with reactive nitrogen sites (N-5, N-6) [10]

The as-synthesized N-doped product has a density of 0.020 g cm^{-3}, which is 99% porous relative to graphite and is consistent with that of undoped 3D graphene. Like undoped 3D graphene, the N doped 3D graphene has a very similar hierarchical structure including a tetrahedrally coordinated network (**Fig. 2.3A**) that consists of macro-pores of 4~6 μm in diameter making it easy for gas/fluid penetration. Again similar to undoped 3D graphene, the tetrahedrally coordinated graphene tubes are 100-400 nm in diameter, and the mesostructure consists of a bundle of nanotubes hexagonally organized at ~6 nm apart, with hundreds of them in each graphene tube (see the low angle x-ray diffraction pattern **in Appendix 1 Fig. 1.1**). The nanotubes with a diameter of 3-6 nm also have the characteristic layer-like structure of graphene at high resolution (**Fig. 2.3D**). Although the hollow tubes in N-doped 3D graphene are still porous as revealed by transmission electron microscopy (TEM, see **Fig. 2.3E**), the small pores indicated by the dark spots lying along the bright strips corresponding to the tubular walls in **Fig. 2.3E** seem to be slightly larger (3~4 nm in size) than those of undoped 3D graphene in **Fig. 2.2F.** This is also evident in pore size distribution (BET, **Fig. 2.3F**): there are no pore smaller than 2 nm in N-doped 3D graphene, while undoped 3D graphene has some pores around 1 nm (BET, **Fig. 2.2I**). Adsorption and desorption isotherms of N-doped 3D graphene revealed pores 4-6 nm in size, which gives rise to a surface area of 637 m^2 g^{-1} and a pore volume of 0.681 cm^3 g^{-1} with an average pore width

of 4.2 nm.

The nature of few-layer graphene (≤5 layers) still holds in N-doped 3D graphene according to high-resolution TEM (**Fig. 2.3 D**) and G band in Raman spectra (**Fig. 2.3G**), which coincide with the ones reported in the literature[10] and found in undoped 3D graphene (**Fig. 2.2E**). Note however that the 2D band peak in N-doped 3D graphene is not as sharp as that in undoped 3D graphene (**Fig. 2.3G**), which indicates that the layer number in N-doped graphene is larger than that in the undoped counterpart. Also, the ratio of D band/ G band in N-doped 3D graphene is larger than that of undoped 3D graphene indicating a higher portion of amorphous regions in N-doped 3D graphene. The polycrystalline feature of N-doped graphene is revealed by the selected area diffraction pattern in **Fig. 2.3C**.

The X-ray photoelectron spectra (XPS) of C1*s* (**Fig. 2.3I**) taken from both the tetrahedral junctions and rod surfaces show identical peaks centered at 284.8 eV that are consistent with the expected sp^2 bonding in the graphene-like structure. Additionally, the peaks of C1*s* at 285.7 eV (N- sp^2 C) and 287.5 eV (N- sp^3 C) relate to the sp^2 and sp^3 carbon that bonds with neighboring nitrogen. From the integrated area of C 1*s*, the sp^2 C atomic percentage is 90.2% over all carbon species, which is consistent with the literature of high-quality C in N-doped graphene.[11] From the XPS survey curve of N-doped 3D graphene (**Fig 2.3H**), there are also C, N and O signals at 284.8 eV, 401.6 eV and 531.9 eV, respectively, where oxygen could be from absorbed air residues on the graphene surface. High resolution N 1*s* spectra (**Fig 2.3J**) also revealed that graphitic N, pyridinic N, and pyrrolic N, corresponding to the peaks at N 401.2 eV, 400.1 eV, and 398.2 eV, respectively, co-exist in N-doped 3D graphene. The N atomic percentage over all species is 4.92 at%, and among N atoms, the percentages of graphitic N, pyrrolic N

and pyridinic N are 85.9%, 3.8%, and 10.2%, respectively. The above overall N atomic percentage is consistent with the value reported in the literature.[12]

2.3.1.3 N-B codoped mesoporous 3D graphene

The synthesis method of N-B doped 3D graphene described in the last section is similar to that of mesoporous 3D graphene but the carbon source now includes B and N dopants. Here pyridine-borane complex was used as the C, B and N source for the graphene growth. The as-synthesized N-B codoped product has a density of 0.015 g cm^{-3}, which is 99% porous relative to graphite, and is consistent with that of undoped and N-doped 3D graphene. Similarly, the N-B co-doped 3D graphene has a hierarchical structure including a tetrahedrally coordinated network (**Fig. 2.4A**) that consists of macro-pores of 4~6 μm in diameter making it easy for gas/fluid penetration. Again similar to N- doped and undoped 3D graphene, the tetrahedrally coordinated graphene tubes are 100-400 nm in diameter.

In addition to mesopores within the graphene tubes, pores with diameters of 10~30 nm reside on the surface of N-B codoped graphene tubes (see **Fig. 2.4B and C**). **Fig. 2.4E** further reveals the porous structure of N-B codoped graphene. The small pores indicated by the dark spots seem to be slightly larger (4~6 nm in size) than those of N doped and undoped 3D graphene in **Fig. 2.2F and 2.3F**; e.g., large pores with a diameter of 20~30 nm in **Fig. 2.4E** cannot be found on N doped and undoped 3D graphene. Also in support of the above is the pore size distribution (BET, **Fig. 2.4F**): while there is no pore smaller than 2 nm in N-B codoped 3D graphene, undoped 3D graphene has some pores around 1 nm (BET, **Fig. 2.2I**). Adsorption and desorption isotherms of N-doped 3D graphene revealed pores 4-6 nm in size, which gives rise to a surface area of 610 m^2 g^{-1} and a pore volume of 0.678 cm^3 g^{-1} with an average pore width of 4.4 nm, which is slightly larger than

those 4.2 nm pores of N-doped 3D graphene.

The nature of few-layer graphene (≤5 layers) still holds in N-B codoped 3D graphene according to high-resolution TEM (**Fig. 2.4 D**) and the G band in Raman spectra (**Fig. 2.4 G**), which coincide with features reported in the literature[13] and are found in both N doped and undoped 3D graphene (**Fig. 2.2E and Fig. 2.3D**). Like N-doped 3D graphene, the 2D band peak in N-B-codoped 3D graphene is not as sharp as that in undoped 3D graphene (**Fig. 2.4G**), which indicates that the layer number in N-B codoped graphene is larger than that in undoped counterpart. Also, the ratio of D band/ G band in N-B codoped 3D graphene is larger than that of undoped 3D graphene indicating a higher portion of amorphous regions in N-B codoped 3D graphene, which is a feature shared with N-doped 3D graphene. The polycrystalline nature of N-B codoped graphene is revealed in the selected area diffraction pattern in **Fig. 2.4C**.

The X-ray photoelectron spectra (XPS) of C1*s* (**Fig. 2.4I**) taken from both the tetrahedral junctions and rod surfaces show identical peaks centered at 284.8 eV that are consistent with the expected sp^2 bonding in the graphene-like structure. Additionally, the peaks of C1*s* at 285.8 eV (N- sp^2 C) and 287.7 eV (N- sp^3 C) relate to the sp^2 and sp^3 carbon that bonds with neighboring nitrogen. The peak of C1*s* at 291.4 indicates the carbon bonds (C-O-B) with B and O atoms. From the integrated area of C 1*s*, the sp^2 C atomic percentage is 84.4% over all carbon specie, which is smaller than that of N-doped graphene (90.2%), indicating a bonding environment variation apparently caused by B doping. In the XPS survey curve of N-B codoped 3D graphene (**Fig 2.4H**), there are also B, N, and O signals at 192 eV, 401 eV and 532 eV, respectively, where O could be from absorbed air residues on the graphene surface. High resolution N 1*s* spectra (**Fig 2.4J**) also

revealed that graphitic N, pyridinic N, and pyrrolic N, corresponding to the peaks at N 401.5 eV, 400.0 eV, and 398.1 eV, respectively, co-exist in N-doped 3D graphene. In addition, the peak at 398.9 eV indicates N bonding (C-N-B) with C and B atoms. The N atomic percentage over all species is 1.64 at%, and among N atoms, the percentages of graphitic N, pyrrolic N, pyridinic N and C-N-B are 59.3%, 17.0%, 14.0% and 9.7%, respectively. The above overall N atomic percentage is consistent with the value reported in the literature of N-B co-doped graphene.[14] The B 1*s* XPS spectra (**Fig. 2.4K**) shows three characteristic peaks at 189.0 eV, 190.9 eV and 192.9 eV, corresponding to boron bonding among carbon atoms (BC3), boron bonding with N atoms (B-N) and boron bonding with carbon and oxygen atoms (BC2O and BCO2), respectively, which is in agreement with the literature. [13,14] In addition, the B atomic percentage over all species is 0.41 at%.

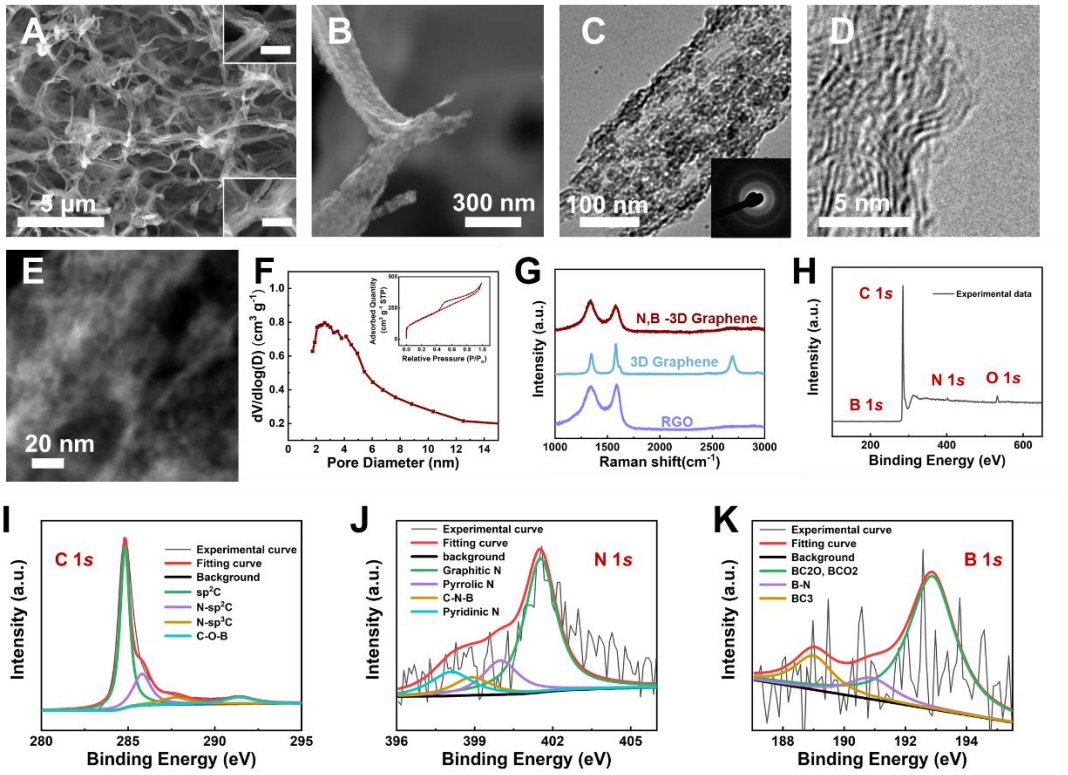

Figure 2.4 Material characterization of N-B codoped 3D graphene. **(A-B)** N-B codoped

3D graphene in scanning electron microscopy (SEM) images showing tetragonal coordination in the inset in (**A**) with a scale bar of 0.5 μm, **(C)** TEM of N-B codoped 3D graphene tube with selected area electron diffraction pattern of graphene in the inset, **(D)** high-resolution TEM, **(E)** high angle annular dark-field TEM, **(F)** nitrogen adsorption/desorption pore size distribution with adsorption/desorption isotherm in the inset, **(G)** Raman spectra of N-B codoped 3D graphene, 3D graphene and rGO, **(H)** X-ray photoelectron spectra survey of N-B codoped 3D graphene, and **(I-J)** high resolution X-ray phonon spectra of C 1*s*,N 1*s*, and B 1*s*.

2.3.2 Mechanical and electrical properties

Typical for a highly porous cellular material, the reversible deformation of undoped 3D graphene features an unloading Young's modules higher than the loading modules, 0.31 MPa vs. 0.17 MPa at 0-30% strain (**Fig. 2.5A**, inset). Such low modulus is fully expected given the very low solid fraction, the hollow nature of nanotubes, and the extreme ease of achieving large macroscopic shape/volume changes by bending a few-layer graphene's sp^2 structure.[15] This is important, because it implies very little local strain, hence very little structural damage, on the tube members despite the very large dimensional changes of the macroscopic composite. Indeed, after 30% to 90% deformation, the unloading curves in the inset of **Fig. 2.5A** faithfully retrace the previous loading curves indicating excellent elasticity. The electrical conduction of 3D graphene is examined in **Fig. 2.5B**, where it shows metallic conduction. The mechanical and electrical properties of N-doped and B-N codoped 3D graphene are discussed in **Appendix 1 Fig. 1.2**, where we find that at 300K, the conductivity of undoped 3D graphene, B-N codoped 3D graphene and N doped 3D graphene are 1.01 S m^{-1}, 0.51 S m^{-1} and 0.49 S m^{-1}, respectively. It is evident that undoped 3D graphene has better conductivity

compared to those of doped 3D graphene.

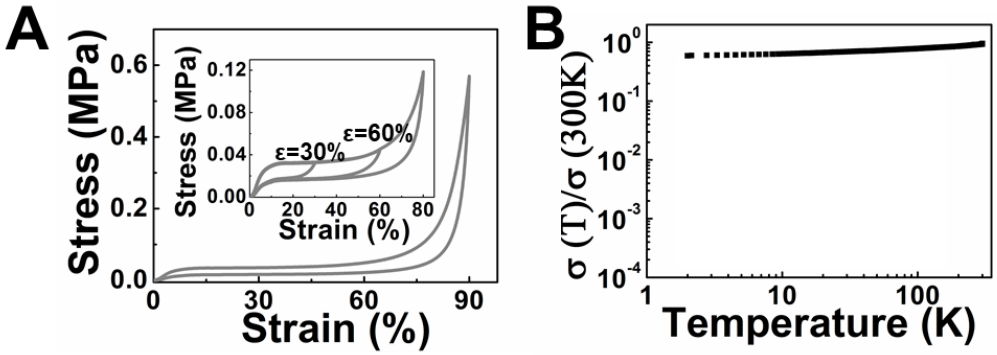

Figure 2.5 Mechanical and electrical properties of undoped 3D graphene. **(A)** Stress-strain curve of 3D graphene up to 90% strain with intermediate unloading. Inset: enlarged view of loading and unloading slopes. (**B**) Normalized conductivity of 3D graphene as a function of temperature from 2K to 300K.

2.3.3 Electrochemical performance

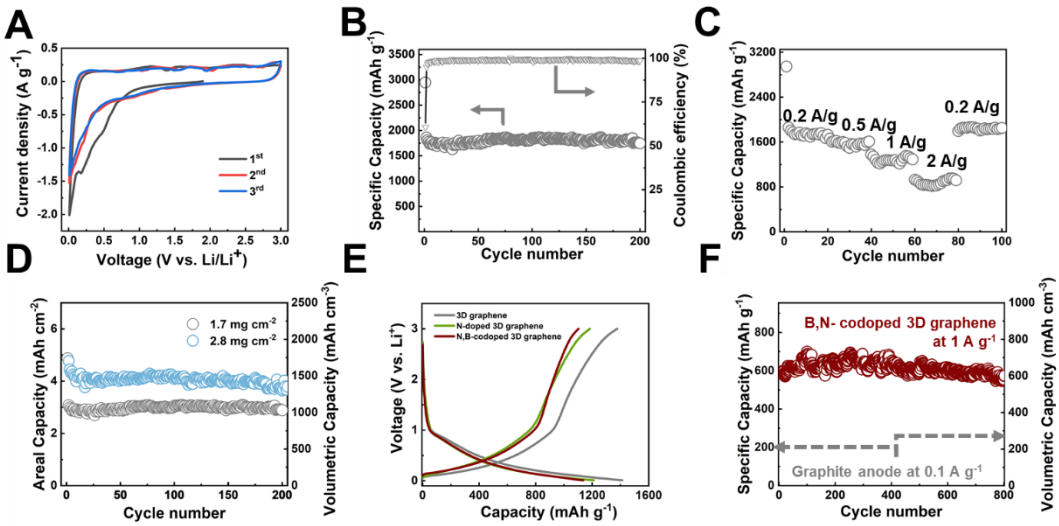

Figure 2.6 Electrochemical performance of undoped, N doped and N-B codoped 3D graphene. **(A)** Cyclic voltammetry (first 3 cycles) of undoped 3D graphene at 1.7 mg cm^{-2}. **(B)** Specific capacity and coulombic efficiency vs. cycle number of undoped 3D graphene at 1.7 mg cm^{-2} under 0.2 A g^{-1}. **(C)** Rate performance of undoped 3D graphene at 1.7 mg cm^{-2} under 0.2, 0.5, 1 and 2 A g^{-1}. **(D)** Areal and volumetric capacity vs. cycle number of

undoped 3D graphene at 1.7 mg cm^{-2} and 2.8 mg cm^{-2}, at 0.2 A g^{-1} **(E)** charge-discharge curve at 10^{th} cycle of 3D graphene, N-doped 3D graphene and N-B codoped 3D graphene at 2.8 mg cm^{-2} under 0.2 A g^{-1}. **(F)** Specific capacity vs. cycle number of B-N codoped 3D graphene at 3 mg cm^{-2} under 1 A g^{-1} after 800 cycles.

We first examine the electrochemical properties of 3D graphene by cyclic voltammetry (CV curves in **Fig. 2.6A**). The first reductive curve of 3D graphene at 1.7 mg cm^{-2} shows a peak at 0.7 V, indicating the formation of solid-electrolyte interphase (SEI), while in the subsequent cycles, this peak disappears, giving a specific capacity of 1850 mAh g^{-1}. This is in agreement with the fact that the initial coulombic efficiency (ICE) is relatively low at 60.1% (**Fig. 2.6B**) due to the large surface area that allows abundant SEI formation during initial cycling. The cyclability of 3D graphene at 1.7 mg cm^{-2} is evaluated under 0.2 A g^{-1} in **Fig. 2.6B**. Indeed, the ICE recovers to 95% starting from the 2^{nd} cycle, and the gravimetric capacity remains at 1746 mAh g^{-1} after 200 cycles. The rate capability is an important consideration for high-performance anode, The rate performance of 3D graphene at 1.7 mg cm^{-2} is evaluated in **Fig. 2.6C**, where it shows a gravimetric capacity of 1747 mAh g^{-1}, 1547 mAh g^{-1}, 1278 mAh g^{-1} and 924 mAh g^{-1} under the current density of 0.2 A g^{-1}, 0.5 A g^{-1}, 1 A g^{-1} and 2 A g^{-1}, respectively. In addition to the rate performance, the high gravimetric capacity of 3D graphene can be extended to high areal and volumetric capacity in high-loading 3D graphene electrode. In **Fig. 2.6 D**, at the loading of 1.7 mg cm^{-2}, 3D graphene electrode after 200 cycles delivers an areal capacity of 2.9 mAh cm^{-2} and volumetric capacity of 1020 mAh cm^{-3}, while at the higher loading of 2.8 mg cm^{-2} it gives an areal capacity of 3.7 mAh cm^{-2} and volumetric capacity of 1303 mAh cm^{-3}. Such volumetric capacity is 4.5 times that of commercial graphite at 286 mAh cm^{-3}. This

is despite the fact that the gravimetric capacity drops substantially at higher loadings (see 3D graphene in **Fig. 2.6E**) and especially at higher rates (**Appendix 1 Fig. 1.3C**). For example, at 3 mg cm^{-2} and 1 A g^{-1}, only 210 mAh g^{-1} is obtained compared to the 5-6 times higher values at lower loadings (1.7 mg cm^{-2}) and rates (1 A g^{-1}).

We also examined the electrochemical performance of N doped and N-B codoped 3D graphene. In the charge and discharge curves (CC curves, **Fig. 2.6E**) at the loading of 2.8 mg cm^{-2}, the undoped, N-doped and N-B codoped 3D graphene show gravimetric capacities of 1412 mAh g^{-1}, 1211 mAh g^{-1} and 1184 mAh g^{-1} at the 10^{th} cycle and under the current density of 0.2 A g^{-1}. So N doped and N-B codoped 3D graphene have lower capacities, by 14.2% and 16.1%, respectively, than that of 3D graphene. Although the gravimetric capacity of N-B codoped 3D graphene is relatively low at the above low rate, it is actually better maintained at the higher rates compared to that of undoped 3D graphene. This is evidenced in **Fig. 2.6F** in which B-N codoped 3D graphene at 3 mg cm^{-2} still gives a gravimetric capacity of 602 mAh g^{-1} and volumetric capacity of 630 mAh cm^{-3} after 800 cycles under 1 A g^{-1}, compared to undoped 3D graphene at the same loading of 3 mg cm^{-2} and the same rate of 1 A g^{-1} (**Appendix 1 Fig. 1.3C**) that can only deliver 210 mAh g^{-1}. Note too that in relation to commercial graphite under a lower current density of 0.1 A g^{-1} after fewer (500) cycles, the above gravimetric capacity and volumetric capacity of B-N codoped 3D graphene are about 2.8 and 2.5 times higher, respectively. The better rate capability of B-N codoped 3D graphene of relatively high loadings is further confirmed in **Appendix 1 Fig. 1.4**, which shows very similar gravimetric capacity at all rates for both 3 mg cm^{-2} and 5 mg cm^{-2}. For example, comparing **Appendix 1 Fig. 1.4A vs. B**, under 1 A g^{-1}, B-N

doped 3D graphene delivers 464 mAh g^{-1} at 5 mg cm^{-2} and 476 mAh g^{-1} at 3 mg cm^{-2}. At an even higher rate of 2 A g^{-1}, it still delivers 234 mAh g^{-1} at 5 mg cm^{-2}, which is higher than undoped material's 210 mAh g^{-1} at a lower loading of 3 mg cm^{-2} under a lower rate of 1 A g^{-1}.

Table 2.1 Comparison of electrochemical performance metrics of our 3D graphene, various carbon anode materials in the literature and commercial graphite anode.

	N-doped nano-graphene	B-N co-doped porous carbon	Hierarchical porous carbon	N-doped carbon @ GF	N-doped porous carbon/3Dgraphene-e sheet	High quality meso graphene-ne	Commercial graphite	3D graphene*	B-N codoped 3D graphene*	
Areal capacity (mA h cm^{-2})	0.9	1.8	0.7	0.9	0.8	1.0	3.1	3.1	4.5	2.1
Volumetric capacity (mA	376	162	265	3600	320	608	286	1109	1585	741

h cm^{-3})										
ICE(%)	N/A	77%	57%	60%	49%	77%	85%	61%	42%	45%
Gravimetric capacity (mA h g^{-1})	470.0	900.0	510.0	1000.0	800.0	950.0	244.8	1,850.0	724.9	700.0
Gravimetric Rate（A g^{-1}）	0.2	0.2	0.1	0.5	0.1	0.4	0.1	0.2	0.2	1.0
Areal rate (mA cm^{-2})	0.4	0.4	0.1	0.5	0.1	0.4	1.6	0.3	1.2	3.0
Volumetric rate	160.0	36.0	36.4	180.0	40.0	238.1	159.8	119.9	437.4	1058.2

(mA cm^{-3})										
Areal loading (mg cm^{-2})	2.0	2.0	1.3	0.9	1.0	1.0	12.5	1.7	6.2	3.0
Volumetric loading (g cm^{-3})	0.8	0.2	0.5	0.4	0.4	0.6	1.3	0.6	2.2	1.1
References	5	7	16	17	18	19	20	This work		

2.4 Discussion

Our results show that the 3D graphene with or without dopants have superior areal and volumetric capacities, and enjoy good rate capabilities at high loadings. In this section, we will further compare and rationalize them with prior work.

2.4.1 Comparison with literature and commercial graphite

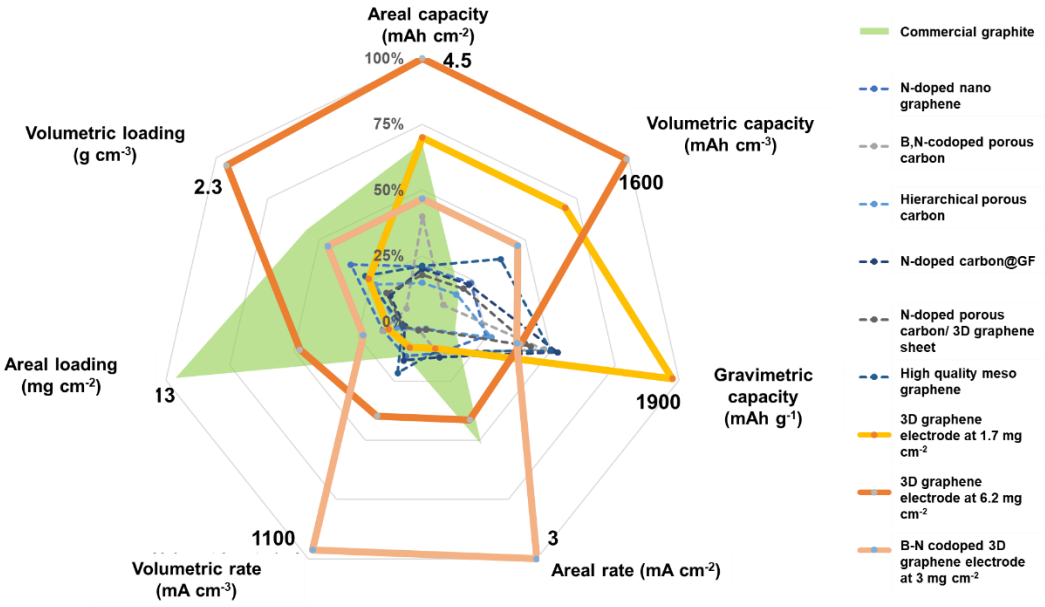

Figure 2.7 Comparison of properties with those of literature at 100th cycle (except for our 6.2 mg cm^{-2} 3D graphene electrode, which is at 80th cycle.) Thickness of 25 μm assumed if the thickness of the electrode was not given in the literature.

3D graphene has an initial coulombic efficiency (ICE) of 61 % at an areal loading of 1.7 mg cm^{-2}. This ICE is higher than or comparable to those (49%, 57%, and 60 %) of typical graphene carbon anodes: "N-doped porous carbon/3Dgraphene sheet" [18], "hierarchical porous carbon"[16] and "N-doped carbon@GF"[17]. However, at higher loadigs, undoped 3D graphene at 6.2 mg cm^{-2}

and B-N co-doped 3D graphene at 3 mg cm^{-2} only deliver the ICE at 42% and 45%, respectively, which is low compared to the average values in the literature [16-18]. The relatively low ICE in these electrodes may result from the abundant nano-scale pores (<4 nm) on the graphene tubes and the defects in the doped graphene, which is evident in BET, micro-structure and Raman spectra. We mitigated this issue by a pre-lithiation treatment (see detail in **Appendix 1 Fig. 1.3A**), which increased the ICE of 3D graphene at 1.7 mg cm^{-2}, 2.2 mg cm^{-2} and 3.2 mg cm^{-2} to 98.9%, 98.4% and 99.0 %, respectively. Therefore, the treatment can effectively reduce further lithium loss in practical applications.

At a comparable rate of 0.2 A g^{-1}, high-loading 3D graphene can achieve a gravimetric capacity, e.g., 1850 mAh g^{-1} at 1.7 mg cm^{-2} and 0.6 g cm^{-3}, superior to that of the literature electrodes, e.g., 900 mAh g^{-1} at a much lower loading 0.2 g cm^{-3}.[7] For our material, stacking multiple sheets of 3D graphene electrodes can further increase the areal and volumetric loading, to 6.2 mg cm^{-2} and 2.2 g cm^{-3}, respectively, whereas in the literature the relatively high areal loading of 2 mg cm^{-2} is accompanied by the ultra-low volumetric loading of 0.2 g cm^{-3}, indicating the existence of a large amount of large pores in it.[7] It is also remarkable that the 3D graphene electrode above with a volumetric loading of 2.2 g cm^{-3} has a higher mass loading than commercial graphite anode, at 1.3 g cm^{-3}, which must contain more porosity (about 43% relative to the theoretical density of graphite, 2.3 g cm^{-3}) to be functional.

Consequently, the areal and volumetric capacities of 3D graphene (both **Fig. 2.6D** and **Appendix 1 Fig. 1.3B**) can easily exceed those of "N-doped nano-Graphene"[5], "B,N co-doped porous carbon"[7], "hierarchical porous carbon"[16], "N-doped carbon@GF"[17], "N-doped porous carbon/3Dgraphene sheet"[18], "high

quality mesographene"[19], as shown in **Table 2.1**. They also outperform commercial graphite: the areal capacity of 3D graphene is 1.5 times that of commercial graphite, while the volumetric capacity is about 5.5 times that of commercial graphite. The rate performance is another important metric for practical applications. On a mass basis, the current density of our 3D graphene with or without dopants is comparable to that in the literature (0.2~1 A g^{-1} vs. 0.1~0.5 A g^{-1}), however, the areal and volumetric current densities of B-N codoped 3D graphene are both up to 30 times higher than those of carbon/graphene anodes in the literature, and 1.9 times and 6.6 times those of commercial graphite.

In **Fig. 2.7**, we summarize the performance of graphene/carbon anodes in the literature, commercial graphite and our 3D graphene with or without dopants at 100^{th} cycle except for the 6.2 mg cm^{-2} 3D graphene electrode taken at 80^{th} cycle. It is evident that literature materials only excel in ICE, but our 3D graphenes outperform them in capacities, loading and rate on all gravimetric, areal and volumetric bases. While commercial graphite enjoys excellent areal loading and ICE, its capacities in gravimetric and volumetric terms are relatively low. So our 3D graphene easily exceeds commercial graphite in capacities and rates, while having comparable high areal loading up to 6.2 mg cm^{-2} and ICE of 99% after pre-lithiation treatment.

2.4.2 Significance and rationale

The most important reason for the outperformance of our 3D graphene is clearly the utilization of its superelasticity and high electrical conductivity. This allows functional invariance despite the compression of graphene monolith, because after the compression the local length scales critical for electron and ion/electrolyte transport and reactions remain unchanged, and a narrower though

still open channel uniformly permeating the entire network still exists. Having the same length scales and not much suffering from discontinuity/interference despite the collapsed shapes, it is then possible to achieve high areal and volumetric capacities, by taking advantage of the high electron and ion transport still available at high loadings. This is unlike the advanced carbon material electrodes in the literature; although they use high quality of graphene, similar doping strategies and hierarchical structures, they all contain a substantial amount of large pores and void space that are poorly utilized in bettering performance. As a result, in order to remain functionality, they are forced to use low areal and volumetric loading, generally less than 1 mg cm^{-2} and 1 g cm^{-3}, respectively.

Disappointingly, the dopants of nitrogen or boron in our 3D graphene did not improve gravimetric capacities (**Fig. 2.6E**). This is evident from their lower capacities, compared to those of undoped graphene, by 14.2% and 16.1%, respectively, for N doped and N-B codoped 3D graphene at the loading of 2.8 mg cm^{-2} under the current density of 0.2 A g^{-1}. This lower performance is probably because both N and N-B codoped 3D graphene have less surface areas (637 and 610 m^2 g^{-1}, respectively) than that of undoped 3D graphene (1035 m^2 g^{-1}). It may also be due to the low preparation temperature of doped 3D graphene, which did result in inferior conductivity (see caption of **Appendix 1 Fig. 1.2**) that affects reactivity. However, B-N doped 3D graphene has a capacity of 600 mAh g^{-1} under a relatively high rate of 1 A g^{-1} and a relatively high loading of 3 mg cm^{-2} after 800 cycles, whereas undoped 3D graphene at the same loading and rate has only 210 mAh g^{-1} after 10 cycles. (see **Appendix 1 Fig 1.3C**). Moreover, when tested under the same rate of 1 A g^{-1}, B-N doped 3D graphene delivers 464 mAh g^{-1} at 5 mg cm^{-2} very comparable to 476 mAh g^{-1} at 3 mg cm^{-2} (see **Appendix 1 Fig 1.4**), but the

gravimetric capacity of the undoped 3D graphene drops from 1278 mAh g^{-1} at 1.7 mg cm^{-2} to 210 mAh g^{-1} at 3 mg cm^{-2}. These results may suggest that at higher rates and higher loadings, larger nanopores are needed for ion transport, which are available in the graphene tubes of B-N codoped graphene (with a pore size of 10~30 nm according to **Fig. 2.4C** and **E**) but not in undoped graphene (with a pore size of <5 nm according to **Fig. 2.2 C** and **F**.) Very likely, this is also an important consideration for long cycle life. Therefore, although from this work it is not clear whether B and N doping can contribute to more capacity by offering additional functional sites, B-N codoping does have the unexpected advantage of forming nano pores of a larger size, which is likely to help electrolyte/Li transport and facilitate reactions, especially at high loadings and high rates.

As the dominant material used in anodes of lithium ion batteries, graphite enjoys good cycle life and high areal loading. But intrinsically low gravimetric capacity and low volumetric loading hinder the further capacity enhancement of the battery. This study of undoped and doped 3D graphene shows the possibility of achieving extraordinarily high loadings, capacities and rate capability on both areal and volumetric bases and with long cycle life by utilizing their superelasticity and high conductivity. This also suggests that they can act as the ultimate electrochemical platform to fabricate composites to embody other active materials with outstanding potentials of extraordinary performance, as we will explore in the subsequent chapters.

2.5 Conclusions

- 3D graphene achieves the areal loading of 6.2 mg cm^{-2}, which is about 7 times that of carbon materials in the literature. The volumetric capacity of 3D

graphene remains at 2.2 g cm^{-3}, which is 11 times that in the literature and 1.7 times that of commercial graphite.

- 3D graphene delivers high gravimetric, areal and volumetric capacities of 1850 mAh g^{-1}, 4.5 mAh cm^{-2} and 1584 mAh cm^{-3}, which are up to 4, 6.4 and 9.8 times those of carbon materials in the literature, and about 7.6, 1.5 and 5.5 times those of the commercial graphite.
- High areal and volumetric capacity can also be achieved in B-N codoped 3D graphene, which enjoys high areal and volumetric rates, up to 30 times those of carbon anodes in the literature, and 1.9 times and 6.6 times those of commercial graphite.
- Compared to undoped 3D graphene, B-N co-doped 3D graphene is much superior in maintaining a high gravimetric capacity at high loadings and in obtaining a better rate performance.

References

1 Chen, M. *et al.* Suppressing the Polysulfide Shuttle Effect by Heteroatom-Doping for High-Performance Lithium–Sulfur Batteries. **6**, 7545-7557 (2018).

2 Yang, C.-P. *et al.* Insight into the effect of boron doping on sulfur/carbon cathode in lithium–sulfur batteries. **6**, 8789-8795 (2014).

3 Lian, P. *et al.* Large reversible capacity of high quality graphene sheets as an anode material for lithium-ion batteries. **55**, 3909-3914 (2010).

4 Wang, G., Shen, X., Yao, J. & Park, J. J. C. Graphene nanosheets for enhanced lithium storage in lithium ion batteries. **47**, 2049-2053 (2009).

5 Wang, H. *et al.* Nitrogen-doped graphene nanosheets with excellent lithium storage properties. **21**, 5430-5434 (2011).

6 Li, X. *et al.* Superior cycle stability of nitrogen-doped graphene nanosheets as

anodes for lithium ion batteries. **13**, 822-825 (2011).

7 Zhang, L. *et al.* Boron and nitrogen co-doped porous carbon nanotubes webs as a high-performance anode material for lithium ion batteries. **41**, 14252-14260 (2016).

8 Xie, Z. *et al.* Hierarchical sandwich-like structure of ultrafine N-rich porous carbon nanospheres grown on graphene sheets as superior lithium-ion battery anodes. **8**, 10324-10333 (2016).

9 Hou, J., Cao, C., Idrees, F. & Ma, X. J. A. n. Hierarchical porous nitrogen-doped carbon nanosheets derived from silk for ultrahigh-capacity battery anodes and supercapacitors. **9**, 2556-2564 (2015).

10 Lin, T. *et al.* Nitrogen-doped mesoporous carbon of extraordinary capacitance for electrochemical energy storage. *Science* **350**, 1508-1513 (2015).

11 Wei, D. *et al.* Synthesis of N-doped graphene by chemical vapor deposition and its electrical properties. **9**, 1752-1758 (2009).

12 Dong, J. *et al.* Improved Li+ Storage through Homogeneous N-Doping within Highly Branched Tubular Graphitic Foam. **29**, 1603692 (2017).

13 Fei, H. *et al.* Boron-and nitrogen-doped graphene quantum dots/graphene hybrid nanoplatelets as efficient electrocatalysts for oxygen reduction. **8**, 10837-10843 (2014).

14 Wu, Z. S. *et al.* Three-dimensional nitrogen and boron co-doped graphene for high-performance all-solid-state supercapacitors. **24**, 5130-5135 (2012).

15 Bi, H., Chen, I. W., Lin, T. & Huang, F. A new tubular graphene form of a tetrahedrally connected cellular structure. *Advanced materials* **27**, 5943-5949 (2015).

16 Hu, Y. S. *et al.* Synthesis of hierarchically porous carbon monoliths with

highly ordered microstructure and their application in rechargeable lithium batteries with high-rate capability. **17**, 1873-1878 (2007).

17 Huang, Y. *et al.* Ultrathin Nitrogen-Doped Carbon Layer Uniformly Supported on Graphene Frameworks as Ultrahigh-Capacity Anode for Lithium-Ion Full Battery. **14**, 1703969 (2018).

18 Su, L. *et al.* Nitrogen-doped porous carbon coated on graphene sheets as anode materials for Li-ion batteries. **25**, 1541-1549 (2019).

19 Mo, R. *et al.* High-quality mesoporous graphene particles as high-energy and fast-charging anodes for lithium-ion batteries. **10**, 1474 (2019).

20 Gallagher, K. G. *et al.* Optimizing areal capacities through understanding the limitations of lithium-ion electrodes. **163**, A138-A149 (2016).

Chapter 3 SnO_2-based 3D composites as high areal and volumetric capacity anodes for lithium ion batteries

3.1 Introduction

The ever-increasing demand for high-performance anodes in lithium ion batteries has driven researchers to new nanomaterials with the hope of higher capacities than that of commercial graphite anodes. With conversion (eq (3.1)) and alloy (eq (3.2)) reactions for lithium incorporation, SnO_2 delivers a theoretical gravimetric capacity of 1494 mAh g^{-1}, which is 5-times higher than that of commercial graphite.

$$SnO_2 + 4Li^+ + 4e^- \leftrightarrow Sn + 2Li_2O \qquad (3\text{-}1)$$

$$Sn + 4.4Li^+ + 4.4e^- \leftrightarrow Li_{4.4}Sn \qquad (3\text{-}2)$$

However, there are several fundamental drawbacks of SnO_2 anode. 1) The large volume change (376%) during lithiation results in poor structural integrity upon cycling. 2) SnO_2 and Li_2O are insulators making eq (3.1) irreversible unless they are located at the surface sites connected to an electrical source, which results in a poor cycle life and capacity decay. 3) Relocation and reconfiguration of Sn metal results in coarsening thus reducing reactivity. Nanostructured SnO_2 has been explored to overcome these problems with some success.[1-9] For example, Dong et al. anchored oxygen-deficient 5 nm SnO_2 nanoparticles to reduced graphene oxides, and the composite delivered 950 mAh g^{-1} after 100 cycles at 0.2 A g^{-1}. In this design, black SnO_{2-x} has improved conductivity and can allow ultra-fine precipitation of Sn metal around Li_2O, which contributes to the enhanced reversibility of conversion reaction. These and similar discoveries were reported on

electrodes with a very small amount of nanomaterials, e.g., at about 1 mg cm^{-2} in areal loading[3,4,6,10,11] or 0.15 g cm^{-3} in volume loading[4,8,12], which is much lower than used in commercial LIB electrodes (>10 mg cm^{-2}, or >1.6 g cm^{-3} in volumetric loading)[6,13,14]. Commercial electrodes must have high loadings because the non-electrode part, which carries no energy, weighs down the overall volumetric/areal loading in a battery assembly[5,6]. For example, when the "dead" volume and weight are included, the gravimetric capacity of a packaged battery is only ~1/3 of the gravimetric capacity of its electrode when the latter has an areal mass loading of ~10 mg cm^{-2}, and the number drops to ~1/12 when the electrode loading is ~1 mg cm^{-2}.[6] But is it possible to achieve high volumetric and areal loadings in nanomaterials?

Clearly, the issue is about scalability. Yet a typical nanofabrication process is difficult to scale up. Why? One fundamental problem lies in the length scale from which comes the kinetic advantage of nanomaterials. For example, if a higher areal loading is achieved by using a thicker electrode, then the longer diffusion distance will slow down ion transport and electron conduction, which will hamper the capacity especially at high charging/discharging rates.[15,16] Another problem is in the process kinetics and thermodynamics, which usually depend on the reaction time and reactant concentrations in a strongly non-linear way. One cannot achieve higher loadings by simply extending the processing time or increasing the reactant concentrations, for the new material from the new process is bound to be so different from the old one that it no longer delivers the same performance. Therefore, for most nanomaterials, presently, there is no way to scale them up to fabricate high-loading electrodes.[6]

Our new idea to deal with this challenge is schematically illustrated in **Fig.**

3.1, which features a flexible core-shell network with an exposed active nanomaterial (the blue part in **Fig. 3.1**) that derives its outstanding electrochemical performance from (i) the structure-supporting and electron-conducting three-dimensional (3D) backbone (i.e., the core) on which the active nanomaterial (the shell) resides, (ii) the nano size of the active-material particles on the network, and (iii) the easy access of nanoparticles to the surrounding electrolyte and to the conducting backbone. Next, as illustrated in the upper panel of **Fig. 3.1**, a transformation that uniformly squeezes out the open space can easily increase the packing density by more than 10×. Importantly, the transformation need not affect the core-shell local structure: tetrahedrally coordinated tubular graphene backbone, nanoparticles themselves, their spacing to nearest-neighbor nanoparticles, and their access to the open surrounding (to be filled by electrolyte) and to the backbone conductivity, are all left unchanged. Therefore, even though a high density/loading is obtained by such transformation, the network composite can still maintain the same physical, chemical and geometrical properties as before transformation, as illustrated in the lower panel of **Fig. 3.1**. In short, the transformation is macroscopically and mesoscopically affine and microscopically and functionally invariant.

To reduce the idea to practice, we started with a highly conductive superelastic 3D graphene backbone that can be compressed by 99% and still fully recover its original shape. Next, we conformally deposited nanoparticles of electrochemically active SnO_{2-x} onto 3D graphene. Lastly, we compressed the active-material-bearing 3D graphene network to the desired final size thus achieving the intended mass/volumetric/areal loading. In the end, what we obtained and fit into a battery cell was a monolithic free-standing network-

composite anode electrode endowed with nanomaterial's electrochemical activity, yet free of any extraneous binder or current collector and still completely robust in macroscopic dimensions.

The advantage of this new anode over the widely used graphite anode lies in the greatly improved volumetric capacity. Because of low volumetric capacity (550 mAh cm^{-3}), graphite anode must occupy as much space as $LiCoO_2$ (LCO) cathode[13] in commercial LIB, which is one reason why the volumetric capacity of the battery is limited to 570 Wh L^{-1}.[5] In contrast, at the same capacity our new SnO_{2-x} composite anode allowing redox reactions (from SnO_2 to SnO to Sn) and Sn-Li alloying occupies much less volume and, in so doing, can significantly increase the energy density of LIB.

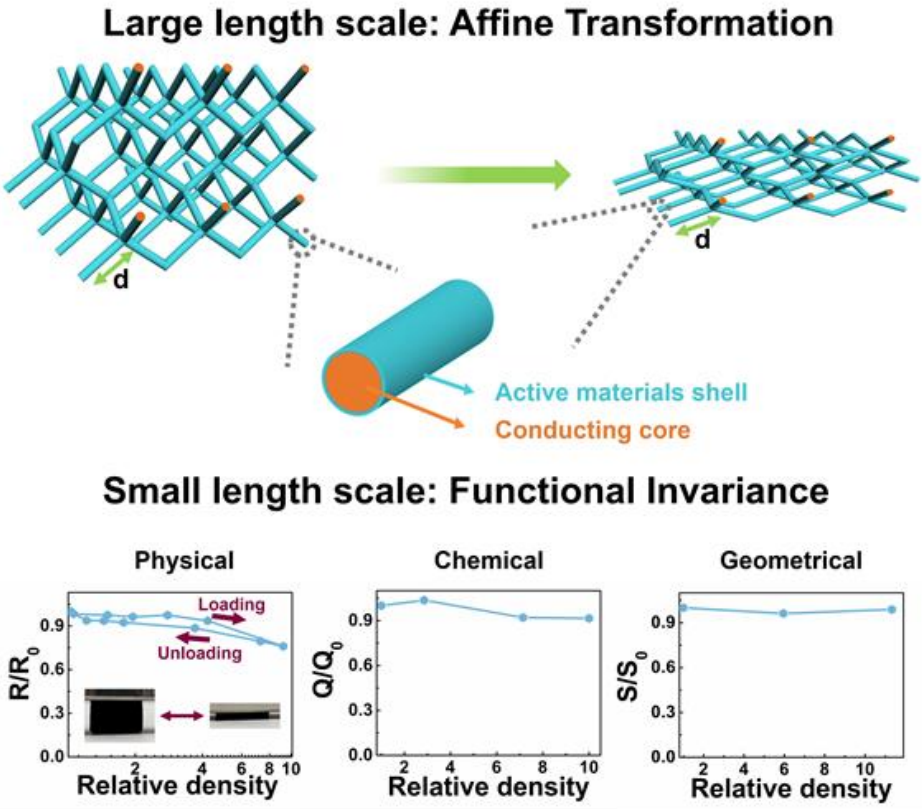

Figure 3.1 Functionally invariant affine transformation approach: a superelastic, highly conducting network backbone, such as one provided by a 3D tubular graphene, can be

used as a scaffold for depositing nanoparticles of another material, acquiring a core-shell structure (upper left). The resulting electrochemically active network can be next compressed uniformly to form a high-loading electrode (upper right). Although there is a 10× increase in the packing density, physical, chemical and geometrical properties are invariant, exemplified by a nearly constant resistance *R* (lower left), gravimetric capacity *Q* (lower middle) and surface area *S* (lower right). At relative density 1, R_0=353.1 Ω, Q_0=1330.6 mAh g^{-1}, S_0= 311.8 m^2 g^{-1}.

3.2 Experimental procedures

3.2.1 Material synthesis

3.2.1.1 Synthesis of black SnO_{2-x}/3D graphene composite

Our synthesis started with a 3D graphene monolith that is used as the conducting backbone. To render the 3D graphene monolith hydrophilic, it was first immersed in nitric acid and heated to 100 ^oC for 12 h, then dried. An aqueous solution of $SnCl_4$ (0.3 mol/L) and urea (1.2 mol/L) was next prepared in an autoclave, and the hydrophilic 3D graphene monolith was placed in the autoclave and immersed in the solution at room temperature for 2 h to be thoroughly soaked. After that, still in the autoclave, the 3D graphene together with the solution was heated to 200^oC and held for 6 h. The recovered 3D graphene remained as a monolith, and it was rinsed by ethanol and distilled water three times. The rinsed product was freeze-dried, then placed in a vacuum furnace with the pressure maintained at lower than 5 Pa. Under such condition, it was subject to reduction by adding aluminum powders to the furnace before heating the furnace to 800 ^oC followed by 450 ^oC, held at each temperature for 1 h. The recovered monolith

containing reduced SnO_{2-x} anchored on the 3D graphene backbone will be called network composite (of SnO_2) in the remainder of this chapter.

3.2.1.2 The controlled group: synthesis of SnO_{2-x}/rGO composite

For control, we used a composite of SnO_{2-x} and reduced graphene oxide. An aqueous solution of $SnCl_4$ (0.3 mol/L) and urea (1.2 mol/L) was first prepared. Graphene oxide (GO) prepared by a modified Hummer's method was then dispersed in the solution with a mass ratio of SnO_2/GO at 7/3. After vigorously stirring for 5 h, the mixture was hydrothermally heated to 200°C and held for 6 h. The obtained product was centrifugated/ultrasonicated by ethanol and distilled water three times, then freeze-dried. To improve electron conductivity, the composite was dried and reduced at 450°C for 1 h using the same process of reducing SnO_2-coated 3D graphene network composite. This non-network composite will be called SnO_{2-x}/rGO composite in the remainder of this chapter.

3.2.1.3 Pre-lithiation treatment of SnO_2-based network composite electrode

The SnO_2-based network composite electrode was pre-lithiated by directly contacting the electrode with a lithium foil while the electrolyte was added to facilitate Li transfer. Specifically, a SnO_2-based network composite electrode was placed over a lithium foil, and $LiPF_6$ electrolyte in a 50:50 w/w mixture of dimethyl carbonate (DMC) and ethylene carbonate (EC) was dropped into 3D graphene. After this, the contact between lithium foil and 3D graphene electrode was reinforced by slight compression using another piece of lithium foil placed on the top. Over the next 24 h, Li entered the composite to pre-lithiate it. After this treatment, the pre-lithiated composite electrode was ready for use without further treatment.

3.2.2 Characterization

3.2.2.1 Material characterization

Scanning electron microscopy (SEM) images were obtained in a field emission Magellan 400 microscope (FEI Company). Transmission electron microscopy (TEM), high angle annular dark field (HAADF) imaging, electron energy loss spectroscopy (EELS, Gatan), and elemental mapping were conducted in a JEOL 2100F microscope operated at 200 kV. Nitrogen adsorption-desorption isotherms at 77 K were measured in a Micromeritics Tristar 3000 system using vacuum-degassed samples (200 °C for 12 h). These isotherms were used to calculate (*a*) the specific surface area by the Brunauer-Emmett-Teller (BET) method and (*b*) the pore volume and pore size by the Barrett−Joyner−Halenda (BJH) method. Small and wide angle X-ray diffraction was performed in a Brucker D8 powder X-ray diffractometer using Cu *K*α radiation. X-ray photoelectron spectra (XPS) were collected in a Thermo Escalab 250Xi with Al *K*α radiation (hν =1,486.6 eV). Binding energies were calibrated using the 284.8 eV peak of delocalized sp^2-hybridized adventitious carbon. Raman spectra were collected in a Thermal Dispersive Spectrometer using a 10 mW laser with an excitation wavelength of 532 nm. The mass ratio of tin oxide in SnO_2-based 3D composite was determined by thermogravimetric analysis (TGA) at a heating rate of 10 ^oC min^{-1} in the temperature range of 25-900^oC in air using a thermal analysis (NETZSCH STA 449 F3). Contact angle of water was measured with a Data-Physics OCA 20 goniometer. Electrical characterization was performed using an electrochemistry workstation (CHI 660) or in a cryostation equipped with a magnetic field (PPMS, Quantum Design). Compression tests were conducted using rectangular monoliths with a height-to-width ratio of 0.8 in a single-column

mechanical testing system (Instron-5566) at a constant loading speed of 2 mm min $^{-1}$.

3.2.2.2 Electrochemical measurement

The SnO_{2-x}-coated 3D graphene monolith, which we call network composite, was sliced into disks, which could be directly used as free-standing, binder-free, additive-free and current collector-free electrodes. This was the working electrode (anode), used against lithium foils (China Energy Lithium Co., Ltd) as the counter electrode in the half-cell configuration, in conjunction with a polymer membrane (Celgard) separator and $LiPF_6$ electrolyte in a 50:50 w/w mixture of DMC and EC. This configuration was assembled in a 2016 coin cell in argon in a glovebox with less than 1 ppm oxygen and moisture. Galvanostatic charge and discharge measurements were conducted using a LAND-CT 2001C testing system within a voltage window of 0.01 V to 3.0 V. The rate capability was investigated by changing the current density from 0.2 A g^{-1} to 2 A g^{-1}. Electrochemical impedance spectroscopy (EIS) and cyclic voltammetry (CV) were conducted by an automated electrochemical workstation (CHI660E). The CV was performed at a scan rate of 0.2 mV/s in the voltage window of 0.01 V to 3 V. The EIS was conducted between 0.01 to 10^5 Hz with an excitation voltage of 0.005 V at different DC voltages.

3.3 Results

3.3.1 Materials characterization

A high-quality superelastic 3D graphene is key to our process schematically shown in **Fig. 3.2A**. Its synthesis and characterization of 3D graphene was described in Chapter 2. Therefore, we only focus on the characterization of SnO_{2-x}-based network composite. As mentioned before, before depositing SnO_2

nanoparticles onto 3D graphene, we first gave the latter an (nitric) acid treatment to render it hydrophilic (**Fig. 3.2B.**) After deposition, we further gave the composite a reduction treatment to improve conductivity (see chapter 3.2). The hydrophilic modification allows SnO_2 nanoparticles to conformally coat the 3D graphene scaffold in **Fig. 3.2C**, which shows a very uniform deposit on both straight rods and junctions. This is also evident from elemental mapping (**Fig. 3.2D**). The diffraction patterns (**Fig. 3.2E**) confirmed the presence of rutile SnO_2 (PDF#77-0450), which is supported by Raman spectroscopy (**Fig. 3.2F**) and X-ray photoelectron spectroscopy (XPS) of Sn^{4+} (**Fig. 3.2G**). At high resolution (**Fig. 3.2H**), it becomes clear that the SnO_2 nanoparticles are 3 to 6 nm in size, which is consistent with the broadening of the diffraction peaks (**Fig. 3.2E**). The high-resolution image in **Fig. 3.2H** further revealed a well-defined interplanar spacing of 0.33 nm corresponding to the (110) plane in SnO_2. Importantly, the selected area diffraction pattern (inset of **Fig. 3.2H**) containing polycrystalline rings attests to the many random orientations of SnO_2 nanoparticles in close vicinity of each other (some of them probably inside the graphene tube), which means they were randomly nucleated. Therefore, there must be a very high density of nucleation sites in the hydrophilic, large surface area, porous tubular 3D graphene—all instrumental to uniform deposition of SnO_2 nanoparticles. To complete characterization, we determined the weight fraction of SnO_2 in the composite: It is 68.8% according to thermal gravimetric analysis (TGA) (**Fig. 3.2I**).

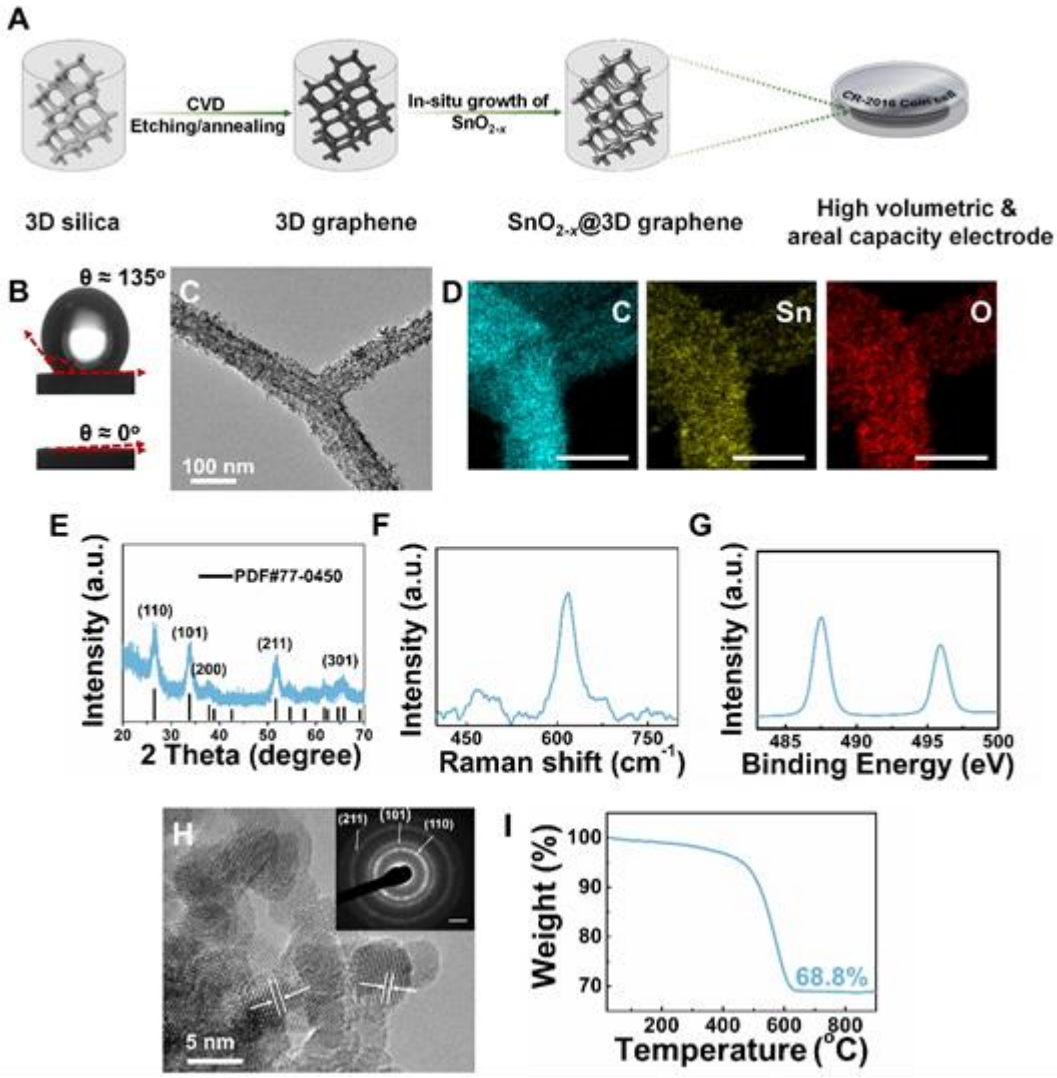

Figure 3.2. Materials characterization. (A) Fabrication schematic from silica template to graphene scaffold to SnO_2 coating to final affine transformation, generating high volumetric and areal electrode in a coin cell. (B) Contact angle of water on 3D graphene before acidification (top); after acidification with (bottom), water disappeared into 3D graphene indicative of good wetting. Characterization of SnO_2-based network composite by (C) TEM image showing (D) elemental mapping with scale bar = 100 nm, (E) X-ray diffraction pattern with rutile SnO_2 (PDF#77-0450) peaks shown as markers below, (F) Raman spectra showing SnO_2 with the characteristic 600 cm^{-1} excitation, (G) X-ray photoelectron spectra showing characteristic spectra of Sn^{4+}, (H) high-resolution TEM image with selected area electron diffraction pattern of SnO_2 in the inset, and (I) thermal gravimetric analysis from 25°C to 900°C in air.

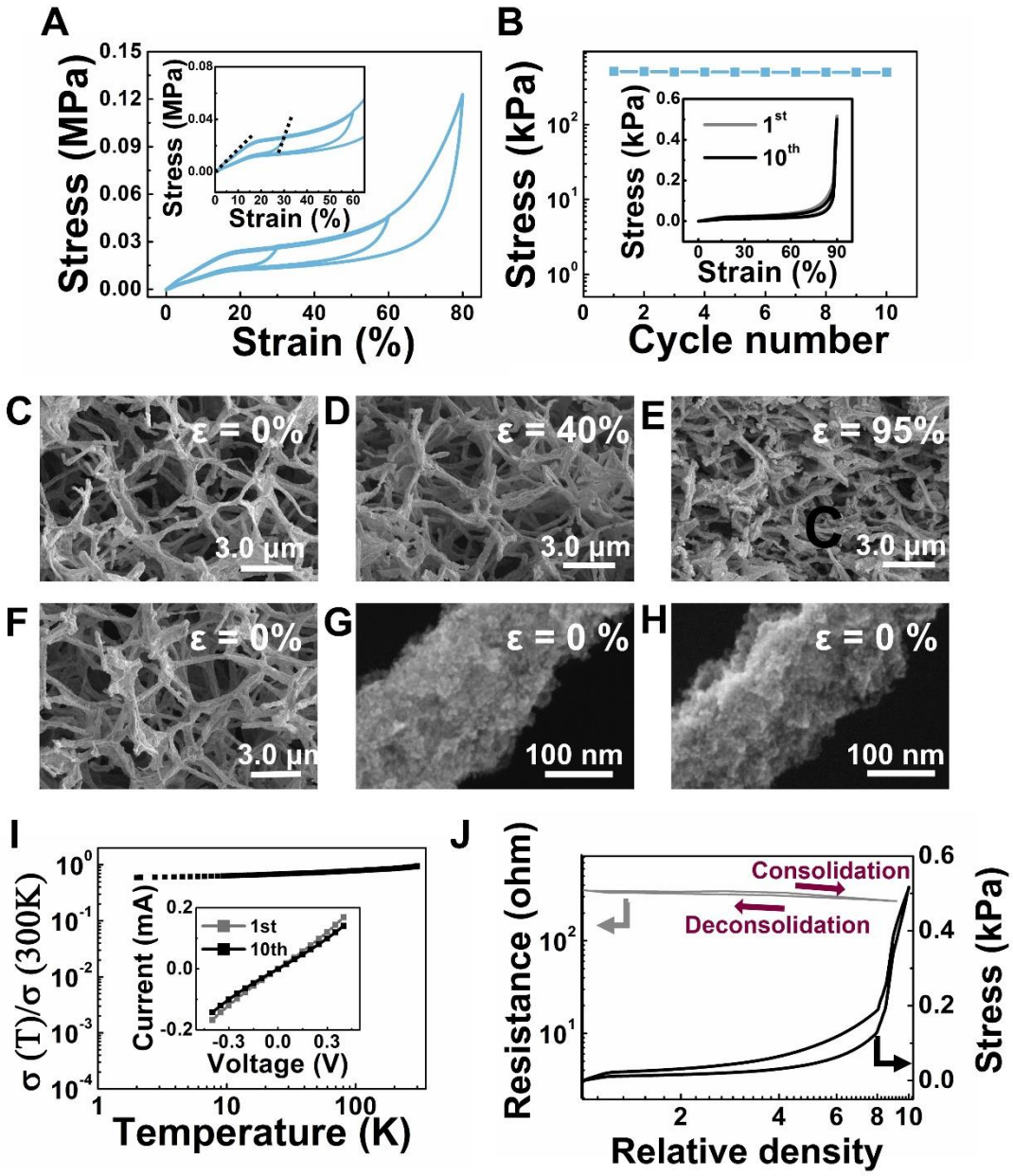

Figure 3.3 Deformation and morphology of superelastic SnO_2-based network composite. (A) Stress-strain curve up to 80% strain with intermediate unloading. Inset: Enlarged view of loading and unloading slopes. (B) Stress at 90% strain versus cycle number. Inset: Stress-strain curves of 1st and 10th cycle. (C to F) SEM at strains of 0%, 40%, 95% and back to 0%. (G) High magnification SEM at 0% strain, and after 95% compression then back to 0% strain for (H).

Despite the rather high weight fraction of SnO_{2-x}, SnO_{2-x}-coated 3D graphene is superelastic just like 3D graphene (**Fig. 3.3A**). Typical for a highly porous cellular material, the reversible deformation features a higher unloading Young's modules than the loading modules, 0.32 MPa vs. 0.14 MPa at 0-30% strain (**Fig. 3.3A**, inset). Such modest modulus is fully expected given the very low solid fraction, the hollow nature of nanotubes, and the extreme ease of bending a few-layer graphene's sp^2 structure[17] to achieve large macroscopic shape/volume changes in this composite, which when undeformed is an aerogel. This is important, because it implies very little local strain, hence very little structural damage to the core-shell member despite the very large dimensional changes of the macroscopic composite. Indeed, after 30% to 80% deformation, the unloading curves in **Fig. 3.3A** faithfully retrace the previous loading curves indicating excellent elasticity. This is further confirmed in **Fig. 3.3B**, where the network composite after repeated 90% compressions still follows overlapping stress-strain curves (see inset) and reaches the same maximum stress. More detailed insight is provided by the micrographs (**Fig. 3.3C-F**) at different compressive strains, showing no apparent damage to the network even with most pore space squeezed out by 95% compression. After the test, no debris of graphene or SnO_{2-x} nanoparticles was found, and the morphology of nanoparticles on the graphene tube after test is identical to that before test (cp. **Fig. 3.3G** and **3.3H**). Therefore, both the graphene backbone and the nanoparticles deposited on it are apparently indestructible.

The integrity of the network composite ensures an invariant nanostructure, which includes the size, the distribution and the spacing of neighboring SnO_{2-x} nanoparticles, and their adherence to as well as intimate contact with the 3D graphene backbone. It also includes the structural integrity of 3D graphene to

maintain outstanding electron conduction of the metallic type (**Fig. 3.3I**). Indeed, the SnO_{2-x}-based network composite delivers nearly identical resistance at 90% strain before and after 10 compression cycles (inset of **Fig. 3.3I**). Meanwhile, the resistance of the network composite remains relatively constant during the course of consolidation to 9× the initial density. Lastly, affirming the absence of damage, unloading to zero strain recovers the original resistance (**Fig. 3.3J**). Together with other illustrations in the lower panel of **Fig. 3.1**, these invariant nanostructure and electro-mechanical properties are indicative of invariant physics, chemistry and local geometry, which is a prerequisite for invariant electrochemical activities, which in turn is a prerequisite for the functionally invariant affine transformation approach that we will use to create high-loading, high-performance electrode materials.

3.3.2 Electrochemical characterization

To evaluate electrochemical performance, we prepared network composites of various packing densities starting with an as-fabricated monolith sliced into sheets of ~800 μm thick with a (SnO_{2-x}+graphene) total mass loading of 0.0625 g cm^{-3} each. They were next compressed to different strains (thicknesses) to reach loading as high as 3.527 g cm^{-3}. Meanwhile, stacking two or more sheets together (i.e., using twice or more thickness) gave a composite of twice or more areal loading. Regardless of initial thickness and final volumetric/areal loading, the final electrodes fit into the coin cells all had the same thickness, and used the same dimensions for the electrolyte, separator and counter electrodes (Li for half-cell). For comparison, we also tested a control electrode, which is a non-network SnO_{2-x}/rGO composite. (See section 3.2) Here we used the less conducting graphene oxide because it has better hydrophilicity thus better bonding with SnO_2 than

graphene.

Electrochemical impedance spectroscopy (EIS, **Fig. 3.4A**) comparing the two composite electrodes at the same loading of 10 mg cm^{-2} found the impedance and charge-transfer impedance of the network composite 10× lower than those of the control (see inset), which augurs well for electrochemical activity, especially at high rates. Below we focus on half cells to highlight the performance of network composite anodes. Electrochemical characterization described below indicates that despite some background electrochemical activity from 3D graphene at low potential (~0.15 V) relative to Li, the main, most identifiable activity of our anodes comes from SnO_2/SnO_{2-x}, which we used at three loadings: 1.76 g cm^{-3}, corresponding to an areal loading of 5 mg cm^{-2}, 2.47 g cm^{-3}/7 mg cm^{-2}, and 3.53 g cm^{-3}/10 mg cm^{-2}. **Fig. 3.5A** presents the first four cycles of cyclic voltammetry of a 1.76 g cm^{-3} electrode. Thermodynamically, reduction of SnO_2 ($SnO_2+2Li=SnO+Li_2O$) occurs at 1.88 V relative to Li, which is the voltage ((i) in **Fig. 3.5A**) where the reaction is initiated in the 1st cycle. This is highly unusual since in the literature the reduction typically starts at <1.5 V and sometimes even at <1.2 V.[2,3,18] The next reduction ($SnO+2Li=Sn+Li_2O$) thermodynamically occurs at 1.58 V, which we also observed at the current dip at about this voltage ((ii) in **Fig. 3.5A**). Because of the accumulation of insulating Li_2O, the completion of the above reactions is delayed to <1 V, at which point a solid-electrolyte interphase (SEI) also forms at ~0.75 V ((iii) in **Fig. 3.5A**). The SEI causes a delay of subsequent alloying reactions forming Li_xSn ($x \leq 4.4$), which otherwise should occur between 0.76 V and 0.38 V according to thermodynamics. For the charging reaction, the peak centered at 0.55 V signals the de-alloying reaction, while the broad peaks at 1.27 V and 1.85 V respectively correspond to the oxidation of Sn to

SnO and further oxidation to SnO_2. In the 2nd cycle, the start of the first reduction is very noticeably shifted to 1.45 V ((iv) in **Fig. 3.5A**). This is also the voltage commonly seen in the 2nd cycle in the literature, so, post 1st-cycle, reactions are generally controlled by the ubiquitously present SEI that covers SnO_2. The above assignments of reactions are confirmed by the galvanostatic charge/discharge curves in **Fig. 3.5B**: the peaks in Fig. **3.5A** correspond to the plateaus in **Fig. 3.5B.**

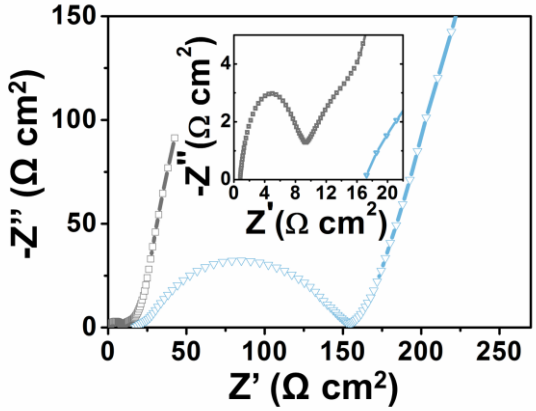

Figure 3.4 (A) Electrochemical impedance spectra of SnO_{2-x}-based network composite, (grey curve) and slurry-cast SnO_2/rGO composite (light blue curve) anodes, both at total mass loading of 10 mg cm^{-2}. Inset: Enlarged view near origin.

Post the 1st cycle, the CV and charge/discharge curves are relatively stable, and from the latter one can read a high Coulomb efficiency at all three loadings, at 70th cycle, as shown in the inset of **Fig. 3.5B** and **Fig. 3.5C**. The good cycle stability is summarized in **Fig. 3.5D** in contrast to the control electrode of slurry-cast SnO_2/rGO composite at 5 mg cm^{-2}, which suffered a relatively fast capacity decay, retaining a much smaller capacity after 100 cycles (**Fig. 3.5E**). The network composites up to a loading of 2.47 g cm^{-3}/7 mg cm^{-2} can maintain their performance at relatively high rates in **Fig. 3.5F**.

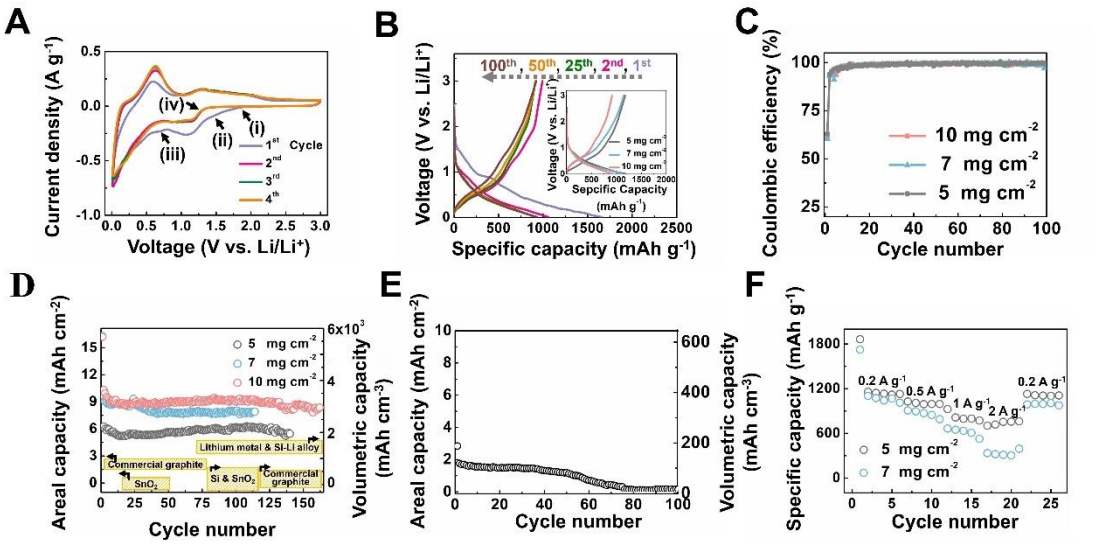

Figure 3.5 Electrochemical performance of SnO_2-based network composite anode of various loadings unless otherwise noted. (A) Cyclic voltammetry (first 4 cycles) of with 5 mg cm^{-2}. Specific reactions (i-iv) as indicated. (See text for details.) (B) Successive charge-discharge curves with 10 mg cm^{-2} at 0.2A g^{-1}. Inset: The 70th cycle charge-discharge curves of three electrodes with loadings as shown. (C) Coulombic efficiency at three loadings: 1.76 g cm^{-3}/5 mg cm^{-2}, 2.47 g cm^{-3}/7 mg cm^{-2}, and 3.53 g cm^{-3}/10 mg cm^{-2}. (D) Areal and volumetric capacity vs. cycle numbers at three loadings. Also shown in bands are anode data of commercial graphite, Si[4,7,11,19], SnO_2 [2,3,10,18,20-22], and theoretical capacity of lithium metal and Si-Li alloy. (E) Areal capacity and volumetric capacity of slurry-cast SnO_{2-x}/rGO composite electrode, at 1.76 g cm^{-3}/5 mg cm^{-2}, as a function of cycles. (F) Rate performance at two loadings.

3.3.3 Postmortem analysis

The good electrochemical performance of network composites can be further understood by the postmortem analysis. First, the finely dispersed SnO_2 nanoparticles anchored on the conducting 3D graphene network and further refined by electrochemical cycling can contribute to the good performance. As shown in **Fig. 3.6A**, SnO_2-based network composite at 10 mg cm^{-2} cycled for 50 times shows a uniform distribution of fine nanoparticles on the 3D graphene tubes. This

is consistent with the rather uniform ultrafine white spots in **Fig. 3.6B** obtained by high angle annular dark-field (HAADF) electron microscopy. Therefore, even at very high loading, there is very little agglomeration, relocation, or coarsening of nanoparticles in the network composite during compression-consolidation and electrochemical cycling, which ensures good electrochemical performance. In the inset of **Fig. 3.6A**, the electron diffraction pattern also confirms the existence of SnO_2 without metallic Sn after the sample was charged at 3.0 V, and in **Fig. 3.6C**, elemental mapping shows a uniform distribution of all the elements throughout the graphene network, which is consistent with having only SnO_2 without metallic Sn. So the network composites are capable for stable reversible reactions between SnO_2 and Sn. This is remarkable for such high loading electrodes because in the literature achieving good reversibility is already difficult even at ~ 1 mg cm^{-2}, and becomes even more difficult at higher loadings. Further analysis via XPS (**Fig. 3.6D**) and Raman spectroscopy (**Fig. 3.6E**) showing evidence of Sn^{4+} and oxide phase are all in agreement with the picture of full oxidation portrayed by **Fig. 3.6A-C**.

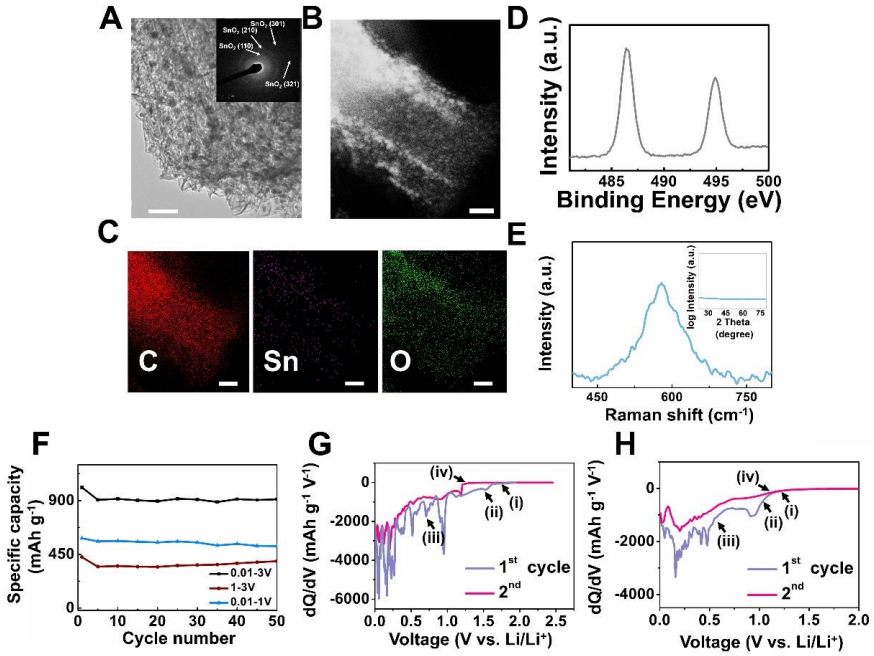

Figure 3.6 (A-E) Postmortem analysis of SnO_{2-x}-based network composite electrode (10 mg cm^{-2}) after 50 cycles at the 3 V charged state. (A) Transmission electron microscopy image (bar=50 nm). Inset: Selected area diffraction pattern showing polycrystalline SnO_2 without metallic Sn. (B) High angle annular dark-field electron microscopy with bright regions corresponding to SnO_{2-x} rich compositions (bar=50 nm). Many SnO_{2-x} nanoparticles visible along two edges because, in viewing a tube in the transverse direction, transmitting electrons see more mass at two edges. (C) Corresponding elemental mapping (bar=50 nm). (D) XPS of Sn after cycling showing only Sn^{4+}. (E) Characteristic SnO_2 Raman spectrum. Inset: Crystallites detectable by TEM (Fig. 3.2 H) were too small to detect by X-ray diffraction because of 56× longer wavelength. (F) Voltage-range-specific capacity of network composite electrode with a mass loading of 3.53 g cm^{-3}/10 mg cm^{-2} as a function of cycles. 1st and 2nd differential discharge capacity of (G) SnO_{2-x}-based network composite electrode, to be compared with (H) slurry cast SnO_{2-x}/rGO composite electrode, both at 5 mg cm^{-2}.

3.3.4 Deconvolution of capacity

One method to quantify the electrochemical reactions is to deconvolute the capacity into two parts according to the alloying and conversion reactions. The 0.01 V – 1 V range may be assigned to the Li-Sn alloying reaction (Reaction 1: $Sn + xLi^+ + xe^- = Li_xSn$, $0<x<4.4$), and the 1 V – 3 V range may be assigned to the conversion reaction (Reaction 2: $SnO_2 + 4Li + 4e^- = Sn + 2Li_2O$). For a network composite electrode with a mass loading of 10 mg cm^{-2}, we used the CC curve for the above assignment, and obtained the capacity of Reaction 1 about 518 mAh g^{-1} corresponding to 56% of the total capacity, and 393 mAh g^{-1} for the second reaction. If one disregards the graphene contribution, then the SnO_2 reactions give 52.4% for the first reaction that uses 4.4 Li per Sn, versus 4 Li per Sn in the second reaction. We found these values mostly constant throughout the 1st 50 cycles (**Fig. 3.6F**), and the above values were taken from the 50th cycle.

3.4 Discussion

3.4.1 Reactivity of SnO_{2-x} electrode

The good reactivity of SnO_{2-x} in the network composite is further illustrated by differentiating the curves in **Fig. 3.5B**, shown in **Fig. 3.6G**, whose peaks find good correspondence to the ones in **Fig. 3.5A**. The same analysis for the slurry cast SnO_{2-x}/rGO composite revealed reaction (i) in the 1st cycle is already delayed to coincide with reaction (iv) (**Fig. 3.6H**). Therefore, the slurry-cast composite behaves just like the standard SnO_2 electrodes in the literature[2,3,18], and they all have inferior reactivity compared to the network composite electrode.

Because synergism between composite components cannot be ruled out, there

is no rigorous way to partition the composite capacity into the SnO_2 contribution and the 3D graphene one. Nevertheless, the theoretical reduction capacity of SnO_2 is 711 mAh g^{-1} for the reduction part (4 Li per Sn) and 783 mAh g^{-1} for the alloying part (4.4 Li per Sn). It is commonly thought that the reduction capacity is easily lost during cycling due to the loss of electrical contact from both Li_2O insulation and SnO_2 reconfiguration, cracking and coalescence. Yet the 100^{th} cycle capacity of the network composite (3.53 g cm^{-3}/10 mg cm^{-2}) in **Fig. 3.5B** already reaches 912 mAh g^{-1}, with the actual SnO_2 contribution. Therefore, the loss of reduction capacity in the network composites must be relatively small.

Three reasons may account for this. (a) The SnO_{2-x} nanoparticles are well dispersed on and adhered to the 3D graphene backbone, thus acquiring better stability against reconfiguration/coalescence and maintaining better electrical contact. (b) The SnO_{2-x} nanoparticles on 3D graphene coexist with widespread nanopores as revealed by electron microscopy (**Fig. 3.6A-C**), which along with the pores on the graphene nanotubes makes available abundant SnO_2/graphene/pore triple points that turn into oxide/electrode/electrolyte triple points in LIB. Analogous to the well-known gas/electrode/electrolyte triple points in solid oxide fuel cells, these triple points are ready for redox reactions, thus giving rise to the excellent reactivity noted in connection to (i) in **Fig. 3.5A**. (c) The size of SnO_2 nanoparticles apparently refines during cycling, which renders them too small to resolve in x-ray diffraction (**Fig. 3.6E** inset) though not in selected area electron diffraction (**Fig. 3.6A**) and Raman spectroscopy (**Fig. 3.6E**). This is informative because Raman senses only the local structure and is insensitive to the particle size, and if the coherent length of the crystallites approaches the wavelength of Cu-$K\alpha$, (0.154 nm) the crystallites can no longer be "seen" by x-ray but can still be by

200 keV electrons whose wavelength is 2.74 pm. Indeed, microstructure refinement can explain why the 2nd and subsequent cycle charging current is significantly higher than the 1st cycle one in **Fig. 3.5A**, and it has also been reported in a recent study of SnO_{2-x}-rGO composite.[2] Further TEM (**Fig. 3.6A**) and XPS (**Fig. 3.6D**) study confirmed that there is no metallic Sn after cycling at the 3 V charged state, which is supportive of relatively complete oxidation to SnO_2. Lastly, dividing the capacity according to the voltage range as described in the next section and in **Fig. 3.6F** found a relatively constant partition of the capacity in support of stable redox reactions and consistent with **Fig. 3.5D**.

3.4.2 Comparison with commercial and experimental anode electrodes

Table 3.1 Comparison of electrochemical performance metrics of our SnO_2-based network composite, and SnO_2-based anode materials in the literature, and commercial graphite

	Commercial graphite	SnO_2/G	C/SnO_2	SnO_2 QD @GO	SnO_2 @carbon sphere	SnO_2 @Maxene	SnO_2-based 3D composite
Initial Coulombic efficiency	85%	62%	41%	71%	49%	56%	63%
Areal rate (mA cm^{-2})	1.6	0.2	0.04	0.1	0.3	0.8	2.0
Areal loading (mg cm^{-2})	12.5	1.9	0.8	1.4	1.5	1.5	10.0
Areal capacity (mAh cm^{-2})	3.1	2.1	0.7	1.4	0.8	1.4	9.4
Volumetric loading (g cm^{-3})	1.3	1.4	0.3	0.6	0.6	0.6	3.5
Volumetric capacity (mAh cm^{-3})	286.0	744.1	280.0	554.4	306.0	540.0	3312.5
Volumetric Rate (mA cm^{-3})	159.8	138.0	16.0	56.0	120.0	300.0	705.5
Gravimetric Rate (A g^{-1})	0.1	0.1	0.05	0.1	0.2	0.5	0.2

Gravimetric capacity (mAh g^{-1})	244.8	1126.7	875.0	990.0	510.0	900.0	939.1
Reference	23	24	25	26	27	28	This work

In **Table 3.1**, we first summarize and compare the electrochemical performance of SnO_2-based network composite with those of "advanced" SnO_2 anodes in the literature and with commercial graphite anode, all after 100 cycles. SnO_2-based 3D composite delivers an initial coulombic efficiency (ICE) of 63% at an areal loading of 10 mg cm^{-2}. As can be seen in Table 3.1, this ICE is higher than or comparable to the typical values (41% ~ 62%) in the literature[24,25,27,28] , but it was achieved in our composites at a loading up to one order of magnitude higher than the highest loading in the previous work (0.8 mg cm^{-2}). [25] Significantly, the high SnO_2 loading in our composites does not deteriorate the gravimetric capacity, which remains at 939 mAh g^{-1} at 10 mg cm^{-2} and 3.5 g cm^{-3} under 0.2 A g^{-1}, whereas an electrode in the literature [25] with a similar performance of 875 mAh g^{-1} under 0.1 A g^{-1} had only 0.8 mg cm^{-2} and 0.3 g cm^{-3}. In addition, our composites can simultaneously achieve high areal and volumetric loading, of 9.3 mg cm^{-2} and 3.25 g cm^{-3}, respectively, whereas in the literature the relatively high areal loading of 1.9 mg cm^{-2} is accompanied by a modest volumetric loading of 1.4 g cm^{-3}, indicating the existence of a large amount of large pores still. [24] Consequently, the areal and volumetric capacities of our composites easily exceed those of "SnO_2/G"[24], "C/SnO_2"[25], "SnO_2 QD @GO"[26], "SnO_2 @carbon sphere"[27], and "SnO_2@Maxene". They also outperform commercial graphite: the areal capacity of our composite is 3 times higher than that of commercial graphite, while the volumetric capacity is about 11.6 times higher than that of commercial graphite. The rate performance is another important metric for practical applications. On a mass basis, the current density of our composite is comparable to that of the literature (0.2 A g^{-1} vs. 0.1~0.5 A g^{-1}), however, the areal and volumetric current densities of our composites are up to 500 times and 44 times, respectively, those of

SnO_2 -based anodes in the literature, and 1.25 times and 4.4 times, respectively, better than those of commercial graphite.

The same comparison of the performance after 100 cycles is made in **Fig. 3.7**. It is evident that the literature materials only excel in gravimetric capacity and rate, but they are rather poor in loadings, rates and capacities on the areal and volumetric basis. While commercial graphite enjoys excellent areal loading and ICE, its capacities in gravimetric and volumetric terms are relatively low. In contrast, our SnO_2-based network composites easily outperform those "advanced" SnO_2 in the literature, as well as commercial graphite, in areal and volumetric metrics of capacities, rates and loadings; they also have an areal loading comparable to that of commercial graphite.

In **Appendix 2 Fig. 2.1**, we further compare the electrochemical performance of SnO_2-based network composite with several other experimental LIB anodes of either the alloying type or the conversion type, at 200 mA g^{-1} and 1,000 mA g^{-1}. Two specific comments are pertinent.

First, a very favorable comparison holds with lithium metal electrode that has a theoretical capacity of ~2,000 mAh cm^{-3} ("lithium metal" in **Fig. 3.5D**), and, in cycling, with Si electrodes[4,7,11,19] and commercial graphite anodes (silicon "band" and commercial graphite "band" in **Fig. 3.5D**). On the other hand, the capacity of lithiated silicon anode despite a theoretical value of ~ 2,000 mAh cm^{-3} is much worse ("Li-Si alloy " in **Fig. 3.5D**).

Second, the SnO_2/G data in **Appendix 2 Fig. 2.1**, from another SnO_2/graphene composite featuring nanostructured SnO_2 nanoparticles caged in a 3D graphene network,[18] are lower than ours. More broadly, it is common for SnO_2 anodes even at very low loading (< 1 mg cm^{-2}) to suffer from poor reversibility,[2]

e.g., having only 52.4% of the theoretical capacity. In comparison, referring to **Fig. 3.5B**, our electrodes have 912 mAh g^{-1} (61% of SnO_2's theoretical capacity) after 100 cycles even though the value is weighed down by 31.2 wt% graphene, which has much less capacity than SnO_2. Note too that 912 mAh g^{-1} after 100 cycles is among the highest capacity ever achieved for any SnO_2 electrode, yet this high gravimetric capacity is obtained at a mass loading of 3.53 g cm^{-3}/ 10 mg cm^{-2} which is at least 10× higher than those in the literature. This is also true in cycling: the literature data of SnO_2 anodes (SnO_2 "band" in **Fig. 3.5D**) have only ~1/50th of the areal capacity (~9 vs. 0.18 mAh cm^{-2} [10]) of our electrodes.[2,3,10,20,21].

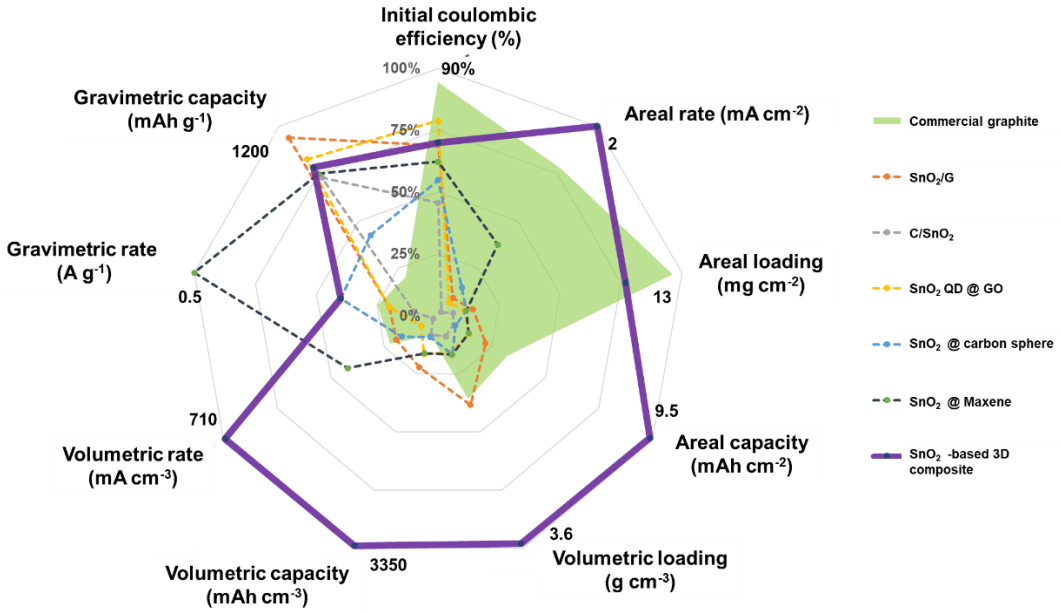

Figure 3.7 Comparison of properties of our network composite, various SnO_2-based anode materials in the literature, and commercial graphite, all after 100 cycles. Thickness of 25 μm assumed if the thickness of the electrode was not specified in the literature.

These comparisons all attest to the advantage of the affine transformation

approach, which can produce high-performance SnO_2 anodes that combine high reversibility and high loading for practical applications. Being free-standing and requiring no binder hence eliminating their dead weight and volume is another advantage. This was not possible from the standard nano materials reported in the literature. For example, while a high volumetric loading can be achieved in thin films, the substrate will add dead volume and weight.[3,10] Likewise, while a high areal density can be achieved by increasing the electrode thickness, a thicker battery assembly is a serious disadvantage for achieving high volumetric loading[29]. Only our anodes using the new network composite approach are able to simultaneously increase areal and volumetric loading without sacrificing any gravimetric performance, which is the essence of functional invariance—the essential element for scaling up nanomaterials.

3.4.3 Shortcomings of SnO_2-based 3D composite

Despite the huge advance over all other nanomaterials, SnO_2-based network composites still have some shortcomings. First, they suffer from low initial Coulombic efficiency, which is a common problem for nanomaterials. Nanomaterials offer an exceedingly large surface area and void space where liquid electrolyte can reside, but a large amount of SEI can also form during the first reduction reaction that sequesters Li and severely reduces the initial Coulombic efficiency.[30] This is evident in **Appendix 2 Fig. 2.2**, where the pristine SnO_2-based network composite exhibits a large irreversible capacity of 737 mAh g^{-1} and low initial coulombic efficiency of 63%. In contrast, the commercial graphite anode delivers an initial coulombic efficiency of ~80%. The low initial coulombic efficiency is problematic because it requires extra lithium to be added to cathodes, which is expensive and weighs down the over-all capacity of the battery pack.

While the above problem has no solution, as a common practice pre-lithiation technique is utilized in industry and academia to compensate for the Li loss.[31 32] Following the standard industrial approach, we pre-lithiated anode using a lithium metal (see details in section 3.2.1.3). In **Appendix 2 Fig. 2.2**, the pre-lithiated SnO_2-based network composite suffers a much reduced irreversible capacity of 39.4 mAh g^{-1}, which is 1/20 of that of an untreated network electrode. Thus, 96% initial coulombic efficiency can now be achieved. In addition, in the pre-lithiated network composite, the coulombic efficiency can be further increased to above 99.5% within 15 cycles, compared to 40 cycles for a pristine SnO_{2x} network composite to reach the same level **(**see **Appendix 2 Fig. 2.3)**. Importantly, pre-lithiation can be practiced on high loading anodes and has no adverse effect on their high capacity. This makes pre-lithiated network composite a potentially very attractive alternative anode to replace commercial graphite anodes.

Another shortcoming of SnO_{2-x}/3D graphene is its void space after compression may not be enough to support the full expansion of SnO_2 during lithiation, and this may cause material interference or incomplete lithiation during cycling, possibly affecting the capacity and the cycling life. To see whether this could be the case or not, we recall that a SnO_2-based network composite has 68.8 wt.% of SnO_{2-x}, which is deposited onto a 3D graphene that is initially 99.07% porous with a (C) density of 0.021 g cm^{-3}. The as-deposited composite has an overall density of 0.069 g cm^{-3}, of which 0.0216 g cm^{-3} is C at 0.96 vol. % (assuming graphite's density 2.25 g cm^{-3}). Thus, 0.048 g cm^{-3} is $SnO_{2-x,}$ which occupies 0.69 vol. % (assuming SnO_2's density 6.95 g cm^{-3}). Compressing this composite of an initial thickness 0.16 cm (thus an areal loading of 10.72 mg cm^{-2}) to a final thickness 0.002835 cm that fits into a coin cell, we obtain a final

composite that is 2.45% of the initial volume after taking into account the lateral (Poisson's) expansion of about 17.62%. So, the final composite has an areal loading of 8.02 mg cm^{-2} and a volumetric loading of 2.83 g cm^{-3} of C and oxide, with their respective volume fraction 39 vol. % and 28 vol. %, leaving 33 vol. % for pores. While this example illustrates how with an extreme compression ratio (56) and volume reduction (40.8×) it is possible to simultaneously achieve high areal and volumetric loadings comparable to those of commercial electrodes while still leaving adequate pore space for electrolyte to infiltrate the network composite, the void to oxide ratio is nevertheless reduced to 33/28 that is much less than the ratio 3.76 needed to fully accommodate volume expansion during lithiation. It is possible that the insufficient pore space does result in cycling deficiency in **Fig. 3.5D**, **w**hich may explain why our electrode at 10 mg cm^{-2} can only maintain 87.5% capacity up to 160 cycles whereas the commercial graphite does so up to 500 cycles. It is possible that with another oxide that entails less volumetric expansion during lithiation, this is less problematic and the network composites may have an even better performance. This possibility will be explored in later chapters.

Despite these shortcomings, the SnO_2-bsed network composite electrode can deliver an areal capacity 5 times higher than that of commercial graphite at 12.5 mg cm^{-2}, and it does provide higher capacity at a rate of 4 mA cm^{-2} that is one to four times that of commercial graphite, see **Appendix 2 Fig. 2.4**. From a practical viewpoint, its capacity after 500 cycles also exceeds that of commercial graphite anode. Another interesting feature is that in the network composites a higher loading actually results in an advantage in a lower contact resistance, see **Fig 3.3J**, which is consistent with the result of pure 3D graphene in **Chapter 2.** In this

context, we also note in **Fig. 3.5D** the better cyclic durability of the higher density electrode (10 mg cm^{-2}) compared to the lower density one (7 mg cm^{-2}), in that the former can sustain longer cycles (160 cycles) than the latter (120 cycles) when holding the capacity above 87.5% of the initial value. This is despite the fact that the higher loading composite has less pore space, which may affect reaction reversibility as pointed out before. Possibly, a higher degree of compression can better hold the active materials to the 3D graphene backbone, hence maintaining better conductivity and allowing less relocation thus benefiting cyclic durability.

3.5 Conclusions

- SnO_2-based network composites deliver areal and volumetric capacity up to about 9 mAh cm^{-2} and 3000 mAh cm^{-3}, respectively, which is 3 times and 6 times those of commercial graphite.
- After 500 cycles, network composites deliver a higher areal capacity than that of commercial graphite, even under a current density 2 to 4 times higher than that of commercial graphite.
- Although the initial coulombic efficiencies of network composites at high loading are only 65%, pre-lithiation can increase them to 96%, which makes these electrodes suitable for practical applications.

References

1 Wu, F. & Yushin, G. Conversion cathodes for rechargeable lithium and lithium-ion batteries. *Energy & Environmental Science* **10**, 435-459 (2017).

2 Dong, W. *et al.* A Robust and Conductive Black Tin Oxide Nanostructure Makes Efficient Lithium-Ion Batteries Possible. *Advanced Materials* **29** (2017).

3 Hu, R. *et al.* Dramatically enhanced reversibility of Li 2 O in SnO 2-based electrodes: the effect of nanostructure on high initial reversible capacity. *Energy & Environmental Science* **9**, 595-603 (2016).

4 Liu, N. *et al.* A pomegranate-inspired nanoscale design for large-volume-change lithium battery anodes. *Nature nanotechnology* **9**, 187 (2014).

5 Whittingham, M. S. History, evolution, and future status of energy storage. *Proceedings of the IEEE* **100**, 1518-1534 (2012).

6 Gogotsi, Y. & Simon, P. True performance metrics in electrochemical energy storage. *Science* **334**, 917-918 (2011).

7 Chockla, A. M. *et al.* Silicon nanowire fabric as a lithium ion battery electrode material. *Journal of the American Chemical Society* **133**, 20914-20921 (2011).

8 Magasinski, A. *et al.* High-performance lithium-ion anodes using a hierarchical bottom-up approach. *Nature materials* **9**, 353 (2010).

9 Ji, X., Lee, K. T. & Nazar, L. F. A highly ordered nanostructured carbon–sulphur cathode for lithium–sulphur batteries. *Nature materials* **8**, 500 (2009).

10 Jiang, Y. *et al.* Spatially-confined lithiation–delithiation in highly dense

nanocomposite anodes towards advanced lithium-ion batteries. *Energy & Environmental Science* **8**, 1471-1479 (2015).

11 Wu, H. *et al.* Stable Li-ion battery anodes by in-situ polymerization of conducting hydrogel to conformally coat silicon nanoparticles. *Nature communications* **4**, 1943 (2013).

12 Zhao, H. *et al.* Conductive polymer binder for high-tap-density nanosilicon material for lithium-ion battery negative electrode application. *Nano letters* **15**, 7927-7932 (2015).

13 Ko, M. *et al.* Scalable synthesis of silicon-nanolayer-embedded graphite for high-energy lithium-ion batteries. *Nature Energy* **1**, 16113 (2016).

14 Jin, Y. *et al.* Self-healing SEI enables full-cell cycling of a silicon-majority anode with a coulombic efficiency exceeding 99.9%. *Energy & Environmental Science* **10**, 580-592 (2017).

15 Chmiola, J., Largeot, C., Taberna, P.-L., Simon, P. & Gogotsi, Y. Monolithic carbide-derived carbon films for micro-supercapacitors. *Science* **328**, 480-483 (2010).

16 Gallagher, K. G. *et al.* Optimizing areal capacities through understanding the limitations of lithium-ion electrodes. *Journal of The Electrochemical Society* **163**, A138-A149 (2016).

17 Bi, H., Chen, I. W., Lin, T. & Huang, F. A new tubular graphene form of a tetrahedrally connected cellular structure. *Advanced materials* **27**, 5943-5949 (2015).

18 Han, J. *et al.* Caging tin oxide in three-dimensional graphene networks for superior volumetric lithium storage. *Nature communications* **9**, 402 (2018).

19 Kovalenko, I. *et al.* A major constituent of brown algae for use in high-

capacity Li-ion batteries. *Science* **334**, 75-79 (2011).

20 Hu, R. *et al.* Inhibiting grain coarsening and inducing oxygen vacancies: the roles of Mn in achieving a highly reversible conversion reaction and a long life SnO 2–Mn–graphite ternary anode. *Energy & Environmental Science* **10** (2017).

21 Hu, R. *et al.* Stabilizing the nanostructure of SnO2 anodes by transition metals: a route to achieve high initial coulombic efficiency and stable capacities for lithium storage. *Advanced Materials* **29** (2017).

22 Liu, J. *et al.* High volumetric capacity three-dimensionally sphere-caged secondary battery anodes. *Nano letters* **16**, 4501-4507 (2016).

23 Gallagher, K. G. *et al.* Optimizing areal capacities through understanding the limitations of lithium-ion electrodes. **163**, A138-A149 (2016).

24 Han, J. *et al.* Caging tin oxide in three-dimensional graphene networks for superior volumetric lithium storage. **9**, 402 (2018).

25 Huang, B. *et al.* Novel Carbon-Encapsulated Porous SnO2 Anode for Lithium-Ion Batteries with Much Improved Cyclic Stability. **12**, 1945-1955 (2016).

26 Zhao, K. *et al.* SnO2 Quantum dots@ graphene oxide as a high-rate and long-life anode material for lithium-ion batteries. **12**, 588-594 (2016).

27 Lou, X. W., Li, C. M. & Archer, L. A. J. A. M. Designed synthesis of coaxial SnO2@ carbon hollow nanospheres for highly reversible lithium storage. **21**, 2536-2539 (2009).

28 Ahmed, B., Anjum, D. H., Gogotsi, Y. & Alshareef, H. N. J. N. E. Atomic layer deposition of SnO2 on MXene for Li-ion battery anodes. **34**, 249-256 (2017).

29 Xia, Y. *et al.* Thickness-independent capacitance of vertically aligned liquid-crystalline MXenes. *Nature* **557**, 409 (2018).

30 Etacheri, V. *et al.* Challenges in the development of advanced Li-ion batteries: a review. **4**, 3243-3262 (2011).

31 Remizov, S., Min, H. S., Kim, B. K. & Jung, H. C. (Google Patents, 2013).

32 Forney, M. W., Ganter, M. J., Staub, J. W., Ridgley, R. D. & Landi, B. J. J. N. l. Prelithiation of silicon–carbon nanotube anodes for lithium ion batteries by stabilized lithium metal powder (SLMP). **13**, 4158-4163 (2013).

Chapter 4 GeO_2-based 3D composites as high areal and volumetric capacity anodes of lithium-ion batteries

4.1 Introduction

Our interest in GeO_2 stems from its potential as a new anode material incorporating Li by the conversion and alloying reactions. The volume change involved in these reactions is 303%, which is slightly less than seen in SnO_2. Therefore, GeO_2-containing network composites constructed in a similar way as the network composites of SnO_2 and 3D graphene described in Chapter 3 will afford an opportunity to evaluate the effect of the volume change of the active material on the electrochemical performance of the composite.

As a potential anode material, GeO_2 has a theoretical volumetric （9098 mAh cm^{-3}) and gravimetric (2152 mAh g^{-1}) capacity that is 11 and 6 times, respectively, higher than those (838 mAh cm^{-3} and 372 mAh g^{-1}) of commercial graphite anode. This may help match anode's volumetric capacity with that of cathode, which will allow a more efficient use of the device volume of a lithium ion battery (LIB). On the other hand, with a large volume expansion during the lithiation process, GeO_2 is expected to suffer from pulverization and cracking, which will cause some loss of its electrical contact with the current collectors thus capacity fading after a few cycles. The problem of volume expansion becomes worse if there are anisotropic strains, which further promote cracking and structural instability. One would also expect the solid electrolyte interphase (SEI) on the surface of GeO_2 particles to break because of volume expansion, necessitating the formation of a new SEI hence sequestering lithium and electrolyte repeatedly. In addition, as shown in our recent study elsewhere, any transport

bottleneck at the phase/crystal boundary can result in unexpected phases to form, including cavities, which may cause further capacity fading. Lastly, the above dynamical electrochemical processes are known to lead to particle coarsening, again resulting in the loss of electrochemical activity. These problems are more severe when the oxide loading is high, yet practical electrodes do demand high loading of active materials in order to obtain a device of reasonable volumetric and areal mass and energy density. In this chapter, we hope to solve these problems by leveraging the superelastic 3D graphene as the backbone of network composites to obtain high performance, high loading GeO_2 composite electrodes. Amorphous GeO_2 will be employed to help lessen the problem of cracking and coarsening.[1-3]

4.1.1 Literature review

Since volume expansion is a major problem for conversion and alloying reactions, hierarchical architectures could be a solution as it provides large pores for ionic transport and small pores for excess volume that accommodates volume expansion. They have been attempted. For example, the 3D hierarchical GeO_2 of Ngo etc.[4] had a stable capacity of 1216 mAh g^{-1} after 1000 cycles at 3.2 A g^{-1}. Yang etc. reported a nano-sized amorphous GeO_x, which offers homogenous isotropic expansion and no grain boundary, that can deliver a relatively stable cycling performance of 1250 mAh g^{-1} after 600 cycles at 0.8A g^{-1}; this may be compared to the crystalline counterpart that could not sustain more than a few cycles.[2] Glassy Li-B-Ge-O(LBGO) anode has also been prepared by Choi et al. to provide 800 mAh g^{-1} at 1 A g^{-1} after 150 cycles.[1]

One reason for the poor reversibility of conversion reactions is the excessive relocation and aggregation (especially the metallic phase, namely Ge in this case) during electrochemical cycling. This causes the loss of contact between Ge and

Li_2O, forming a gap between large Ge grains and Li_2O. Since triple point junctions of Ge, Li_2O and electrolyte are required for the conversion reaction of Ge, back to GeO_2, this, along with the poor electrical conductivity of Li_2O, hinders the reactivity of reversible reactions. Doping transitional metals into GeO_2 to improve electrical conductivity may help in this respect. For example, Kim etc.[5] used GeO_2 and Cu nanoparticles to form Cu-GeO_2 composites that have greatly enhanced reversibility (74%) compared to undoped GeO_2 (43%). Other transition metals (e.g., Fe, Ni, Co, etc.) have also been shown to be effective.[5,6] Coating GeO_2 with carbon materials of high electrical conductivity and mechanical flexibility is another nanomaterial approach. For example, Cho etc.[7] designed a yolk-shell nanostructured Ge-carbon composite with Ge nano-clusters encapsulated within a CVD carbon shell. This composite gave 1200 mAh g^{-1} after 50 cycles at 0.32 A g^{-1}.

Although the above development is encouraging, none of these "advanced" electrode materials have been prepared and tested in the high loading form, which is mandatory for practical applications. Therefore, we seek to apply the 3D network composite approach to GeO_2, while at the same time incorporate the best practice of the literature. This includes improved conductivity by Fe-doping, carbon coating and reduction, and elimination of anisotropic expansion by amorphization.

4.2 Experimental procedures

4.1.1 Material synthesis

4.1.1.1 Coating amorphous Fe-doped GeO_2 onto 3D graphene

To render the 3D graphene monolith hydrophilic, it was first immersed in nitric acid and heated to 100^{o}C for 12 h, then dried. Next, 257 μl $GeCl_4$ (Alfa

Aesar), 0.527 g citric acid (Alfa Aesar) and 0.041 g $FeCl_3$ were dissolved in a mixture solution of 2 ml ethanol and 3 ml ethelyn glycol. In this solution the hydrophilic 3D graphene monolith was immersed for 2 h at room temperature to become thoroughly soaked. After that, the soaked 3D graphene was removed and freeze-dried for 6 h. Thus dried 3D graphene remained as a monolith, and it was finally subject to calcination in air at 350 ^oC for 1 h.

4.1.1.2 CVD coating of carbon and hydrogen reduction

To coat the above monolith by CVD carbon in a tube furnace, Ar at a flow rate of 300 sccm and H_2 at a flow rate of 30 sccm were used to carry a liquid carbon source (benzene) and to flush the furnace for 20 min. After that, the furnace was ramped to 550^oC in 30 min and the argon/carbon-source/H_2 flow was kept to grow CVD carbon and to reduce the 3D monolith. At the end of 30 min, the coated 3D monolith was immediately removed from the tube furnace to prevent over-reduction; in addition, it was exposed to the air to re-oxidize the surface.

4.1.2 Characterization

4.1.2.1 Material characterization

Scanning electron microscopy (SEM) images were obtained in a field emission Magellan 400 microscope (FEI Company). Transmission electron microscopy (TEM), high angle annular dark field (HAADF) imaging, electron energy loss spectroscopy (EELS, Gatan), and elemental mapping were conducted in a JEOL 2100F microscope operated at 200 kV. Nitrogen adsorption-desorption isotherms at 77 K were measured in a Micromeritics Tristar 3000 system using vacuum-degassed samples (200 °C for 12 h). These isotherms were used to calculate (*a*) the specific surface area by the Brunauer-Emmett-Teller (BET) method and (*b*) the pore volume and pore size by the Barrett−Joyner−Halenda (BJH) method. Small

and wide-angle X-ray diffraction was performed in a Brucker D8 powder X-ray diffractometer using Cu *K*α radiation. X-ray photoelectron spectra (XPS) were collected in a Thermo Escalab 250Xi with Al *K*α radiation (hν =1,486.6 eV). Binding energies were calibrated using the 284.8 eV peak of delocalized sp^2-hybridized adventitious carbon. Raman spectra were collected in a Thermal Dispersive Spectrometer using a 10 mW laser with an excitation wavelength of 532 nm. The mass ratio of doped germanium oxide in GeO_2-based 3D composite was determined by thermogravimetric analysis (TGA) at a heating rate of 10^{o}C min^{-1} in the temperature range of 25-900^{o}C in air using a thermal analyzer (NETZSCH STA 449 F3). Electrical characterization was performed using an electrochemistry workstation (CHI 660) or in a cryostat equipped with a magnetic field (PPMS, Quantum Design).

4.1.2.2 Electrochemical measurement

The as-prepared GeO_2-based 3D graphene composite monolith, which we call network composite, was sliced into disks for later use. They could be directly used as free-standing electrode that is free of binder and additional conductive additive or current collector. This was used as the working electrode (anode) against a counter electrode of lithium foils (China Energy Lithium Co., Ltd) in the half-cell configuration, in conjunction with a polymer membrane (Celgard) separator and $LiPF_6$ electrolyte in a 50:50 w/w mixture of dimethyl carbonate (DMC) and ethyl carbonate (EC). This configuration was assembled in a 2016 coin cell in argon in a glovebox with less than 1 ppm oxygen and moisture. Galvanostatic charge and discharge measurements were conducted using a LAND-CT 2001C testing system within a voltage window of 0.01 V to 3.0 V. The rate capability was investigated by changing the current density from 0.2 A g^{-1} to 2 A g^{-1}. Cyclic voltammetry (CV)

was conducted by an automated electrochemical workstation (CHI660E), at a scan rate of 0.2 mV/s in the voltage window of 0.01 V to 3 V.

4.3 Results

4.3.1. Materials characterization

Table 4.1 Summary of elemental analysis of GeO_2-based 3D composite.

Elements	Atomic ratio
O	63.5%
Ge	30.1%
Fe	6.4 %

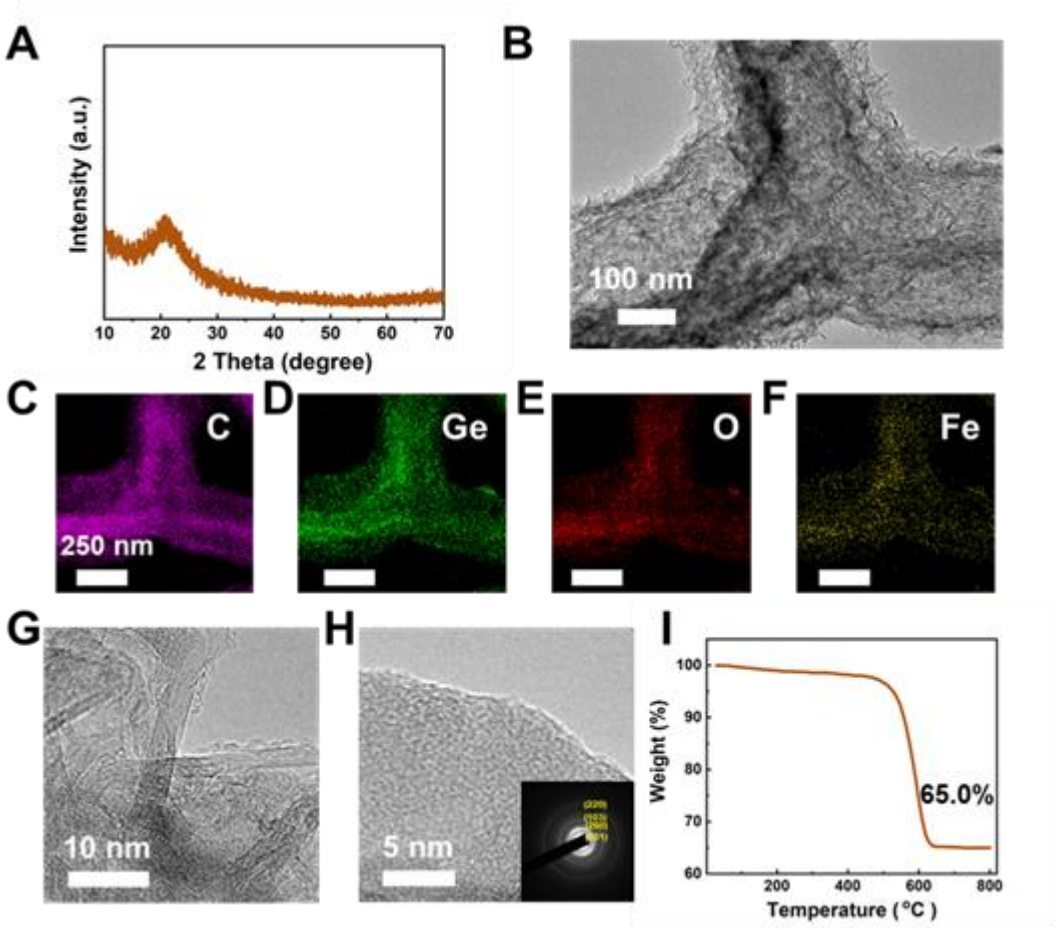

Figure 4.1 Materials characterization of GeO_2-based network composite. (A) X-ray diffraction pattern of GeO_2-based composite with broad diffusion peak between 20~ 30°, (B) Transmission electron microcopy (TEM) image, (C~F) Mapping of C, germanium, oxygen and Fe element, (G and H) High-resolution TEM image with selected area electron diffraction pattern of GeO_2 in the inset. (I) Thermogravimetric analysis spectrum of GeO_2-based network composite.

For doping, the Fe/(Ge+Fe) mole ratio was set at around 10% by controlling the amount of $GeCl_4$ and $FeCl_3$ in the solution. The actual ratio was determined by the energy dispersive spectrum analysis, summarized in **Table 4.1,** giving 6.4% Fe compared to 30.1 % Ge, and the ratio is similar to what have been reported in the literature of transition metal doping.[5,6] Importantly, the oxygen ratio confirmed that the oxide is deficient in oxygen, so our brief reduction treatment by hydrogen/argon gas was effective. The composite exhibited amorphous phase features in X-ray diffraction patterns (**Fig.4.1A).** The advantage of acid treatment to promote hydrophilicity and uniform oxide precipitation was confirmed by TEM in **Fig. 4.1B** in which a triple junction of 3D graphene is homogeneously coated by GeO_2-based oxide. Coating uniformity was further confirmed by elemental mapping in **Fig 4.1 C-F**, in which the distributions of Ge, O and Fe all seem rather uniform. A closer look at the corner site of the junction (**Fig 4.1G**) finds oxide coating even at the edge of the graphene tube made of a vertically aligned few-layer graphene sheet. In **Fig. 4.1 H,** the disordered nature of amorphous germanium-based oxide (as evidenced by the white halo in the selected area electron diffraction pattern in the inset) is apparent in grains of an ultra-fine size (<1 nm)—there are also many small pores among them. However, the (101), (200),

(103) and (220) diffraction lines of GeO_2 (PDF#36-1463) are also revealed by electron diffraction. Therefore, the oxide formed is likely to be an porous amorphous/nanocrystalline mixture. To complete the characterization, we determined the weight fraction of germanium-based oxides by thermal gravimetric analysis (TGA) (**Fig. 4.1 I**), which gave 65.0%.

4.3.2 Electrochemical performance

In our material design, we aim to use Fe doping to enhance reversibility of conversion reactions. Cyclic voltammetry **(**CV, **Fig. 4.2A)** was first used to confirm the reversible reactions of germanium oxidation, where the peak at 1.2 V indicates the formation of GeO_2 from Ge and Li_2O, while the peak at 0.5V corresponds to the de-alloying reaction of Li_xGe. Despite the first cathodic scan revealing the formation of SEI via a broad peak from 1 V to 0.6 V, the overlapping of 2^{nd}-4^{th} cyclic curves confirms the good reversibility of the electrochemical process. In addition to CV, the reversibility is also evaluated in **Fig. 4.2 B**, which shows the first cycle charge-discharge curves of a 13 mg cm^{-2} composite with an initial coulombic efficiency (ICE) of 72.6%. This ICE is higher than that (65%) of the SnO_2-based 3D composite described in Chapter 3. The gravimetric capacity of GeO_2 based-3D composite at 13 mg cm^{-2} remained higher than 1225 mAh g^{-1} at 0.2A g^{-1} after 100 cycles (**Fig. 4.2A**). Although the above gravimetric capacity is only comparable to the best data in the literatures[2,4], the areal and volumetric capacities of the composite (**Fig. 4.2C**), 16.5 mAh cm^{-2} and 5873 mAh cm^{-3}, respectively, are already 5 times and 11 times higher than those of commercial graphite anodes, which could not be achieved in previous studies because of low loading. The rate performance is also evaluated in **Fig. 4.2D**, in which a composite at 7 mg cm^{-2} delivers 1698 mAh g^{-1} at 0.2A g^{-1}, 1301 mAh g^{-1} at 0.5 A g^{-1}, 960

mAh g^{-1} at 1 A g^{-1} and 680 mAh g^{-1} at 2 A g^{-1}, which outperforms those in the literature.[1,8] In the Appendix, another high areal loading (11 mg cm^{-2}) composite is also described offering an areal capacity of 4 mAh cm^{-2} after 700 cycles at the rate of 9 mA cm^{-2} **(Appendix 3 Fig. 3.1**), compared to commercial graphite anodes that typically feature an area capacity of 2.1 mAh cm^{-2} at 2.75 mA cm^{-2} after 700 cycles.

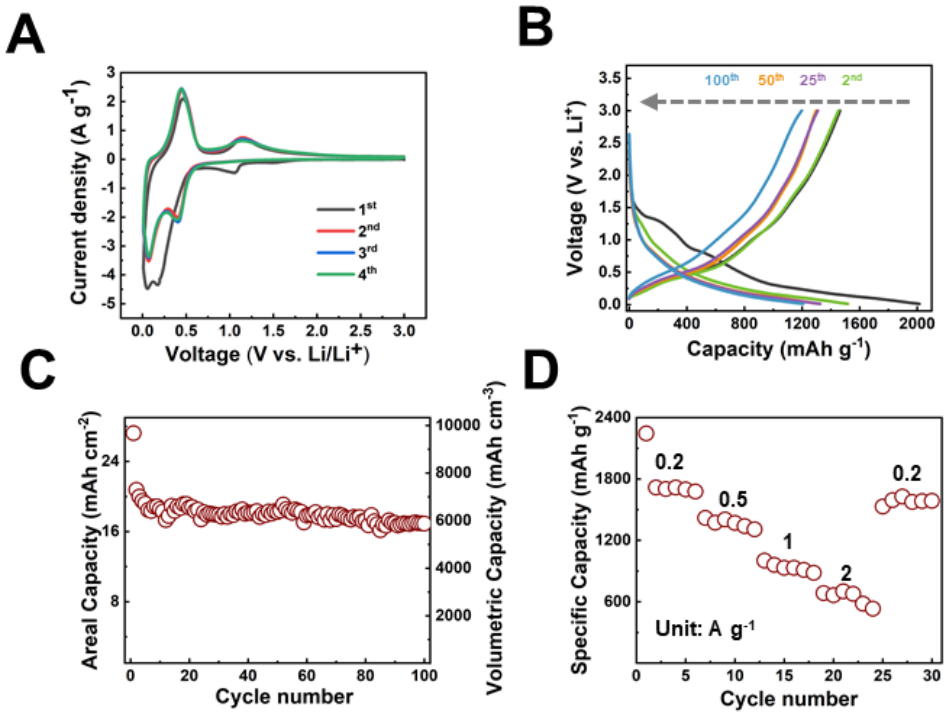

Figure 4.2 Electrochemical performance of GeO_2-based network composite at 13 mg cm^{-2} in (A) cyclic voltammetry (first 4 cycles), （B) successive charge-discharge curves at 0.2A g^{-1} and (C) areal and volumetric capacity vs. cycle numbers at 0.2A g^{-1}. (D) Rate performance of GeO_2-based network composite with 7 mg cm^{-2} at 0.2, 0.5, 1 and 2 A g^{-1}.

4.4 Discussion

Our work has shown that GeO_2-based 3D networks composites have the potential of achieving high capacity at high loading, and they enjoy better initial

Coulombic efficiency (ICE) than similarly constructed SnO_2 composites. Below, we will further discuss these results and their significance.

4.4.1 ICE, areal loading and areal and volumetric capacities

Table 4.2 Comparison of electrochemical performance metrics of our network composite, various GeO_2-based anode materials in the literature, and commercial graphite.

	3D graphene-Ge	Carbon-Interconnected Ge	Germanium NPs in C-box	GeO_x/multi-walled CNT	Mesoporous Ge/GeO_2/Carbon	Nano-GeO_2/C	Nano-GeO_2	Bulk-GeO_2	Commercial graphite	Amorphous GeO_x	Fe_2GeO_4/rGO	CuGeO_3	FeGeO_3	CoGeO_3	GeO_2-based network composite	
Areal loading(mg	1.80	0.32	0.80	0.56	1.35	0.50	0.50	0.50	12.50	N/A	N/A	N/A	N/A	N/A	7.00	13.00

cm^{-2}) Volumetric loading (g cm^{-3})	0.04	0.13	0.32	0.22	0.54	0.75	0.75	0.75	1.29	N/A	N/A	N/A	N/A	N/A	2.47	4.59
Initial coulomb	76%	63%	75%	75%	73%	75%	55%	32%	85%	70%	72%	74%	71 %	70%	76%	73%

ic efficiency																
Gravimetric capacity (mAh g^{-1})	1,200	1,300	1,150	1,100	1,510	1,650	1,300	500	245	1728	934	1007	1038	932	1,716	1,518
Areal	2.16	0.42	0.92	0.60	2.04	0.83	0.65	0.25	3.06	N/A	N/A	N/A	N/A	N/A	12.00	19.70

capacity (mAh cm^{-2})																
Volumetric capacity (mAh cm^{-}	43	166	368	246	815	1,237	975	375	286	N/A	N/A	N/A	N/A	N/A	4,237	6,961

^{3})																
gravimetric rate (A g^{-1})	1.60	0.16	0.80	0.10	0.20	0.10	0.10	0.10	0.12	0.08	0.36	0.1	0.10	0.10	0.20	0.20
Areal rate (mA cm^{-2})	2.88	0.05	0.64	0.06	0.27	0.05	0.05	0.05	1.55	N/A	N/A	N/A	N/A	N/A	1.40	2.60
Volu	58	20	256	22	108	75	75	75	160	N/A	N/A	N/A	N/A	N/A	494	917

metric rate (mA cm^{-3})																
Reference	9	10	11	12	13	14	14	14	15	2	6	5	5	5	This work	This work

Our composites can deliver ICE comparable to the best values in the literature of GeO_2-based anode materials, but at an areal loading about one order of magnitude higher. This is evident in **Table 4.2**, showing the best ICE in the literature, at about 75%, is also achieved in our composites, but at areal densities of 7 and 13 mg cm^{-2} compared to ~0.5 mg cm^{-2} of prior work. Importantly, this was achieved with no loss of the gravimetric capacity, which is 1716 mAh g^{-1} at 7 mg cm^{-2} and 1518 mAh g^{-1} at 13 mg cm^{-2} in our composites versus the best value of 1728 mAh g^{-1} in the literature for a composite of unknown (typically lower than ~1 mg cm^{-2}) areal loading. As a result, the areal and volume capacities of our materials are much higher, as shown in **Fig. 4.3**. This comparison included literature materials of amorphous GeO_x[2], composites of GeO_x/multi-walled CNT[12] and mesoporous Ge/GeO_2/Carbon[13], transition-metal-doped GeO_2, and nano-GeO_2/C. It also included nano and bulk GeO_2[14]. For example, Yang etc.[9] reported a 3D structured Ge composite that delivered 2.16 mAh cm^{-2} and 43 mAh cm^{-3}, respectively about one order and two orders of magnitude lower than those of our material. Note that literature did not always give volumetric loading; if this is the case we assumed a slurry-cast electrode on a 10 μm thick copper foil with a total thickness of 25 μm in the above comparison for the calculation of volumetric loading and capacity. While it is evident in **Fig. 4.3**, commercial graphite enjoys excellent areal loading, its capacities in gravimetric and volumetric terms are relatively low. In contrast, our GeO_2-based 3D composites easily outperform commercial graphite in these metrics of capacities and rates, while having slightly higher areal loading and comparable ICE of commercial graphite.

From a practical consideration, it is also important that our composites can

deliver unprecedentedly high areal and volumetric capacities at high rates. Specifically, at 0.2A g^{-1}, the composite offers 12.5 mAh cm^{-2} and 4320 mAh cm^{-3} at 7 mg cm^{-2}; at 13 mg cm^{-2}, it delivers 18.4 mAh cm^{-2} and 6487 mAh cm^{-3}. At 1 A g^{-1}, our composite at 7 mg cm^{-2} can provide 7 mAh cm^{-2} and 2469 mAh cm^{-3}. So, our composites can deliver up to about 6 times higher areal capacity and 30 times higher volumetric capacity than those of commercial graphite. With respect to cycle life, **Appendix 3 Fig. 3.1** shows that our composite delivers 4.5 mAh cm^{-2} after 700 cycles at 9 mA cm^{-2}, which is higher than what commercial graphite delivers, 1.9 mAh cm^{-2}, after 700 cycles at 2.75 mA cm^{-2}. Clearly, in all metrics, our composite easily outperforms commercial graphite and GeO_2-based anode materials in the literature.

4.4.2 Rationale and significance

The high areal loading (~ 10 mg cm^2) and initial coulombic efficiency (ICE>70%) obtained in our network composites are unprecedented for GeO_2 and GeO_2-based composites, and better than those achieved in the corresponding network composites containing SnO_2. To understand why it is possible for our network composites to have high ICE and reversible capacity at high loadings, we turn to the most likely source, namely the synergy between 3D graphene, amorphization, Fe dopant, oxygen-deficiency and ultra-thin carbon coating in the nanostructured composite. Among them, the highly superelastic 3D graphene construct must be most important because other elements in the above list were also present in some of the advanced GeO_2 and GeO_2 composites studied in the past. Such superelastic scaffold offers an effective route to high loading (thus allowing the composite behaving in a bulk manner) without affecting material processing, already tailored to be conducive to forming doped GeO_2 nanoparticles

with a highly disordered, even amorphous structure. These attributes present in the as-formed composite were all preserved after compressing the superelastic composite to render it high loading. As demonstrated by the research in the past decade, improving GeO_2 and similar materials (e.g., SnO_{2-x})[16] by imparting better conductivity, via doping and reduction, helps performance but by itself it cannot lead to high loading. By demonstrating that the network composites of both SnO_2 and GeO_2 combining a superelastic conductive scaffold with functionally invariant nano-oxide deposits can maintain a high ICE at high loading while improving all other electrochemical performance metrics, we have firmly established the viability of this approach. In fact, the higher ICE of GeO_2 compared to that of SnO_2 is also instructive, for GeO_2 has a smaller, though still very large volumetric expansion during the lithiation process. This suggests that the approach can work with with a very large volume expansion, albeit the efficacy may begin to diminish when the volumetric expansion becomes extreme.

To make use of all the volume available in the network composite while providing room for volumetric expansion during lithiation, clearly it is important not to introduce additional phases unnecessarily. Therefore, we have eschewed the approach in the literature of using extra phases ($CuGeO_3$, etc.) to improve electrical conductivity, because such phases unavoidably reduce the theoretical capacity given the fact that it is electrochemically less potent than GeO_2. Choosing Fe doping with the aid of hydrogen reduction is advantageous in this respect, for a relatively small amount of Fe doping suffices to enhance conductivity significantly. An amorphous GeO_2 helps too, for it homogenizes volumetric expansion while lowering the GeO_2 density only slightly (the lower density may actually provide some room to accommodate volumetric expansion.) Lastly, in our composite a very

thin carbon coating is achieved by CVD, which improves conductivity without significantly adding the volume. These material designs all help to obtain a high ICE and high areal and volumetric capacity, both initially and in cycling. With these superior properties and a clearly scalable processing route, GeO_2-containing network composites may offer a new alternative anode material to replace commercial graphite in practical lithium ion batteries.

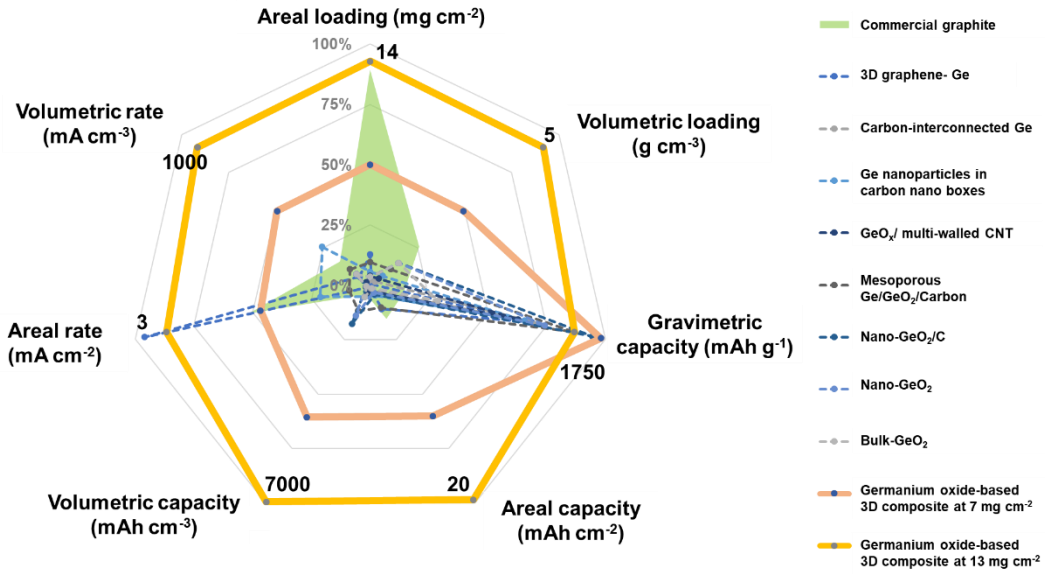

Figure 4.3 Comparison of properties with those of literature at 10th cycle. Thickness of 25 um assumed if the thickness of the electrode was not given in the literature.

4.5 Conclusions

- GeO_2-containing 3D graphene network composites can deliver high initial columbic efficiency (76.5%) and high areal and volumetric capacity at high loading (7 and 13 mg cm^{-2}). These properties place the material into the realm of practical applications in lithium ion batteries.
- These composites deliver about 6 times higher areal capacity and 30 times higher volumetric capacity than those of commercial graphite.

- After 700 cycles, these composites deliver an areal capacity of 4 mAh cm^{-2} at the current density of 9 mA cm^{-2}, compared to commercial graphite anodes that typically gives an area capacity of 2.1 mAh cm^{-2} at 2.75 mA cm^{-2} after same cycles.

References

1 Choi, S. H., Lee, S. J., Kim, H. J., Park, S. B. & Choi, J. W. J. J. o. M. C. A. Li 2 O–B 2 O 3–GeO 2 glass as a high performance anode material for rechargeable lithium-ion batteries. **6**, 6860-6866 (2018).

2 Wang, X.-L. *et al.* Amorphous hierarchical porous GeO x as high-capacity anodes for Li ion batteries with very long cycling life. **133**, 20692-20695 (2011).

3 Yu, Y. *et al.* Three-Dimensional (3D) Bicontinuous Au/Amorphous-Ge Thin Films as Fast and High-Capacity Anodes for Lithium-Ion Batteries. **3**, 281-285 (2013).

4 Ngo, D. T. *et al.* Mass-scalable synthesis of 3D porous germanium–carbon composite particles as an ultra-high rate anode for lithium ion batteries. **8**, 3577-3588 (2015).

5 Kim, C. H., Jung, Y. S., Lee, K. T., Ku, J. H. & Oh, S. M. J. E. A. The role of in situ generated nano-sized metal particles on the coulombic efficiency of MGeO3 (M= Cu, Fe, and Co) electrodes. **54**, 4371-4377 (2009).

6 Jin, S. & Wang, C. J. N. E. Synthesis and first investigation of excellent lithium storage performances of Fe2GeO4/reduced graphene oxide nanocomposite. **7**, 63-71 (2014).

7 Seng, K. H., Park, M. H., Guo, Z. P., Liu, H. K. & Cho, J. J. A. C. I. E. Self-assembled germanium/carbon nanostructures as high-power anode material for the lithium-ion battery. **51**, 5657-5661 (2012).

8 Dong, J. *et al.* Improved Li+ Storage through Homogeneous N-Doping within Highly Branched Tubular Graphitic Foam. **29**, 1603692 (2017).

9 Mo, R., Rooney, D., Sun, K. & Yang, H. Y. J. N. c. 3D nitrogen-doped graphene foam with encapsulated germanium/nitrogen-doped graphene yolk-shell nanoarchitecture for high-performance flexible Li-ion battery. **8**, 13949 (2017).

10 Ngo, D. T. *et al.* Carbon-Interconnected Ge Nanocrystals as an Anode with Ultra-Long-Term Cyclability for Lithium Ion Batteries. **24**, 5291-5298 (2014).

11 Li, D., Wang, H., Liu, H. K. & Guo, Z. J. A. E. M. A new strategy for achieving a high performance anode for lithium ion batteries—encapsulating germanium nanoparticles in carbon nanoboxes. **6**, 1501666 (2016).

12 He, W., Tian, H., Wang, X., Xin, F. & Han, W. J. J. o. M. C. A. Three-dimensional interconnected network GeO x/multi-walled CNT composite spheres as high-performance anodes for lithium ion batteries. **3**, 19393-19401 (2015).

13 Hwang, J. *et al.* Mesoporous Ge/GeO2/carbon lithium-ion battery anodes with high capacity and high reversibility. **9**, 5299-5309 (2015).

14 Seng, K. H., Park, M.-h., Guo, Z. P., Liu, H. K. & Cho, J. J. N. l. Catalytic role of Ge in highly reversible GeO2/Ge/C nanocomposite anode material for lithium batteries. **13**, 1230-1236 (2013).

15 Gallagher, K. G. *et al.* Optimizing areal capacities through understanding the limitations of lithium-ion electrodes. **163**, A138-A149 (2016).

16 Dong, W. *et al.* A robust and conductive black tin oxide nanostructure makes efficient lithium-ion batteries possible. **29**, 1700136 (2017).

Chapter 5 Fe_2O_3-based 3D composites as high areal and volumetric capacity anodes of lithium-ion batteries

5.1 Introduction

5.1.1 Overview

To find an alternative to commercial graphite anode that has a long cycle life but suffers from relatively low capacity for lithium ion batteries (LIB), many materials that can form lithium alloys have been studied intensively. One major problem of such materials is the huge volume expansion, up to 400%, during lithiation, which causes pulverization of the material and a rapid loss of capacity after cycling. In theory, materials that involve less severe (~100%) volume expansion could better withstand cycling and would be of interest if they still offer a large enough boost of capacity. One such material is Fe_2O_3, which has an expansion of 93% during the conversion reaction, a theoretical capacity of 1006 mAh g^{-1} and 5379 mAh cm^{-3}, compared to graphite's 372 mAh g^{-1} and 837 mAh cm^{-3}. In addition, Fe_2O_3 (red, with a band gap of 2.2 eV) is relatively conducting compared to some wide band-gap oxides (e.g., white SnO_2 with a band gap of 4 eV) that are being considered as potential anode materials, which should be advantageous in promoting uniform reactions and high-rate electrochemical processes. This study aims to incorporate Fe_2O_3 into superelastic 3D graphene to obtain a network composite, and to evaluate its potential as an alternative anode material replacing graphite. The knowledge gained could be transferable to other conversion type materials for use in either cathode (sulfur, FeF_3, etc.) or anode (Co_3O_4, CoN, FeP, etc.).

5.1.2 Literature review

Nanostructures have been used to improve the performance of iron oxide. It takes advantage of the reduced length scale in such structures, thus facilitating electron and ion transport. It also takes advantage of the distributed void space in the structures, thus accommodating volume expansion during the lithiation process. In **Table 5.1**, we summarize various forms of nanostructured Fe_2O_3 [1,2] that have been reported to deliver high gravimetric capacity close to the theoretical value. Among them, nano-Fe_2O_3 with hierarchical pores in a 3D framework is particularly notable as it can deliver high capacity at high rates.[3]

Table 5.1 Comparison of electrochemical properties for different morphologies of Iron oxide.

Dimensions	Morphological description	Electrochemical properties	References
0D	Fe_2O_3 nanoparticles	1100 mAh g^{-1} at 100 mA g-1 and 980 mAh g^{-1} at 1000 mA g-1	1
1D	Fe_2O_3 nanotubes	1000 mAh g^{-1} after 50 cycles at 0.5 C, 500–800 mAh g^{-1} at 1–2 C	2
	Fe_2O_3 nanowires	456 mAh g^{-1} after 100 cycles at 0.1 C	4
2D	Fe_2O_3 nanosheets	700 mAh g^{-1} after 80 cycles at a current density of 65 mA g^{-1}	5

3D	3D Hierarchical Porous α-Fe_2O_3	877.7 mAh g^{-1} at 2.01 A g^{-1} after 1000 cycles	3

Another common strategy is to combine Fe_2O_3 with carbon materials to improve electrical conductivity, which often benefits structural integrity and cycling performance. For example, Ruoff etc.[6] reported a rGO-Fe_2O_3 composite in which Fe_2O_3 nanoparticles are uniformly distributed on rGO nanosheets, delivering a reversible capacity of 982 mAh g^{-1} at 100 mA g^{-1}. Encapsulating Fe_2O_3 inside carbon materials has also been explored. For example, coating Fe_2O_3 by carbon via the pyrolysis of organic precursors such as dopamine and glucose[7,8] can improve rate performance and prevent pulverization and aggregation during cycling, in addition to providing a relatively robust substrate to the solid electrolyte interphase (SEI) film thus reducing capacity decay caused by the repeated growth of such film. Hierarchical composite structures of Fe_2O_3 and 3D carbon frameworks have also been shown[9-11] to endow faster electrolyte and ion transport thus better rate capability. For example, such composite reported by Wei et al. achieved 363 mAh g^{-1}at 4800 mA g^{-1}.

Despite the progress in improving the gravimetric capacity and rate performance, none of these “advanced” electrodes are practical because materials of nanostructures are fundamentally low loading, making it impossible to obtain high energy density anodes. In this chapter, we will incorporate Fe_2O_3 into superelastic 3D graphene to form a functionally invariant network composite, which can be later compressed into a high-density electrode without affecting its gravimetric electrochemical performance.

5.2 Experimental procedures

5.2.1 Synthesis of Fe_2O_3-based 3D composite

To render the 3D graphene monolith hydrophilic, it was first immersed in nitric acid and heated to 100^{o}C for 12 h, then dried. Next, 0.012 mol $FeCl_3$ (Alfa Aesar) was dissolved in a mixture solution of 10 ml ethylene glycol. In this solution the hydrophilic 3D graphene monolith was immersed for 2 h at room temperature to become thoroughly soaked. After that, the soaked 3D graphene and the solution was sealed in an autoclave for hydrothermal reaction at 150^{o}C for 2 h. After hydrothermal reaction, the 3D graphene was removed, rinsed by DI water and freeze-dried for 6 h. Thus dried 3D graphene remained as a monolith, and it was finally subject to calcination in air at 350^{o}C for 1 h.

5.2.2 Characterization

5.2.2.1 Material characterization

Scanning electron microscopy (SEM) images were obtained in a field emission Magellan 400 microscope (FEI Company). Transmission electron microscopy (TEM), high angle annular dark field (HAADF) imaging, electron energy loss spectroscopy (EELS, Gatan), and elemental mapping were conducted in a JEOL 2100F microscope operated at 200 kV. Nitrogen adsorption-desorption isotherms at 77 K were measured in a Micromeritics Tristar 3000 system using vacuum-degassed samples (200 °C for 12 h). These isotherms were used to calculate (*a*) the specific surface area by the Brunauer-Emmett-Teller (BET) method and (*b*) the pore volume and pore size by the Barrett−Joyner−Halenda (BJH) method. Small and wide-angle X-ray diffraction was performed in a Brucker D8 powder X-ray diffractometer using Cu *K*α radiation. Binding energies were calibrated using the 284.8 eV peak of delocalized sp^2-hybridized adventitious

carbon. Raman spectra were collected in a Thermal Dispersive Spectrometer using a 10 mW laser with an excitation wavelength of 532 nm. The mass ratio of Fe_2O_3 in Fe_2O_3-based 3D composite was determined by thermogravimetric analysis (TGA) at a heating rate of 10^oC min^{-1} in the temperature range of 25-900^oC in air using a thermal analyzer (NETZSCH STA 449 F3). Contact angle of water was measured with a Data-Physics OCA 20 goniometer. Compression tests were conducted using rectangular monoliths with a height-to-width ratio of 0.8 in a single-column mechanical testing system (Instron-5566) at a constant loading speed of 2 mm min^{-1}.

5.2.2.2 Electrochemical measurement

The as prepared Fe_2O_3-based 3D composite monolith was sliced into disks for later use. They could be directly used as free-standing electrode that is free of binder and additional conductive additive or current collector. This was used as the working electrode (anode) against a counter electrode of lithium foils (China Energy Lithium Co., Ltd) in the half-cell configuration, in conjunction with a polymer membrane (Celgard) separator and $LiPF_6$ electrolyte in a 50:50 w/w mixture of dimethyl carbonate (DMC) and ethyl carbonate (EC). This configuration was assembled in a 2016 coin cell in argon in a glovebox with less than 1 ppm oxygen and moisture. Galvanostatic charge and discharge measurements were conducted using a LAND-CT 2001C testing system within a voltage window of 0.01 V to 3.0 V. The rate capability was investigated by changing the current density from 0.2 A g^{-1} to 2 A g^{-1}. Cyclic voltammetry (CV) was conducted by an automated electrochemical workstation (CHI660E) at a scan rate of 0.2 mV/s in the voltage window of 0.01 V to 3 V.

5.3 Results

5.3.1 Materials characterization

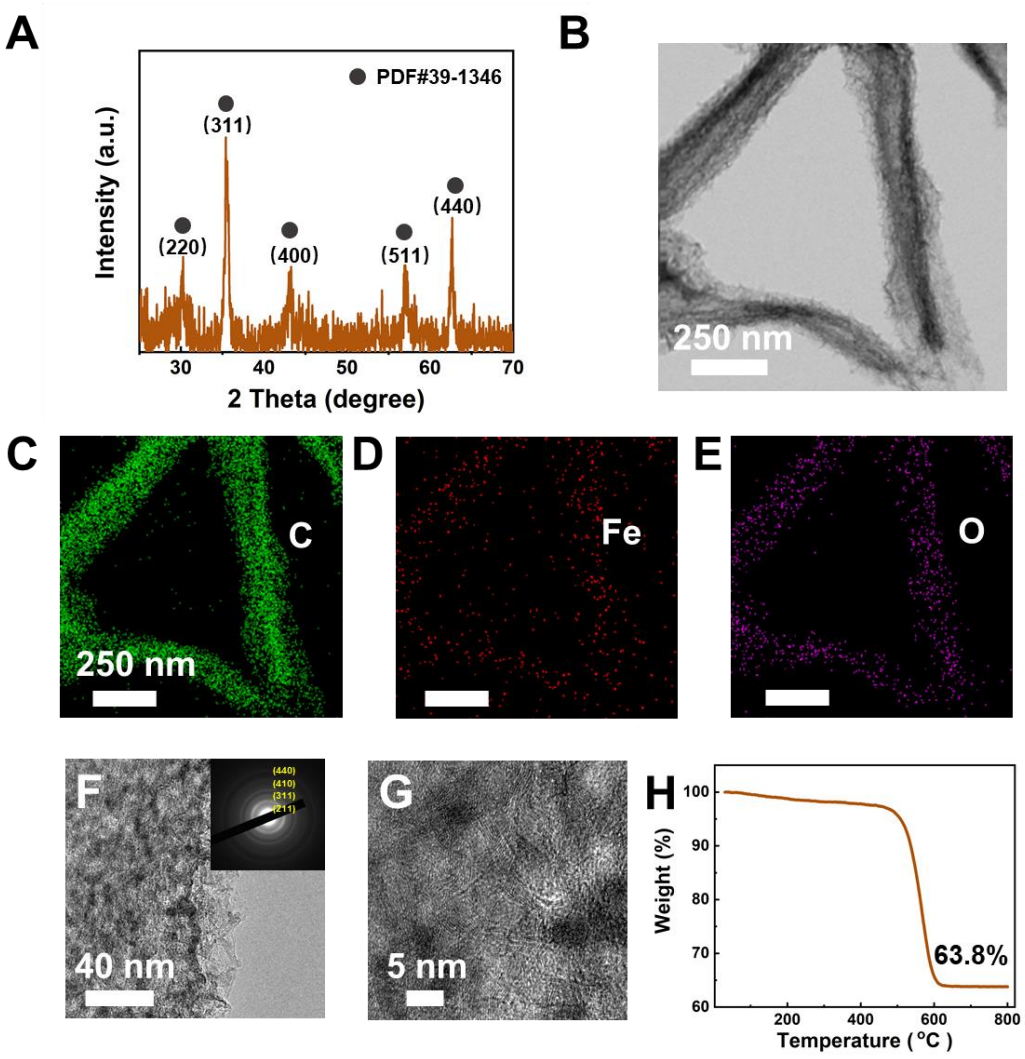

Figure 5.1 Materials characterization of Fe_2O_3-based network composite. **(A)** X-ray diffraction pattern with Fe_2O_3 (PDF#39-1346) peaks. **(B)** Transmission electron microcopy (TEM) image, **(C~E)** the mapping of C, Fe and O. **(F)** High-resolution TEM image with selected area electron diffraction pattern of Fe_2O_3 in the inset. **(G)** High-resolution TEM image. **(H)** Thermogravimetric analysis spectrum.

Iron oxide as Fe_2O_3 (PDF #39-1346) was first confirmed by X-ray diffraction in **Fig. 5.1A.** Its precipitation was uniform, as shown by bright field TEM in **Fig. 5.1B** in which 3D graphene is homogeneously coated by black particles. Coating

uniformity was further confirmed by elemental mapping in **Fig. 5.1 C-E**, which reveals a uniform distribution of O and Fe on C. The edge of a graphene tube in **Fig. 5.1F** is also evenly coated by Fe_2O_3. From **Fig. 5.1G**, the primary particle size of Fe_2O_3 is found to be 5~8 nm (dark region), and the particles are partitioned by many small pores (<3 nm) that appear as white spots. The SAED pattern in the inset of **Fig. 5.1F** is consistent with the diffraction lines of (211), (311), (410) and (440) of Fe_2O_3. To complete the characterization, we determined the weight fraction of Fe_2O_3 oxides by thermal gravimetric analysis (TGA) (**Fig. 5.1 I**), which gave 63.8%.

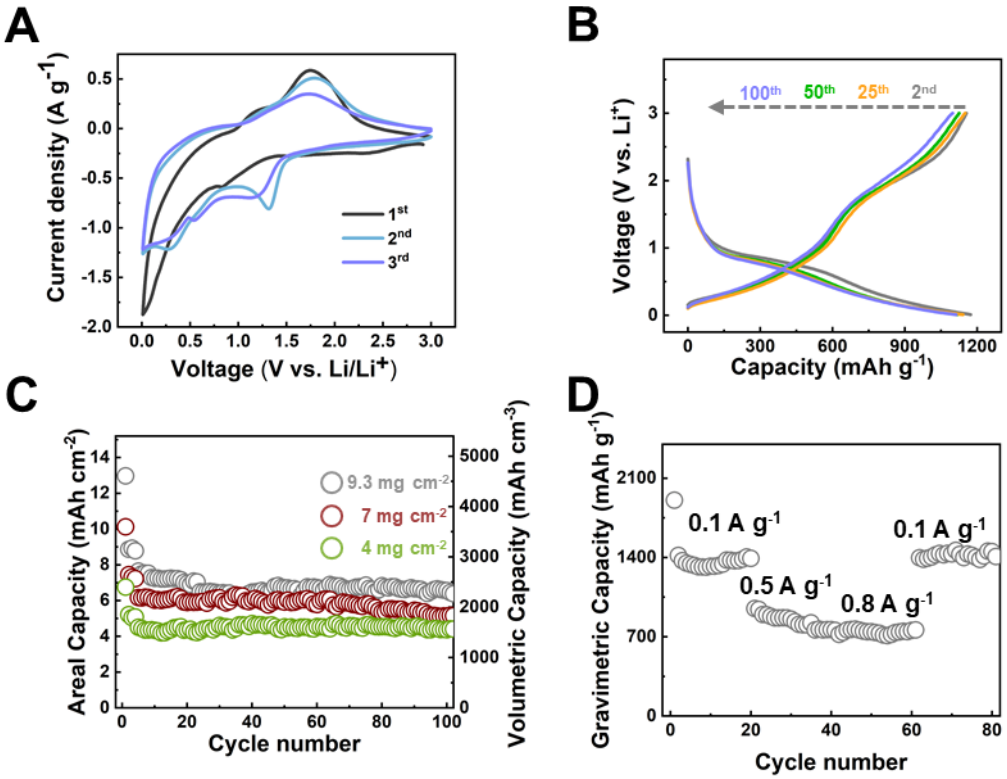

Figure 5.2 Electrochemical performance of Fe_2O_3-based network composite with 4 mg cm^{-2} in **(A)** cyclic voltammetry (first 3 cycles) an **（B)** successive charge-discharge curves at 0.5 A g^{-1}. **(C)** Areal and volumetric capacity vs. cycle numbers of network composites

with 4, 7 and 9.3 mg cm^{-2} at 0.5 A g^{-1}. **(D)** Rate performance of network composites with 7 mg cm^{-2} at 0.1, 0.5 and 0.8 A g^{-1}.

5.3.2 Electrochemical performance

In cyclic voltammetry (**Fig. 5.2A**), we first evaluated the reversible conversion reaction of Fe_2O_3-based network composite by the peaks centered at 1.2 V and 1.8 V, corresponding to the reduction of Fe_2O_3 and the oxidation of iron metal. The good reversibility coincides with the high initial coulombic efficiency (ICE) ranging from 77.1% to 68.9% in **Appendix 4 4.1** for Fe_2O_3-based network composites at 4, 7 and 9.3 mg cm^{-2}. In comparison, the ICE of nano-Fe_2O_3 is 42%, and a Fe_2O_3/graphene composite at a loading of 1.03 mg cm^{-2} is 65%.[12] The capacity in **Fig. 5.2B** of a 4 mg cm^{-2} network composite charged/discharged at 0.5 A g^{-1} for 100 cycles is maintained at above 1100 mAh g^{-1}, with corresponding areal and volumetric capacities of 4.4 mAh cm^{-2} and 1550 mAh cm^{-3}, respectively. At higher loadings and 0.5 A g^{-1} (after using 0.2 A g^{-1} in the first 5 cycles), shown in **Fig. 5.2C**, the areal and volumetric capacities after 100 cycles are respectively 6.6 mAh cm^{-2} and 2328 mAh cm^{-3} at 9.3 mg cm^{-2}, and 5.2 mAh cm^{-2} and 1827 mAh cm^{-3} respectively at 7 mg cm^{-2}. The above areal capacity at 9.3 mg cm^{-2} is 2 times higher than that of commercial graphite anodes, while the volumetric capacity is 8 times higher. The rate performance is evaluated in **Fig. 5.2D,** where Fe_2O_3- based network composite with the loading of 7 mg cm^{-2} shows a gravimetric capacity of 1367 mAh g^{-1}, 805 mAh g^{-1} and 720 mAh g^{-1} at the current density of 0.1 A g^{-1}, 0.5 A g^{-1} and 0.8 A g^{-1}, respectively.

5.4 Discussion

Our results show that the Fe_2O_3-based network composites have superior areal and volumetric capacities, and they enjoy good initial coulombic efficiency at high loadings. In this section, we will further compare and rationalize them with prior work.

5.4.1 Comparison with literature and commercial graphite

Fe_2O_3-based network composites enjoy high initial coulombic efficiency (ICE) of 77.2% at an areal loading of 4 mg cm^{-2}, 75.4% at 7 mg cm^{-2}, and 68.9% at 9.3 mg cm^{-2}. These values are higher than or comparable to the best value in the literature as shown in **Table 2**, yet they are achieved at a loading up to one order of magnitude higher than the highest loading in the previous work (1 mg cm^{-2}) [13]. Significantly, the high loading of Fe_2O_3 in our composites does not undermine the gravimetric capacity, which remains at 714 mAh g^{-1} at 9.3 mg cm^{-2} and 3.25 g cm^{-3} under 0.5 A g^{-1}, whereas the highest loaded electrode in the literature had only 1 mg cm^{-2} and 1.35 g cm^{-3}, at which it had 650 mAh g-1 under 0.2 A g^{-1}. [13] In addition, our composites can simultaneously achieve high areal and volumetric loading, of 9.3 mg cm^{-2} and 3.25 g cm^{-3}, respectively, whereas in the literature the relatively high areal loading of 3.8 mg cm^{-2} is accompanied by a modest volumetric loading of 0.76 g cm^{-3}, indicating the existence of a large amount of large pores.[14] Consequently, the areal and volumetric capacities of our composites easily exceed those of "porous Fe_2O_3/3D graphene"[14], "compact Fe_2O_3/graphene"[13], "Fe_2O_3/$LiBH_4$"[15], Fe_3O_4/polypyrrole-cage"[16], " Fe_2O_3@3D CNT"[17], and "Fe_2O_3-CNT web."[18] They also outperform commercial graphite: the areal capacity of our composite is 2 times higher than that of commercial graphite, while the volumetric

capacity is about 10 times higher than that of commercial graphite. The rate performance is another important metric for practical applications. On a mass basis, the current density of our composite is comparable to that of the literature (0.5 A g^{-1} vs. 0.1~0.2 A g^{-1}), however, the areal and volumetric current densities of our composites are up to 40 times and 25 times, respectively, higher than those of Fe_2O_3-based anodes in the literature, and 3 times and 10 times, respectively, better than those of commercial graphite.

In **Fig. 5.3**, we summarize the performance of Fe_2O_3-based anodes in the literature, commercial graphite and our Fe_2O_3-based network composite at the 100^{th} cycle. It is evident that the literature materials only excel in gravimetric capacity, which is close to the theoretical value, but they are rather poor in rate performance and in areal and volumetric capacities. While commercial graphite enjoys excellent areal loading and ICE, its capacities in gravimetric and volumetric terms are relatively low. In contrast, our composites easily outperform commercial graphite and Fe_2O_3-based materials in the literature in those metrics of capacities and rates, while having comparable areal loading and ICE of commercial graphite.

Table 5.1 Comparison of electrochemical performance metrics of our network composite, various Fe_2O_3-based anode materials in the literature and commercial graphite

Materials	Porous Fe_2O_3/ 3D graphene	compact Fe_2O_3/graphene	Fe_2O_3/$LiBH_4$	Fe_3O_4/ Polypyrrole -cage	Fe_2O_3 @3D CNT	Fe_2O_3-CNTweb	Commercial graphite	Fe_2O_3-based network composite		
Areal rate (mA cm^{-2})	0.76	0.2	0.15	0.3	0.15	0.12	1.55	4.65	3.5	2
Areal loading (mg cm^{-2})	3.8	1	1.5	1.5	1.5	1.2	12.5	9.3	7	4
Areal capacity (mAh cm^{-2})	4.29	0.62	1.68	1.425	1.0875	0.99	3.06	6.6	5.2	4.4

Volumetric loading(g cm^{-3})	0.76	1.35	0.6	0.6	0.6	0.6	1.289	3.28	2.47	1.41
Volumetric capacity (mAh cm^{-3})	658	878	672	570	435	495	286	2328	1827	1550
Volumetric rate (mA cm^{-3})	152	270	60	120	60	60	159.8	1640	1235	705
Initial coulombic efficiency (%)	63	66	76	75	65	71	80	69	75	77
Gravimetric rate (A g^{-1})	0.2	0.2	0.1	0.2	0.1	0.1	0.124	0.5	0.5	0.5
Gravimetric capacity	1129	650	1120	950	725	825	244.8	714	744	1138

(mAh g^{-1})								
References	14	13	15	16	17	18	19	This work

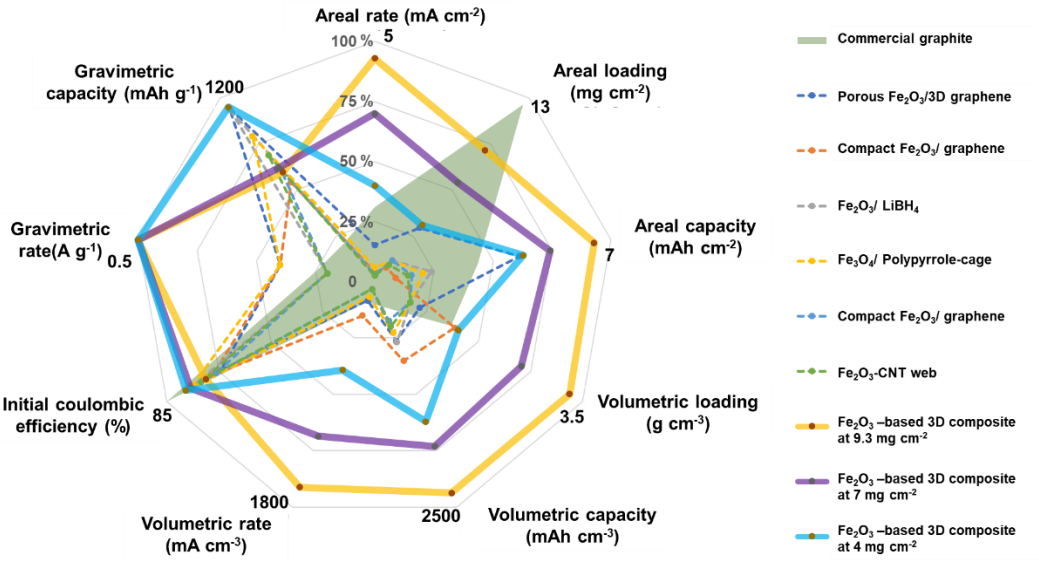

Figure 5.3 Comparison of properties of our composite, commercial graphite and various Fe_2O_3-based materials in the literature, after 100 cycle. Thickness of 25 μm assumed if the thickness of the electrode was not specified in the literature.

5.4.2 Rationale and significance

The most important reason for the outperformance of our composites is clearly the utilization of superelastic conductive 3D graphene and the robust adhesion of oxide nanoparticles onto such network. This allows functional invariance despite the compression of the overall composite, because after the compression the local length scales critical for electron and ion/electrolyte transport and reactions remain unchanged, and a narrower though still open channel uniformly permeating the entire network still exists. Having the same length scales and not much suffering from interparticle interference, it is then possible to achieve a relatively high ICE of 77.2% and good cycle performance by taking advantage of the high reactivity of nanomaterials, good rate performance at high loading, and the abundant mesoscale accommodating sites availed by the 3D

graphene network for the volume expansion of Fe_2O_3 during repeated lithiation. This is unlike the advanced Fe_2O_3 electrodes and their composites in the literature, which despite their complicated nanoporous and hierarchical structures still contain a large amount of large pores and void space that are poorly utilized in bettering performance. As a result, in order to remain functional, they are forced to use low areal and volumetric loading, generally less than 1 mg cm^{-2} and 1.5 g cm^{-3}, respectively.

As a purely conversion-type material without alloying reactions, Fe_2O_3 has a volume change of 93%, which is relatively modest, much less than that of SnO_2 (376%) and GeO_2 (306%). The smaller volume change of Fe_2O_3 correlates to smaller areal and volumetric capacities of 6.6 mAh cm^{-2} and 2328 mAh cm^{-3}, respectively, which is about 3/4 and 1/3, respectively, of those of SnO_2 (18.4 mAh cm^{-2} and 6487 mAh cm^{-3}) and GeO_2 (9 mAh cm^{-2} and 3000 mAh cm^{-3}). This study on Fe_2O_3-based network composites is nevertheless useful in that it provides a case study for the conversion type of materials, most of them have even less volume change (~100%) and should have even fewer difficulties in achieving an extreme compression ratio in their network composites. One such material could be sulfur, which may be suitable for practical batteries.

Lastly, Fe_2O_3 is much cheaper than GeO_2. As a rule of thumb, one pound of steel is just $0.4, and the price of zinc is about 3-4 times of that, while the price of ZnO is only 1/300 that of GeO_2. This makes Fe_2O_3-based electrodes with much better performance a practical alternative to the commercial graphite anode.

5.5 Conclusions

- Fe_2O_3-3D graphene network composites deliver high initial columbic efficiency (77.2% to 68.9 %) at high loading (4 mg cm^{-2} to 9.3 mg cm^{-2}), which are comparable to the best initial coulombic efficiency values in the literature despite a much higher loading in our composites.
- The areal capacities of these composites are up to 10 times higher than those of Fe_2O_3 based materials in the literature, and about 2 times higher than that of commercial graphite. In terms of volumetric capacity, the values are up to 5 times higher than those in the literature and about 10 times higher than that of commercial graphite.
- In addition to higher areal and volumetric capacity, the composites enjoy high areal and volumetric rates, up to 40 times and 25 times, respectively, higher than those of Fe_2O_3 in the literature. In these measures, they also outperform commercial graphite by 3 times (in areal rates) and 10 times (in volumetric rates).

References

1 Tang, J. *et al.* Pushing the theoretical capacity limits of iron oxide anodes: capacity rise of γ-Fe 2 O 3 nanoparticles in lithium-ion batteries. **4**, 18107-18115 (2016).

2 Wang, Z., Luan, D., Madhavi, S., Li, C. M. & Lou, X. W. D. J. C. C. α-Fe 2 O 3 nanotubes with superior lithium storage capability. **47**, 8061-8063 (2011).

3 Cao, K. *et al.* 3D hierarchical porous α-fe2o3 nanosheets for high-performance lithium-ion batteries. **5**, 1401421 (2015).

4 Liu, H., Wexler, D., Wang, G. J. J. o. A. & Compounds. One-pot facile synthesis of iron oxide nanowires as high capacity anode materials for lithium ion batteries. **487**, L24-L27 (2009).

5 Reddy, M. *et al.* α-Fe2O3 nanoflakes as an anode material for Li-ion batteries. **17**, 2792-2799 (2007).

6 Zhu, X., Zhu, Y., Murali, S., Stoller, M. D. & Ruoff, R. S. J. A. n. Nanostructured reduced graphene oxide/Fe2O3 composite as a high-performance anode material for lithium ion batteries. **5**, 3333-3338 (2011).

7 Lei, C. *et al.* Dopamine as the coating agent and carbon precursor for the fabrication of N-doped carbon coated Fe 3 O 4 composites as superior lithium ion anodes. **5**, 1168-1175 (2013).

8 Zhang, W. M., Wu, X. L., Hu, J. S., Guo, Y. G. & Wan, L. J. J. A. F. M. Carbon coated Fe3O4 nanospindles as a superior anode material for lithium-ion batteries. **18**, 3941-3946 (2008).

9 Guan, C. *et al.* Confined Fe2O3 Nanoparticles on Graphite Foam as High-Rate and Stable Lithium-Ion Battery Anode. **33**, 487-492 (2016).

10 Li, M. *et al.* Scalable Dry Production Process of a Superior 3D Net-Like

Carbon-Based Iron Oxide Anode Material for Lithium-Ion Batteries. **56**, 12649-12653 (2017).

11 Wei, W. *et al.* 3D graphene foams cross-linked with pre-encapsulated Fe3O4 nanospheres for enhanced lithium storage. **25**, 2909-2914 (2013).

12 Ye, J., Zhang, J., Wang, F., Su, Q. & Du, G. J. E. A. One-pot synthesis of Fe2O3/graphene and its lithium-storage performance. **113**, 212-217 (2013).

13 Li, Z. *et al.* Twin-functional graphene oxide: compacting with Fe2O3 into a high volumetric capacity anode for lithium ion battery. **6**, 98-103 (2017).

14 Jiang, T. *et al.* Porous Fe2O3 nanoframeworks encapsulated within three-dimensional graphene as high-performance flexible anode for lithium-ion battery. **11**, 5140-5147 (2017).

15 Cao, Y. *et al.* A new strategy to effectively suppress the initial capacity fading of iron oxides by reacting with LiBH4. **27**, 1700342 (2017).

16 Liu, J., Xu, X., Hu, R., Yang, L. & Zhu, M. J. A. E. M. Uniform hierarchical Fe3O4@ polypyrrole nanocages for superior lithium ion battery anodes. **6**, 1600256 (2016).

17 Bhattacharya, P., Suh, D. H., Nakhanivej, P., Kang, Y. & Park, H. S. J. A. F. M. Iron Oxide Nanoparticle-Encapsulated CNT Branches Grown on 3D Ozonated CNT Internetworks for Lithium-Ion Battery Anodes. **28**, 1801746 (2018).

18 Bhattacharya, P., Kota, M., Suh, D. H., Roh, K. C. & Park, H. S. J. A. E. M. Biomimetic Spider-Web-Like Composites for Enhanced Rate Capability and Cycle Life of Lithium Ion Battery Anodes. **7**, 1700331 (2017).

19 Gallagher, K. G. *et al.* Optimizing areal capacities through understanding the limitations of lithium-ion electrodes. **163**, A138-A149 (2016).

Chapter 6 ZnO-based 3D composites as high areal and volumetric capacity anodes of lithium-ion batteries

6.1 Introduction

6.1.1 Overview

New practical anode materials as an alternative to commercial graphite anode must have high volumetric and areal capacity in addition to low cost. ZnO as an earth abundant material is priced at about 1/300 of GeO_2 (3 $/kg vs. 1000 $/kg), thus comparable to that of commercial graphite. Its theoretical gravimetric and volumetric capacities are 988 mAh g^{-1} and 5533 mAh cm^{-3}, respectively, much higher than graphite's 372 mAh g^{-1} and 837 mAh cm^{-3}. These attributes have made ZnO an interesting potential anode material for lithium ion batteries (LIB).

However, there are fundamental issues of using ZnO for electrodes. One is its high resistivity, 1 Ω m vs graphite's 10^{-8} Ω m, because ZnO has a large band gap. Another is the volume change of 153% during the alloying and conversion reactions to incorporate lithium. Although already much smaller than seen in SnO_2 (376%) and GeO_2 (306%), the volume expansion/contraction during the alloying and conversion reactions can still cause severe pulverization of ZnO particles and the loss of its electrical contact. Lastly and partly related to the volume change, which causes relocation, there is progressive coarsening of Zn grains, which diminishes the reversibility of Li_2O, resulting in a severe capacity decay within a few cycles.

This chapter explores the possibility of using a network composite of ZnO and 3D graphene to partially mitigate the above problems and to achieve a loading and capacity high enough for using such composite in practical LIB, hopefully

replacing commercial graphite anodes. To do so, we will employ the best practice in the prior work to form ZnO nanoparticles and to deposit them onto a superelastic, highly conductive 3D graphene backbone. The resulting composite will be compared with other network composites that similarly incorporate nanoparticles of other oxides capable of conversion and alloying reactions, namely SnO_2 and GeO_2, to evaluate the utility of this approach.

6.1.2 Literature review

Nanosized ZnO has a shorter length for electron and ion transport and because of it nanostructured ZnO anodes have higher capacities. For example, Park et al.[1] reported ZnO hollow nanotubes with ultra-thin walls that gave a capacity of 386 mAh g^{-1} after 50 cycles; this compared to 83 mAh g^{-1} of bulk solid ZnO rods. Similarly, nanosheets of ZnO have a capacity of 400 mAh g^{-1} after 100 cycles vs. 170 mAh g^{-1} after 50 cycles for commercial ZnO powders.[2] Adding carbon materials to form a ZnO-based composite has also been widely used to improve electrical conductivity. For example, ZnO self-assembled with reduced graphene oxide (rGO) was reported to deliver an enhanced electrical conductivity of 1.32 $\times 10^{-1}$ S cm^{-1}, which in turn led to a capacity of 753 mAh g^{-1} after 65 cycles under 100 mA g^{-1} compared to pure ZnO's capacity of less than 100 mAh g^{-1}.[3] Composites with derivatives of graphene/carbon materials are likewise attractive. A ZnO-loaded porous carbon composite with ZnO nanoparticles placed within the pores of a carbon host reached a capacity of 654 mAh g^{-1} after 100 cycles, whereas without porous carbon the same ZnO only gave 125 mAh g^{-1}.[4] Similarly, Ahn etc. prepared amorphous mesoporous carbon fibers with embedded ZnO quantum dots, and obtained 832 mAh g^{-1} after 100 cycles under 100 mA g^{-1}.[5]

In the above efforts on composites, although the overall conductivity is

greatly improved by the addition of conductive carbon, the conductivity of ZnO is not. Doping ZnO with transition metal or otherwise aliovalent cations, on the other hand, is known to endow better conductivity to ZnO. Passerini et al. showed that Fe and Co doping can make ZnO of the wurtzite structure better conducting, thus improve the reversible capacity to 900 mAh g^{-1}, which is more than twice the value of commercial graphite.[6] In addition, better conductivity helps stabilize metallic Zn grains and prevent them from coarsening. This is also evidenced by the improvement in the initial coulombic efficiency (ICE) to reach 70%,[6] compared to that of undoped ZnO that generally falls in 50%- 60%.

Another advantage of nanostructure engineering is in dealing with pulverization caused by the 153% volume expansion of ZnO. Duan et al. developed ZnO quantum dots and embedded them in porous carbon on a 3D carbon cloth.[7] By providing abundant extra space at the meso and nano scales to accommodate the volume expansion, the composite delivered 700 mAh g^{-1} under 500 mA g^{-1} after 100 cycles. Nevertheless, none of the above capacities was demonstrated at high loading. Yet high loading is mandatory for any practical electrode. Therefore, we hope to explore the use of network composites, of doped nano ZnO and superelastic 3D graphene, to transform ZnO into a high loading, high performance practical electrode.

6.2 Experimental procedures

6.2.1 Synthesis of ZnO-based 3D composites

To make the composite, we started with a 3D graphene monolith. To render the 3D graphene monolith hydrophilic, it was first immersed in nitric acid and heated to 100^{o}C for 12 h, then dried. Next, 0.001 mol $FeCl_3$ (Alfa Aesar) and 0.09

mol $ZnCl_2$ (Alfa Aesar) were dissolved in a mixture solution of 8 ml glycerol and 2 ml DI water. In this solution the hydrophilic 3D graphene monolith was immersed for 2 h at room temperature to become thoroughly soaked. After that, the soaked 3D graphene along with the solution was sealed in an autoclave for hydrothermal reaction at 100^{o}C for 4 h. The reacted 3D graphene monolith was removed, rinsed by DI water and freeze-dried for 6 h, and the dry monolith was finally subject to calcination in air at 350^{o}C for 1 h.

6.2.2 Characterization

6.2.2.1 Material characterization

Scanning electron microscopy (SEM) images were obtained in a field emission Magellan 400 microscope (FEI Company). Transmission electron microscopy (TEM), high angle annular dark field (HAADF) imaging, electron energy loss spectroscopy (EELS, Gatan), and elemental mapping were conducted in a JEOL 2100F microscope operated at 200 kV. Small and wide-angle X-ray diffraction was performed in a Brucker D8 powder X-ray diffractometer using Cu *K*α radiation. X-ray photoelectron spectra (XPS) were collected in a Thermo Escalab 250Xi with Al *K*α radiation (hν =1,486.6 eV). Binding energies were calibrated using the 284.8 eV peak of delocalized sp^2-hybridized adventitious carbon. Raman spectra were collected in a Thermal Dispersive Spectrometer using a 10 mW laser with an excitation wavelength of 532 nm. The mass ratio of ZnO in ZnO-based 3D composites was determined by thermogravimetric analysis (TGA) at a heating rate of 10^{o}C min^{-1} in the temperature range of 25-900^{o}C in air using a thermal analyzer (NETZSCH STA 449 F3).

6.2.2.2 Electrochemical measurement

The as prepared ZnO-based 3D composite, still a monolith which we call a

network composite, was sliced into disks for later use. One or more pieces of these disks were directly used as a free-standing electrode (the working electrode, the anode); such electrode is free of binder and additional conductive additive or current collector. The counter electrode was made of lithium foils (China Energy Lithium Co., Ltd), and the set up was in the half-cell configuration in conjunction with a polymer membrane (Celgard) separator and $LiPF_6$ electrolyte in a 50:50 w/w mixture of dimethyl carbonate (DMC) and ethylene carbonate (EC). This configuration in a 2016 coin cell was assembled in argon in a glovebox with less than 1 ppm oxygen and moisture. Galvanostatic charge and discharge measurements were conducted using a LAND-CT 2001C testing system within a voltage window of 0.01 V to 3.0 V. The rate capability was investigated by changing the current density from 0.2 A g^{-1} to 2 A g^{-1}. Cyclic voltammetry (CV) was conducted using an automated electrochemical workstation (CHI660E), typically performed at a scan rate of 0.2 mV/s in the voltage window of 0.01 V to 3 V.

Table 6.1 Summary of elemental analysis of ZnO- based 3D composites.

Elements	Atomic ratio (%)
O	56.5
Zn	36.7
Fe	6.8

6.3 Results

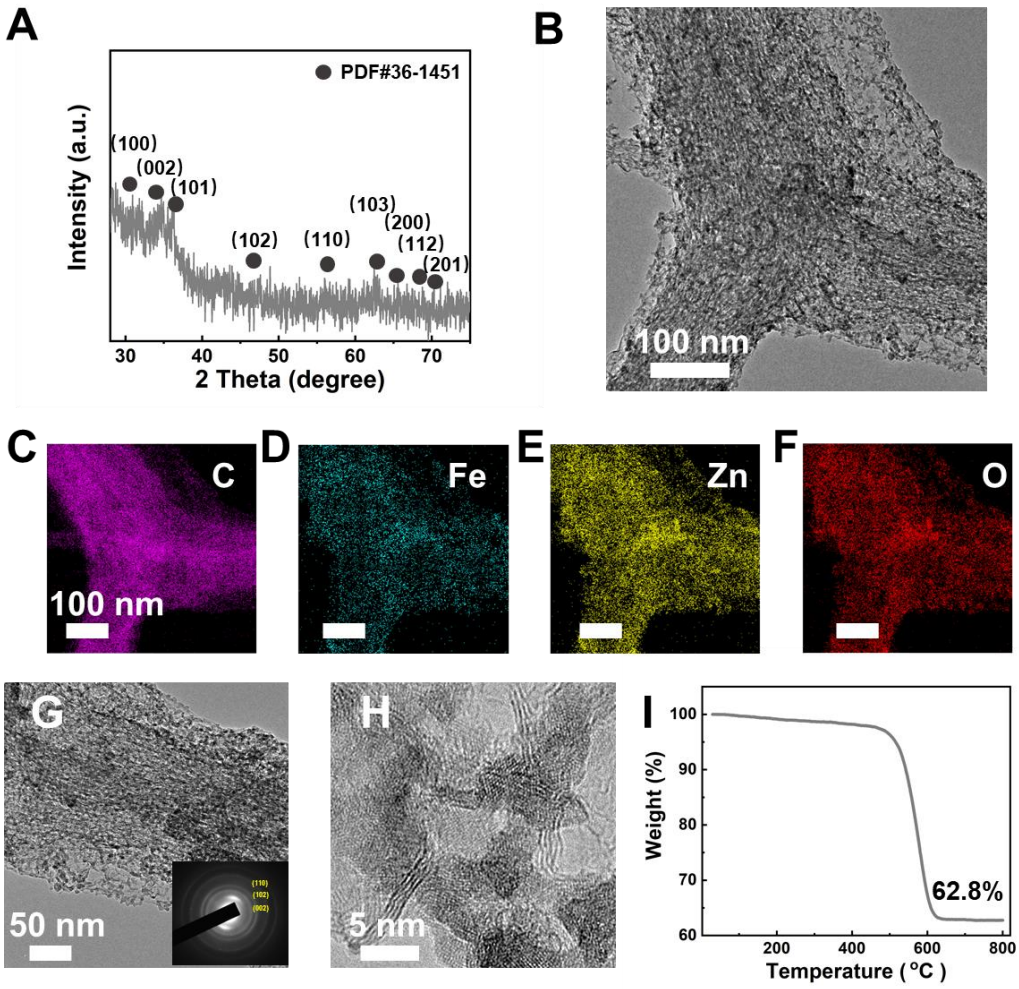

Figure 6.1 Materials characterization of ZnO-based network composite. **(A)** X-ray diffraction pattern with ZnO (PDF#36-1451) peaks, **(B)** transmission electron microcopy (TEM) image, **(C~F)** mapping of C, Fe, Zn and Zn, **(G)** TEM image with selected area electron diffraction pattern of ZnO in the inset, **(H)** high-resolution TEM image, and **(I)** thermogravimetric analysis spectrum.

6.3.1 Material Characterization

For doping, the Fe/(Zn+Fe) ratio was set at around 15 mol. % by controlling the amount of $ZnCl_2$ and $FeCl_3$ in the solution. The actual ratio was determined by energy dispersive spectrum analysis summarized in **Table 6.1,** which gives 36.7%

Fe and 6.8 % Zn. Thus determined 15.6 mol. % is comparable to what was reported in the literature for Fe doping[6].

The X-ray diffraction pattern (**Fig. 6.1A**) of the composite reveals the phase of ZnO (PDF#36-1451). Thanks to the hydrophilic treatment of 3D graphene, nanoparticle coating is uniform throughout the 3D graphene backbone, as evident in TEM (**Fig. 6.1B**). The uniform distribution of ZnO is confirmed by elemental mapping, shown in **Fig. 6.1C-F**: Fe, Zn and O are all evenly dispersed in a background of elemental C reflecting the 3D graphene backbone. The hydrothermal reaction apparently left porosity inside the coating, in which pores of 3-5 nm dia. are seen among relatively uniform ZnO nanoparticles in **Fig. 6.1G** and **Fig. 6.1H**. These nanoparticles (**Fig. 6.1H**) have a diameter of 3-8 nm, which is consistent with the line broadening of diffraction peaks seen in **Fig. 6.1A**. In the inset of **Fig. 6.1G**, the electron diffraction pattern further confirms the presence of crystalline ZnO with its (002), (102) and (110) diffraction rings, but its prominent white halo also reveals the coexistence of amorphous regions in the composite. Such crystalline-amorphous mixture is not surprising in view of the very low calcination temperature of 350^{o}C. By TGA analysis (**Fig. 6.1I**), we also determined the weight fraction of Fe-doped zinc oxide in the composite was 62.8%.

6.3.2 Electrochemical performance

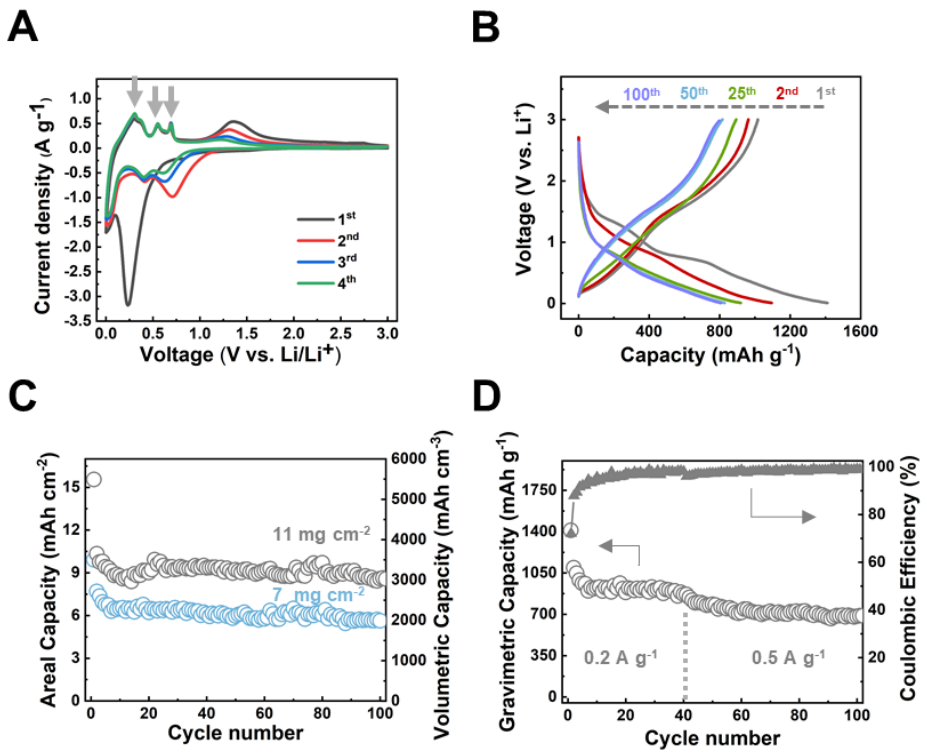

Figure 6.2 Electrochemical performance of ZnO-based network composite with 7 mg cm^{-2} unless otherwise noted. **(A)** Cyclic voltammetry (first 4 cycles), **(B)** successive charge-discharge curves at 0.2 A g^{-1}, **(C)** areal and volumetric capacity vs. cycle numbers of ZnO-based network composites with 7 and 11 mg cm^{-2} at 0.2 A g^{-1}, and **(D)** rate performance of ZnO-based network composite with 7 mg cm^{-2} at 0.2 and 0.5 A g^{-1}.

Through Fe doping, we sought to improve the electrochemical reversibility of ZnO, which was first evaluated in cyclic voltammetry (CV, **Fig. 6.2A**). It confirms reversible reactions of ZnO through the peaks at 0.75 V and 1.3 V in the 1st to 4th reductive and oxidative cycles, while three oxidative peaks at 0.3 V, 0.6 V and 0.7 V indicate the progressive de-alloying of Li_xZn (designated by three arrows.) The enhanced reversibility is also confirmed by the initial coulombic efficiency (ICE) of 72.1% in the first-cycle charge and discharge curves of a network composite of

7 mg cm^{-2} (**Fig. 6.2B**); in another composite of 11 mg cm^{-2}, it is 65.2% (**Fig. 6.2C**). These ICEs are higher than the typical ICE (59.6%) of undoped ZnO[8], and comparable to what was reported for Fe-doped ZnO in the literature.[6] The gravimetric capacity of the network composite at 7 mg cm^{-2} remained higher than 801 mAh g^{-1} at 0.2 A g^{-1} after 100 cycles (**Fig. 6.2B**) and comparable to the best result in the literatures[5], but it is significant that this was achieved at a very high loading. So the areal and volumetric capacities of 5.6 mAh cm^{-2} and 1990 mAh cm^{-3}, respectively (**Fig. 6.2C**), are all higher than the literature values; indeed, they are twice the corresponding values of commercial graphite electrodes. At a higher loading of 11 mg cm^{-2}, these capacities are 8.6 mAh cm^{-2} and 3031 mAh cm^{-3}, respectively, or 3 times and 6 times higher than those of commercial graphite anodes. The rate performance evaluated in **Fig. 6.2D** shows that a composite at 7 mg cm^{-2} can deliver 870 mAh g^{-1} at 0.2 A g^{-1} after 40 cycles, and 685 mAh g^{-1} at 0.5 A g^{-1} after 100 cycles, which is comparable to those in the literature,[5,7] but again the network composites outperform in volumetric and areal capacities in these tests.

6.4 Discussion

Our results show that the ZnO-based network composites have enhanced volumetric capacities and good initial coulombic efficiencies at high loadings. In this section, we will further compare them with the work in the literature and rationalize our findings.

Table 6.2 Comparison of electrochemical performance metrics for our network composites, various ZnO-based anode materials in the literature and commercial graphite.

Materials	ZnO/C Carbon Cloth	PEDOT-PSS ZnO/C	ZnO/ZnFe$_2$O$_4$	ZnO/NC	ZnO-Mn-C	Fe-doped ZnO/C	Commercial graphite	ZnO-based 3D composite
Initial coulombic efficiency (%)	71	59.6	70	69.6	67.3	62	85	72.1	65.2
Areal capacity (mAh cm^{-2})	1.2	1.02	0.5034	1.251	1.094	1.156	3.06	5.6	8.6
Volumetric capacity (mAh cm^{-3})	33	408	335.6	500.4	437.6	462.4	285.98	1990	3031
Gravimetric capacity	699	680	839	834	1094	680	244.8	800	779

(mAh g^{-1})									
Gravimetric rate (A/g)	0.5	0.49	0.5	0.5	0.1	0.2	0.124	0.2	0.2
Areal rate (mA cm^{-2})	0.85	0.735	0.3	0.75	0.1	0.34	1.55	1.4	2.2
Volumetric rate (mA cm^{-3})	23.5	294	200	300	40	136	159.8	500	780
Areal loading (mg cm^{-2})	1.7	1.5	0.6	1.5	1	1.7	12.5	7	11
Volumetric loading (g cm^{-3})	0.047	0.6	0.4	0.6	0.4	0.68	1.3	2.5	3.9
References	7	8	9	10	11	6	12	This work	

6.4.1 Comparison with literature and commercial graphite

The loadings of our network composites, from 7 mg cm^{-2} to 11 mg cm^{-2}, corresponding to 2.5 g cm^{-3} to 3.9 gcm^{-3}, are about one order of magnitude higher than that in the literature, 0.6 to1.7 mg cm^{-2}, and 3 times higher than the volumetric loading (1.29 g cm^{-3}) in commercial graphite. Yet as shown in **Table 2** our composites can maintain the same ICE (as high as 72%) and gravimetric capacity (as high as 800 mAh g^{-1}) as the best values in the literature[6-11]. Most remarkably, the gravimetric capacity of our composite is almost independent of loading, being 800 mAh g^{-1} at 7 mg cm^{-2} and 779 at 11 mg cm^{-2} after 100 cycles under 0.2 A g^{-1}, all higher or comparable to the best values in the literature of very low loading materials.[6-8] This is a direct manifestation that our network composites are functionally invariant, electrochemically. Thanks to the invariance, network composites can take full advantage of high loading, so that the areal and volumetric capacities ranging from 5.6 mAh cm^{-2} to 8.6 mAh cm^{-2} and from 1990 mAh cm^{-3} to 3031 mAh cm^{-3}, respectively, are 17 to 90 times higher than those of representative ZnO-based "advanced" electrodes in the literature: "ZnO/C Carbon Cloth", "PEDOT-PSS ZnO/C", "ZnO/$ZnFe_2O_4$", "ZnO/NC", "ZnO-Mn-C" and "Fe-doped ZnO/C". [6-11] Importantly, they also outperform commercial graphite by 2.5 times and 10 times, respectively. Correspondingly, the areal and volumetric rate capabilities of our composites are too outstanding, up to 33 times and 17 times, respectively, higher than those in the literature, [6-11] and 5 times higher than the rate capability of commercial graphite.

To clearly appreciate the attributes of ZnO-based network composite, we compare these attributes with those of ZnO-based "advanced" electrodes in the

literature and commercial graphite, in **Fig. 6.3**. Advanced electrodes only stand out in gravimetric capacity but pale in all other metrics that are of practical importance, including loadings, volumetric and areal capacities and rates. Commercial graphite is excellent in ICE, cyclic performance and loadings, but its volumetric and areal capacities and rates are incomparable to those of network composites. Accordingly, the low-cost ZnO-based network composites having significantly improved volumetric capacities and rate capabilities while maintaining good ICE stand as a real alternative to commercial graphite anodes for practical applications in lithium ion batteries.

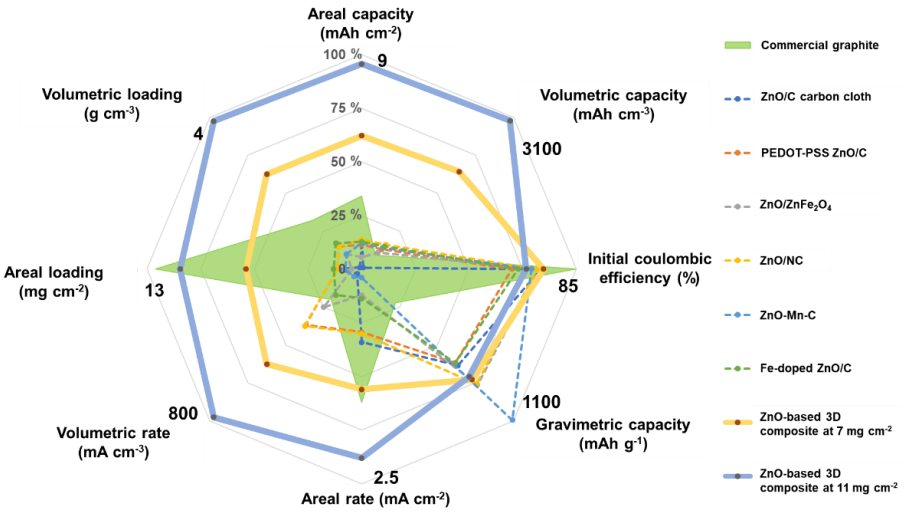

Figure 6.3 Comparison of properties of our composite with those of commercial graphite and ZnO-based materials in the literature after 100 cycles. Thickness of 25 μm assumed if the thickness of the electrode was not specified in the literature.

6.4.2 Rationale and significance

As already discussed in previous chapters, the key of achieving good performance for network composites is super-elasticity and high conductivity of

the 3D graphene backbone and the robust dispersion of oxide nanoparticles in the network. This is also the case here. It allows the advantage of 3D graphene (conductivity) and the synergy between 3D graphene and active ZnO nanoparticles to remain invariant to large compression ratios, which remove unnecessary macro-pores while preserve essential nano pores that allow access to electrolyte and accommodate volume expansion. In this way, the all critical length scale on the nanoscale for electron and ion transport remains unchanged, as does the finely distributed porosity important for mechanical integrity and liquid access. So, functional invariance is achieved despite a very extreme compression ratio. These hold the key to the superior performance of the network composite at high loadings. Of course, Fe doping of nanosized ZnO to improve intrinsic conductivity as practiced in this study is always important. Along this line, other promising methods to further refine the size and pore distribution may be worthwhile, such as urea-assisted synthesis of ZnO which generates substantial nanopores (3-5 nm) via gas release (CO_2 and H_2O). In contrast, standard approaches of combining carbon materials and ZnO, e.g., by simply adding nonelastic carbon cloth to bare ZnO as reported by Zhang et al.[7], are bound to fail, as evident from the extremely low loading of 0.047 g cm^{-3} indicating the existence of large pores in such composite.

6.5 Conclusions

Ultra-low-cost ZnO, at only $1/300^{th}$ of that of GeO_2 and comparable to that of commercial graphite, has been successfully incorporated into a network composite featuring high loading, high rate capability and high volumetric and areal capacity superior to those of graphite. It stands as a real alternative to graphite for practical anodes in commercial lithium ion batteries.

References

1 Park, K. T. *et al.* Facile synthesis of ultrathin ZnO nanotubes with well-organized hexagonal nanowalls and sealed layouts: applications for lithium ion battery anodes. **117**, 1037-1043 (2013).

2 Huang, X., Xia, X., Yuan, Y. & Zhou, F. J. E. A. Porous ZnO nanosheets grown on copper substrates as anodes for lithium ion batteries. **56**, 4960-4965 (2011).

3 Kim, C. *et al.* Graphene oxide assisted synthesis of self-assembled zinc oxide for lithium-ion battery anode. **28**, 8498-8503 (2016).

4 Shen, X. *et al.* Enhanced electrochemical performance of ZnO-loaded/porous carbon composite as anode materials for lithium ion batteries. **5**, 3118-3125 (2013).

5 An, G.-H., Lee, D.-Y., Ahn, H.-J. J. A. a. m. & interfaces. Tunneled mesoporous carbon nanofibers with embedded ZnO nanoparticles for ultrafast lithium storage. **9**, 12478-12485 (2017).

6 Bresser, D. *et al.* Transition-metal-doped zinc oxide nanoparticles as a new lithium-ion anode material. **25**, 4977-4985 (2013).

7 Zhang, G. *et al.* High-performance and ultra-stable lithium-ion batteries based on MOF-derived ZnO@ ZnO quantum Dots/C core–shell nanorod arrays on a carbon cloth anode. **27**, 2400-2405 (2015).

8 Xu, G.-L. *et al.* PEDOT-PSS coated ZnO/C hierarchical porous nanorods as ultralong-life anode material for lithium ion batteries. **18**, 253-264 (2015).

9 Hou, L. *et al.* Self-Sacrifice Template Fabrication of Hierarchical Mesoporous Bi-Component-Active ZnO/ZnFe2O4 Sub-Microcubes as Superior Anode Towards High-Performance Lithium-Ion Battery. **25**, 238-246 (2015).

10 Zhou, Z., Zhang, K., Liu, J., Peng, H. & Li, G. J. J. o. P. S. Comparison study of electrochemical properties of porous zinc oxide/N-doped carbon and pristine zinc oxide polyhedrons. **285**, 406-412 (2015).

11 Xie, Q. *et al.* Dual Electrostatic Assembly of Graphene Encapsulated Nanosheet-Assembled ZnO-Mn-C Hollow Microspheres as a Lithium Ion Battery Anode. **28**, 1707433 (2018).

12 Gallagher, K. G. *et al.* Optimizing areal capacities through understanding the limitations of lithium-ion electrodes. **163**, A138-A149 (2016).

Chapter 7 TiO_2-based 3D composites as high areal and volumetric capacity anodes of lithium-ion batteries

7.1 Introduction

7.1.1 Overview

As a potential electrode material, B-form (monoclinic) TiO_2 has a theoretical capacity of 335 mAh g^{-1}, which is comparable to the commercial graphite anode and better than that of commercial $Li_4Ti_5O_{12}$ anode (175 mAh g^{-1}). As an insertion-type of anode, it undergoes nearly negligible volume change (~3%) during lithiation/de-lithiation, which assures structural stability. It is also earth abundant making it suitable for commercial applications of lithium ion batteries (LIB). Meanwhile, pseudocapacitive lithium storage in nano-TiO_2 has been much explored and is believed to help the rate performance. Lastly, although the operating voltage of TiO_2 is > 1 V whereas Li metal formation requires one close to 0 V—making the energy density of the TiO_2/Li battery much lower than ideal, it does avoid the formation of Li metal which requires close to 0 V and happens to graphite anode thus presenting a safety issue. For these reasons, TiO_2 seems to offer a new potential anode material with the possibility of high-rate performance, high capacity, safety, and low cost.

However, as an anode material TiO_2 has the following drawbacks. First, the resistivity of TiO_2 is high, 10^{11} Ω m (vs graphite's 10^{-8} Ω m) due to its wide band gap (3.2 eV). Second, the theoretical gravimetric capacity of anatase TiO_2 (165 mAh g^{-1}) while comparable to that of graphite is quite low relative to other oxides (SnO_2, GeO_2, Fe_2O_3 and ZnO) described in this thesis. Of course, if one contemplates to use nanostructured TiO_2 for better electrochemical performance,

such material also tends to have a low packing density thus not suitable for commercial applications; this is a common problem for nanostructured materials as already mentioned in previous chapters.

This chapter aims to study whether a network composite of reduced nano-TiO_2 and superelastic conductive 3D graphene can achieve high conductivity and high loading good enough for practical use. Reduced nano-TiO_2 is used because of better conductivity, and anchoring it on a 3D graphene scaffold will hopefully further improve conductivity and make possible a robust composite whose performance is comparable to the best TiO_2-based anode materials in the prior work—albeit at a much higher mass loading. As an insertion-type material of very little volume change, it also provides a final case study in our development of network composites that incorporate various active oxides into a superelastic 3D graphene scaffold with the aim of superior electrochemical performance at a dramatically improved mass loading.

7.1.2 Literature review

Nanostructured TiO_2 with a shorter transport length of electrons and ions enjoys higher capacities. For example, Bruce et al.[1] reported that B-form TiO_2 nanoparticles can deliver a capacity of 240 mAh g^{-1} compared to 205 mAh g^{-1} of bulk TiO_2 at the rate of 50 mA g^{-1}; at the rate higher than 1000 mA g^{-1}, B-form TiO_2 with a further reduced diameter of 3 nm still outperforms that of TiO_2 of 6 nm. Wang etc.[2] prepared anatase-TiO_2 nanotubes of 10 nm diameter and 200 nm length, which when used as the anode of LIB delivered 200 mAh g^{-1}, higher than the theoretical capacity (165 mAh g^{-1}, which is lower than the value of 335 mAh g^{-1} for B-TiO_2). Similarly, nanosheets of anatase TiO_2 [3]have also been prepared to deliver a capacity of 202 mAh g^{-1} compared to 160 mAh g^{-1} of commercial TiO_2.

In another approach, carbon materials were combined with TiO_2 to improve the electrical conductivity of the electrode and enhance the rate performance. Liu et al.[4] utilized graphitic-carbon coated TiO_2 to obtain a capacity of 175 mAh g^{-1} at 80 mA g^{-1}, which is an improvement over the value of 150 mAh g^{-1} of TiO_2 without carbon coating. Similarly, nanostructured TiO_2 dispersed on graphene was reported to deliver 130 mAh g^{-1} at 1600 mA g^{-1} compared to 60 mAh g^{-1} of bulk TiO_2.[5]

Although carbon addition can enhance the conductivity of the composite, it does not affect the high resistance of TiO_2, which can be lowered by doping and reduction. Nb-doped TiO_2 nanofibers[6] were reported to have a capacity of 128 mAh g^{-1}, while undoped ones give 92 mAh g^{-1}. Likewise, Wang etc.[7] demonstrated a two-order-of-magnitude enhancement in conductivity by doping TiO_2 with Nb. Some N-doped TiO_2 has also been shown to have better performance. For example, Li et al. prepared N-doped TiO_2/ graphene sheets as an anode material, which delivered 165 mAh g^{-1} at 1 A g^{-1} vs. 135 mAh g^{-1} for the undoped counterpart.[8] Meanwhile, oxygen-deficient TiO_2 [9] obtained by a reduction treatment (e.g., H_2 thermal reduction) gave an enhanced capacity of 160 mAh g^{-1} at 0.336 A g^{-1} compared to 60 mAh g^{-1} for pristine TiO_2, again thanks to the improved conductivity of reduced TiO_2, which can reach two orders of magnitude.

Another effective method is to construct a nanostructured hierarchy to improve electrolyte transport within electrodes, which can facilitate the rate performance of TiO_2. For example, Shin etc.[10] found a hierarchical nanoporous TiO_2 could deliver a capacity of 138 mAh g^{-1} at 1.5 A g^{-1} vs. 25 mAh g^{-1} at 1.5 A g^{-1} without the hierarchical structure. As another example, from a paper-assisted synthesis method Zhao et al. obtained a hierarchical TiO_2 of a capacity of 100 mAh g^{-1} at the rate of 1.7 A g^{-1}.

Although the various forms of “advanced” TiO_2 as anode materials of LIB have achieved higher gravimetric performance, none of them has realized the high mass loading necessary for commercial utilization as will become apparent in a tabulated comparison presented later in this chapter. Therefore, encouraged by our success in previous chapters, we seek to combine conducting superelastic 3D graphene and N-doped nanoporous TiO_2 to obtain a high loading anode that can maintain a high capacity at high rates.

7.2 Experimental procedures

7.2.1 Synthesis

7.2.1.1 Synthesis of TiO_2-based 3D composite

To render the 3D graphene monolith hydrophilic, it was first immersed in nitric acid and heated to 100^{o}C for 12 h, then dried. Next, 0.005 mol $Ti(SO_4)_2$ (Alfa Aesar) and 0.01 mol urea (Alfa Aesar) and 0.0005 mol oleyl amine (Alfa Aesar) was dissolved in a mixture solution of 12 ml ethylene glycol and 3 ml DI water. In this solution the hydrophilic 3D graphene monolith was immersed for 2 h at room temperature to become thoroughly soaked. After that, the soaked 3D graphene and the solution was sealed in an autoclave for hydrothermal reaction at 120^{o}C for 2 h. After hydrothermal reaction, the 3D graphene was removed, rinsed by DI water and freeze-dried for 6 h. Thus dried 3D graphene remained as a monolith, and it was finally subject to calcination in air at 350^{o}C for 1 h.

7.2.1.2 NH_3 treatment of TiO_2-based 3D composite

According to the literature,[11,12] NH_3 treatment is effective for not only oxide reduction but also N doping of TiO_2. In this treatment, NH_3 at a flow rate of 500 sccm was used to flush the furnace for 20 min. After that, the furnace was ramped

to 550^{o}C in 120 min and the NH_3 flow was kept to dope TiO_2 with N and to reduce it. At the end of 120 min, the treated 3D monolith was removed from the tube furnace.

7.2.2 Characterization

7.2.2.1 Material characterization

Scanning electron microscopy (SEM) images were obtained in a field emission Magellan 400 microscope (FEI Company). Transmission electron microscopy (TEM), high angle annular dark field (HAADF) imaging, electron energy loss spectroscopy (EELS, Gatan), and elemental mapping were conducted in a JEOL 2100F microscope operated at 200 kV. Small and wide angle X-ray diffraction was performed in a Brucker D8 powder X-ray diffractometer using Cu *K*α radiation. The mass ratio of TiO_2 in TiO_2 -based 3D composites was determined by thermogravimetric analysis (TGA) at a heating rate of 10^{o}C min^{-1} in the temperature range of 25-900^{o}C in air using a thermal analyzer (NETZSCH STA 449 F3).

7.2.2.2 Electrochemical measurement

The as prepared TiO_2-based 3D composite, still a monolith which we call a network composite, was sliced into disks for later use. One or more pieces of these disks were directly used as a free-standing electrode (the working electrode, the anode); such electrode is free of binder and additional conductive additive or current collector. The counter electrode was made of lithium foils (China Energy Lithium Co., Ltd), and the set up was in the half-cell configuration in conjunction with a polymer membrane (Celgard) separator and $LiPF_6$ electrolyte in a 50:50 w/w mixture of dimethyl carbonate (DMC) and ethylene carbonate (EC). This configuration in a 2016 coin cell was assembled in argon in a glovebox with less

than 1 ppm oxygen and moisture. Galvanostatic charge and discharge measurements were conducted using a LAND-CT 2001C testing system within a voltage window of 0.01 V to 3.0 V. The rate capability was investigated by changing the current density from 0.2 A g^{-1} to 2 A g^{-1}. Cyclic voltammetry (CV) was conducted using an automated electrochemical workstation (CHI660E) at a scan rate of 0.2 mV/s in the voltage window of 0.01 V to 3 V.

7.3 Results

7.3.1 Material Characterization

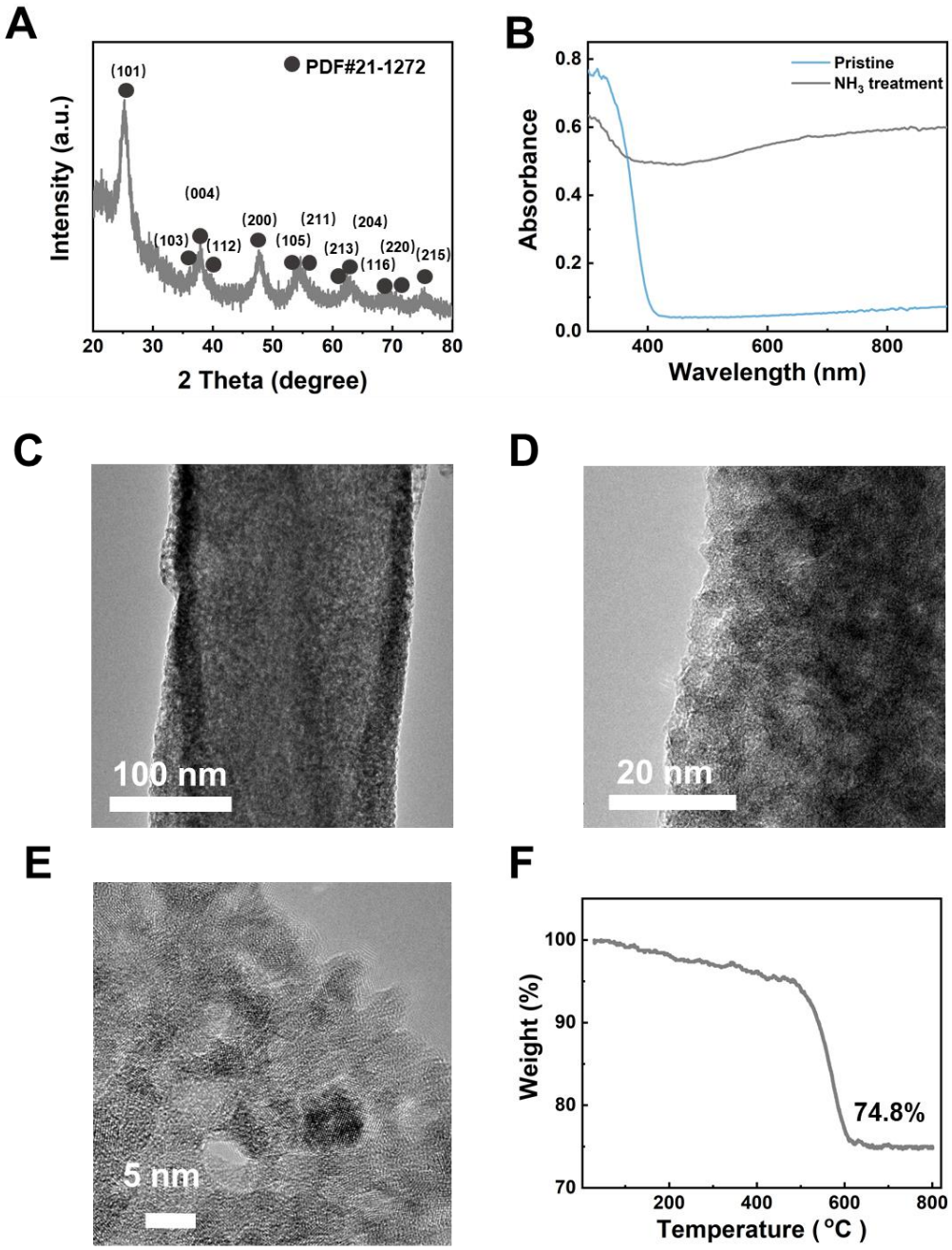

Figure 7.1 Materials characterization of TiO_2-based network composite unless otherwise noted. (A) X-ray diffraction pattern with TiO_2 (PDF#21-1272) peaks. (B) UV-Vis spectra of pristine TiO_2 powder and N-doped reduced TiO_2 powder (after NH_3-treatment). (C-D) Transmission electron microcopy (TEM) image, (E) high-resolution TEM image and (F) thermogravimetric analysis spectrum.

The X-ray diffraction pattern (**Fig. 7.1A**) of the composite shows the

anatase phase of TiO_2 (PDF#21-1272). The UV-Vis spectra in **Fig. 7.1B** comparing the pristine TiO_2 powder and N-doped reduced TiO_2 powder (after NH_3-treatment) reveal more optical absorbance of the latter. In pristine TiO_2, the absorption edge corresponding to the band gap is 3.2 eV, which is reduced to 2.5 eV in NH_3 treated TiO_2 consistent with a similar report for N-doped reduced TiO_2.[12] The above UV-Vis spectra were obtained using TiO_2 powders to avoid the interference of metallic graphene that has strong absorption.

A uniform coating of nanoparticles on the 3D graphene backbone is seen in **Fig. 7.1C**. The hydrothermal growth can generate 4-6 nm pores, which present as porosity in the coating as evident in **Fig. 7.1D**. Dispersed among such pores, TiO_2 nanoparticles of a diameter of 3-7 nm can be seen in **Fig. 7.1D**. These particles contain both amorphous and crystalline phases according to **Fig. 7.1D**, which is consistent with the literature report of an amorphous/crystalline mixed phase in N-doped TiO_2.[12] By TGA analysis (**Fig 7.1F**), we also determined the weight fraction of TiO_2 in the composite was 74.8%.

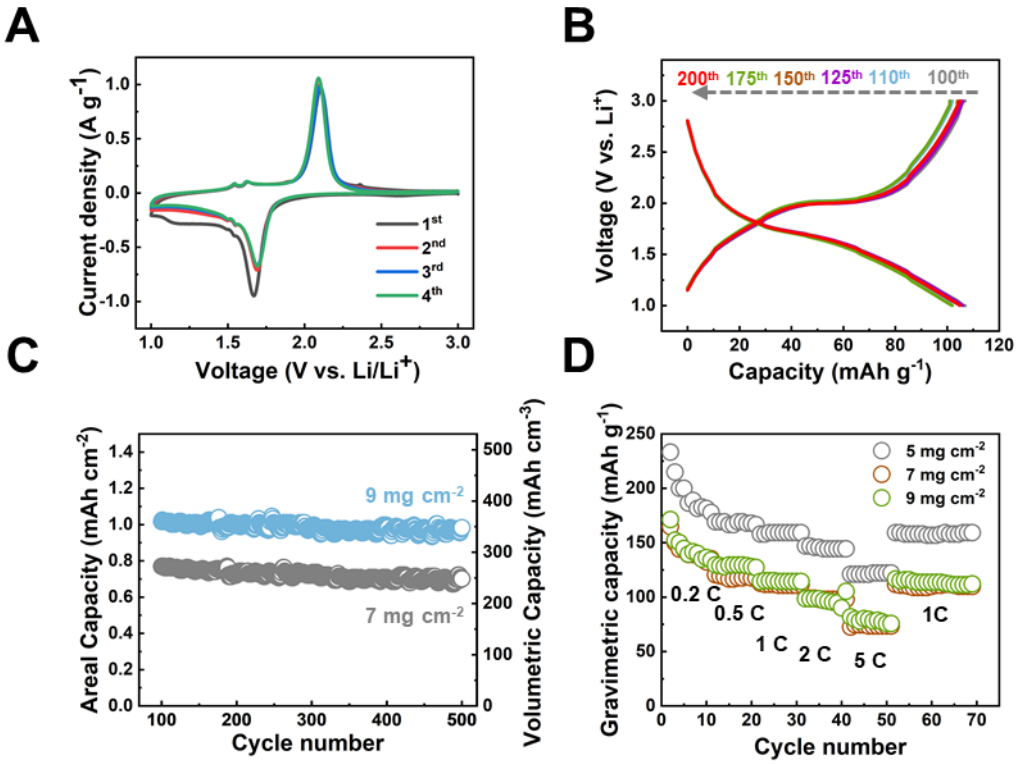

Figure 7.2 Electrochemical performance of TiO_2-based 3D composite with 7 mg cm^{-2} unless otherwise noted. (A) Cyclic voltammetry (first 4 cycles). (B) Successive charge-discharge curves at 0.168 A g^{-1} (1 C). (C) Areal and volumetric capacity vs. cycle numbers with 7 and 9 mg cm^{-2} at 0.168A g^{-1}(1 C). (D) Rate performance with 5, 7 and 9 mg cm^{-2} at 0.2C, 0.5C, 1C, 2C and 5C.

7.3.2 Electrochemical performance

The TiO_2-based 3D network at 7 mg cm^{-2} was first evaluated by cyclic voltammetry in **Fig. 7.2A**, where lithium extraction from titania was confirmed by the peaks at 1.7 V and 2.1 V in the 1st to 4th cycles. This is consistent with the successive charge-discharge curve of the network composite at 7 mg cm^{-2} under the current density of 1 C (168 mA g^{-1}, **Fig. 7.2B)**, where the corresponding two-phase plateaus appear at around 1.7 and 2.1 V. Owing to the high loading of these composites, their areal and volumetric capacities greatly exceed those of

"advanced" anatase-phase TiO_2-based anode materials in the literature. In **Fig. 7.2C**, at the current density of 1C and after 500 cycles, the composite of 7 mg cm^{-2} delivers 0.7 mAh cm^{-2} and 248 mAh cm^{-3}, while at 9 mg cm^{-2} it gives 1 mAh cm^{-2} and 348 mAh cm^{-3}. The high volumetric capacity of 348 mAh cm^{-3} is even higher than the value of 286 mAh cm^{-3} of commercial graphite anode. It is also notable that the composite suffers only a 5% capacity decay (from 367 mAh cm^{-3} to 348 mAh cm^{-3}) after 500 cycles. This is most remarkable since it is better than that of graphite, which decays by 13% after 500 cycles, a performance that is widely touted as one of the most advantageous features of commercial graphite electrodes. The rate capability of the network composite was evaluated in **Fig. 7.2D**, in which the composite loaded to 5 mg cm^{-2} of TiO_2 delivers 181 mAh g^{-1}, 168 mAh g^{-1}, 159 mAh g^{-1}, 144 mAh g^{-1} and 121 mAh g^{-1} at 0.2C, 0.5C, 1C, 2C and 5C, respectively (1C= 168 mA g^{-1}). At the loading of 7 mg cm^{-2}, the corresponding gravimetric capacities are 132 mAh g^{-1}, 118 mAh g^{-1}, 111 mAh g^{-1}, 98 mAh g^{-1} and 74 mAh g^{-1}, again at 0.2C, 0.5C, 1C, 2C and 5C, respectively. At 9 mg cm^{-2}, they are 135 mAh g^{-1}, 128 mAh g^{-1}, 114 mAh g^{-1}, 90 mAh g^{-1} and 76 mAh g^{-1}, respectively.

7.4 Discussion

Our results show that the TiO_2-based 3D graphene composites have superior areal and volumetric capacities, and despite high loadings they enjoy good capacity retention after long cycling. In this section, we will further compare them with literature work and rationalize this finding.

7.4.1 Comparison with literature and commercial graphite

Table 7.1 Comparison of electrochemical performance metrics of our network composites, various TiO_2-based anode materials in the literature, and commercial graphite.

Materials	H_2-reduced TiO_2-x	TiO_2/G	Nb-doped TiO_2	TiO_2/CMC	TiO_2 nanocube	Commercial graphite	TiO_2-based 3D composite		
Areal capacity (mAh cm^{-2})	0.13	0.13	0.15	0.36	0.15	3.06	0.72	0.78	1.03
Volumetric capacity (mAh cm^{-3})	52.40	143.98	58.80	144.27	58.00	285.98	253.97	274.07	361.90
Gravimetric capacity (mAh g^{-1})	131.00	130.00	98.00	142.00	145.00	244.80	144.00	111.00	114.00
Gravimetric rate （A g^{-1}）	0.34	1.00	0.07	0.66	0.08	0.12	0.34	0.17	0.17
Areal rate (mA cm^{-2})	0.34	1.03	0.10	1.68	0.08	1.55	1.68	1.18	1.51
Volumetric rate (mA cm^{-}	134.40	1107.53	40.20	670.56	33.60	159.80	592.5	414.81	533.33

^{3})							9		
Areal loading (mg cm^{-2})	1.00	1.03	1.50	2.54	1.00	12.50	5.00	7.00	9.00
Volumetric loading (g cm^{-3})	0.40	1.11	0.60	1.02	0.40	1.29	1.76	2.47	3.17
References	9	13	6	14	15	23	This work		

Our TiO_2-based network composites can achieve high areal loading of 9 mg cm^{-2} cm^{-3}, which is at much as 9 times that of the literature value[9,15], and close to that of commercial graphite (~10 mg cm^{-2}). The volumetric loading of our 3D composite can even surpass that of commercial graphite by ~2.5 times, and is at much as 8 times higher than that of the literature. Significantly, our composites can simultaneously offer high areal and volumetric loading (9 mg cm^{-2} and 3.17 g cm^{-3}, respectively), whereas other TiO_2 electrodes[14] with the highest areal loading of 2.54 mg cm^{-2} in the literature can just achieve 0.6 g cm^{-3} in volumetric loading indicating a substantial amount of excess pores still remaining in them. Even at such high loadings, our network composites can retain high gravimetric capacities relatively well. The composite at 5 mg cm^{-2} gives the capacity of 144 mAh g^{-1}, which is comparable to the highest values of anatase titania in the literature. [15] At 9 mg cm^{-2}, the composite still offers 114 mAh g^{-1}, comparable to the values in the literature for an electrode of a much lower loading (98 mAh g^{-1} at 1 mg cm^{-2}) [6]. Thanks to the high loading, the areal and volumetric capacities of network composites easily outperform those of "advanced" TiO_2: "H_2-reduced TiO_{2-x}" [9], "TiO_2/G"[13], "Nb-doped TiO_2"[6], TiO_2/CMC"[14], and " TiO_2 nanocube"[15]. The volumetric capacity of network composites also exceeds that of commercial graphite: it is 1.5 times that of commercial graphite. The rate performance is important for practical applications. On a mass basis, the current density of our composite is comparable to that of the literature (0.34 A g^{-1} vs. 0.08~0.34 A g^{-1}), however, the areal and volumetric current densities of our composites are up to 20 times and 18 times, respectively, higher than those of "advanced" TiO_2 in the literature. Importantly, these volumetric rates are 3 times better than those of

commercial graphite.

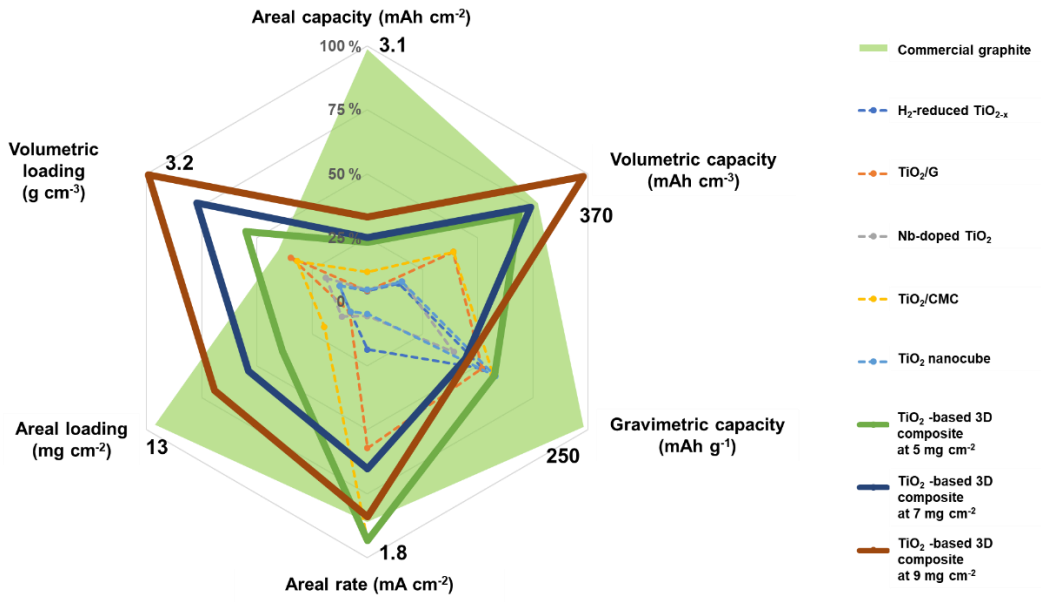

Figure 7.3 Comparison of properties of our network composite with those of literature materials after 100 cycle. Thickness of 25 μm assumed if the thickness of the electrode was not specified in the literature.

In **Fig. 7.3**, we summarize the 10th-cycle performance of "advanced" TiO_2 in the literature and our network composites. It is evident that the literature materials are comparable with ours in gravimetric capacity, which is close to the theoretical value, but they are rather poor in areal/volumetric capacities and loadings. While commercial graphite enjoys excellent areal loading, areal capacity and gravimetric capacity, its capacities and loadings in volumetric terms are relatively low compared to our composites. In addition, our composites suffer less capacity decay (only 5%) than commercial graphite (12.5%) after 500 cycles.

7.4.2 Rationale and significance

We believe the most important reason for the outperformance of our composites is the utilization of superelastic conductive 3D graphene and the robust adhesion of oxide nanoparticles onto 3D graphene. This allows functional invariance despite the extreme compression of the overall composite, because the local length scales critical for electron and ion/electrolyte transport and reactions remain unchanged, and a narrower though still open channel uniformly permeating the entire network still exists. Having the same length scales and not much additional interparticle interference, it is then possible to achieve a relatively high gravimetric capacity approaching the theoretical bulk capacity of anatase TiO_2, by taking advantage of the high reactivity of nano TiO_2, good rate/cycle performance at high loading, and the abundance of mesoscale accommodating sites availed by the 3D graphene network for ion transport. The N-doping strategy is critical for improving the electrical conductivity, which facilitates the rate capability, while the nano-scale pores generated through hydrothermal approach is important for ion transport as well. In contrast, notwithstanding a sophisticated set of nanostructured hierarchical porosity, materials produced in past efforts as reported in the literature still consist of large quantities of unnecessary pores/voids that are largely useless for electrochemical purposes. This has limited their maximum loading that can be utilized before the high rate-performance is compromised, and because of that, their low-loading electrodes (< 1 mg cm^{-2} and 1.5 g cm^{-3}) have little prospect for industrial applications.

As a purely insertion-type material, TiO_2 has a volume change of 3%, which is rather small and essentially negligible— it is even less than that of commercial graphite (10%). The smaller volume change has the drawback in not providing the

additional gravimetric capacities enjoyed by those anode oxides with conversion and alloying reactions. However, it does avoid the problem of capacity decay during cycling, which is a major drawback of other anode oxides. Indeed, the decay of these network composites after 500 cycles is less (by 60%) than that of commercial graphite anode. Therefore, even without the additional capacity, thanks to the cycle stability and the high volumetric loading made possible by the superelastic, functionally invariant compression, our anatase- TiO_2-based network composites can still deliver a better volumetric capacity than commercial graphite anode both initially and after repeated charging/discharging.

Lastly, this study suggests other insertion-type Li-accommodating materials, which all have relatively small volume changes (<50 %) during lithiation, can also be similarly incorporated into network composites of high loadings. This offers a feasible pathway to transition many advanced nanomaterials to a form closer to that of a practical electrode, thus greatly increase their chance for the actual use in lithium ion batteries.

7.5 Conclusions

A representative insertion-type of Li-incorporating oxide, TiO_2, with only 3% volume change during lithiation, has been successfully incorporated into network composites at high areal and volumetric loadings. These composites have high rate capability, high volumetric capacity and exceedingly low capacity decay after long cycling. This finding may encourage using other insertion-type of materials for practical electrodes of both cathodes and anodes in commercial lithium ion batteries.

References

1 Ren, Y. *et al.* Nanoparticulate TiO2 (B): an anode for lithium-ion batteries. **51**, 2164-2167 (2012).

2 Xu, J., Jia, C., Cao, B. & Zhang, W. J. E. a. Electrochemical properties of anatase TiO2 nanotubes as an anode material for lithium-ion batteries. **52**, 8044-8047 (2007).

3 Hao, B., Yan, Y., Wang, X., Chen, G. J. A. a. m. & interfaces. Synthesis of anatase TiO2 nanosheets with enhanced pseudocapacitive contribution for fast lithium storage. **5**, 6285-6291 (2013).

4 Liu, H., Li, W., Shen, D., Zhao, D. & Wang, G. J. J. o. t. A. C. S. Graphitic carbon conformal coating of mesoporous TiO2 hollow spheres for high-performance lithium ion battery anodes. **137**, 13161-13166 (2015).

5 Xin, X., Zhou, X., Wu, J., Yao, X. & Liu, Z. J. A. N. Scalable synthesis of TiO2/graphene nanostructured composite with high-rate performance for lithium ion batteries. **6**, 11035-11043 (2012).

6 Fehse, M. *et al.* Nb-doped TiO2 nanofibers for lithium ion batteries. **117**, 13827-13835 (2013).

7 Wang, Y., Smarsly, B. M. & Djerdj, I. J. C. o. m. Niobium doped TiO2 with mesoporosity and its application for lithium insertion. **22**, 6624-6631 (2010).

8 Li, Y., Wang, Z. & Lv, X.-J. J. J. o. M. C. A. N-doped TiO 2 nanotubes/N-doped graphene nanosheets composites as high performance anode materials in lithium-ion battery. **2**, 15473-15479 (2014).

9 Shin, J.-Y., Joo, J. H., Samuelis, D. & Maier, J. J. C. o. M. Oxygen-deficient TiO2− δ nanoparticles via hydrogen reduction for high rate capability lithium batteries. **24**, 543-551 (2012).

10 Shin, J. Y., Samuelis, D. & Maier, J. J. A. F. M. Sustained Lithium-Storage Performance of Hierarchical, Nanoporous Anatase TiO2 at High Rates: Emphasis on Interfacial Storage Phenomena. **21**, 3464-3472 (2011).

11 Chen, Y., Cao, X., Lin, B. & Gao, B. J. A. S. S. Origin of the visible-light photoactivity of NH3-treated TiO2: Effect of nitrogen doping and oxygen vacancies. **264**, 845-852 (2013).

12 Lin, T. *et al.* Effective nonmetal incorporation in black titania with enhanced solar energy utilization. **7**, 967-972 (2014).

13 Hu, T. *et al.* Flexible free-standing graphene–TiO2 hybrid paper for use as lithium ion battery anode materials. **51**, 322-326 (2013).

14 Mancini, M., Nobili, F., Tossici, R., Wohlfahrt-Mehrens, M. & Marassi, R. J. J. o. P. S. High performance, environmentally friendly and low cost anodes for lithium-ion battery based on TiO2 anatase and water soluble binder carboxymethyl cellulose. **196**, 9665-9671 (2011).

15 Yang, X. *et al.* Size-tunable single-crystalline anatase TiO2 cubes as anode materials for lithium ion batteries. **119**, 3923-3930 (2015).

Chapter 8 Summary and outlook

In this thesis, we have developed a new graphene monolith that is superelastic, meso-porous, three-dimensional and metallic conducting, both with and without dopants which may be used to tune nanopores in addition to providing functionality. While the 3D graphene itself is an active anode material, it also serves as an ideal backbone scaffold to bear active oxide nanoparticles, to obtain an oxide-graphene composite monolith that can be further compressed, still as a monolith, into a high-density electrode. This composite form proves to be an effective way to transform a series of high-capacity oxide materials, SnO_2, GeO_2, Fe_2O_3, ZnO and TiO_2, into high areal and volumetric loading anodes. In this chapter, we will further compare these material systems among themselves and with graphite—currently the commercial anode material—to highlight the significance of this research. We will also suggest possible future work to further develop this approach.

Table 8.1 Comparison of electrochemical performance, at 100th cycle, of 3D graphene, oxide-based network composites, and commercial graphite.

Material system	3D graphene	B-N codoped 3D graphene	SnO_2-based composite	GeO_2-based composite		Fe_2O_3-based composite		ZnO-based composite		TiO_2-based composite	Commercial graphite
Areal loading (mg cm^{-2})	6.2	3.0	10.0	7.0	13.0	9.3	7.0	7.0	11.0	9.0	12.5
Volumetric loading (g cm^{-3})	2.2	1.1	3.5	2.5	4.6	3.3	2.5	2.5	3.9	3.2	1.3
Initial Coulombic efficiency (ICE)	42%	45%	63%	76%	73%	69%	75%	72%	65%	36%	85%

Gravimetric capacity (mAh g^{-1})	724.9	700.0	939.1	1716.0	1518.0	714.0	744.0	800.0	779.0	114.0	244.8
Areal capacity (mAh cm^{-2})	4.5	2.1	9.4	12.0	19.7	6.5	5.2	5.6	8.6	1.0	3.1
Volumetric capacity (mAh cm^{-3})	1585.3	740.7	3312.5	4237.0	6961.0	2341.9	1827	1990	3031	361.9	286.0
Gravimetric rate (A g^{-1})	0.2	1.0	0.2	0.2	0.2	0.5	0.5	0.2	0.2	0.2	0.12
Areal rate (mA cm-2)	1.2	3.0	2.0	1.4	2.6	4.7	3.5	1.4	2.2	1.5	1.55
Volumetric rate (mA cm-3)	437.4	1058.2	705.5	494.0	917.0	1640	1235	500.0	780.0	533.3	159.80

8.1 Screening of oxide-based composites

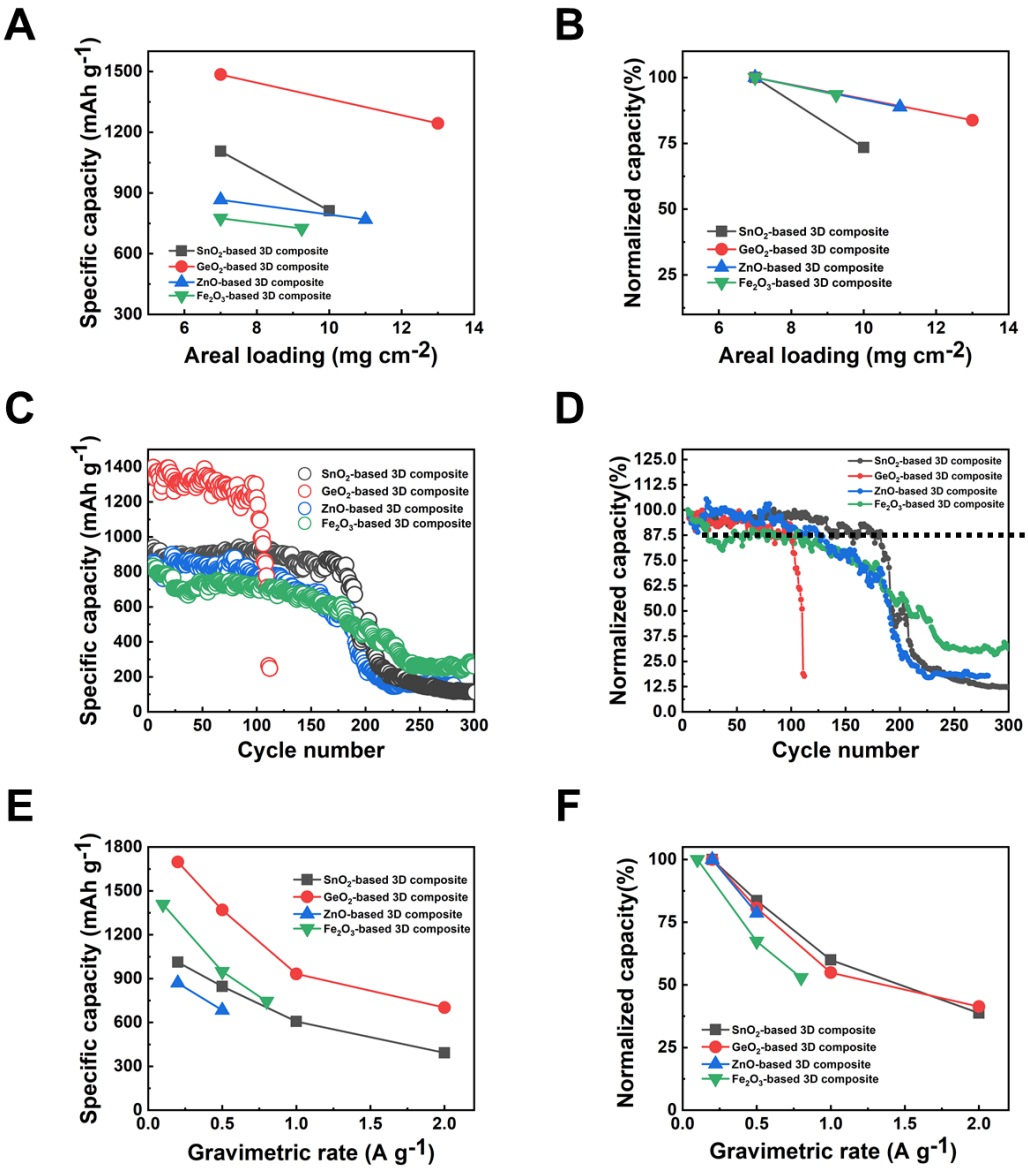

Figure 8.1 (A) Specific capacity vs. areal loading for oxide-based composites, capacities recorded after 12.5% decay under current density of 0.2 A g^{-1}, except for Fe_2O_3 under 0.5 A g^{-1}. **(B)** Normalized capacity of **(A)**. **(C)** Specific capacity vs. cycle number for oxide-based composites: SnO_2-based composite at 10 mg cm^{-2}, GeO_2-based composite at 13 mg cm^{-2}, ZnO-based composite at 11 mg cm^{-2} and Fe_2O_3-based composite at 9 mg cm^{-2}; capacities recorded under current density of 0.2 A g^{-1}, except for Fe_2O_3 under 0.5 A g^{-1}.

(D) Normalized capacity of **(C)**, with dotted line indicating capacity retention of 87.5%. **(E)** Specific capacity vs. gravimetric rate for 3D composites at same loading of 7 mg cm^{-2}. **(F)** Normalized capacity of **(E)**.

Before proceeding to the comparison with literature and commercial materials, we first conducted a screening study for the four high-performance composite systems based on SnO_2, GeO_2, ZnO and Fe_2O_3, using the criteria of insensitivity to loading, cycling and rate. This is shown in **Fig. 8.1A** and **B,** screened by loading, **in Fig. 8.1C** and **D**, screened by cycle durability, and **Fig. 8.1E** and **F**, screened by rate capability. Here, the screening study is made on the gravimetric basis because it reflects the intrinsic merit of a material that goes through electrochemical procedures.

First, it is seen that with the exception of SnO_2, which is slightly inferior, all three other composites show similar dependence on loading. Second, at a relatively high loading, the cyclic durability is largely maintained up to about 200 cycles except for GeO_2, which fades rapidly after about 100 cycles. Third, at the same loading of 7 mg cm^{-2}, the rate capability is similarly withstood in all composites. Therefore, it appears that all composites except those GeO_2-based ones are of practical interest. Nonetheless, thanks to high loading, GeO_2-based composites containing a relatively low-density oxide can still deliver very substantial areal and volumetric capacities after its gravimetric capacity suffers a 85% loss due to cycling; this is shown in **Table 8.2**.

8.2 Comparison of material systems

We summarize in **Table 8.1** the electrochemical performance of all our oxide-based network composites, along with commercial graphite and 3D

graphene, tested after 100 cycles, for which the following observations are pertinent.

First, SnO_2, GeO_2, Fe_2O_3, ZnO and TiO_2-based network composites can easily achieve areal and volumetric loadings of no less than 9 mg cm^{-2} and 3.2 g cm^{-3}, respectively. Specifically, GeO_2-based composite has the highest areal and volumetric loadings of 13 mg cm^{-2} and 4.6 g cm^{-3}, respectively, higher than graphite's 12.5 mg cm^{-2} and 1.29 g cm^{-3}, respectively. At the other extreme is 3D graphene, which has the lowest areal and volumetric loadings of 6.2 mg cm^{-2} and 2.2 g cm^{-3}, respectively, Although the areal loading of commercial graphite is exceeded only by GeO_2-based composite, the volumetric loadings of all the composites and 3D graphene easily surpass that of commercial graphite.

Second, the highest initial Coulombic efficiency (ICE), no less than 72%, is achieved in the composites of GeO_2, Fe_2O_3 and ZnO, but the value is still much lower than that of commercial graphite (85%). Since the reason for the lower initial ICE is the high surface area in these nanocomposites, it can be remedied by pre-lithiation, which covers the surface and increases the efficiency to 99% even in 3D graphene that initially has an efficiency of only 42%.

Third, capacities on the gravimetric, areal and volumetric bases of all of our materials follow the same decreasing sequence from GeO_2, SnO_2, ZnO, Fe_2O_3, 3D graphene to TiO_2, which is almost identical to the sequence of their volume expansion in %, from 376% (SnO_2), 306% (GeO_2), 153% (ZnO), 93% (Fe_2O_3), 10% (graphite) to 3% (TiO_2).

Fourth, Fe_2O_3 achieves the highest areal and volumetric rates of 4.7 mA cm^{-2} and 1640 mA cm^{-3}, which are 2.9 and 10.3 times those of commercial graphite. Even B-N codoped 3D graphene at a modest loading of 3 mg cm^{-2} achieves 3 mA

cm^{-2} and 1058 mA cm^{-3}, which are 2.9 and 10.3 times those of commercial graphite. This, however, is strongly dependent on the nanostructure. For example, in undoped 3D graphene that has smaller pores though a higher surface area, the areal and volumetric rates are lower, only 1.2 mA cm^{-2} and 437 mA cm^{-3}, respectively, at 6.2 mg cm^{-2}.

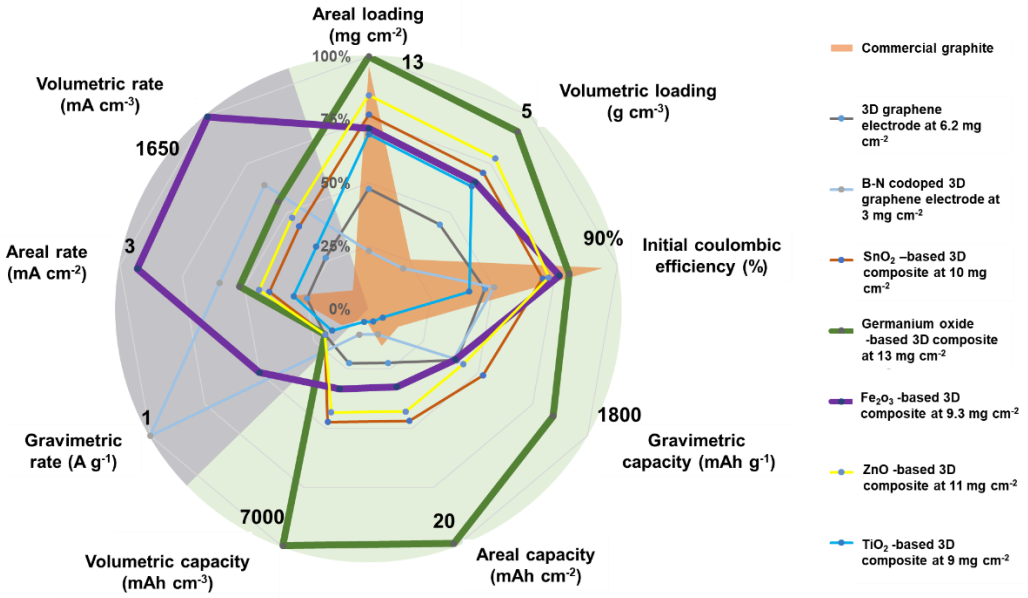

Figure 8.2 Comparison of properties of oxide-based network composites, 3D graphenes and commercial graphite, at 100^{th} cycle.

Properties listed in **Table 8.1** are plotted in **Fig. 8.2** for further comparison. Although commercial graphite maintains excellent areal loading and ICE, most oxide-based network composites outperform it in other metrics, especially in volumetric loading and capacities, and rates on the gravimetric, volumetric and areal bases. In particular, Fe_2O_3-based network composite and N-B codoped 3D graphene excel in rates on gravimetric, volumetric and areal bases, whereas the ICE, loadings and capacities on gravimetric, areal and volumetric bases of GeO_2-based 3D composite exceed those of all others. This is because the combination of high loading and a high gravimetric capacity of a light oxide such as GeO_2 can

endow to the composite a very large areal/volumetric capacity.

Table 8.2 Comparison of electrochemical performance, after 700 cycles, of selected material systems: commercial graphite, oxide-based network composites, and 3D graphene.

Material system	Commercial graphite	SnO_2-based composite	GeO_2-based composite	B-N codoped 3D graphene	TiO_2-based composite
Areal rate (mA cm^{-2})	2.8	4.0	9.6	3.0	1.0
Volumetric rate (mA cm^{-3})	283.5	1410.9	3386.2	1058.2	352.7
Gravimetric rate (A g^{-1})	0.1	0.2	0.2	1.0	0.2
Volumetric loading (g cm^{-3})	1.3	1.8	4.2	1.1	1.8
Areal loading (mg cm^{-2})	12.5	5.0	12.0	3.0	5.0
Gravimetric capacity (mAh g^{-1})	152.0	502.0	369.0	590.7	145.7
Areal capacity (mAh cm^{-2})	1.9	2.5	4.4	1.8	0.8
Volumetric capacity	195.9	885.0	1562.6	617.9	287.1

(mAh cm^{-3})

To compare them after longer cycling, in **Table 8.2** and **Fig. 8.3** we summarize the performance metrics of several materials that have been cycled 700 times. These include N-B codoped 3D graphene and three network composites, based on SnO_2, GeO_2, and TiO_2. After 700 cycles, commercial graphite features a higher areal loading than our materials, while all three composites are much superior in volumetric loadings and capacities. In addition, even at a slight lower areal loading than that of commercial graphite (12 mg cm^{-2} vs 12.5 mg cm^{-2}), GeO_2-based 3D composite easily outperforms commercial graphite in all other metrics. Of all the materials in **Table 8.2** and **Fig. 8.3**, B-N codoped 3D graphene and SnO_2-based 3D composite have the best gravimetric capacities and rates, whereas thanks to its high loadig GeO_2-based 3D composite performs best in areal and volumetric rates, loadings, and capacities. It is interesting to note that the above holds even after the gravimetric capacity of GeO_2 has suffered 85% loss during cycling. This is because the combination of high loading and an oxide of just a modestly high gravimetric capacity can endow to the composite a relatively large areal/volumetric capacity.

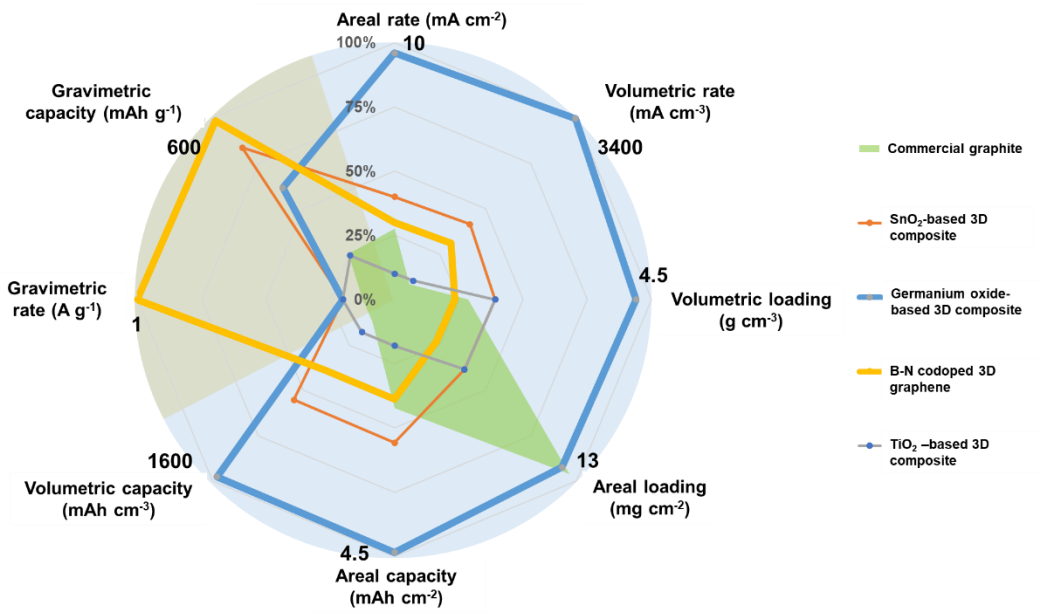

Figure 8.3 Comparison of properties of selected oxide-based network composites, 3D graphene and commercial graphite at 700th cycle.

8.3 Significance, rationale and concluding remarks

The outperformance of all 3D composites in most metrics clearly attests to the merit of our approach, which takes a superelastic, conductive 3D graphene monolith and various high-capacity oxide nanoparticles, applies robust adhesion between them, and forms an oxide-graphene network composite monolith. This composite can withstand large compression that removes the unnecessary void space in the composite, and thanks to its network microstructure the compressed monolith still maintains functional invariance as reflected in nearly the same gravimetric electrode properties with and without compression. This is possible because after the compression the local length scales critical for electron and ion/electrolyte transport and reactions remain unchanged, members in the network interfere with each other only at a few point contacts that are hardly obstructing, and a narrower though still open channel uniformly permeating the entire network

still exists. Having the same transport length scales and not much suffering from interparticle interference, the composite can achieve good cycle performance by taking advantage of the high reactivity of nanomaterials, good rate performance at high loading, and the abundant mesoscale accommodating sites availed by the 3D graphene network for the volume expansion (from 3% to 376%) of oxides during repeated lithiation. Advanced oxide electrodes and their composites in the literature typically perform poorly at high loadings. This is because despite their complicated nanoporous and hierarchical structures they still contain a large amount of large pores and void space that are poorly utilized in bettering performance, or have microstructures and nanostructures that rapidly deteriorate with loading due to increasingly unfavorable processing kinetics and/or compaction damage. Consequently, to remain functional, they are forced to use low areal and volumetric loadings, generally less than 1 mg cm^{-2} and 1.5 g cm^{-3}, respectively, which make them unsuitable for practical applications.

We thus conclude,

1. Superelastic conductive 3D graphene, after compression, is already an outstanding anode material as shown by our work on the B-N codoped composition. It is likely that such monolith is the ultimate scaffold/backbone for all composites that must endow much improved conductivity to relatively insulating active materials to qualify for electrode applications. B and N cooping, and possibly other doping schemes, can further optimize the nanostructure of 3D graphene for the best electrochemical performance for the network composites.
2. For short operating cycles (less than 100), Fe_2O_3-based network composite can be charged/discharged at the highest rates on all three bases,

gravimetric, volumetric and areal, whereas GeO_2-based 3D composite has the highest ICE, loadings and capacities on gravimetric, areal and volumetric bases.

3. For longer cycles (700), GeO_2-based 3D composite remains to be the best, outperforming in areal and volumetric rates, loadings, and capacities, despite its gravimetric rate and capacity are not the highest.
4. While commercial graphite has the advantage of highest ICE and generally outstanding cycle durability, oxide-based network composites, especially the GeO_2-based ones, outperform it in all other metrics.
5. Pre-lithiation is effective for overcoming the poor ICE of 3D composites and 3D graphene, which all have high surface areas.

8.4 Future work

- Although nanomaterials have many advantages such as better reactivity and conductivity that help improve the reversibility of conversion reactions, their large surface area poses a fundamental issue that need to be resolved. The most notable drawback is the formation of SEI, which consumes lithium in the battery. ALD coating of inert Al_2O_3 onto the surface of the 3D composite may help. It will result in an artificial, robust SEI that obviates the need for the further formation of a natural SEI, which is usually gel-like and of poor integrity as it is formed by the decomposition of electrolytes.
- With high oxide loading made possible by the network composite approach, our high loading anodes can deliver high areal and volumetric capacities under high areal and volumetric rates even after long cycles (700 cycles). However, cycle durability of the high loading composites is still unsatisfactory under

high gravimetric rates. Therefore, there is much room for improvement, especially for oxides with intrinsically higher electrical conductivity and smaller band gaps, such as Fe_2O_3.

- While we have discovered 3D graphene is potentially a high-loading, high-performance anode itself after it is compressed, there is room for further optimization as demonstrated by our finding that B-N codoping can greatly improve its high loading performance. Since 3D graphene is likely the ultimate scaffold/backbone for constructing network composites to incorporating active oxides of all kinds, it will be worthwhile to develop the optimized 3D graphene and form composites with it. These composites are likely to have improved properties especially in the rate performance and cycle life.

Appendix

Appendix 1 Supplementary materials of Chapter 2

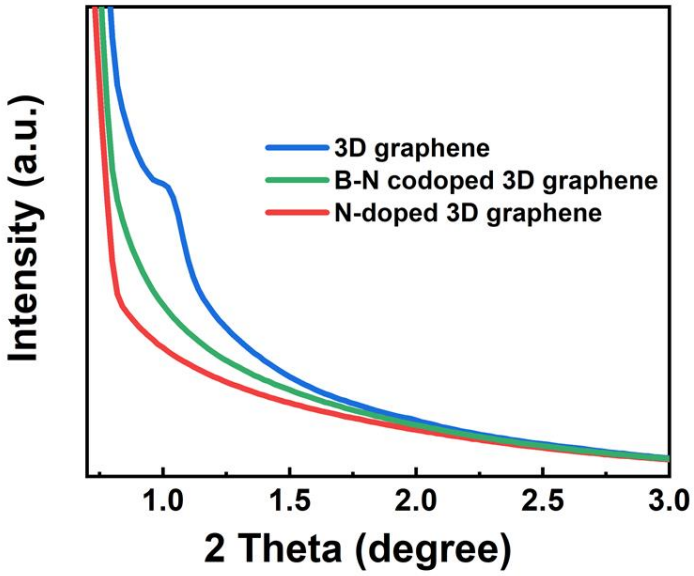

Appendix Figure 1.1 Small angle x-ray diffraction patterns of undoped 3D graphene, B-N codoped 3D graphene and N-doped 3D graphene. The peak at 1 degree in undoped 3D graphene consistent with the (100) reflection of a hexagonally ordered cylindrical structure, which is apparently lost after N and B-N doping 3D because of heteroatom disordering.

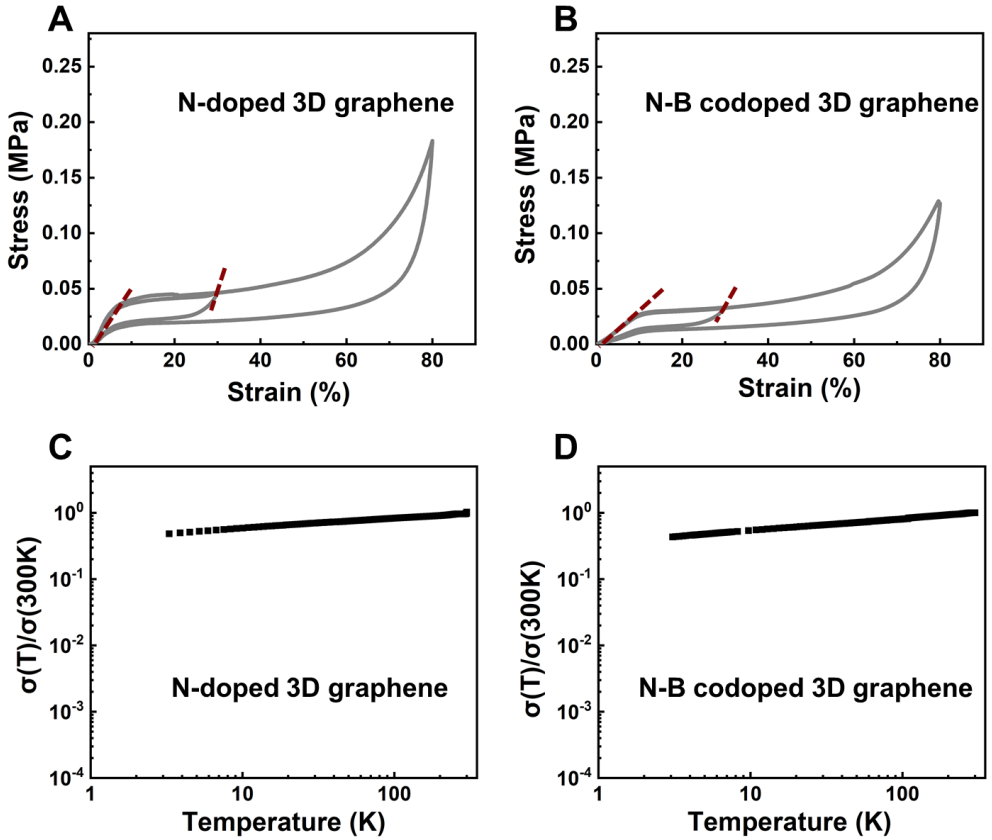

Appendix Figure 1.2 Stress-strain curve of **(A)** N-doped 3D graphene up to 80% strain with intermediate unloading, and **(B)** N-B codoped 3D graphene up to 80% strain with intermediate unloading, both with full recovery after unloading. The modulus is 800 KPa during unloading vs. 528 KPa during loading at 0-30% strain for N-doped 3D graphene, and likewise 386 KPa vs. 265 KPa for N-B codoped 3D graphene. Normalized conductivity of **(C)** N-doped 3D graphene and **(D)** N-B codoped 3D graphene as a function of temperature from 2K to 300K, both of the metallic type similar to that seen in undoped 3D graphene. At 300K, conductivities of undoped 3D graphene, B-N codoped 3D graphene and N doped 3D graphene are 1.01 S m^{-1}, 0.51 S m^{-1} and 0.49 S m^{-1}, respectively, respectively.

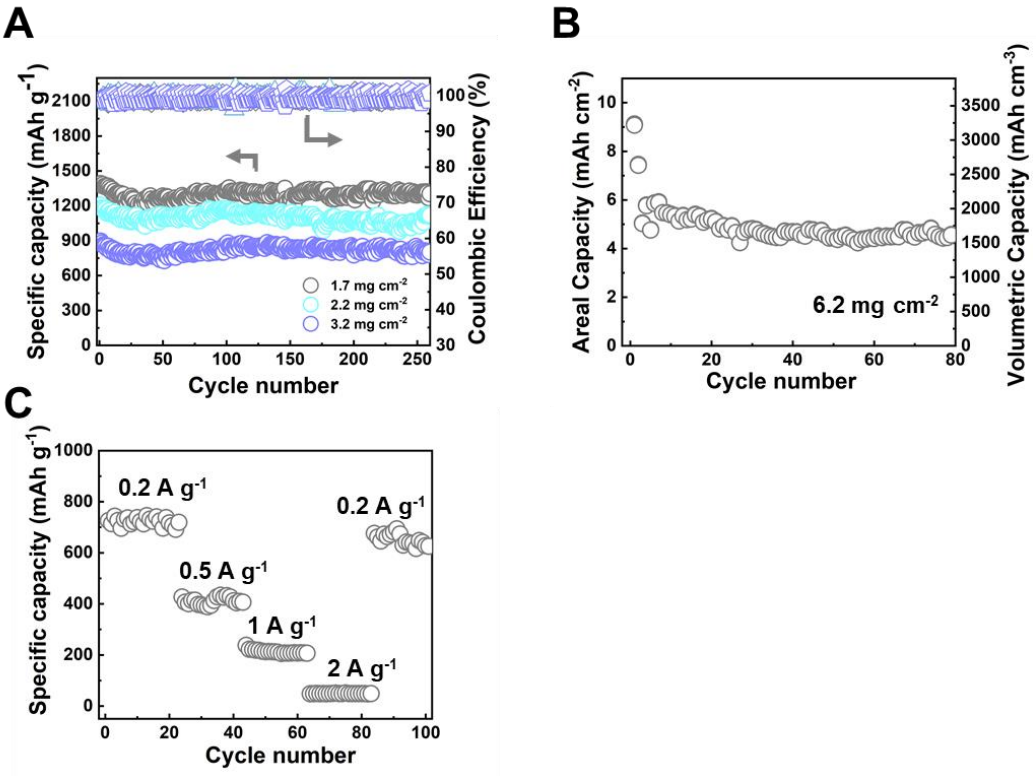

Appendix Figure 1.3 Electrochemical performance of undoped 3D graphene. **(A)** Specific capacity and coulombic efficiency vs. cycle number of pre-lithiated sample at 1.7, 2.2 and 3.2 mg cm^{-2} under 0.2 A g^{-1} **(B)** Areal and volumetric capacity vs. cycle number at 6.2 mg cm^{-2} under 0.2 A g^{-1}. **(C)** Rate performance at 3 mg cm^{-2} under 0.2, 0.5, 1 and 2 A g^{-1}.

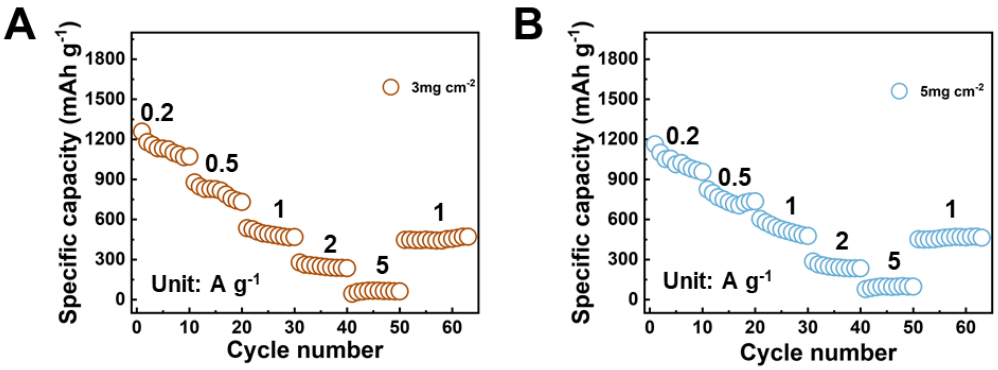

Appendix Figure 1.4 Electrochemical performance of B-N codoped 3D graphene. **(A)** Rate performance at 3 mg cm^{-2} under 0.2, 0.5, 1, 2 and 5 A g^{-1}. **(B)** Rate performance at 5 mg cm^{-2} under 0.2, 0.5, 1, 2 and 5 A g^{-1}.

Appendix 2 Supplementary materials of Chapter 3

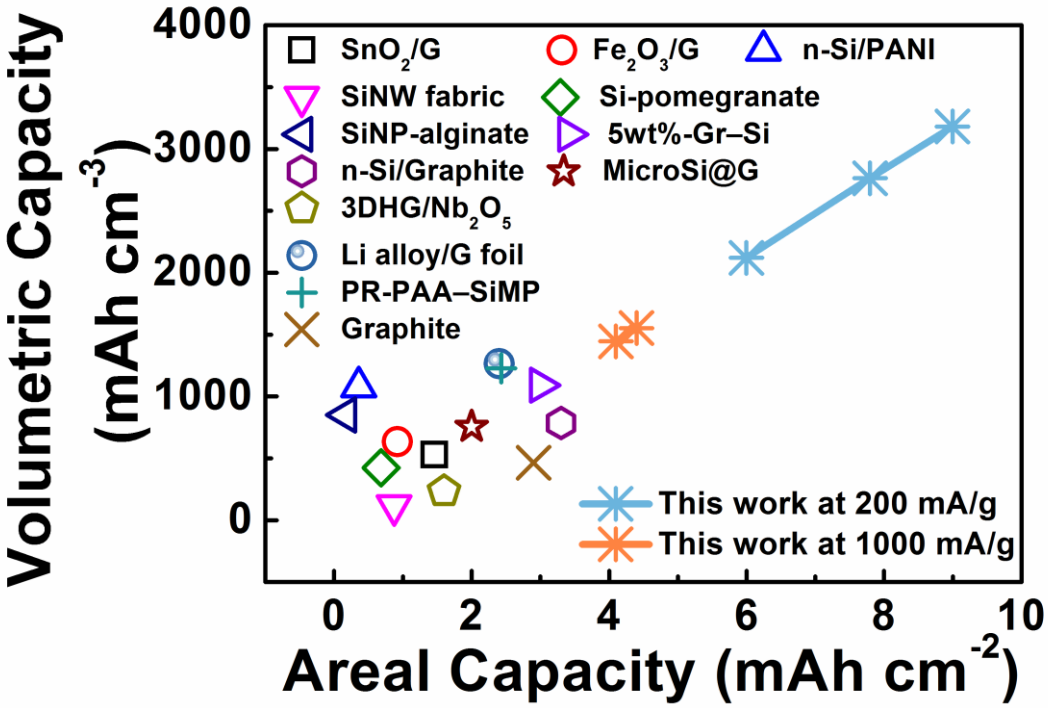

Appendix Figure 2.1 Volumetric and areal capacities of anodes. Network composite data are shown at two loading rates. Other anodes are SnO_2/G[1], Fe_2O_3/G[2], n-Si/PANI[3], SiNW fabric[4], Si-pomegranate[5], SiNP-alginate[6], 5wt%-Gr-Si[7], n-Si/Graphite[8], MicroSi@G[9], 3DHG/Nb_2O_5[10], Li alloy/G foil[11], PR-PAA-SiMP[12], and Graphite[13]. Capacity calculated using dimensions of the whole electrode, including current collectors, if any. Wherever unspecified, a 10 µm thick copper collector is assumed.

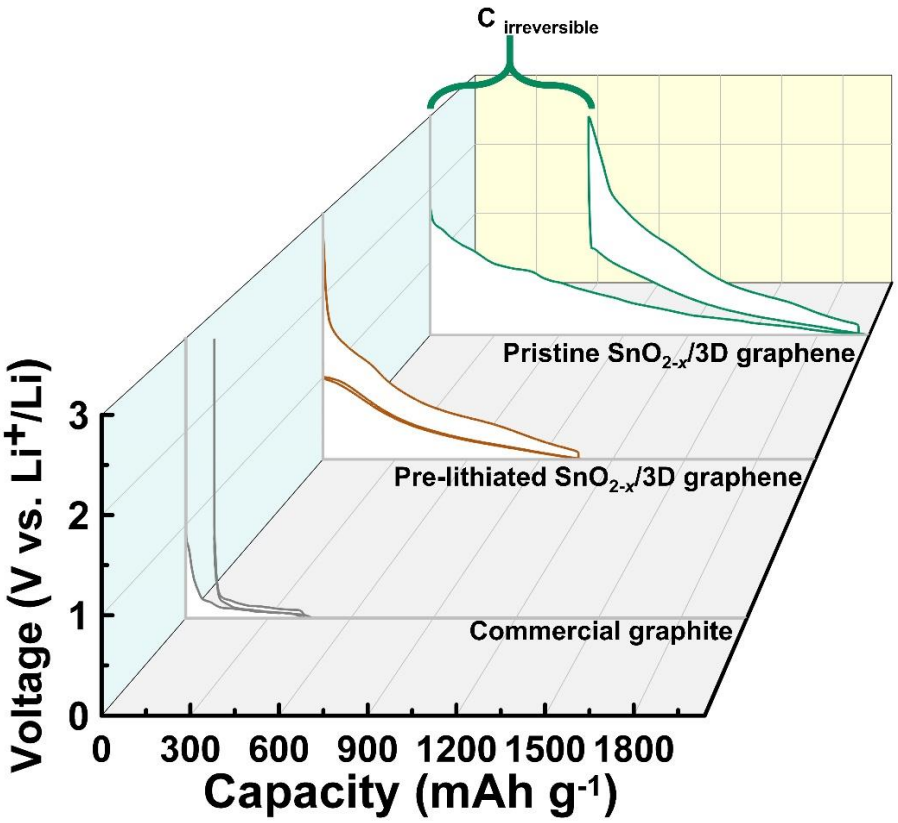

Appendix Figure 2.2 The voltage vs. capacity profile of the 1st discharging curve (the curve on the left), the 1st charging curve and 2nd discharge curve (the curve on the right) of commercial graphite anode, and SnO_2-based 3D composite at 5 mg cm^{-2} with and without pre-lithiation treatment, tested at 0.2 A/g.

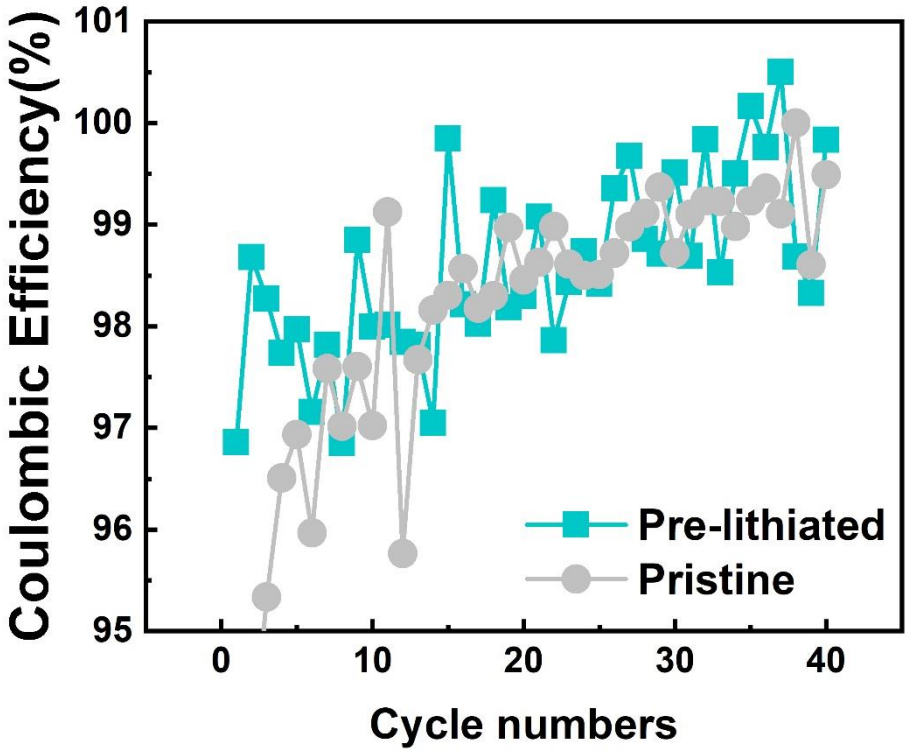

Appendix Figure 2.3 The coulombic efficiency vs. cycle number of SnO_2-based 3D composite at 5 mg cm^{-2} with and without pre-lithiation treatment; all tested at 0.2 A/g.

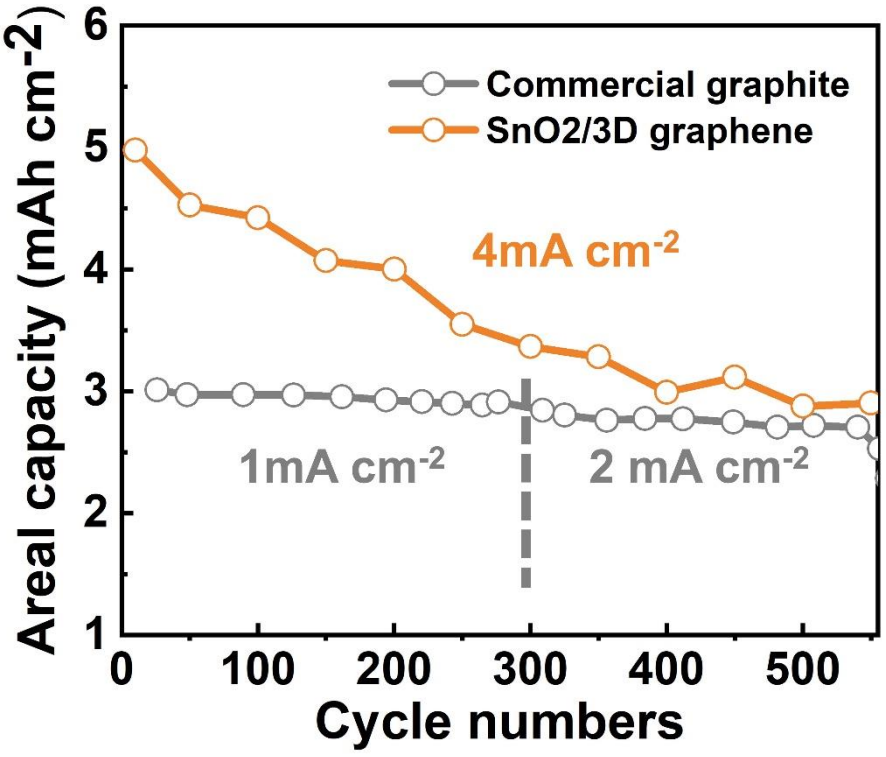

Appendix Figure 2.4 The areal capacity vs. cycle number of commercial graphite tested at 1 mA cm^{-2} and 2 mA cm^{-2}, and SnO_2-based 3D composite at 5 mg cm^{-2} tested at 4 mA cm^{-2}.

Appendix 3 Supplementary materials of chapter 4

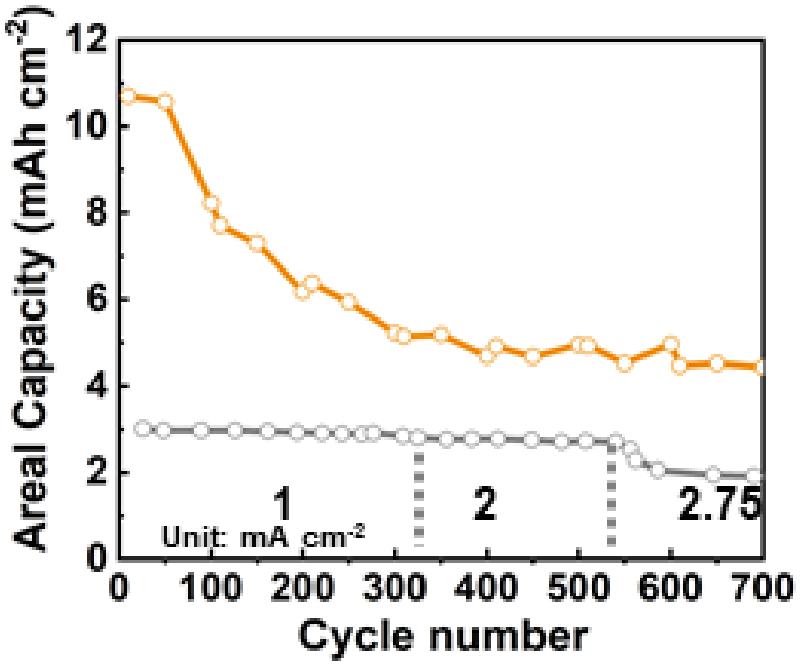

Appendix Figure 3.1 The areal capacity vs. cycle number of commercial graphite tested at 1 mA cm^{-2} 2 mA cm^{-2} and 2.75 mA cm^{-2}, and GeO_2-based 3D composite at 12 mg cm^{-2} tested at 9.6 mA cm^{-2}. Grey curve refers to commercial graphite, and orange curve refers to GeO_2-based 3D composite.

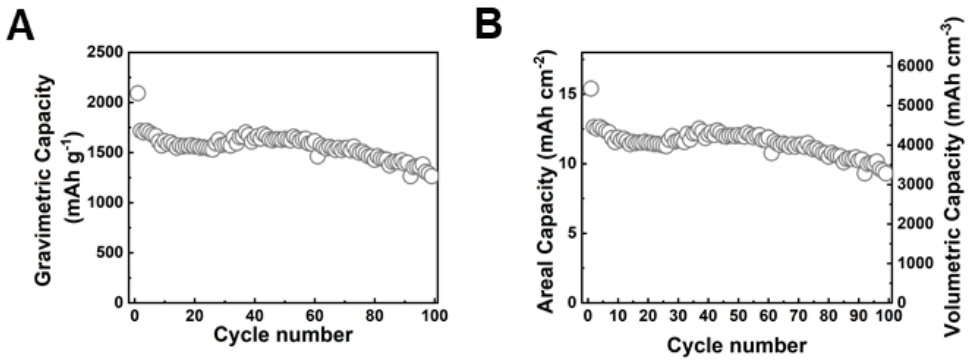

Appendix Figure 3.2 (A)The gravimetric capacity vs. cycle number of GeO_2-based 3D composite at 7 mg cm^{-2} under 0.2 A g^{-1}, (B) The areal and volumetric capacity vs. cycle number of GeO_2 -based 3D composite at 7 mg cm^{-2} under 0.2 A g^{-1}.

Appendix 4 Supplementary materials of chapter 5

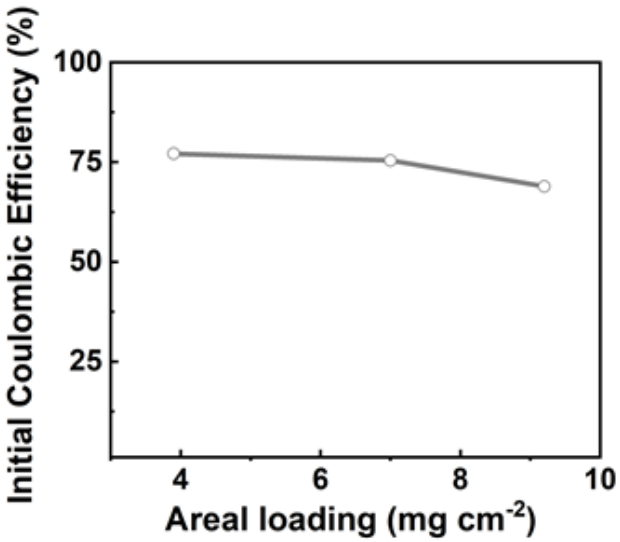

Appendix Figure 4.1 The initial coulombic efficiency vs. areal loading for Fe_2O_3-based 3D composite.

Appendix 5 Summary of void, compression ratio, dimensional information for alloy and conversion type anode 3D composite electrodes

Appendix Table 5.1 Summary of void, compression ratio, dimensional information for alloy and conversion type anode 3D composite electrodes

Network composite	SnO_2-based 3D composite		GeO_2-based 3D composite	ZnO-based 3D composite	Fe_2O_3-based 3D composite	3D graphene
Weight Ratio determined by TGA	68.8%		65.0%	62.8%	63.8%	N/A
Mass (mg)	1.43	1.02	0.92	1.44	1.36	0.99
Thickness of electrode before compression (cm)	0.160	0.117	0.093	0.147	0.143	0.298
Diameter of electrode before	0.4053	0.3832	0.3912	0.4061	0.4025	0.4220

compression (cm)						
volume before compression--Vb (cm^3)	0.0206	0.0135	0.0112	0.0190	0.0182	0.0417
density of electrode before compression (g cm^{-3})	0.0693	0.0756	0.0823	0.0757	0.0748	0.0237
Thickness of electrode after compression (cm)	0.0028	0.0028	0.0028	0.0028	0.0028	0.0028
Diameter of electrode after compression (cm)	0.4767=1.176	0.4421	0.4572=1.168	0.4762=1.171	0.4671=1.161	0.4891
volume after compression-Va (cm^3)	0.00051	0.00043	0.00047	0.00050	0.00049	0.00053

lateral (Poisson's) expansion	17.62%	15.37%	16.87%	17.26%	16.05%	15.90%
Va/Vb	2.45%	3.23%	4.16%	2.65%	2.67%	1.28%
(Thickness) Compression ratio	56	41	33	52	50	105
Theoretical density of oxide (g cm^{-3})	6.95		4.23	5.6	5.24	N/A
Volume fraction of oxide before compression	0.69%	0.75%	1.27%	0.85%	0.91%	N/A
Volume fraction of carbon before compression	0.96%	1.05%	1.28%	1.25%	1.20%	1.06%
Volume fraction of oxide after	28%	23%	30%	32%	34%	N/A

compression.						
Volume fraction of carbon after compression.	39%	33%	31%	47%	45%	83%
Volume fraction of pores after compression	33%	44%	39%	21%	21%	17%
Areal loading (mg cm^{-2}) after compression	8.02	6.65	5.61	8.09	7.94	5.27
Volumetric loading (g cm^{-3}) after compression	2.83	2.34	1.98	2.85	2.80	1.86
Volume change of oxide after full lithiation	376%		306%	153%	93%	N/A

Space-allowed fraction of oxide lithiation	31%	51%	42%	43%	66%	N/A
Calculated capacity (C_1)	760.9	1098.5	1231.8	789.2	933.2	N/A
The actual capacity(C_2)	930.0	1150	1518.0	835.0	956.0	N/A
The remaining capacity portion($1-C_1/C_2$)	18.2%	4.5%	18.9%	5.5%	2.4%	N/A

Note: In Chapter 3, we have illustrated these calculations for a SnO_2-based 3D composite. We concluded that in the SnO_2-based 3D composite, the available void space can only allow 31% of the theoretically-possible lithiation to proceed, which will deliver 463 mAh g^{-1} from the oxide. Taking the capacity contribution of 3D graphene (1412 mAh g^{-1} at 3 mg cm^{-2}, compared to (8.02 times 31.2%) 2.50 mg cm^{-2} of carbon in the composite after compression) into account, the calculated capacity of SnO_2-based 3D composite is (463x68.8%+1412x31.2%) 759 mAh g^{-1}, which is about 82% of actual capacity of SnO_2-based 3D composite of 930 mAh g^{-1}. The remaining 18% capacity can be accounted for if the 3D composite is allowed to expand by about 18% in volume (or 9% laterally) in the coin cell without experiencing interference and fractures,

which is possible because our coin cell was not full. These calculations are repeated here for all other composites containing oxides of the conversion and alloy type.

Appendix 6 Error analysis of electrochemical data

In this section, an error analysis of gravimetric capacity, areal capacity, volumetric capacity, and other electrochemical data is provided.

6.1 Error from mass measurement

The balance used (Quintix35-1CN) has a readability of 0.01 mg and repeatability of 0.02 mg. For the intermediate loading of 7 mg cm^{-2}, the sample mass is ~ 1.02 mg. So the fractional uncertainty = (0.01+0.02)/1.02 = 2.9 %. Similarly, for 10 mg cm^{-2}, the uncertainty is 2.1%, and for 5 mg cm^{-2}, the uncertainty is 4.2 %.

6.2 Error from the electrochemical tester[14]

The Electrochemical tester used (CT2001A-5V10mA) has an accuracy of ± 0.1% of FS + 0.1% RD. For the capacity of 1 mAh, the error as 1*0.1% +0.001=0.002 mAh, and the fractional uncertainty 0.002/1 =0.2 %.

6.3 Error of diameter, thickness, area and volume of 3D electrode

The precision of measurement of the diameter and thickness after compression of 3D graphene is 0.001 mm. The measured data and error analysis are listed in the following table.

Table 6.1 The measured data and error analysis of 3D composite electrodes

	1#	2#	3#	4#	5#	6#	Mean	Standard Error	Fractional Uncertainty
Diameter (cm)	0.4269	0.4358	0.4227	0.4323	0.4365	0.4216	0.4293	0.0059	0.6%
Area (cm^2)	0.1431	0.1491	0.1403	0.1467	0.1496	0.1395	0.1447	0.0040	1.2%
Thickness After Compression (cm)	0.0028	0.0024	0.0034	0.0028	0.0031	0.0027	0.0028	0.0001	5.2%
Volume (cm^3)	51.8	63.2	41.1	53.2	48.9	52.5	51.8	2.9	5.6%

In a recent study of lithium ion battery in the literature, a nominal fractional uncertainty of 4.0% for electrochemical measurement was reported.[15] In comparison, we have the following fractional uncertainty. For gravimetric capacity, the fraction uncertainty is 8.4 %, 7.1% and 6.3 % at the loading of 5, 7 and 10 mg cm^{-2}, respectively. For areal capacity, the fraction uncertainty is 9.6 %, 8.3% and 7.5%, respectively, at the above loadings. For volumetric capacity, the fraction uncertainty is 15.2 %, 13.9 % and 13.1 %, respectively, at the above loadings.

Table 6.2 Summary of fractional uncertainty for different capacities and loadings.

Loading (mg cm^{-2})	Fractional uncertainty of gravimetric capacity (%)	Fractional uncertainty of areal capacity (%)	Fractional uncertainty of volumetric capacity (%)
5	4+4.2 + 0.2 = 8.4	8.4 +1.2 = 9.6	9.6 +5.6 =15.2
7	4+2.9+0.2 = 7.1	7.1+1.2 = 8.3	8.3 +5.6 =13.9
10	4+2.1+0.2 =6.3	6.3+1.2 =7.5	7.5 +5.6 =13.1

References

1 Han, J. *et al.* Caging tin oxide in three-dimensional graphene networks for superior volumetric lithium storage. *Nature communications* **9**, 402 (2018).

2 Li, Z. *et al.* Twin-functional graphene oxide: compacting with Fe2O3 into a high volumetric capacity anode for lithium ion battery. *Energy Storage*

Materials **6**, 98-103 (2017).

3 Wu, H. *et al.* Stable Li-ion battery anodes by in-situ polymerization of conducting hydrogel to conformally coat silicon nanoparticles. *Nature communications* **4**, 1943 (2013).

4 Chockla, A. M. *et al.* Silicon nanowire fabric as a lithium ion battery electrode material. *Journal of the American Chemical Society* **133**, 20914-20921 (2011).

5 Liu, N. *et al.* A pomegranate-inspired nanoscale design for large-volume-change lithium battery anodes. *Nature nanotechnology* **9**, 187 (2014).

6 Kovalenko, I. *et al.* A major constituent of brown algae for use in high-capacity Li-ion batteries. *Science* **334**, 75-79 (2011).

7 Son, I. H. *et al.* Silicon carbide-free graphene growth on silicon for lithium-ion battery with high volumetric energy density. *Nature communications* **6**, 7393 (2015).

8 Ko, M. *et al.* Scalable synthesis of silicon-nanolayer-embedded graphite for high-energy lithium-ion batteries. *Nature Energy* **1**, 16113 (2016).

9 Li, Y. *et al.* Growth of conformal graphene cages on micrometre-sized silicon particles as stable battery anodes. *Nature Energy* **1**, 15029 (2016).

10 Sun, H. *et al.* Three-dimensional holey-graphene/niobia composite architectures for ultrahigh-rate energy storage. *Science* **356**, 599-604 (2017).

11 Zhao, J. *et al.* Air-stable and freestanding lithium alloy/graphene foil as an alternative to lithium metal anodes. *Nature nanotechnology* **12**, 993 (2017).

12 Choi, S., Kwon, T.-w., Coskun, A. & Choi, J. W. Highly elastic binders integrating polyrotaxanes for silicon microparticle anodes in lithium ion

batteries. *Science* **357**, 279-283 (2017).

13 Gallagher, K. G. *et al.* Optimizing areal capacities through understanding the limitations of lithium-ion electrodes. *Journal of The Electrochemical Society* **163**, A138-A149 (2016).

14 Error analysis. *https://www.webassign.net/question_assets/unccolphysmechl1/measurements/manual.html*; *http://www.phy.cuhk.edu.hk/djwang/teachlab/old%20material/Data%20Analysis/error_analysis.pdf*.

15 Taylor, J. *et al.* An insight into the errors and uncertainty of the lithium-ion battery characterisation experiments. *The Journal of Energy Storage* **24**, 100761 (2019).